Universiteit Gent
Faculteit Ingenieurswetenschappen
Vakgroep Elektronica en Informatiesystemen

Incorporatie van anisotrope geleidbaarheden in EEG-bronlokalisatie

Incorporation of Anisotropic Conductivities in EEG Source Analysis

Hans Hallez

Proefschrift tot het bekomen van de graad van
Doctor in de Ingenieurswetenschappen:
Biomedische Ingenieurstechnieken
Academiejaar 2008-2009

Universiteit Gent
Faculteit Ingenieurswetenschappen
Vakgroep Elektronica en Informatiesystemen
Voorzitter: prof. dr. ir. Jan Van Campenhout

Promotoren: prof. dr. Ignace Lemahieu
dr. ir. Bart Vanrumste
prof. dr. ir. Yves D'Asseler

Universiteit Gent
Faculteit Ingenieurswetenschappen

Vakgroep Elektronica en informatiesystemen (ELIS)
Instituut voor Biomedische Techniek (IBITECH)
Medische Signaal en Beeldverwerking (MEDISIP)
Campus Heymans, Blok B, 5e verdieping
De Pintelaan 185,
B-9000 Gent,
België

Tel.: +32-9-332.46.21
Fax.: +32-9-332.41.59

Dit werk kwam tot stand in het kader van een specialisatiebeurs van het IWT-Vlaanderen (Instituut voor de aanmoediging van Innovatie door Wetenschap en Technologie in Vlaanderen).

Proefschrift tot het behalen van de graad van
Doctor in de Ingenieurswetenschappen:
Biomedische Ingenieurstechnieken
Academiejaar 2008-2009

Acknowledgments

Even as a computer science engineer, I was always fascinated by the processes and mechanisms governing the human body and life. By doing this work I could apply my engineering skills on a problem involving one of the most complex organ of the human body: the human brain. A close collaboration with the department of Neurology and department of Radiology has given me new insights in this interesting scientific field. This and knowing that the work might be useful for applications in the scientific or clinical practice, has been my major motivation for completing this dissertation.

In the first place, I would like to express my gratitude to my promotors, ***prof. dr. Ignace Lemahieu****,* ***prof. dr. ir. Yves D'Asseler*** *and* ***dr. ir. Bart Vanrumste****. I especially would like to thank* ***prof. dr. Ignace Lemahieu*** *for offering me the opportunity to perform this research in the MEDISIP group and for his support and motivation. Much of gratitude is owed to* ***prof. dr. ir. Yves D'Asseler*** *for his suggestions and support. To* ***dr. ir. Bart Vanrumste*** *I owe much gratitude for critically evaluating my work for the past 4 years and for his permanent devotion and interest in my research. His knowledge and his willingness to answer my questions have led to this work in its current form.*

Furthermore, I would like to thank ***prof. dr. ir. Jan Van Campenhout****, chairman of the department of Electronics and Information Systems, for his interest in my work.* ***Prof. dr. Paul Boon****, head of the Department of Neurology, is kindly acknowledged for his hospitality to host me in his department. I want to thank* ***prof. dr. Rik Achten****, head of the MR department, for his hospitality during my visits to the MR department.*

I wish to thank my colleagues of the MEDISIP group and the IBITECH members for a pleasant working environment. More specifically, I am very grateful to ***dr. ir. Peter Van Hese****, for guiding me in my first steps of the biomedical signal processing and for his never-ending motivation. His challenging critical questioning of my work has been very stimulating for me. I hope we can still publish our article in* Nature *regarding the reuse of coffee pads. Much of gratitude is owed to* ***ir. Steven Delputte*** *and* ***dr. ir. Els Fieremans****, for the comprehensive answers to my many questions on diffusion tensor magnetic resonance imaging and for helping me with the data. I want to thank* ***ir. Sara Assecondi*** *for her support and suggestions. I want to thank to the members of the MEDISIP research meetings, chaired by* ***prof. dr. Stefaan Vandenberghe*** *and* ***dr. ir. Steven Staelens****, for their interest and support:* ***Jan****,* ***Erwann****,* ***Steven****,* ***Long****,* ***Roel****,* ***Vincent****,* ***Mahir****,* ***Jeroen****,* ***Tom****,* ***Ronald*** *and* ***Jelle****. I also want to thank* ***Rita****,* ***Ayfer*** *and* ***Anne-Marie*** *for their secretarial assistance.*

I would like to thank the staff of the Reference Center for Refractory Epilepsy of the Department of Neurology for their sympathy and interest in my work. Especially ***prof. dr. Kristl Vonck, MD*** *for her extensive knowledge and her dedication. Also* ***Evelien Carrette*** *is acknowledged for providing me with the extensive dataset. I would like to thank the members of the Laboratory of Clinical and Experimental Neurology (LCEN),* ***prof. Wytse Wadman****,* ***Robrecht****,* ***Tine****,* ***Veerle****,* ***Annelies****,* ***Liesbet*** *and* ***Dimitri*** *for their interest in my work. The former members,* ***Pieter Claeys*** *and* ***Tim Desmedt****, are gratefully acknowledged for giving me new insights in the neurophysiological processes behind brain activity.*

I would like to express my gratitude to ***prof. dr. ir. Rik Van de Walle****,* ***prof. dr. ir. Luc Dupré*** *and* ***Guillaume Crevecoeur*** *for the fruitful collaboration regarding*

the space mapping techniques. Guillaume, idea's and future projects are easy made with cocktails and beers till 2 o'clock at night or at least the intentions... I hope we can still put them into practice.

Much of gratitude is owed to ***dr. Karel Deblaere*** *and* ***Pieter Vandemaele*** *for providing the MR images, the manual segmentation of the MR images, showing my way around an MR scanner and their interest in my work.*

I am very grateful toward ***dr. rer. nat. Carsten Wolters*** *for the fruitful discussions about anisotropy and his constructive remarks.*

I wish to thank ***prof. Zoltan Koles, PhD*** *and* ***Michael Cook*** *for their interest in my technique and the validation of my AFDRM code.*

I am thankful to ***prof. dr. ir. Daniel De Zutter*** *for his suggestions regarding the electrical fields and anisotropic media.*

I wish to thank ***prof. dr. Jan De Munck*** *for providing me with the analytical formula for solving the forward problem.*

To ***prof. dr. ir. Sabine Van Huffel***, ***ir. Maarten De Vos***, ***ir. Katrien Vanderperren***, ***ir. Wouter Deburchgraeve***, ***ir. Anneleen Vergult*** *and* ***dr. ir. Wim De Clercq***, *I wish to express my gratitude for their collaboration and their hospitality during my visits at the idyllic Kasteelpark Arenberg.*

*This work was funded by a grant from the Institute for the Promotion of Innovation through Science and Technology in Flanders (****IWT-Vlaanderen****), to which I am grateful for supporting my work.*

I want to thank everyone who shared their experiences and their advice with me and made me realize the how complex the world can be. The world is not all based on science and it is mostly common sense that prevails. Although our roads may have split up already a long time ago, it is you who helped me to obtain my own common sense.

Of course, this work would never have been possible without the unconditional support from my family and friends. I especially want to thank ***my parents***, ***my family*** *and* ***grandmother*** *who have always supported me. Ik weet dat het niet makkelijk was om wat nieuws te verkrijgen van een druk bezette doctoraatsstudent, maar ik hoop dat jullie hiermee trots zijn op jullie eigen kersverse doctor.*

Finally, I want to dedicate this work to my girlfriend ***Sofie****, who woke up the interest in medicine in me and stood by me throughout this work. Without her love, caring and understanding it would never been possible to successfully complete this dissertation. Liefste Sofie, ookal heb ik de wedstrijd naar de titel "dr." verloren, je hebt geen moment getwijfeld aan mijn capaciteiten om dit werk te vervolledigen. Ik hoop dat we dan ook samen met onze nieuwe woonst een mooie toekomst tegemoet gaan. Ze lacht ons immers toe... Voor alles wat je voor mij gedaan hebt: dank je wel!*

Gent, 29 september 2008,
ir. Hans Hallez

Table of Contents

List of Figures

List of Tables

Notation and Symbols

Notation

Vectors, Matrices, Tensors,...

x,$\mathbf{x}$,$\mathbf{X}$	scalars, vectors, matrices,...
X	Tensor
$\mathbf{x}_i$	i-th element of vector $\mathbf{x}$
$\mathbf{X}_{ij}$	ij-th element of matrix $\mathbf{x}$
$\|.\|$	L_2-norm or the euclidean norm
$\mathbf{X}^T$	transpose of matrix $\mathbf{X}$
$\mathbf{X}^{-1}$	inverse of a matrix $\mathbf{X}$
$\mathbf{X}^+$	Moore-Penrose pseudo inverse of a matrix $\mathbf{X}$

Symbols

Na^+	Sodium ions
K^+	Potassium ions
Cl^-	Chloride ions
$\mathbf{E}$	The electric field
$\mathbf{B}$	The magnetic field
ρ	The charge density
$\mathbf{J}$	The current density
I_m	the current source density
ϵ_0	The permeability of vacuüm
μ_0	The susceptibility in vacuüm
c	The speed of light
V	The continuous potential field
φ_i	The potential field discretized at point x_i,y_i and z_i
σ	The conductivity (scalar)
$\mathsf{\Sigma}$	The second order conductivity tensor

$\mathbf{\Sigma}$	The matrix representation of the second order conductivity tensor
$\mathbf{L}(\mathbf{r})$	The lead field matrix caused by a dipolar source at location $\mathbf{r}$
ξ_i	The radial conductivity at the layer S_i
η_i	The tangential conductivity at the layer S_i
$\Delta_{S_k,j}$	the j-th triangle on the surface S_k
$\tilde{V_k}$	The approximated solution of V on the surface S_k
h_i	A basis function to construct the $\tilde{V_k}$ over the surface S_k
$\mathbf{\Phi}$	The discretized potential value arranged in a vector
ψ	A test function in the FEM
(u, v)	bilinear operator defined by $\int_G v(x,y,z)w(x,y,z)dG$
$a(u, v)$	bilinear operator defined by $-(\nabla v, \mathbf{\Sigma} \cdot \nabla u)$
$\mathbf{A}$	The stiffness matrix
RRE	The relative residual energy
$\mathbf{e}(\phi, \theta)$	The unitary dipole orientation at spherical angles at ϕ and θ.
$\mathbf{D}$	the matrix representation of the diffusion tensor
d_i	the eigenvalues of the diffusion tensor
Δ	A diagonal matrix containing the eigenvalues d_i
nl	The noise level
U^b_{RMS}	The root-mean-square value of a fragment of background EEG
U_{RMS}	The root-mean-square value of a fragment of signal EEG

List of Acronyms

A

aFDM	Anisotropic Finite Difference Method
AFDRM	Anisotropic Finite Differences with Reciprocity Method
AR	Anisotropic Ratio
ASM	Aggressive Space Mapping

B

BCGa	BallistoCardioGraphic Artefact
BEM	Boundary Element Method

C

CSF	Cerebro-Spinal Fluid
CNS	Central Nervous System
CT	Computed Tomography

D

DLE	Dipole Location Error
DT-MRI	Diffusion Tensor Magnetic Resonance Imaging
DW-MRI	Diffusion Weighted Magnetic Resonance Imaging
DWI	Diffusion Weighted Images

E

EEG	Electroencephalography
EIT	Electric Impedance Tomography
ERP	Event Related Potential
ECG	Electrocardiogram
EPSP	Excitatory post-synaptic potential

F

FEM	Finite Element Method
FDM	Finite Difference Method
fMRI	Functional Magnetic Resonance Imaging

H

HASM	Hybrid Aggressive Space Mapping

I

iFDM	Isotropic Finite Difference Method
IPSP	Inhibitory post-synaptic potential

M

MEDISIP	MEDical Image and Signal Processing
MR	Magnetic Resonance
MRI	Magnetic Resonance Imaging
MEG	Magnetoencephalography

P

PET	Positron Emission Tomography

P

RRE	Relative Residual Energy

S

SM	Space Mapping
SPECT	Single Photon Emission Computed Tomography
SOR	Successive Over-Relaxation

T

TRASM	Trust Region Aggressive Space Mapping

V

VCM	Volume Conductor Model

English Summary
Nederlandse Samenvatting

English summary

The electroencephalogram (EEG) is a measurement of brain activity over a period of time by placing electrodes at the scalp (surface EEG) or in the brain (depth EEG) and is used extensively in the clinical practice. In the past 20 years, EEG source analysis has been increasingly used as a tool in the diagnosis of neurological disorders (like epilepsy) and in the research of brain functionality. EEG source analysis estimates the origin of brain activity given the electrode potentials measured at the scalp. This involves solving an inverse problem where a forward solution, which depends on the source parameters, is fitted to the given set of electrode potentials. The forward solution are the electrode potentials caused by a source in a given head model. The head model is dependent on the geometry and the conductivity. Often an isotropic conductivity (i.e. the conductivity is equal in all directions) is used, although the skull and white matter have an anisotropic conductivity (i.e. the conductivity can differ depending on the direction the current flows). In this dissertation a way to incorporate the anisotropic conductivities is presented and the effect of not incorporating these anisotropic conductivities is investigated.

Spherical head models are simple head models where an analytical solution to the forward problem exists. A small simulation study in a 5 shell spherical head model was performed to investigate the estimation error due to neglecting the anisotropic properties of skull and white matter. The results show that the errors in the dipole location can be larger than 15 mm, which is unacceptable for an accurate dipole estimation in the clinical practice. Therefore, anisotropic conductivities have to be included in the head model.

However, these spherical head models are not representative for the human head. Realistic head models are usually made from magnetic resonance scans through segmentation and are a better approximation to the geometry of the human head. To solve the forward problem in these head models numerical methods are needed. In this dissertation we proposed a finite difference technique that can incorporate anisotropic conductivities. Moreover, by using the reciprocity theorem the forward calculation time during an dipole source estimation procedure can be significantly reduced.

By comparing the analytical solution for the dipole estimation problem with the one using the numerical method, the anisotropic finite difference with reciprocity method (AFDRM) is validated. Therefore, a cubic grid is made on the 5 shell spherical head model. The electrode potentials are obtained in the spherical head model with anisotropic conductivities by solving the forward problem using the analytical solution. Using these electrode potentials the inverse problem was solved in the spherical head model using the AFDRM. In this way we can determine the location error due to using the numerical technique. We found that the incorporation of anisotropic conductivities results in a larger location error when the head models are fully isotropical conducting. Furthermore, the location error due to the numerical technique is smaller if the cubic grid is made finer. To minimize the errors due to the numerical technique, the cubic grid should be smaller than or equal to 1 mm.

Once the numerical technique is validated, a realistic head model can now be constructed. As a cubic grid should be used of at most 1 mm, the use of segmented T1 magnetic resonance images is best suited the construction. The anisotropic conductivities of skull and white matter are added as follows: The anisotropic conductivity of the skull is derived by calculating the normal and tangential direction to the skull at each voxel. The conductivity in the tangential direction was set 10 times larger than the normal direction.
The conductivity of the white matter was derived using diffusion weighted magnetic resonance imaging (DW-MRI), a technique that measures the diffusion of water in several directions. As diffusion is larger along the nerve fibers, it is assumed that the conductivity along the nerve fibers is larger than the perpendicular directions to the nerve bundle. From the diffusion along each direction, the conductivity can be derived using two approaches. A simplified approach takes the direction with the largest diffusion and sets the conductivity along that direction 9 times larger than the orthogonal direction. However, by calculating the fractional anisotropy, a well-known measure indicating the degree of anisotropy, we can appreciate that a fractional anisotropy of 0.8715 is an overestimation. In reality, the fractional anisotorpy is mostly smaller and variable throughout the white matter. A realistic approach was therefore presented, which states that the conductivity tensor is a scaling of the diffusion tensor. The volume constraint is used to determine the scaling factor. A comparison between the realistic approach and the simplified approach was made. The results showed that the location error was on average 4.0 mm with a maximum of 10 mm. The orientation error was found that the orientation could range up to 60 degrees. The large orientation error was located at regions where the anisotropic ratio was low using the realistic approach but was 9 using the simplified approach.
Furthermore, as the DW-MRI can also be used to measure the anisotropic diffusion in a gray matter voxel, we can derive a conductivity tensor. After investigating the errors due to neglecting these anisotropic conductivities of the gray matter, we found that the location error was very small (average dipole location error: 2.8 mm). The orientation error was ranged up to 40 degrees, although the mean was 5.0 degrees. The large errors were mostly found at the regions that had a high anisotropic ratio in the anisotropic conducting gray matter. Mostly these effects were due to missegmentation or to partial volume effects near the boundary interfaces of the gray and white matter compartment.
After the incorporation of the anisotropic conductivities in the realistic head model, simulation studies can be performed to investigate the dipole estimation errors when these anisotropic conductivities of the skull and brain tissues are not taken into account. This can be done by comparing the solution to the dipole estimation problem in a head model with anisotropic conductivities with the one in a head model, where all compartments are isotropic conducting. This way we determine the error when a simplified head model is used instead of a more realistic one. When the anisotropic conductivity of both the skull and white matter or the skull only was neglected, it was found that the location

error between the original and the estimated dipole was on average, 10 mm (maximum: 25 mm). When the anisotropic conductivity of the brain tissue was neglected, the location error was much smaller (an average location error of 1.1 mm). It was found that the anisotropy of the skull acts as an extra shielding of the electrical activity as opposed to an isotropic skull. Moreover, we saw that if the dipole is close to a highly anisotropic region, the potential field is changed reasonable in the near vicinity of the location of the dipole.
In reality EEG contains noise contributions. These noise contribution will interact with the systematical error by neglecting anisotropic conductivities. The question we wanted to solve was "Is it worthwhile to incorporate anisotropic conductivities, even if the EEG contains noise?" and "How much noise should the EEG contain so that incorporating anisotropic conductivities improves the accuracy of EEG source analysis?". When considering the anisotropic conductivities of the skull and brain tissues and the skull only, the location error due to the noise and neglecting the anisotropic conductivities is larger then the location error due to noise only. When only neglecting the anisotropic conductivities of the brain tissues only, the location error due to noise is similar to the location error due to noise and neglecting the anisotropic conductivities. When more advanced MR techniques can be used a better model to construct the anisotropic conductivities of the soft brain tissues can be used, which could result in larger errors even in the presence of noise. However, this is subject to further investigation. This suggests that the anisotropic conductivities of the skull should be incorporated.
The technique presented in the dissertation can be used to epileptic patients in the presurgical evaluation. In this procedure patients are evaluated by means of medical investigations to determine the cause of the epileptic seizures. Afterwards, a surgical procedure can be performed to render the patient seizure free. A data set from a patiënt was obtained from a database of the Reference Center of Refractory Epilepsy of the Department of Neurology and the Department of Radiology of the Ghent University Hospital (Ghent, Belgium). The patient was monitored with a video/EEG monitoring with scalp and with implanted depth electrodes. An MR image was taken from the patient with the implanted depth electrodes, therefore, we could pinpoint the hippocampus as the onset zone of the epileptic seizures. The patient underwent a resective surgery removing the hippocampus, which rendered the patient seizure free. As DW-MRI images were not available, the head model constructed in chapter 4 and 5 was used. A neuroradiologist aligned the hippocampus in the MR image from which the head model was constructed. A spike was picked from a dataset and was used to estimate the source in a head model where all compartments were isotropic conducting, on one hand, and where the skull and brain tissues were anisotropic conducting, on the other. It was found that using the anisotropic head model, the source was estimated closer to the segmented hippocampus than the isotropic head model. This example shows the possibilities of this technique and allows us to apply it in the clinical practice. Moreover, a thorough validation of the technique has yet to be performed. There is a lot of

discussion in the clinical community whether the spikes and epileptical seizures originate from the same origin in the brain. This question can be solved by applying our technique in patient studies.
The research was performed in the MEDical Image and SIgnal Processing (MEDISIP) research group, part of the department of ELectronics and Information Systems (ELIS) of the faculty of Engineering (FIRW) of the Ghent University, Ghent, Belgium. The work was done in close collaboration with the Reference Center for Refractory Epilepsy (RCRE) of the Department of Neurology and the Department of Radiology at the Ghent University Hospital. The work resulted in 2 publications [70, 64] as first author and 3 publications [33, 32] as second author in international A1 journals, 3 publications [60, 68, 69] as first author in international peer-reviewed journals (A2) and many of these results [56, 61, 62, 57, 65, 58, 63, 59, 66, 30, 5] were submitted and presented at national and international conferences.

Nederlandse Samenvatting

Het elektroencefalogram (EEG) is een registratie van de hersenactiviteit gedurende een tijdsperiode. De hersenactiviteit kan gemeten worden door het plaatsen van elektrodes aan het hoofdoppervlak (oppervlakte EEG) of in de hersenen (diepte EEG). Het EEG wordt intensief gebruikt in de klinische praktijk. In de laatste 20 jaar is EEG bronanalyse veelvuldig gebruikt als onderzoek in de diagnose van neurologische aandoeningen (zoals epilepsie) en in fundamenteel onderzoek naar de werking van de hersenen. EEG-bronanalyse schat de oorsprong van hersenactiviteit gegeven de elektrodepotentialen gemeten aan het hoofdoppervlak en bestaat uit twee problemen. Het voorwaarts problem bepaalt de elektrodepotentialen gegeven een bron in een welbepaald hoofdmodel. Het inverse probleem schat de bronparameters die het best overeenkomen met de gemeten elektrodepotentialen. Het hoofdmodel is afhankelijk van de geometrie en de geleidbaarheden. In de realiteit zijn de schedel en de witte materie van de hersenen anisotroop geleidend (i.e. de geleidbaarheden zijn niet even groot in verschillende richtingen). Dit proefschrift handelt over de incorporatie van deze geleidbaarheden en over de fouten die gemaakt worden indien deze anisotrope geleidbaarheden niet in rekening gebracht worden.

In bolvormige hoofdmodellen kan een analytische formule gebruikt worden om het voorwaarts probleem op te lossen. Een kleine studie in een vijfvoudig bolvormig hoofdmodel toont immers aan dat het niet in rekening brengen van de anisotrope geleidbaarheden een schattingsfout op de locatie kan geven van meer dan 15 mm. Dergelijke fouten zijn onaanvaardbaar voor een nauwkeurige localizatie in de klinische praktijk. Anisotrope geleidbaarheden moeten dus in het hoofdmodel geïncorporeerd worden.

Bolvormige hoofdmodellen zijn echter een vereenvoudiging van de echte geometrie van het menselijk hoofd. Realistische hoofdmodellen kunnen geconstrueerd worden aan de hand van magnetische resonantie scans. Hierdoor kan de geometrie van het menselijk hoofd beter benaderd worden, maar moet het voorwaarts probleem opgelost worden door middel van een numerieke techniek. In dit proefschrift stellen we eindige differentie methode voor die anisotrope geleidbaarheden in rekening kan brengen. Te meer, kan het reciprociteitstheorema gebruikt worden om de berekening van het voorwaarts probleem tijdens de dipoolbronschatting aanzienlijk te versnellen.

Numerieke technieken veroorzaken echter wel een fout te wijten aan de discretizatie. Door de oplossing van de dipoolbronbepaling in een bolvormig hoofdmodel door middel van de analytische formule te vergelijken met deze in een gediscretizeerd bolvormig hoofdmodel door middel van de anisotrope eindige differentie met reciprociteit methode (AFDRM). Er werd getoond dat er een fout is te wijten aan de discretizatie van de potentialen en een fout te wijten aan de discretizatie van de anisotrope geleidbaarheden. Om de discretizatiefouten te minimalizeren moet immers een kubisch berekeningsrooster van kleiner of gelijk aan 1 mm gebruikt worden.

Na de validatie van de numerieke techniek, kan deze gebruikt worden in een real-

istisch hoofdmodel. Hiervoor worden T1 gewogen magnetische resonantie scans gesegmenteerd in compartimenten, die in een realitisch hoofdmodel gecombineerd worden. De anisotrope geleidbaarheden van de schedel en witte materie worden dan als volgt bepaald. De anisotrope geleidbaarheid van de schedel wordt bekomen door de tangentiele geleidbaarheid aan een schedelsegment 10 keer groter te maken dan de loodrechte geleidbaarheid.
De geleidbaarheid van de witte materie kan afgeleid worden met een recente techniek dat de diffusierichtingen van water kan meten: diffusie gewogen magnetische resonantie beeldvorming (DW-MRI). De diffusie van water is immers groter in de richting van de zenuwbundels. Hierdoor veronderstelt men dat geleidbaarheid langs de zenuwbundels groter is dat loodrecht op de zenuwbundel. Een eenvoudig model stelt dat de geleidbaarheid 9 keer groter is langs de zenuwbundel dan loodrecht. Echter, een vizualisatie van de fractionele anisotropie, een maat voor de anisotropie, toont aan dat de overeenkomende fractionele anistropie van 0.8715 een overschatting is. In de realiteit is de fractionele anisotropie variabel en meestal lager dan 0.8715. Realistischer zou zijn dat de geleidbaarheidstensor een schaling is van de diffusietensor. De volume beperking is gebruikt om de onbekende schalingsfactor te bepalen. Het vereenvoudig model gebruiken in plaats van een realistisch model veroorzaakt dipoolestimatiefouten van gemiddeld 4.0 mm met een maximum van 10 mm. De fout in orientatie kan tot 60 graden bedragen. Grote fouten in de orientatie kwamen meestal voor in regio's die een lage fractionele anisotropie hebben gebruik makend van het realistisch model maar 0.8715 indien het eenvoudig model wordt gebruikt.
De resultaten van DW-MRI kunnen ook gebruikt worden geleidbaarheidstensor te construeren in de grijze materie. Wanneer de anisotrope geleidbaarheden van de grijze materie niet in rekening gebracht worden, kunnen er fouten gemaakt worden die slechts heel klein zijn (gemiddelde localizatiefout: 2.8 mm). De orientatiefout kan maximaal 40 graden bedragen, het gemiddelde is echter 5.0 graden. Grote fouten kwamen voor in regio's die een hoge fractionele anisotropie hadden in de anisotroop geleidende grijze materie. Deze resultaten zijn belangrijk voor de constructie van het hoofdmodel aangezien er fouten kunnen optreden in de segmentatie tussen witte en grijze materie. Hierdoor kunnen stukken witte materie met een hoge anisotropie verkeerdelijk tot de grijze materie geklassificeerd worden.
Wanneer anisotrope geleidbaarheden in het hoofdmodel kunnen geïncorporeerd worden, kunnen simulaties uitgevoerd worden die de fout te wijten aan het niet in rekening brengen van de anisotrope geleidbaarheden onderzoeken. Hierdoor gaan we na welke fouten er gemaakt worden indien een eenvoudig hoofdmodel zonder anisotrope geleidbaarheden gebruikt wordt in plaats van een realistisch hoofdmodel wel anisotrope geleidbaarheden bevat. Het niet in rekening brengen van de anisotrope geleidbaarheden van schedel veroorzaakt immers fouten van gemiddeld 10 mm (maximaal: 25 mm). De schedel is dus een belangrijke parameter in het hoofdmodel en dus in EEG-bronanalyse. Wanneer enkel de anisotrope geleidbaarheden van de zachte hersenweefsels (witte en grijze ma-

terie) niet in rekening gebracht worden, is de fout in de localizatie veel kleiner, namelijk 1.1 mm gemiddeld. De anisotrope geleidbaarheid van de schedel werkt immers als een extra afscherming van de elektrische activiteit in vergelijking met een isotroop geleidende schedel. Bovendien wordt het potentiaalveld in de nabijheid van de dipoolbron aanzienlijk beinvloed wordt door de anisotrope geleidbaarheden van de zachte hersenweefsels.
In realiteit bevat het EEG ruis. Deze ruisbijdragen zullen interageren met de systematische fout te wijten aan het niet in rekening brengen van anisotrope geleidbaarheden. De vraag die we willen beantwoorden is "Is het de moeite om anisotrope geleidbaarheden te incorporeren, zelfs bevat het EEG ruis?" en "Hoeveel ruis kan het EEG maximaal bevatten zodat het incorporeren van anisotrope geleidbaarheden kan bijdragen tot een nauwkeurigere bronschatting?". Wanneer de anisotrope geleidbaarheden van de schedel en zachte hersenweefsels of deze van enkel de schedel niet in rekening gebracht worden en ruis is toegevoegd aan de elektrode potentialen, is de localizatiefout groter dan wanneer enkel ruis is toegevoegd. Wanneer enkel de anisotrope geleidbaarheden van de zachte hersenweefsels beschouwd worden, is de fout te wijten aan ruis en het niet in rekening brengen van de anisotrope geleidbaarheden gelijkaardig aan de fout te wijten door enkel ruis. Dit suggereert dat de anisotrope geleidbaarheden van de zachte hersenweefsels weinig invloed hebben op de dipoolbronestimatie.
Het model gebruikt in dit proefschrift is best geschikt voor DW-MRI scans met een resolutie van 2 mm bij 2 mm bij 2 mm. Wanneer er geavanceerde MR technieken gebruikt worden, kan een beter model voor de constructie van de geleidbaarheidstensor in zachte weefsels gebruikt worden. Hierdoor kunnen er grotere fouten optreden wanneer de anisotrope geleidbaarheden van de zachte hersenweefsels niet in rekening gebracht worden, dan hier beschreven.
De techniek beschreven in dit proefschrift kan toegepast worden in de prechirugische evaluatie van patiënten met epilepsie. In deze evaluatie worden patiënten geëvalueerd door middel van onderzoeken wat de oorsprong is van de epileptische aanvallen. Nadien kan een chirurgische ingreep uitgevoerd worden die de patient aanvalsvrij kan maken. Een dataset werd geselecteerd uit de databank van het ReferentieCentrum voor Refractaire Epilepsie van de Afdeling Neurologie van het Universitair Ziekenhuis Gent. De patiënt onderging een video/EEG monitoring met oppervlakte en diepte-electroden. Een MR scan werd genomen van de patiënt met de geïmplanteerde diepte-electroden. Hierdoor kon de linker hippocampus gedetermineerd worden als oorsprong van de epilepsie-aanvallen. De patiënt werd geöpereerd waarbij de linker hippocampus weggenomen werd. Hierdoor werd de patiënt aanvalsvrij. Een spike (i.e. een kortstondig epileptisch fenomeen in het EEG dat zich typisch voordoet tussen de aanvallen) werd uitgekozen en gebruikt in de dipoolbronschatting in een hoofdmodel met isotrope geleidbaarheden enerzijds en in een hoofdmodel met anisotrope geleidbaarheden anderzijds. In het anisotroop geleidende hoofdmodel was de bronschatting dichter bij de gesegmenteerde linker hippocampus. Dit voorbeeld toont de mogelijkheden en laat ons toe om deze techniek toe te

passen in de klinische praktijk. Een grondige validatie van deze techniek is nog deel van toekomstig onderzoek. Er is namelijk nog steeds een grote discussie in de klinische wereld dat spikes en aanvallen hun oorsprong vinden uit eenzelfde regio in de hersenen. Met deze techniek kan deze klinische dialoog opgelost worden.

Dit onderzoek werd uitgevoerd in de MEDical Image and SIgnal Processing onderzoeksgroep (MEDISIP) van het departement ELektronica en InformatieSystemen (ELIS) van de faculteit ingenieurswetenschappen (FIRW) van de Universiteit Gent te Gent, Belgie. Dit werk kwam tot stand mits een hechte samenwerking met het Referentie Centrum voor Refractaire Epilepsy (RCRE) van de dienst Neurologie en de dienst Radiologie van het Universitair Ziekenhuis Gent (UZGent). Bovendien resulteerde dit werk in 2 publicaties [70, 64] als eerste auteur en2 publicaties [33, 32] als tweede auteur in internationale A1 tijdschriften, 3 publicaties als eerste auteur [60, 68, 69] in internationale (A2) tijdschriften. Veel van deze resultaten [56, 61, 62, 57, 65, 58, 63, 59, 66, 30, 5] werden ingediend en gepresenteerd in internationale en nationale congressen en symposia.

Incorporation of Anisotropic Conductivities in EEG Source Analysis

Chapter 1

General Introduction

An idea that is developed and put into action is more important than an idea that exists only as an idea.
—Buddha

1.1 Situation

The electroencephalogram (EEG) measures potentials at electrodes at the scalp of a human head over a period of time. These potential differences are generated by electrical activity inside the brain. The EEG is particularly useful for diagnostic purposes, where a neurologist wants to determine the origin of a neurologic disorder (e.g. epilepsy). Typically, 20 to 40 electrodes are placed at the scalp. Furthermore, measuring the EEG is useful in fundamental research in the functionality of the brain. This is investigated by an event-related potential (ERP), a potential waveform in time generated by a specific task or stimulus. In this case, 64 to 256 electrodes are typically used.

Starting from a given set of potential differences measured at the scalp and a volume conductor model (VCM) or head model, we can estimate the source, which causes the potential differences, which is called *EEG source analysis*. This is done by finding the source parameters which best represents the measured potential differences. In literature this also often called as *EEG source localization* or *EEG source estimation*.

The potential differences caused by the activity in the brain are dependent on the conductivities of the tissue types of the head. Commonly used head models define the conductivity as isotropic. This means the conductivity is equal in each direction. However, recently it has been shown that some brain tissues have a direction dependent conductivity, which means the conductivity is different depending on the direction. These tissues have a so-called anisotropic

conductivity. The incorporation of these anisotropic conductivities of in EEG source analysis will be the main topic of this dissertation.

EEG source analysis has been proven to be useful in the diagnosis of neurological disorders like epilepsy. Patients with epilepsy have an characteristic waveform which can be detected by a neurologist. In special cases of epilepsy, the waveforms are generated by a specific focal region or multiple focal regions in the brain. EEG source analysis estimates the origin of these waveforms non-invasively using electrodes placed at the scalp. The determination of the origin can help the neurologist to pinpoint the origin of the epilepsy and evaluate the patient for resective surgery. In the latter, the brain region responsible for the epileptic phenomena is surgically removed, which could reduce the epileptic seizures or render the patient seizure free.

Another field where EEG source analysis can be useful is the research of brain functionality during a specific task. Since the 1960s the EEG has also been used to measure event-related potentials (ERPs). Here, brain waves are triggered by a stimulus. These stimuli could be of visual, auditory and somatosensory nature. Different ERP protocols are now routinely used in a clinical neurophysiology lab. Researchers nowadays are still searching for new ERP protocols which may be able to distinguish between ERPs of patients with a certain condition and ERPs of normal subjects. This is used in disorders, such as psychiatric and developmental disorders, where there is often a lack of biological objective measures.

1.2 Outline

In chapter 2 an introduction to the EEG source analysis is given. Throughout the beginning of the chapter we build a model for the generators of the EEG and how we can estimate the parameters of this model using the EEG. Therefore, we start with a brief overview of the anatomy of the brain and the neurophysiological processes behind the activity generated in the brain. A mathematical description is given of the dipole model, which will represent the source of our brain activity. Next, we focus on EEG source analysis problem, which consists of two subproblems. The so-called forward problem calculates the potentials at the scalp electrodes for given source of brain activity. The problem will be stated as mathematical formulation, in which the anisotropic conductivity is introduced. In spherical head models an analytical solution to the forward problem exist. A solution that can incorporate these anisotropic conductivities is illustrated. For realistic head models, which better represent the actual geometry of the human head, numerical methods must be applied. Different numerical methods are discussed. The anisotropic finite difference reciprocity method (AFDRM) is introduced and will be used throughout the remainder of the dissertation. Next, the chapter deals with the so-called inverse problem. The inverse problem tries to find the source parameters that best describe the measured potentials. The inverse problem is introduced as

an optimization problem in the least squares sense. An algorithm is presented which solves the inverse problem for a single time instant and for multiple time series. Finally, the different causes of estimation errors are discussed. The focus will be head model related errors concerning the conductivity. The skull and white matter (i.e. a specific brain tissue which consists of fibers which connect brain regions) as anisotropic conductors are introduced.

In chapter 3 the anisotropic finite difference reciprocity method (AFDRM) will be validated in a spherical head model. We start by illustrating the need to incorporate anisotropic conductivities in head models by a simulation study in a spherical head model. A current dipole was placed in an spherical head model where the skull and white matter were anisotropic conductors. By performing one forward calculation using the analytical solution, we obtain the electrode potentials which are used to estimate the source in a spherical head model where each compartment was set to isotropic. The result is a current dipole, of which parameters deviate from the original ones due to assuming a simplified conductivity. The simulation is repeated for a set of uniformly distributed current dipoles. Next, the numerical method (AFDRM) is applied to estimate the source in a spherical head model. The method requires that the volume conductor is subdivided in cubic elements and computational points between the elements. However, a large number of computational points is used. This leads to iterative solvers for large sparse linear systems as will be explained. Reciprocity is used to decrease the computing time of the forward problem. The AFDRM is validated as follows: (i) a current dipole is placed in a spherical head model and the electrode potentials are calculated using the analytical solution; (ii) the electrode potentials are used to solve the inverse problem in a spherical head model using the AFDRM method. This was repeated for a grid of dipoles with different orientation and in different slices of the spherical head model.

In chapter 4 we discuss a methodology to construct a realistic head model and to incorporate realistic anisotropic conductivities in the head model. We start with a brief introduction of magnetic resonance imaging (MRI) and diffusion weighted magnetic resonance imaging (DW-MRI). The first technique was used to image the structural geometry of the human head. Using segmentation techniques and image processing techniques the compartments representing the different tissue types are constructed. The geometry of the skull is also used to construct the anisotropic conductivity of the skull. The conductivity tangential to a segment of the skull was set to 10 times larger than the conductivity along the normal direction. DW-MRI measures the diffusion of water in the brain. Because of the microscopic fiber structure of the white matter in the brain the diffusion is anisotropic. Using the anisotropic information of the diffusion, the anisotropic conductivities of the white matter can be derived. A realistic and simplified approach to derive the anisotropic conductivity is discussed. Using the simplified approach instead of the realistic approach, errors in the dipole estimation can occur. These errors are investigated by performing simulation studies in which the AFDRM method is used to calculated the forward problem

where the conductivity was derived using the realistic approach. The inverse problem was solved using the AFDRM in a realistic head model where the conductivity was derived using the simplified approach. Finally, the DW-MRI images can also be used to derive the conductivity in the gray matter compartment in a similar way as in white matter. The influence of not incorporating the anisotropic conductivities of gray matter are also investigated by simulation studies using the AFDRM.

In chapter 5 the AFDRM is used to investigate the effect of neglecting the anisotropic conductivities in EEG source estimation. A simulation study was done to quantify the estimation errors due to neglecting the anisotropic conductivities of skull and/or brain compartments. Therefore, a dipole was placed in an anisotropic head model and the forward problem was calculated yielding the electrode potentials. The electrode potentials are then used to solve the inverse problem in an isotropic head model. For one simulation this procedure is repeated for a set of dipole locations organized in a grid and orientations along three orthogonal axes. Furthermore, the simulation is repeated for a different anisotropic head model. The estimation errors due to neglecting the anisotropic properties of the skull and brain tissues are discussed. Next, a qualitative study was done. The influence of the anisotropic conductivities on the potential distribution is discussed and a physical explanation of the dipole estimation errors determined in the first part is given. Finally, a simulation study to determine the dipole location errors due to neglecting anisotropic conductivities in the presence of noise was done. The question we want to solve is the following:"Is it still worthwhile to incorporate anisotropy in the presence of noisy EEG?" and "At what amount of noise is it still worthwhile to incorporate anisotropic conductivities in the head model?". Inferring noise on the electrode potentials contributes to a random error in the dipole location error. When a simplified isotropic head model was used then the total dipole location error consists of a error due to neglecting the anisotropy and due to the inferred noise. The amount of noise will be quantified by the noise level. The larger the amount noise in the EEG signal, the larger the contribution to the total error will be as the systematical error is fixed.

In chapter 6 a prospective study is performed. The EEG source analysis is applied to a neurological disorder, epilepsy. Moreover, the patient suffered from a special kind of epilepsy, which is characterized by a focal onset zone of the epileptic attacks. A patient was chosen from the extensive database of the Reference center of Epilepsy at the department of Neurology at the Ghent University Hospital (Ghent, Belgium). The patient underwent extensive studies such as video/EEG monitoring, intracranial depth electrodes and several MR investigations. However, a diffusion weighted image was not available. Therefore, the head model constructed in chapter 4 was used to estimate a specific waveform related to epilepsy. The aim of this chapter is to demonstrate an application of the method using real data. Hence, we discuss how a validation study can be performed and what kind of information is needed based on the results of this dissertation.

Finally, In chapter 7 the methodology and the findings of the dissertation are summarized. Furthermore, future work will be discussed.

Chapter 2

EEG source analysis

Sufficiently advanced technology is indistinguishable from magic.
—Arthur C. Clarke

2.1 Introduction

Since the 1930s electrical activity of the brain has been measured by surface electrodes connected to the scalp [22]. These electrode position are carefully placed at the scalp according to the 10-20 international system electrode placement, illustrated at figure 2.1. Potential differences between these electrodes were then plotted as a function of time in a so-called electroencephalogram (EEG) . An illustration of such a registration is shown in figure 2.2. The information extracted from these brain waves was, and still is used in the diagnoses of neurological diseases, such as epilepsy [107].

During the last two decades, increasing computational power has given researchers the tools to go a step further and try to find the underlying sources which generate the EEG. This technique is called *EEG source analysis* or *EEG source estimation* . It consists of solving a forward and inverse problem. Solving the forward problem starts from a given electrical source configuration representing active neurons in the head. Then the potentials at the electrodes are calculated for this configuration. The inverse problem attempts to find the electrical source which generates a measured EEG.

First we will give a short introduction of neurophysiology and anatomy of the human brain. Next, a mathematical description of the EEG source analysis problem will be given. A model will be given of the source based on the neurophysiological processes. Techniques to solve the EEG source analysis problem are described next. The chapter ends with an overview of which kind of errors may occur during the EEG source analysis and what the causes are. Here the skull and white matter as an anisotropic conductor will be introduced.

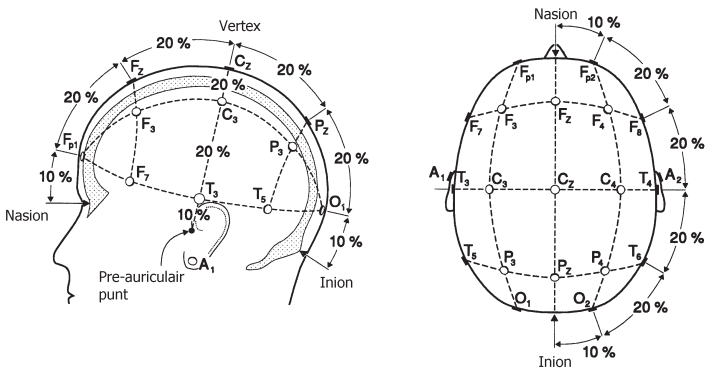

Figure 2.1: The 10-20 international system for the placement of the electrodes at the scalp.

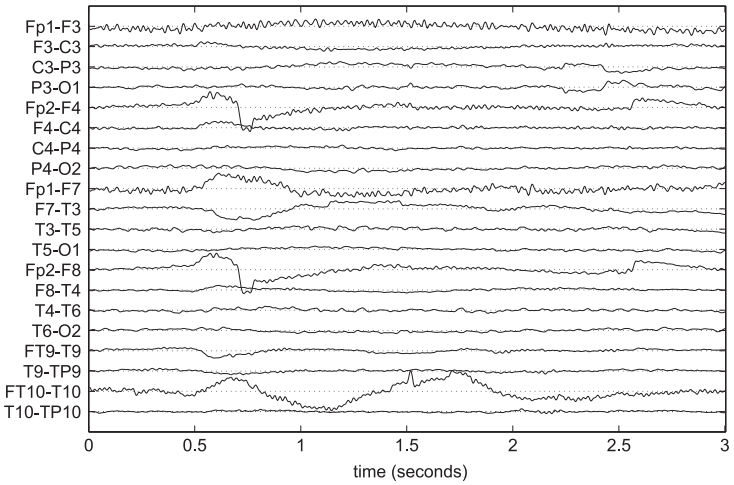

Figure 2.2: An example of an EEG of 3 seconds. Potential differences are measured between electrodes, indicated by a label according to figure 2.1.

2.2 Physiology and anatomy of the neuron

In order to understand the EEG source analysis problem, it is, in our opinion, important to know the underlying mechanisms of the EEG . Moreover, forward modeling also involves a good model for the generators of the EEG. The mechanisms of the neuronal action potentials, excitatory post synaptic potentials and inhibitory post synaptic potentials are very complex. In this section we want to give a very concise overview of the anatomy of the brain and the underlying neurophysiology behind brain activity.

2.2.1 Anatomy of the brain and neuron

The human brain is the most important organ in the central nervous system (CNS). In the brain, different regions can be designated according to their motor or higher cognitive function. For example, a specific region in the brain is responsible for hand movement, while another region processes the information concerning language. The main task of the brain is the processing and communication of information. This information can be sent to or received from parts of the human body or other designated regions of the human brain. The brain is situated inside the skull and scalp, which act as a protective layer against shock and impact (see figure 2.3). Moreover, it floats in the ventricular system which is drained with the cerebro-spinal fluid (CSF). The CSF provides essential substances for the metabolism of the brain and some protection to shock. Concerning tissue types, the actual brain tissues can be divided in three parts: white matter, gray matter and the ventricles (see figure 2.4).

The white matter mainly consists of connections from and to different parts of the gray matter. An important connection contained in the white matter is the *corpus callosum* which connects the right and left hemisphere (see figure 2.4). The actual brain activity is generated in the gray matter. The gray matter at the edge of the brain has a folded structure to increase the surface so complex connections can be made. The outer layer is also called the *cortex* or *cortical gray matter*. In the gray matter many structures can be identified according to their function in the processing of information. An example of such a structure is the *hippocampus*, which is related to the short term memory (see figure 2.3). The hippocampus has very complicated folded structure. Specific types of epilepsy are related to this structure. In the gray matter nerve cells are the generators of the electro-chemical activity.

Neurons or nerve cells are the building blocks of the human central nervous system. The brain consists of about 10^{10} nerve cells or neurons. The neuron's task is to process signals coming from other neurons and transmit signals to other neurons or tissue (muscle or organs). The shape and size of the neurons vary but all neurons possess the same anatomical subdivision. Neurons can be subdivided in 3 parts: the dendrites, the cell body or soma and the axon (see figure 2.5). The dendrites, originating from the soma and repeatedly branching,

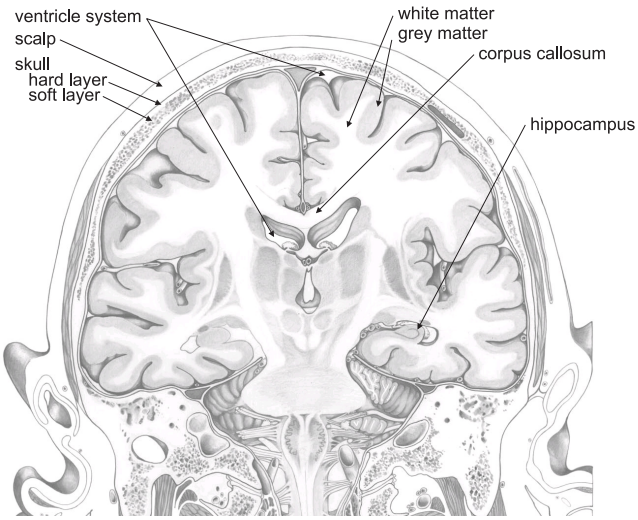

Figure 2.3: A coronal slice of the human head. Adopted from Mai et al. [93]
.

are specialized in receiving inputs from other nerve cells. The soma or cell body contains the nucleus of the cell and processes the incoming signals and decides if a signal has to be transmitted to the axon. In that case the neuron *fires* and an *action potential* is generated which propagates through the axon. Via the axon, impulses are sent to other neurons or tissue (muscles or organs). The axon's end is divided into branches which connect to other neurons or tissues. An axon can only transmit a signal to another neuron via the dendrites. Therefore, a physiological connection has to be made. This is called a *synapse*. The larger the dendrites, the more connections from other neurons can be made.

The synapse is a specialized interface between two nerve cells. The synapse consists of a cleft between a presynaptic and postsynaptic neuron. At the end of the branches originating from the axon, the presynaptic neuron contains small rounded swellings which contain the neurotransmitter substance. Further readings on the anatomy of the neuron and the brain can be found in Kiloh et al. [87] and Gray [51].

2.2.2 Physiology of the neuron

At rest the intracellular environment of a neuron is negatively polarized at approximately -70 mV compared with the extracellular environment. A neuron can depolarize or hyperpolarize. A *depolarization* means that the potential difference between the intra- and extracellular environment increases. Instead of -70mV the potential difference becomes -40mV. A *hyperpolarization* means

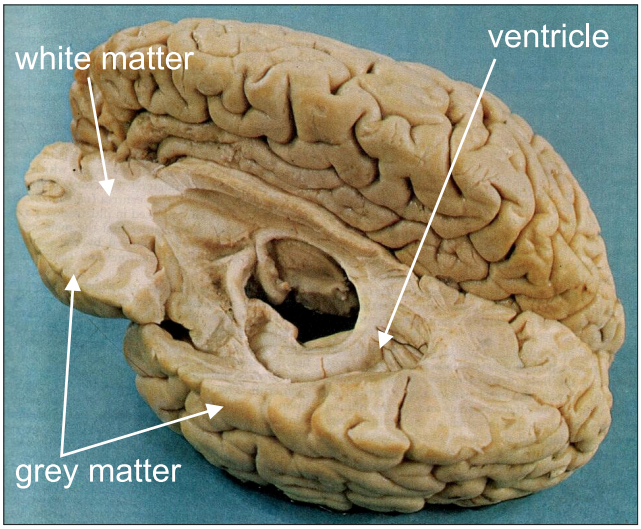

Figure 2.4: The brain where the upper half the left hemisphere is cut out. Adopted from Gray [51].

that the potential difference between intra- and extracellular environment decreases. After a depolarization or hyperpolarization occurred, the neuron returns to the resting state. This is called a *repolarization* and takes some time. This is called the *refractory period* and the neuron cannot fire an action potential during this period. The potential difference at rest is due to an unequal distribution of Na^+, $K^+$and Cl^--ions across the cell membrane. This unequal distribution is maintained by the $Na^+$and K^+-ion pumps located in the cell membrane.

The processing and the transmission of the signals are done by an alternating chain of electrical and chemical reactions. Neurons activated by an action potential will secrete a chemical substance called a neurotransmitter, at the synaptical side. The secretion of neurotransmitter at the presynaptic neuron (the neuron at the axon side) is generated by action potentials.

A postsynaptic neuron (the neuron at the dendrite side) has a large number of receptors on its membrane that are sensitive for this neurotransmitter. The neurotransmitter in contact with the receptors changes the permeability of the membrane for charged ions. Two kinds of neurotransmitters exist. On the one hand there is a neurotransmitter which lets signals proliferate. These molecules cause an influx of positive ions. Hence depolarization of the intracellular space takes place. This depolarization is also called an excitatory postsynaptic potential (EPSP) . On the other hand there are neurotransmitters that stop the proliferation of signals. These molecules will cause an outflow of positive ions. Hence a hyperpolarization can be detected in the intracellular volume. This po-

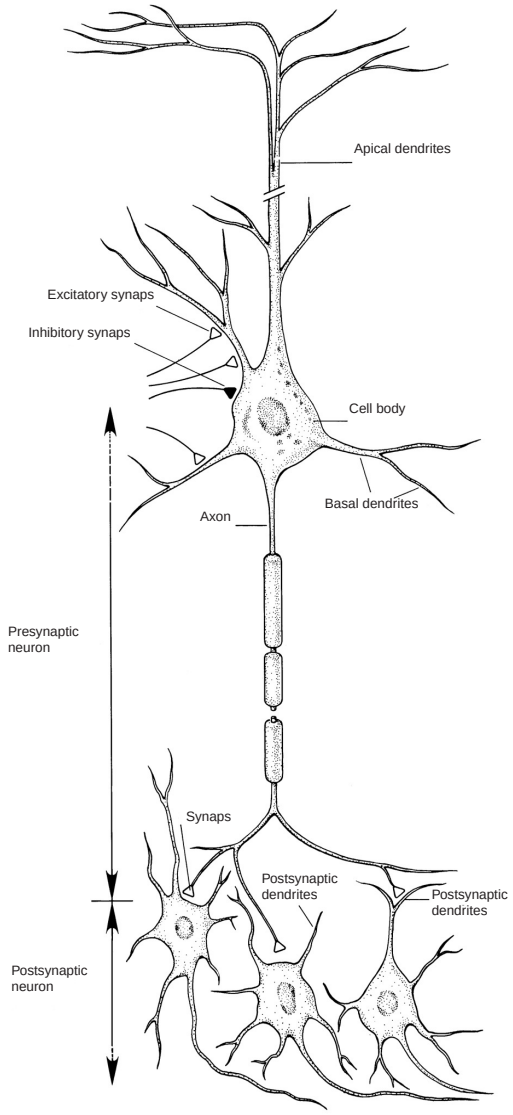

Figure 2.5: The neuron. Signals are sent through the dendrites to the cell body and when a depolarization occurs, an action potential is transmitted through the axons to other neurons or to muscles.

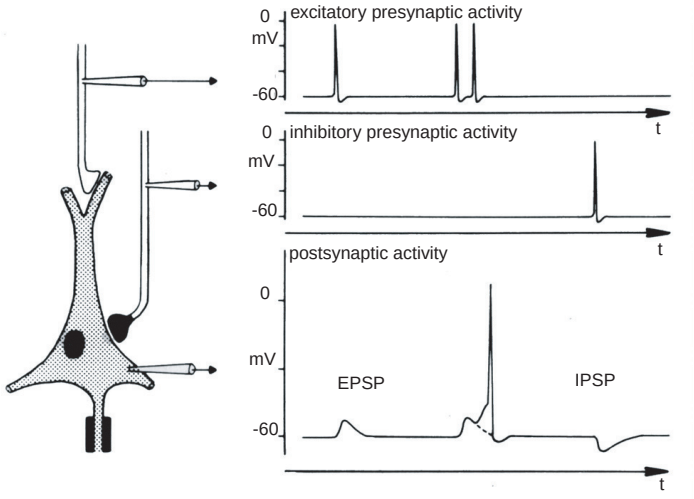

Figure 2.6: An illustration of the action potentials and post synaptic potentials measured at different locations at the neuron. On the left a neuron is displayed and three probes are drawn at the location where the potential is measured. The top graph on the right shows the incoming excitatory action potentials measured at the probe at the top, at the probe in the middle the incoming inhibitory action potential is measured and shown. The neuron processes the incoming potentials: the excitatory action potentials are transformed into excitatory post synaptic potentials, the inhibitory action potentials are transformed into inhibitory post synaptic potentials. When two excitatory post synaptic potentials occur in a small time frame, a threshold is reached and the neuron fires. This is shown at the bottom figure. The dotted line shows the EPSP, in case there was no second excitatory action potential following. Adopted from Speckmann and Elger [137]

tential change is also called an inhibitory postsynaptic potential (IPSP). There are a large number of synapses from different presynaptic neurons in contact with one postsynaptic neuron. At the cell body all the EPSP and IPSP signals are integrated. When a net depolarization of the intracellular compartment at the cell body reaches a certain threshold, an action potential is generated. An action potential then propagates along the axon to other neurons. Figure 2.6 illustrates the excitatory and inhibitory postsynaptic potentials. It also shows the generation of an action potential. Further readings on the electrophysiology of neurons can be found in Niedermeyer and Lopez da Silva [106], Gulrajani [54], Johnston and Wu [84].

2.3 The generators of the EEG

The electrodes used in scalp EEG are large and are attached to the scalp, which is distant from the neurons compared to the size of the neuron. Consequently, an electrode only detects summed activities of a large number of neurons which are synchronously electrically active . The action potentials can be large in amplitude (70-110 mV) but they have a small time course (0.3 ms). A synchronous firing of action potentials of neighboring neurons is unlikely. The postsynaptic potentials are the generators of the extracellular potential field which can be recorded with an EEG. Their time course is larger (10-20 ms). This enables the detection and measurements of summed activity of neighboring neurons. However their amplitude is smaller (0.1-10 mV) [54, 8].

Apart from having more or less synchronous activity, the neurons need to be regularly arranged to result in a measurable scalp EEG signal. The spatial properties of the neurons must be so that they amplify each other's extracellular potential fields. Pyramidal neuron cells are a special type of neuron which consist of a large dendrite branch (so-called *apical dendrite*) which is oriented orthogonally to the surface of the gray matter. An example of such an pyramidal neuron is shown in figure 2.5. Neighboring pyramidal cells are organized so that the axes of their dendrite tree are parallel with each other and normal to the cortical surface. Figure 2.7 illustrates these pyramidal neurons. Figure 2.7a shows a coloring of the pyramidal neurons. A schematic of these pyramidal neurons in the human brain is given in figure 2.7b. We can see the orthogonal direction of the apical dendrite to the edge of the grey matter cortex. Hence, these cells are suggested to be the generators of the EEG.

The following is focused on excitatory synapses and EPSP, located at the apical dendrites of a pyramidal cell. An analog reasoning can be made for IPSPs .

As mentioned before, at the resting state there is a potential difference between the inside and outside of the cell (shown as V_r in figure 2.8). The incoming action potential shown in figure 2.8(b) releases the neurotransmitters in the cleft. The neurotransmitters causes an influx of positive ions at the post synaptic membrane as illustrated in figure 2.8(b) and depolarizes the local cell membrane. Positive ions will enter the cell. This causes a lack of extracellular

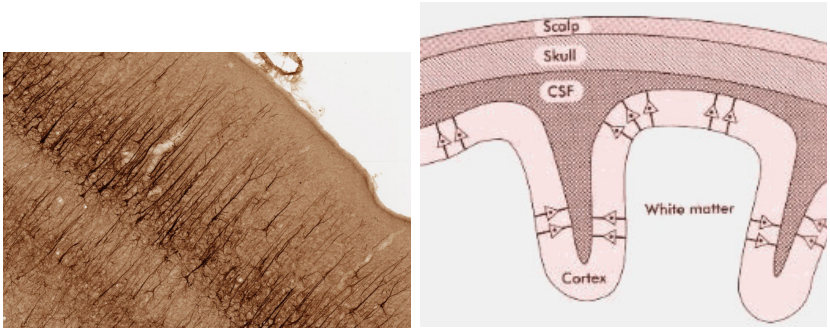

(a) (b)

Figure 2.7: (a) a cortical slice is shown, the black coloring shows the pyramidal neurons which are orthogonal to the surface. (b) a schematic picture of the alignment of the pyramidal neurons in the cortex.

positive ions at the apical dendrites of the post synaptic neuron. A redistribution of positively charged ions also takes place at the intracellular side. These ions flow from the apical dendrite to the cell body and depolarize the membrane potentials at the cell body. Subsequently positively charged ions become available at the extracellular side at the cell body and basal dendrites. The neuron is thus an element that withdraws current from the extracellular space (a so-called *current sink*) and that injects a current with the same intensity (*current source*). The electrical activity can be modeled as a current dipole (see figure 2.9). The current flow causes an electric field and also a potential field inside the human head, which extends to the scalp.

One neuron generates a small amount of electrical activity in the order of femto-Ampere. This small amount cannot be picked up by surface electrodes, as it is overwhelmed by other electrical activity from neighboring neuron groups. When a large group of neurons (approximately 1000) is simultaneously active, the electrical activity is large enough to be picked up by the electrodes at the surface, thus generating a meaningful EEG signal. Moreover, in order to produce a detectable signal the dipoles corresponding to each of the neurons should be oriented in the same direction, as shown in figure 2.7. The superposition of all these dipoles creates a sufficiently strong potential field that is sensed by the surface electrodes. A large group of electrically active pyramidal cells in a small patch of cortex can be represented as one equivalent dipole on macroscopic level [41, 74]. It is very difficult to estimate the extent of the active area of the cortex as the potential distribution on the scalp is almost identical to that of an equivalent dipole [71].

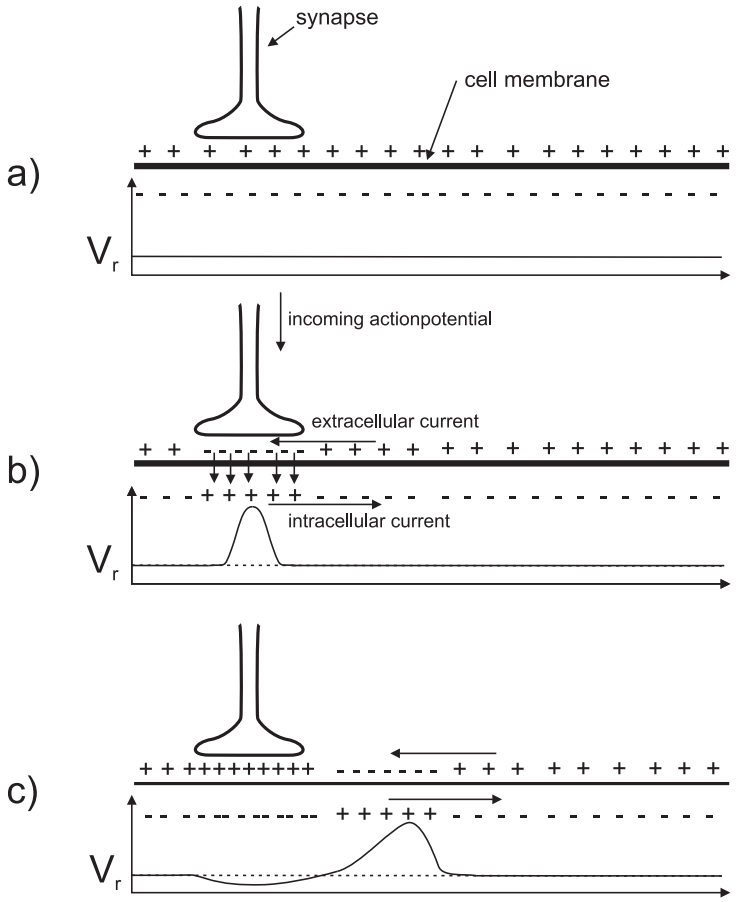

Figure 2.8: The generation of the EPSP is illustrated. If we start from the resting state (a), there is a potential difference between inside and outside the cell. If an incoming EPSP is generated, the synapse will release neurotransmitters in the cleft and the ion channels of the cell membrane will open. This causes an influx of positive ions ($Na^+$and K^+), which locally will cause a potential difference at neighboring sites inside and outside the neuron, respectively (b). Therefore, an intracellular current and an extracellular current will flow, which is the propagation of the EPSP (c).

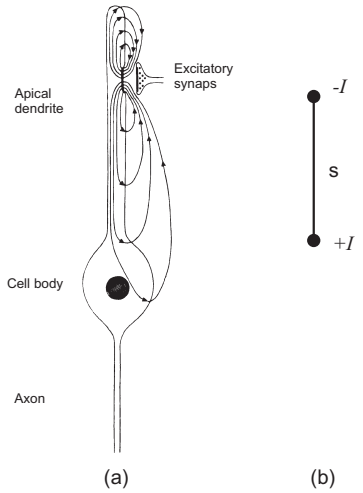

Figure 2.9: (a) An illustration of the post synaptic current flow in the intracellular and extracellular space by a excitatory synapse. (b) The current sink and current source as a model for the post synaptic current flow.

2.3.1 The current dipole

Current source and current sink inject and remove the same amount of current I and they represent an active pyramidal cell at microscopic level. They can be modeled as a current dipole as illustrated in figure 2.10(a). The position parameter $\mathbf{r}_{dip}$ of the dipole is typically chosen half way between the two monopoles.

The dipole moment $\mathbf{d}$ is defined by a unit vector $\mathbf{e_d}$ (which is directed from the current sink to the current source) and a magnitude given by $d = \|\mathbf{d}\| = I.p$, with p the distance between the two monopoles. Hence one can write:

$$\mathbf{d} = I.p\ \mathbf{e_d}. \tag{2.1}$$

It is often so that a dipole is decomposed in three dipoles located at the same position of the original dipole and each oriented along one of the Cartesian axes. The magnitude of each of these dipoles is equal to the orthogonal projection on the respective axis as illustrated in figure 2.10(b). one can write:

$$\mathbf{d} = d_x\mathbf{e}_x + d_y\mathbf{e}_y + d_z\mathbf{e}_z, \tag{2.2}$$

with $\mathbf{e}_x$, $\mathbf{e}_y$ and $\mathbf{e}_z$ being the unit vectors along the three axes. Furthermore, d_x, d_y and d_z are often called the dipole components.

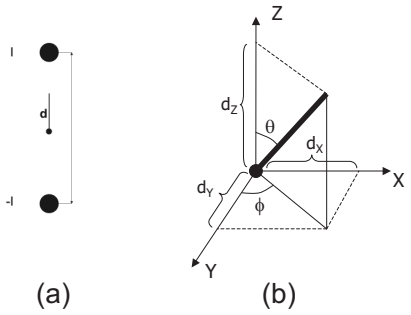

Figure 2.10: (a) The dipole parameters for a given current source and current sink configuration. (b) The dipole as a vector consisting of 6 parameters. 3 parameters are needed for the location of the dipole. 3 other parameters are needed for the vector components of the dipole. These vector components can also be transformed into spherical components: an azimuth, elevation and magnitude of the dipole.

2.4 The source localization problem

As mentioned before, EEG source localization consists of two problems: a forward problem and an inverse problem. The forward problem consists of calculating the electrode potentials at the scalp given a source. In this section, we describe how the electrode potentials can be calculated and a mathematical description is derived to calculate the potential distribution caused by a dipole source. Using the Maxwell equations, we will show that the potential field due to a dipole can be written as a Poisson's equation . Next, we derive a numerical approximation to the dipole source. Finally, we describe the several techniques (analytical and numerical) to solve Poisson's equation.

2.4.1 The forward problem

2.4.1.1 Maxwell equations and the continuity equation

Electromagnetic fields in media or in vacuum can be described by the Maxwell equations [81], which can be written as :

$$\nabla \cdot \mathbf{E} = \frac{\rho}{\epsilon_0} \textit{ (Gauss' Law)} \tag{2.3}$$

$$\nabla \times \mathbf{B} - \frac{\partial \mathbf{E}}{c^2 \partial t} = \mu_0 \mathbf{J} \tag{2.4}$$

$$\nabla \times \mathbf{E} + \frac{\partial \mathbf{B}}{\partial t} = 0 \textit{ (Faraday's Law)} \tag{2.5}$$

$$\nabla \cdot \mathbf{B} = 0 \tag{2.6}$$

where $\mathbf{E}$ and $\mathbf{B}$ are the electric and magnetic field respectively. ϵ_0 and μ_0 are the permeability and susceptibility of vacuum, respectively, which can be relate to the speed of light $c = \sqrt{\epsilon_0 \mu_0}$. ρ is the charge density, which is the amount of charge in a volume G (unit C/m^3).

As shown in the previous section the generators of the EEG can be described by a current source and sink or a current dipole source. A current corresponds to charges in motion and can be described by a current density, which is the current passing through an elementary surface. The current density $\mathbf{J}(x, y, z)$ is a 3D position-dependent vector field, where the direction of the vector indicates the direction of motion of the charges. The unit of the current density is A/m^2. The divergence of a vector field $\mathbf{J}$ is defined as follows :

$$\nabla \cdot \mathbf{J} = \lim_{G \to 0} \frac{1}{G} \oint_{\partial G} \mathbf{J} d\mathbf{S} \tag{2.7}$$

The integral over a closed surface ∂G represents a flux or a current through the volume G. This integral is positive when a net current leaves the volume G and is negative when a net current enters the volume G. The vector $d\mathbf{S}$ for a surface element of ∂G with area dS and outward normal $\mathbf{e}_n$, can also be written as $\mathbf{e}_n dS$. The unit of $\nabla \cdot \mathbf{J}$ is A/m^3 and is often called the current source density which in Plonsey [113] is symbolized with I_m.

From the Maxwell equations the continuity equation can be derived

$$\frac{\partial \rho}{\partial t} + \nabla \cdot \mathbf{J} = 0, \tag{2.8}$$

where ρ is the charge density and $\nabla \cdot \mathbf{J}$ is the current source density. Equation 2.8 states that the change in charge inside a volume conductor with time must correspond to a flow of charge out through the surface of the volume conductor. In other words, a current leaving or entering the volume conductor G causes a change in the total amount of charges in G.

2.4.1.2 Quasi-static conditions

It is shown in Plonsey and Heppner [114] that no charge can be piled up in the conducting extracellular volume for the frequency range of the signals measured in the EEG . At one moment in time all the fields are triggered by the active electric source. Hence, no time delay effects are introduced. All fields and currents behave as if they were stationary at each instance in time. These conditions are also called quasi-static conditions. They are not static because the neural activity changes with time, but the changes are slow compared to the propagation effects. Therefore the charge density in the volume G is constant, thus equation 2.8 yields:

$$\nabla \cdot \mathbf{J} = 0, \tag{2.9}$$

2.4.1.3 Derivation of Poisson's equation using Ohm's law

Due to the linearity of the Maxwell equations the current density inside the volume conductor, representing the human head, consists of the current density imposed by the dipole source or *primary current density* $\mathbf{J}_p$ and the current density flowing in the volume conductor or *return current density* $\mathbf{J}_r$:

$$\mathbf{J} = \mathbf{J}_p + \mathbf{J}_r. \tag{2.10}$$

The return current density generates an electric field. The relationship between the return current density $\mathbf{J}_r$ in A/m^2 and the electric field $\mathbf{E}$ in V/m is given by Ohm's law :

$$\mathbf{J}_r = \mathbf{\Sigma}\mathbf{E}, \tag{2.11}$$

with $\mathbf{\Sigma}$ being the position dependent conductivity. The conductivity $\mathbf{\Sigma}$ depends entirely on the nature of the material of which the conductor is composed, the state of aggregation of its parts and its temperature [97]. In the case of isotropic conductivities the conductivity is position-dependent scalar, $\sigma(x, y, z)$. For anisotropic conductivities the conductivity can be written as a position-dependent second order tensor Σ, whose matrix representation $\mathbf{\Sigma}(x, y, z) \in \mathbb{R}^{3\times3}$ according to a basis ($\mathbf{e}_x$,$\mathbf{e}_y$,$\mathbf{e}_z$) given by :

$$\mathbf{\Sigma} = \begin{bmatrix} \sigma_{xx}\, \sigma_{xy}\, \sigma_{xz} \\ \sigma_{xy}\, \sigma_{yy}\, \sigma_{yz} \\ \sigma_{xz}\, \sigma_{yz}\, \sigma_{zz} \end{bmatrix}, \tag{2.12}$$

and with units $A/(Vm) = S/m$. There are tissues in the human head that have an anisotropic conductivity. This means that the conductivity is not equal in every direction and that the electric field can induce a current density component perpendicular to it. Combining equation 2.11 with equation 2.10 yields :

$$\mathbf{J} = \mathbf{J}_p + \mathbf{\Sigma}\mathbf{E}. \tag{2.13}$$

The scalar potential field V, having volt as unit, is now introduced. This is possible due to Faraday's law (see equation 2.5) in which the time derivative of $\mathbf{B}$ is zero under quasi-static conditions ($\nabla \times \mathbf{E} = \mathbf{0}$) [123]. The link between the potential field and the electric field is given utilizing the gradient operator,

$$\mathbf{E} = -\nabla V. \tag{2.14}$$

The vector ∇V at a point gives the direction in which the scalar field V, having volt as its unit, most rapidly increases. The minus sign in equation (2.14)

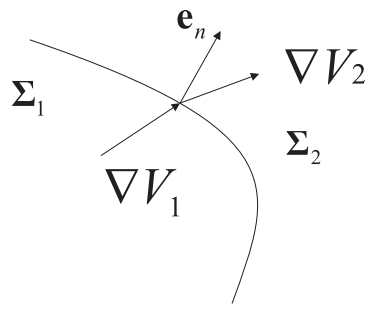

Figure 2.11: The boundary between two compartments, with conductivity σ_1 and σ_2. The normal vector $\mathbf{e}_n$ to the interface is also shown.

indicates that the electric field is oriented from an area with a high potential to an area with a low potential. Figure 2.12 also illustrates some equipotential lines generated by a current source and current a sink.

When equation 2.13, equation 2.9 and equation 2.14 are combined, Poisson's differential equation is obtained in general form:

$$\nabla \cdot (\boldsymbol{\Sigma} \nabla V) = \nabla \cdot \mathbf{J}_p. \tag{2.15}$$

Notice that Poisson's equation (2.15) is linear. Due to a dipole at a position $\mathbf{r}_{dip}$ and dipole moment or orientation $\mathbf{d}$, a potential V at an arbitrary scalp measurement point $\mathbf{r}$ can be decomposed in:

$$V(\mathbf{r}, \mathbf{r}_{dip}, \mathbf{d}) = d_x V(\mathbf{r}, \mathbf{r}_{dip}, \mathbf{e}_x) + d_y V(\mathbf{r}, \mathbf{r}_{dip}, \mathbf{e}_y) + d_z V(\mathbf{r}, \mathbf{r}_{dip}, \mathbf{e}_z). \tag{2.16}$$

where $\mathbf{r}$ and $\mathbf{r}_{dip}$ are the locations of the measurement electrode and the dipole source respectively. This decomposition will be used to solve the inverse problem and will be explained later on.

2.4.1.4 Boundary conditions

At the interface between two compartments, two boundary conditions are found. Figure 5 illustrates such an interface. A first condition is based on the inability to pile up charge at the interface. All charge leaving one compartment through the interface must enter the other compartment. In other words, all current (charge per second) leaving a compartment with conductivity $\boldsymbol{\Sigma}_1$ through the interface enters the neighboring compartment with conductivity $\boldsymbol{\Sigma}_2$:

$$\mathbf{J_1}.\mathbf{e}_n = \mathbf{J_2}.\mathbf{e}_n,$$

$$(\mathbf{\Sigma}_1 \nabla V_1).\mathbf{e}_n = (\mathbf{\Sigma}_2 \nabla V_2).\mathbf{e}_n, \tag{2.17}$$

where $\mathbf{e}_n$ is the normal component on the interface.

In particular no current can be injected into the air outside the human head due to the very low conductivity of the air. Therefore the current density at the surface of the head reads:

$$\begin{aligned} \mathbf{J_1}.\mathbf{e}_n &= 0, \\ (\mathbf{\Sigma}_1.\nabla V_1).\mathbf{e}_n &= 0. \end{aligned} \tag{2.18}$$

Equations (2.17) and (2.18) are called the Neumann boundary condition and the homogeneous Neumann boundary condition, respectively.

The second boundary condition only holds for interfaces between non-air compartments. By crossing the interface the potential cannot have discontinuities,

$$V_1 = V_2. \tag{2.19}$$

This equation represents the Dirichlet boundary condition.

2.4.1.5 Applying the divergence operator to the extracellular current density

In this paragraph, we will focus on the right hand side of the equation 2.15. We will apply the divergence operator on the current density keeping the dipole model in mind. In particular, we want to approximate the dipole model into a numerical representation, which will be used to solve the forward problem in realistic head model using numerical techniques.

First a small volume in the extracellular space, which encloses a current source and current sink, is investigated. The current flowing into the infinitely small volume, must be equal to the current leaving that volume. This is due to the fact that no charge can be piled up in the extracellular space. The surface integral of equation (2.7) is then zero, hence $\nabla \cdot \mathbf{J}_p = 0$.

In the second case a volume enclosed by the current sink with position parameters $\mathbf{r_1}(x_1, y_1, z_1)$ is assumed (see figure 2.12). The current sink represents the removal of positively charged ions at the apical dendrite of the pyramidal cell. The integral of equation (2.7) remains equal to $-I$ while the volume G in the denominator becomes infinitesimally small. This gives a singularity for the current source density. This singularity can be written as a delta function: $-I\delta(\mathbf{r} - \mathbf{r}_1)$. The negative sign indicates that current is removed from the extracellular volume. The delta function indicates that current is removed at one point in space.

For the third case a small volume around the current source at position $\mathbf{r_2}(x_2, y_2, z_2)$ is constructed. The current source represents the injection of

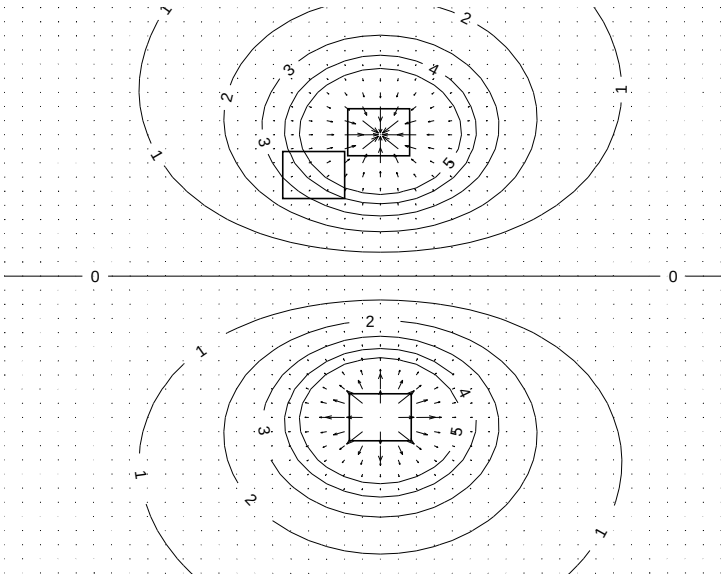

Figure 2.12: The current density and equipotential lines in the vicinity of a current source and current sink is depicted. Equipotential lines are also given. Boxes are illustrated which represent the volumes G.

positively charged ions at the cell body of the pyramidal cell. The current source density equals $I\delta(\mathbf{r} - \mathbf{r}_2)$. Figure 2.12 represents the current density vectors for a current source and current sink configuration. Furthermore, three boxes are presented corresponding with the three cases discussed above.

Uniting the three cases given above, one obtains:

$$\nabla \cdot \mathbf{J}_p = I\delta(\mathbf{r} - \mathbf{r}_2) - I\delta(\mathbf{r} - \mathbf{r}_1). \tag{2.20}$$

2.4.1.6 General formulation of Poisson's equation

In the Cartesian coordinate system equation (2.15) becomes for isotropic conductivities and when substituting the right hand side by equation 2.20:

$$\frac{\partial}{\partial x}(\sigma\frac{\partial V}{\partial x}) + \frac{\partial}{\partial y}(\sigma\frac{\partial V}{\partial y}) + \frac{\partial}{\partial z}(\sigma\frac{\partial V}{\partial z}) =$$
$$-I\delta(x - x_2)\delta(y - y_2)\delta(z - z_2) + I\delta(x - x_1)\delta(y - y_1)\delta(z - z_1)$$

and for anisotropic conductivities:

$$\sigma_{11}\frac{\partial^2 V}{\partial x^2} + \sigma_{22}\frac{\partial^2 V}{\partial y^2} + \sigma_{33}\frac{\partial^2 V}{\partial z^2} + 2\left(\sigma_{12}\frac{\partial^2 V}{\partial x \partial y} + \sigma_{13}\frac{\partial^2 V}{\partial x \partial z} + \sigma_{23}\frac{\partial^2 V}{\partial y \partial z}\right)$$

$$+\left(\frac{\partial\sigma_{11}}{\partial x}+\frac{\partial\sigma_{12}}{\partial y}+\frac{\partial\sigma_{13}}{\partial z}\right)\frac{\partial V}{\partial x}$$
$$+\left(\frac{\partial\sigma_{12}}{\partial x}+\frac{\partial\sigma_{22}}{\partial y}+\frac{\partial\sigma_{23}}{\partial z}\right)\frac{\partial V}{\partial y}+\left(\frac{\partial\sigma_{13}}{\partial x}+\frac{\partial\sigma_{23}}{\partial y}+\frac{\partial\sigma_{33}}{\partial z}\right)\frac{\partial V}{\partial z}=$$
$$-I\delta(x-x_2)\delta(y-y_2)\delta(z-z_2)+I\delta(x-x_1)\delta(y-y_1)\delta(z-z_1), \tag{2.21}$$

where $\mathbf{r}_2=(x_2,y_2,z_2)^T$ and $\mathbf{r}_1=(x_1,y_1,z_1)^T$ is the location of the current sink and current source respectively. σ_{ij} are the elements of the tensor $\mathbf{\Sigma}$. Moreover, in media where the anisotropic conductivity tensor is constant, equation 2.21 becomes:

$$\sigma_{11}\frac{\partial^2 V}{\partial x^2}+\sigma_{22}\frac{\partial^2 V}{\partial y^2}+\sigma_{33}\frac{\partial^2 V}{\partial z^2}+2\left(\sigma_{12}\frac{\partial^2 V}{\partial x\partial y}+\sigma_{13}\frac{\partial^2 V}{\partial x\partial z}+\sigma_{23}\frac{\partial^2 V}{\partial y\partial z}\right)=$$
$$-I\delta(x-x_2)\delta(y-y_2)\delta(z-z_2)+I\delta(x-x_1)\delta(y-y_1)\delta(z-z_1). \tag{2.22}$$

2.4.1.7 General algebraic formulation of the forward problem

In symbolic terms, the EEG forward problem is that of finding, in a reasonable amount of time, the scalp potential $V(\mathbf{r},\mathbf{r}_{dip},\mathbf{d})$ at an electrode positioned at $\mathbf{r}$ due to a single dipole with dipole moment $\mathbf{d}$ and position $\mathbf{r}_{dip}$. Due to the linearity of the Poisson's equation, the potential due to multiple dipole sources can be written as a superposition of the potential due to each dipole source. Hence, the potential due to a arbitrary dipole can be written as the sum of the potential the three orthogonal components of the dipole $\mathbf{d}=d_x\mathbf{e}_x+d_y\mathbf{e}_y+d_z\mathbf{e}_z$:

$$V(\mathbf{r},\mathbf{r}_{dip},\mathbf{d})=d_xV(\mathbf{r},\mathbf{r}_{dip},\mathbf{e}_x)+d_yV(\mathbf{r},\mathbf{r}_{dip},\mathbf{e}_y)+d_zV(\mathbf{r},\mathbf{r}_{dip},\mathbf{e}_z). \tag{2.23}$$

where $\mathbf{r}$ and $\mathbf{r}_{dip}$ are the locations of the measurement electrode and the dipole source respectively.

For M electrodes carefully placed at the scalp at positions $\mathbf{r}_i$ with $i=1,\ldots,M$, the electrode potentials can be written as:

$$\begin{aligned}\mathbf{V}&=\begin{bmatrix}V(\mathbf{r}_1)\\ \vdots\\ V(\mathbf{r}_M)\end{bmatrix}\\ &=\begin{bmatrix}V(\mathbf{r}_1,\mathbf{r}_{dip},\mathbf{e}_x) & V(\mathbf{r}_1,\mathbf{r}_{dip},\mathbf{e}_y) & V(\mathbf{r}_1,\mathbf{r}_{dip},\mathbf{e}_z)\\ \vdots & \vdots & \vdots\\ V(\mathbf{r}_M,\mathbf{r}_{dip},\mathbf{e}_x) & V(\mathbf{r}_M,\mathbf{r}_{dip},\mathbf{e}_y) & V(\mathbf{r}_M,\mathbf{r}_{dip},\mathbf{e}_z)\end{bmatrix}\begin{bmatrix}d_x\\ d_y\\ d_z\end{bmatrix}\\ &=\mathbf{L}(\mathbf{r})\cdot\mathbf{d}\end{aligned} \tag{2.24}$$

where the matrix operator $\mathbf{L}(\mathbf{r}) \in \mathbb{R}^{M\times 3}$ is the so-called *lead field matrix*, which is dependent on the dipole position, electrode positions and the properties of the head model. The lead field matrix can also be written as $\mathbf{L}(\mathbf{r}) = (\mathbf{V}_x, \mathbf{V}_y, \mathbf{V}_z)$ where $\mathbf{V}_x \in \mathbb{R}^{M\times 1}$ represents the electrode potentials for a unity dipole, oriented along the x-axis and similar $\mathbf{V}_y$ and $\mathbf{V}_z$

2.4.2 Solving the forward problem

In the next paragraph we will give an overview of methods to solve the forward problem given by equations 2.21, 2.21 and 2.22 in a head model with isotropic or anisotropic conductivities respectively. First, we will focus on analytical methods that can be used in simple head models consisting of concentric spheres. Next, several numerical methods will be discussed that can solve the forward problem in more realistic and complex head models. This results in a linear system of equations, which is large and sparse. In order to solve this system, an iterative method, successive over-relaxation (SOR), is briefly explained.

2.4.2.1 Notational conventions

In the following paragraph we will describe techniques to solve the forward problem. Simple head models with a spherical shape can use an analytical formula, while realistic head models need numerical techniques. For now on, we will denote the continuous potential as $V(x, y, z)$, where x,y and z are continuous. For the numerical techniques the potential field has to be discretized in points. We will denote the discrete potential $\varphi_i = V(x_i, y_i, z_i)$, where $i = 1 \ldots N$. x_i,y_i and z_i are the points where the potential is discretized. N is the number of points used to discretize the geometry.

2.4.2.2 Dipole field in an infinite homogeneous isotropic conductor

The potential field generated by a current dipole with dipole moment $\mathbf{d} = d\ \mathbf{e_d}$ at a position $\mathbf{r}_{dip}$ in an infinite conductor with conductivity σ, is introduced. The potential field is given by:

$$V(\mathbf{r}, \mathbf{r}_{dip}, \mathbf{d}) = \frac{\mathbf{d}.(\mathbf{r} - \mathbf{r}_{dip})}{4\pi\sigma\|\mathbf{r} - \mathbf{r}_{dip}\|^3}, \tag{2.25}$$

with $\mathbf{r}$ being the position where the potential is calculated. Assume that the dipole is located in the origin of the Cartesian coordinate system and oriented along the z-axis. Then we can write:

$$V(\mathbf{r}, \mathbf{0}, d\mathbf{e}_z) = \frac{d\cos\theta}{4\pi\sigma r^2}, \tag{2.26}$$

where θ represents the angle between the z-axis and $\mathbf{r}$ and $r = \|\mathbf{r}\|$.

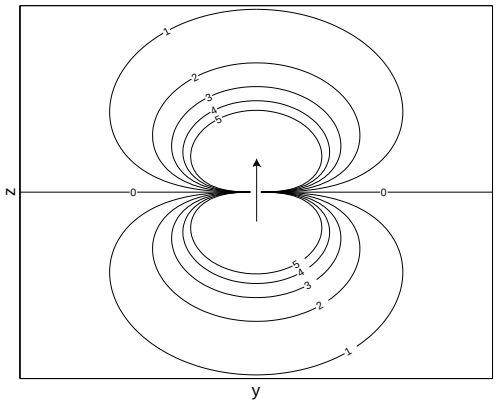

Figure 2.13: The equipotential lines of a dipole oriented along the z-axis. The numbers correspond to the level of intensity of the potential field generated of the dipole. The zero line divides the dipole field into two parts: a positive one and a negative one.

Equation (2.26) shows that a dipole field attenuates with $1/r^2$. It is significant to remark that V, from equation (2.25), added with an arbitrary constant, is also a solution of Poisson's equation. A reference potential must be chosen. One can choose to set one electrode to zero or one can opt for average referenced potentials. The latter result in electrode potentials that have a zero mean.

2.4.2.3 The N-shell concentric spherical head model

The first volume conductor models of the human head consisted of a homogeneous sphere [46]. However it was soon noticed that the skull tissue had a conductivity significantly lower than scalp and brain tissue. Therefore the volume conductor model of the head needed further refinement and a three-shell concentric spherical head model was introduced.

In this model, the inner sphere represents the brain, the intermediate layer represents the skull and the outer layer represents the scalp. For this geometry a semi-analytical solution of Poisson's equation exists . The derivation is based on Ary et al. [4], Sarvas [132] and Salu et al. [131]. Variants of the three-shell spherical head model, such as the Berg-Scherg approximation [21], in which a single-sphere model is used to approximate a three- (or four-) layer sphere, have also been used to further improve the computational efficiency of multi-layer spherical models.

There are also semi-analytical solutions available for layered spheroidal anisotropic volume conductors [78, 40, 159]. Here the conductivity in the tangential direction can be chosen differently than in the radial direction of the sphere. Analytic solutions also exist for eccentric spheres and ellipsoidal models [98, 85, 147].

In this dissertation we use the analytical solution in a layered anisotropic spheroidal volume according to de Munck [39]. The spherical head model consists of concentric spheres with radii $r_1 < r_2 < \ldots < r_{N-1} < r_N$. The layers S_i for $i = 1, \ldots, N$ are defined as the regions between the boundaries of two spheres as shown in figure 2.14. In each layer S_i a radial conductivity ξ_i and tangential conductivity η_i is defined. A dipole with moment $\mathbf{d}$ is located at $\mathbf{r}_{dip}$ within the innermost layer S_1, $\|\mathbf{r}_{dip}\| = r_{dip} < r_1$. Then, the observed electrode potential on the outermost surface at $\mathbf{r}_e$ ($\|\mathbf{r}_e\| = r_e = r_N$) is

$$V(\mathbf{r}_{dip}, \mathbf{d}, \mathbf{r}_e) = \frac{d}{4\pi\xi_N r_e^2} \sum_{n=1}^{\infty} \frac{2n+1}{n} \left(\frac{r_{dip}}{r_e}\right)^{n-1} \left(f_n n \cos\alpha P_n(\cos\gamma) + g_n \cos\beta \sin\alpha P_n^1(\cos\gamma)\right) \tag{2.27}$$

where d is the L_2-norm of the dipole moment $\mathbf{d}$, α is the angle between the dipole location $\mathbf{r}_0$ and the dipole moment $\mathbf{d}$. γ is the angle between $\mathbf{r}_{dip}$ and $\mathbf{r}_e$. β is the angle between the planes P1 and P2. P1 is the plane defined by the vectors $\mathbf{r}_{dip}$ and $\mathbf{d}$ and P2 the plane is defined by the vectors $\mathbf{r}_{dip}$ and $\mathbf{r}_e$. P_n and P_n^1 are the Legendre and the associated Legendre polynomials, respectively. The other symbols are defined as:

$$f_n = \frac{\nu_1}{n} g_n$$

$$g_n = \frac{n(2\nu_N + 1)}{(2\nu_N + 1)(\nu_N m_{22} + (\nu_N + 1)m_{21})} \left(\frac{r_{dip}}{r_e}\right)^{2\nu_1 - n} \prod_{k=1}^{N} \left(\frac{r_{k-1}}{r_k}\right)^{-\nu_k}$$

$$\nu_i = \frac{\sqrt{1 + 4n(n+1)\eta_i/\xi_i} - 1}{2} \; (i = 1, 2, \ldots, N)$$

$$\begin{bmatrix} m_{11}\, m_{12} \\ m_{21}\, m_{22} \end{bmatrix} = \prod_{k=1}^{N-1} \frac{1}{2\nu_k + 1} \begin{bmatrix} \nu_{k+1} + \frac{\xi_k}{\xi_{k+1}}(\nu_k + 1) & \\ \left(\frac{\xi_k}{\xi_{k+1}}(\nu_k+1) - (\nu_{k+1}+1)\right)\left(\frac{r_e}{r_k}\right)^{2\nu_{k+1}+1} & \\ \left(\frac{\xi_k}{\xi_{k+1}}(\nu_k+1) - (\nu_{k+1}+1)\right)\left(\frac{r_e}{r_k}\right)^{2\nu_{k+1}+1} & \\ \left[(\nu_{k+1}+1) + \frac{\xi_k}{\xi_{k+1}}\nu_k\right]\left(\frac{r_e}{r_k}\right)^{2(\nu_{k+1}\nu_k)} & \end{bmatrix} \tag{2.28}$$

Equation (2.27) gives the scalp potentials generated by a dipole. In practice, the infinite sum is transformed into a finite one. de Munck and Peters [40] simplified the computation, which significantly reduces the number of terms needed for computing the potentials. Zhang [159] used different fast computation method, which is based Berg and Scherg approximation in the three spherical head model [21].

Recently however, it is becoming more apparent that the actual geometry of the head [124, 125, 80] together with the varying thickness and curvatures

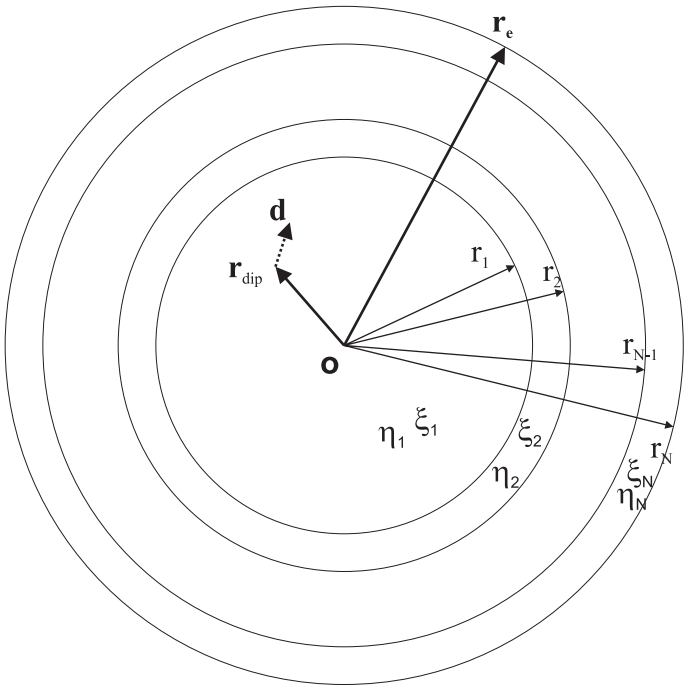

Figure 2.14: Illustration of the N-layered anisotropic spherical head model. The outermost layer radius of the sphere is r_N. The potential at $\mathbf{r}_e$ due to a dipole located at $\mathbf{r}_0$ within the innermost layer with moment $\mathbf{d}$ is computed. The dotted line indicates that the dipole moment $\mathbf{d}$ may not be in the plane defined by $\mathbf{r}_0$ and $\mathbf{r}_e$.

of the skull [34, 28], affects the solutions appreciably. So-called realistic head models are becoming much more common in the literature, in conjunction with either boundary-element, finite-element, or finite-difference methods. However, the computational requirements for a realistic head model are higher than that for a multi-layer sphere.

An approach which is situated between the spherical head model approaches and realistic ones is the sensor-fitted sphere approach [42]. Here a multilayer sphere is fitted to each sensor located on the surface of a realistic head model.

2.4.2.4 The boundary element method (BEM)

The boundary element method (BEM) is a numerical technique for calculating the surface potentials generated by current sources located in a piecewise homogeneous volume conductor. Although it restricts us to use only isotropic conductivities, it is still widely used because of its low computational needs. The method originated in the field of electrocardiography in the late sixties and made its entrance in the field of EEG source localization in the late eighties [73]. As the name implies, this method is capable of providing a solution to a volume problem by calculating the potential values at the interfaces and boundary of the volume induced by a given current source (e.g. a dipole). The interfaces separate regions of differing conductivity within the volume, while the boundary is the outer surface separating the non-conducting air with the conducting volume.

In practice, a head model is built from surfaces, each encapsulating a particular tissue. Typically, head models consist of 3 surfaces: brain-skull interface, skull-scalp interface and the outer surface (see figure 2.15. The regions between the interfaces are assumed to be homogeneous and isotropically conducting. To obtain a solution in such a piecewise homogeneous volume, each interface is tessellated with small boundary elements.

The integral equations describing the potential $V(\mathbf{r})$ in a piecewise volume conductor G, divided by a R interfaces $S_j \subset G$, at any point $\mathbf{r}$ on the r-th interface (S_r) were described in Geselowitz [49], Barnard et al. [13, 14], Sarvas [132]:

$$V(\mathbf{r}) = \frac{2\sigma_0}{\sigma_r^- + \sigma_r^+} V_0(\mathbf{r}) + \frac{1}{2\pi} \sum_{k=1}^{R} \frac{\sigma_k^- - \sigma_k^+}{\sigma_r^- + \sigma_r^+} \int_{\mathbf{r}' \in S_j} V(\mathbf{r}') \frac{\mathbf{r}' - \mathbf{r}}{\|\mathbf{r}' - \mathbf{r}\|^3} d\mathbf{S_j}, \tag{2.29}$$

where σ_0 corresponds to the medium in which the dipole source is located (the brain compartment) and $V_0(\mathbf{r})$ is the potential at $\mathbf{r}$ for an infinite medium with conductivity σ_0 as in equation (2.25). σ_j^- and σ_j^+ are the conductivities of, respectively, the inner and outer compartments divided by the interface S_j. $d\mathbf{S}$ is a vector oriented orthogonal to a surface element and $\|d\mathbf{S}\|$ the area of that surface element.

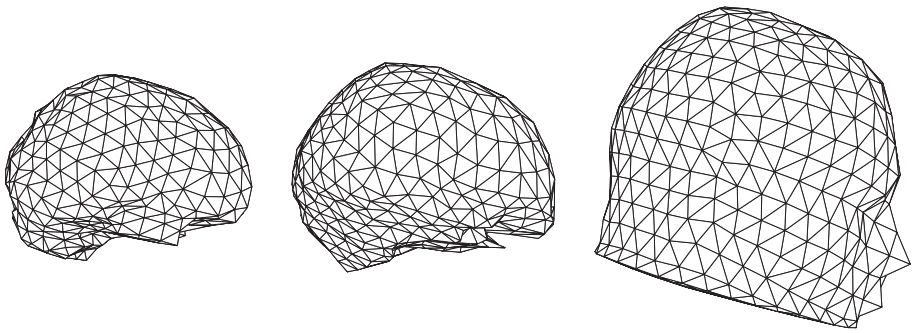

Figure 2.15: Triangulated surfaces of the brain, skull and scalp compartment used in BEM. The surfaces indicate the different interfaces of the human head: air-scalp, scalp-skull and skull-brain.

Each interface S_j with $j = 1, \ldots, R$ is digitized in N_{S_j} triangles, (see figure 2.15) and in each triangle center the potentials are calculated using equation (2.29). The integral over the surface S_j is transformed into a summation of integrals over triangles on that surface. Assume the scalp surface is the outer surface S_R. The potential values on surface S_R can be written as

$$V(\mathbf{r}) = \frac{2\sigma_0}{\sigma_R^- + \sigma_R^+} V_0(\mathbf{r}) + \frac{1}{2\pi} \sum_{k=1}^{R} \frac{\sigma_k^- - \sigma_k^+}{\sigma_R^- + \sigma_R^+} \sum_{j=1}^{N_{S_k}} \int_{\Delta_{S_k,j}} V(\mathbf{r}') \frac{\mathbf{r}' - \mathbf{r}}{\|\mathbf{r}' - \mathbf{r}\|^3} d\mathbf{S_k}, \tag{2.30}$$

where the integral is over $\Delta_{S_j,k}$, the j-th triangle on the surface S_j, R is the number of interfaces in the volume. An exact solution of the integral is generally not possible, therefore an approximated solution $\widetilde{V}^k(\mathbf{r})$ on surface S_k may be defined as a linear combination of N_{S_k} simple basis functions

$$\widetilde{V^k}(\mathbf{r}) = \sum_{i=1}^{N_{S_k}} \phi_i^k h_i(\mathbf{r}). \tag{2.31}$$

The basis functions $h_i(\mathbf{r})$ can be defined in several ways. The "constant-potential" approach for triangular elements uses basis functions defined by

$$h_i(\mathbf{r}) = \begin{cases} 1 \, \mathbf{r} \in \Delta_i \\ 0 \, \mathbf{r} \notin \Delta_i \end{cases} \tag{2.32}$$

where Δ_i denotes the ith planar triangle on the tessellated surface. The collocation points are typically the centroids of the surface elements or the vertices [38]. The coefficients φ_i^k represent unknowns on surface S_k whose values are

determined by constraining $\widetilde{V}(\mathbf{x})$ to satisfy (2.30) at discrete points, also known as collocation points. Moreover, equation (2.30) can be rewritten as

$$V(\mathbf{r}) = \frac{2\sigma_0}{\sigma_r^- + \sigma_r^+} V_0(\mathbf{r}) + \frac{1}{2\pi} \sum_{k=1}^{R} \frac{\sigma_k^- - \sigma_k^+}{\sigma_r^- + \sigma_r^+} \sum_{i,j=1}^{N_{S_k}} \varphi_i^k \int_{\Delta_{S_k,j}} \frac{h_i(\mathbf{r})(\mathbf{r}' - \mathbf{r})}{\|\mathbf{r}' - \mathbf{r}\|^3} d\mathbf{S_k}. \tag{2.33}$$

This equation can be transformed into a set of linear equations:

$$\mathbf{\Phi} = \mathbf{A}\mathbf{\Phi} + \mathbf{V}_0, \tag{2.34}$$

where $\mathbf{\Phi} \in \mathbb{R}^{N\times 1}$,$\mathbf{\Phi} = (\varphi_0, \varphi_1, \ldots, \varphi_N)^T$ and $\mathbf{V}_0 \in \mathbb{R}^{N\times 1}$ are column vectors denoting at every node the wanted potential value and the potential value in an infinite homogeneous medium due to a source, respectively. N is the total amount of discretization points of all the surfaces. Thus, $\mathbf{A}$ is a matrix generated from the integrals, which depends on the geometry of the surfaces and the conductivities of each region.

2.4.2.5 The finite element method (FEM)

Another method to solve Poisson's equation in a realistic head model is the finite element method (FEM). The Galerkin approach [83] is used to equation (2.15) with boundary conditions (2.17), (2.18), (2.19). First, equation (2.15) is multiplied with a test function (or *Ansatz-function*) ψ and then integrated over the volume G representing the entire head. Using Green's first identity for integration:

$$\int_G \psi \nabla \cdot (\mathbf{\Sigma} \cdot \nabla V) dG = \int_{\partial G} \psi (\mathbf{\Sigma} \cdot \nabla V) \mathbf{dS} - \int_G \nabla\psi \cdot (\mathbf{\Sigma} \cdot \nabla V) dG, \tag{2.35}$$

in combination with the boundary conditions (2.18), yields the 'weak formulation' of the forward problem:

$$-\int_G \nabla\psi \cdot (\mathbf{\Sigma} \cdot \nabla V) dG = \int_G \psi I_m dG. \tag{2.36}$$

If $(v, w) = \int_G v(x, y, z)w(x, y, z)dG$ and $a(u, v) = -(\nabla v, \mathbf{\Sigma} \cdot \nabla u)$, this can be written as:

$$a(V, \psi) = (I_m, \psi) \tag{2.37}$$

The entire 3D volume conductor is digitized in small elements. Figure 2.16 illustrates a 2D volume conductor digitized with triangles. Here I_m denotes the source configuration. Solving the above equation for an ideal dipole would result in a singularity at the position of the dipole. However, many approaches exist to circumvent this. One can model the dipole by monopoles distributed in the neighboring nodes (Saint Venant's principle) [154] or using partial integration approach of the right hand side of equation 2.37 [133, 101]. An alternative approach is the subtraction method in which the total potential at the electrodes is divided into a singularity potential (dipole in infinite medium with homogeneous conductivity) and a correction potential [158].

The computational points φ_i, with $i = 1, \ldots, N$ can be identified with the vertices of the elements (n is the number of vertices). The unknown potential $V(x, y, z)$ is given by

$$V(x, y, z) = \sum_{i=1}^{n} \varphi_i \psi_i(x, y, z), \tag{2.38}$$

where ψ_i with $i = 1, \ldots, N$ denotes a set of test functions also called basis functions. They have a local support, i.e. the area in which they are non-zero is limited to adjacent elements. Moreover, the basis functions span a space of piecewise polynomial functions.

Furthermore, they have the property that they are each equal to unity at the corresponding computational point and equal to zero at all other computational points. Substituting equation 2.38 in equation 2.37 produces n equations in n unknowns:

$$a(\sum_{i=1}^{n} \varphi_i \psi_i, \psi_j) = (I_m, \psi_j), \tag{2.39}$$

$$\sum_{i=1}^{n} a(\psi_i, \psi_j)\varphi_i = (I_m, \psi_j) \tag{2.40}$$

Due to the local support of the basis function, each equation consists only of a linear combination of φ_i's for the point itself and its adjacent computational points. Hence the system $\mathbf{A} \in \mathbb{R}^{n \times n}, A_{ij} = a(\psi_i, \psi_j)$ is sparse. The matrix $\mathbf{A}$ is the so-called *stiffness matrix*. In matrix notation one can obtain:

$$\mathbf{A}.\mathbf{\Phi} = \mathbf{I}, \tag{2.41}$$

with $\mathbf{I} \in \mathbb{R}^{n \times 1}$ being the column vector of the source terms obtained by the right hand side of equation 2.40.

In general the stiffness matrix is very big, making the computation of the electrode potentials very computationally intensive. To solve equation (2.41),

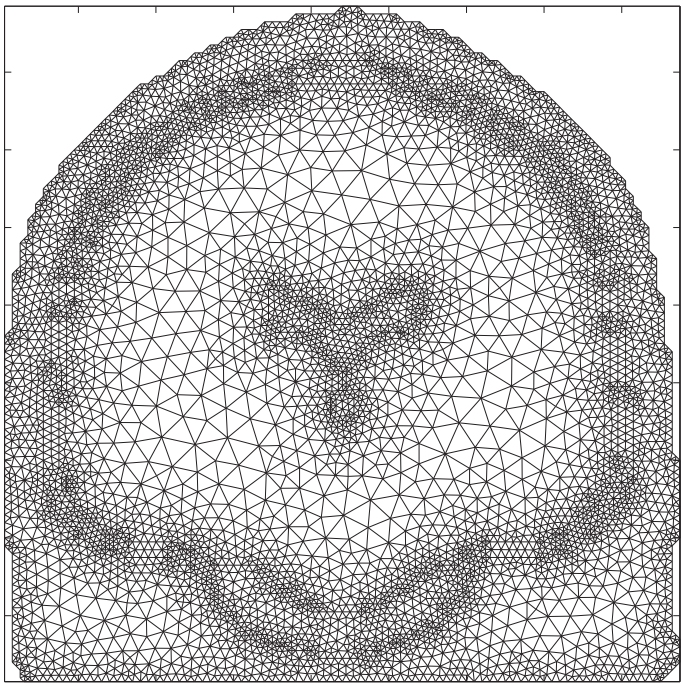

Figure 2.16: A digitization of the 2D coronal slice of the head. The 2D elements are the triangles.

iterative solvers for large sparse systems are used as given in Saad [128]. Some techniques have been proposed to reduce the computational burden and increase efficiency [6]. A freely licensed software package that implements both FEM and BEM is NEUROFEM [152, 155, 151, 1].

2.4.2.6 The finite difference method (FDM)

2.4.2.6.1 Basics and notations

For the sake of simplicity and better understanding, some basics are explained and some notations are mentioned in this paragraph. A finite difference formulation of a partial differential equation uses a uniform cubic grid, which covers the domain. The partial differential domain is approximated at the nodes of the grid by a finite difference operator. In the one dimensional case the Poisson's equation can be written as:

$$\frac{\partial^2 V}{\partial x^2} = f(x) \text{ in } \Omega = [0, c] \text{ with } c > 0 \tag{2.42}$$

where u is the potential. A grid has to be defined over the domain Ω. For the sake of simplicity we divide Ω with n equidistant subintervals with nodes at $[0, h_x, 2h_x, 3h_x, \ldots, (n-1)h_x, c = nh_x]$ such that $x_i = i \cdot h_x$ where h_x is the constant grid size over the domain and $i = 1, 2, 3, \ldots, (n-1), n$. An example of this discretization of the domain is shown in 2.17. Moreover, we use the notation φ_i to indicate the potential at point x_i. Hence, $\varphi_i = V(x_i) = V(i \cdot h_x)$ and $f_i = f(x_i) = f(i \cdot h_x)$.

Assuming that V is Lipshitz continuous, we can write φ_{i+1} and φ_{i-1} as Taylor expansion series with respect to φ_i:

$$\varphi_{i+1} = \varphi_i + h_x \frac{\partial V}{\partial x}\bigg|_i + \frac{h_x^2}{2} \frac{\partial^2 V}{\partial x^2}\bigg|_i + \frac{h_x^3}{6} \frac{\partial^3 V}{\partial x^3}\bigg|_i + \frac{h_x^4}{24} \frac{\partial^4 V}{\partial x^4}\bigg|_i + \ldots \tag{2.43}$$

$$\varphi_{i-1} = \varphi_i - h_x \frac{\partial V}{\partial x}\bigg|_i + \frac{h_x^2}{2} \frac{\partial^2 V}{\partial x^2}\bigg|_i - \frac{h_x^3}{6} \frac{\partial^3 V}{\partial x^3}\bigg|_i + \frac{h_x^4}{24} \frac{\partial^4 V}{\partial x^4}\bigg|_i + \ldots \tag{2.44}$$

where the subscript i denotes an evaluation of the values at node i. The second derivative $\frac{\partial^2 V}{\partial x^2}$ can then be approximated by adding equations 2.43 and 2.44:

$$\frac{\partial^2 V}{\partial x^2}\bigg|_i = \frac{1}{h_x^2} (\varphi_{i-1} - 2\varphi_i + \varphi_{i+1}) - \frac{h_x^2}{12} \frac{\partial^4 V}{\partial x^4} + \ldots \tag{2.45}$$

If we allow a truncation error of $\frac{h_x^2}{12} \cdot \frac{\partial^4 V}{\partial x^4} + \ldots$ the Poisson equation 2.42 can be written as:

$$\frac{\varphi_{i-1} - 2\varphi_i + \varphi_{i+1}}{h_x^2} = f_i \text{ for } i = 1, 2, \ldots, (n-1). \tag{2.46}$$

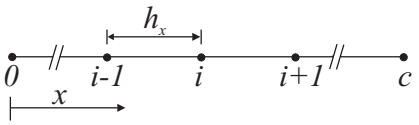

Figure 2.17: The 1D grid

2.4.2.6.2 The finite difference method in isotropic media (iFDM)

The differential equation (2.21) with boundary conditions (2.17), (2.18), (2.19) is transformed into a linear equation utilizing the 'box integration' scheme [100] for the cell-centered iFDM. This numerical technique was used in Vanrumste et al. [146, 144, 145].

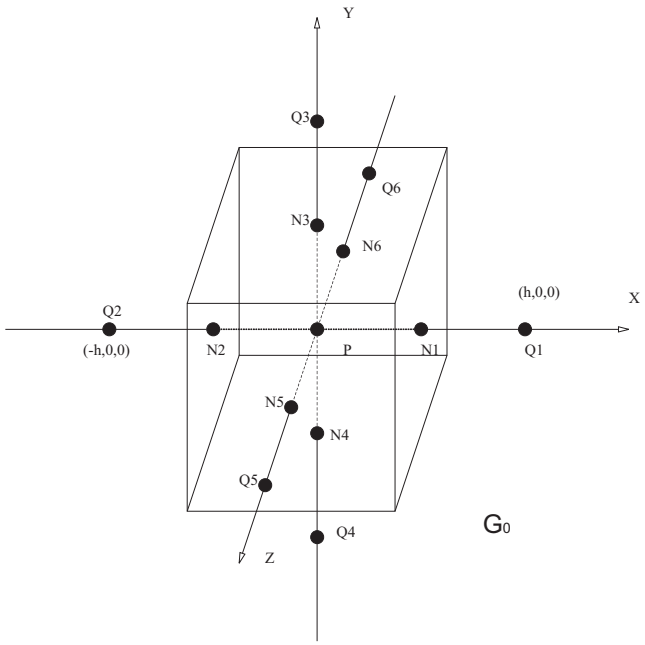

Figure 2.18: A typical node P in an FDM grid with its neighbours Q_i $(i = 1 \cdots 6)$. The volume G_0 is given by the box.

Consider a typical node P in a cubic grid with internode spacing h. The six neighboring nodes are Q_i $(i = 1, \ldots, 6)$ as illustrated in figure 2.18.

Introducing α_i and α_0 as,

$$\begin{aligned} \alpha_i &= 2h\frac{\sigma_0\sigma_i}{\sigma_0 + \sigma_i} \\ \alpha_0 &= \sum_{i=1}^{6} \alpha_i, \end{aligned} \tag{2.47}$$

a finite difference approximation of (2.21) is obtained:

$$\sum_{i=1}^{6} \alpha_i \phi_{Q_i} - \alpha_0 \phi_P = I_P, \tag{2.48}$$

with

$$I_P = I\delta(\mathbf{r} - \mathbf{r}_1) - I\delta(\mathbf{r} - \mathbf{r}_2). \tag{2.49}$$

The current injected or removed is denoted by I and the location of the current source and sink is denoted by $\mathbf{r}_1$ and $\mathbf{r}_2$, respectively. The location of node at P

is denoted by $\mathbf{r}$. For volumes G, which contain a current monopole, I_P becomes I or $-I$. α_i has the dimension of Ω^{-1} and corresponds with the conductance between P and Q_i. Furthermore, for $I_P = 0$ Kirchoff's law holds at the node P.

2.4.2.6.3 Finite difference formulation of the Poisson equation in anisotropic media (aFDM)

In this paragraph we introduce a finite difference method that can incorporate anisotropic conductivities. It was first used in the field of electrocardiography by Saleheen and Kwong [129], where it was used to calculate potential field due to a defibrilation procedure. Originally Malik et al. [94] also applied finite difference method for the same purpose, as the heart is a highly anisotropic tissue.

The approach to obtain the finite difference formulation in the 3D domain is similar to the formulation in 1D. In 3D the Poisson equation is written as:

$$\nabla \cdot (\mathbf{\Sigma}(x,y,z) \cdot \nabla V(x,y,z))) = f(x,y,z) \text{ in } \Omega \subset \mathbb{R}^3 \tag{2.50}$$

where $f(x,y,z)$ is the representation of the dipole source in Ω. $\mathbf{\Sigma}$ is a position dependent, symmetric, positive definite, conductivity tensor:

$$\mathbf{\Sigma} = \begin{bmatrix} \sigma_{xx}\, \sigma_{xy}\, \sigma_{xz} \\ \sigma_{xy}\, \sigma_{yy}\, \sigma_{yz} \\ \sigma_{xz}\, \sigma_{yz}\, \sigma_{zz} \end{bmatrix} \tag{2.51}$$

Expanding equation 2.50 yields

$$\begin{aligned} &\sigma_{xx}\frac{\partial^2 V}{\partial x^2} + \sigma_{yy}\frac{\partial^2 V}{\partial y^2} + \sigma_{zz}\frac{\partial^2 V}{\partial z^2} + \\ &2\left(\sigma_{xy}\frac{\partial^2 V}{\partial x \partial y} + \sigma_{xz}\frac{\partial^2 V}{\partial x \partial z} + \sigma_{yz}\frac{\partial^2 V}{\partial y \partial z}\right) + \left(\frac{\partial \sigma_{xx}}{\partial x} + \frac{\partial \sigma_{xy}}{\partial y} + \frac{\partial \sigma_{xz}}{\partial z}\right)\frac{\partial V}{\partial x} \\ &+ \left(\frac{\partial \sigma_{xy}}{\partial x} + \frac{\partial \sigma_{yy}}{\partial y} + \frac{\partial \sigma_{yz}}{\partial z}\right)\frac{\partial V}{\partial y} + \left(\frac{\partial \sigma_{xz}}{\partial x} + \frac{\partial \sigma_{yz}}{\partial y} + \frac{\partial \sigma_{zz}}{\partial z}\right)\frac{\partial V}{\partial z} = \\ &-I\delta(x-x_2)\delta(y-y_2)\delta(z-z_2) + I\delta(x-x_1)\delta(y-y_1)\delta(z-z_1), \end{aligned} \tag{2.52}$$

where the right-hand-side, source term representing the dipole, is substituted by the approximation as a source term and sink term at $\mathbf{r}_1 = [x_1, y_1, z_1]^T$ and $\mathbf{r}_2 = [x_2, y_2, z_2]^T$, respectively.

A cubic grid is defined over the domain Ω as illustrated in figure 2.19. In order to obtain the finite difference formulation of equation (2.52), the potential in points 1 to 18 are expanded into a Taylor series with respect to the potential in point 0 (see figure 2.19). The expansions are done for $\sigma \cdot \varphi_i$ for $i = 1, \ldots, 18$.

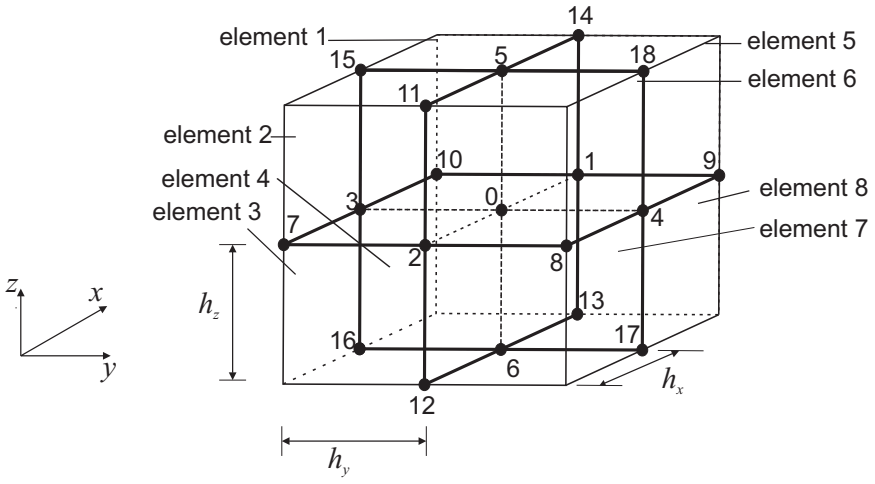

Figure 2.19: The 3D cubic grid. The potential in points 1 to 18 are expanded in to Taylor series with respect to the potential in 0 in order to obtain the finite difference formulation of the partial differential equation 2.52

To express the partial derivatives from equation (2.52) in terms of finite difference formula using the potential in the neighboring points, Taylor series expansions are made in this case for eighteen neighbors to the central node. More precisely, expansions are done with respect to the central node for the following products:

$$\begin{aligned} &\sigma_{xx}\varphi_1,\ \sigma_{yy}\varphi_2,\ \sigma_{xx}\varphi_3,\ \sigma_{yy}\varphi_4,\ \sigma_{zz}\varphi_5,\ \sigma_{zz}\varphi_6,\\ &\sigma_{xy}\varphi_7,\ \sigma_{xy}\varphi_8,\ \sigma_{xy}\varphi_9,\ \sigma_{xy}\varphi_{10},\sigma_{xz}\varphi_{11},\sigma_{yz}\varphi_{12},\\ &\sigma_{xz}\varphi_{13},\sigma_{yz}\varphi_{14},\sigma_{xz}\varphi_{15},\sigma_{yz}\varphi_{16},\sigma_{xz}\varphi_{17},\sigma_{yz}\varphi_{18}. \end{aligned} \tag{2.53}$$

However, before expanding the expression $\sigma_{**} \cdot \varphi_i$ in a Taylor series, a difficulty has to be overcome. As the cubic grid is defined over the domain, the conductivity tensor $\mathbf{\Sigma}$ is defined on a regular grid. Consequently the domain can be described as discrete, inhomogeneous and anisotropic. The conductivity tensor can be discontinuous, which can lead to singularities in the Taylor series expansion. In order to circumvent this problem, a transition layer of thickness t is introduced between the elements. This idea was adopted from Panizo et al. [111] and Saleheen and Kwong [129]. Using that technique the potential can be calculated in 8 nodes at a very small ($t << h_x$) distance from the central node. This is illustrated in figure 2.20. If we denote the eight neighboring nodes as $\varphi_{(i)}, i = a, \ldots, h$, it is clear from the linearity of the Maxwell equations that

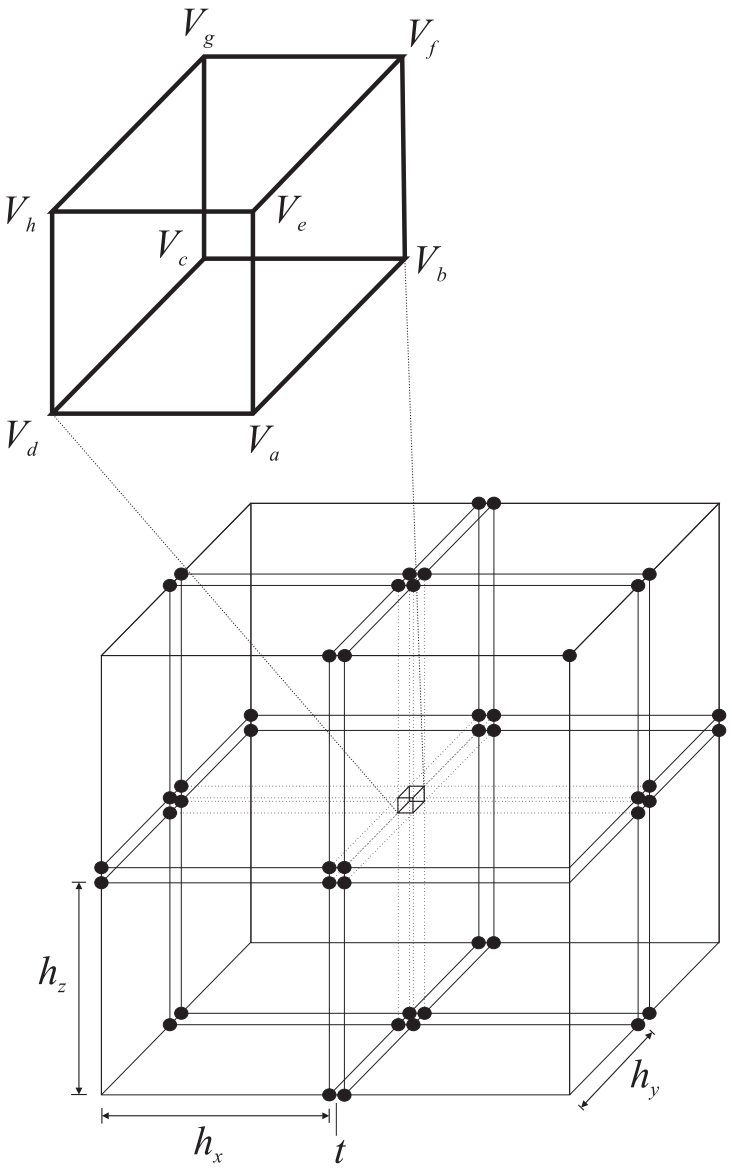

Figure 2.20: The 3D cubic grid with the transition layer. The transition layers are interposed between the elements to circumvent the discontinuity of the conductivity tensors. The central node is therefore replaced by 8 neighboring nodes, indicated by the little center cube.

the potential at the center node can be written as a limit $t \to 0$:

$$\varphi_0 = \lim_{t \to 0} \sum_{i=a}^{h} \frac{\varphi_{(i)}}{8} \tag{2.54}$$

The Taylor expansions of the aforementioned products are derived with respect to each of the 8 central nodes. As in each element the conductivity tensors are assumed to be constant, the partial derivatives in the third, fourth and fifth term in the left hand side of equation 2.52 vanishes. In that way eight different expressions for the partial differentials are obtained and are substituted into equation (2.52). Equation (2.52) is written eight times in function of the potential in the 18 neighboring nodes. The final difference formula is obtained by applying the formula (2.54) and taking the limit of the transition layer $t \to 0$. This results in the following formula:

$$\sum_{i=1}^{18} A_i \varphi_i = \left(\sum_{i=1}^{18} A_i \right) \varphi_0 + I_P \tag{2.55}$$

where φ_0 is the potential at the central discrete point and φ_i is the potential at the i-th neighboring point. A_i are coefficients depending on the conductivity tensors of the elements shown in figure 2.19. Note that the cubes indicate the conductivity tensors and the geometry of the head model, but the potential values are computed at the nodes between the voxels. I_P denotes the current depending on the position of the center node. If the center node is at a monopole of the current source or sink, than $I_P = 1$ or $I_P = -1$, respectively, else $I_P = 0$.

For nodes at the corners of the compartments as illustrated in figure 2.19, for example node 11, the boundary normal cannot be unambiguously defined. Therefore, the Neumann boundary equations (2.18) and (2.17) contain singularities in spatial derivatives of the conductivities. The method presented in Hallez et al. [64] and Saleheen and Kwong [129] has an advantage if one wants to enforce such a Neumann boundary condition: the formulation allows a discrete change or discontinuity in conductivity between neighboring elements and will automatically incorporate the boundary between two different materials. In short, the boundary condition is already implicitly formulated in equation (2.55) under the condition that a natural boundary is in the calculation grid. In our case, the head model should be surrounded with elements representing the air, which have a zero conductivity.

The coefficients A_i for $i = 1, \ldots, 18$ are factors that can be written as a function of the elements of the conductivity tensors in each element. This is due to the transition layer. The $A_i (k = 1, \ldots, 18)$ in equation 2.55 can be expressed as:

$$A_1 = \frac{1}{4h_x^2} \left[\sigma_{11(1)} + \sigma_{11(4)} + \sigma_{11(5)} + \sigma_{11(6)} \right]$$

$$
\begin{aligned}
A_2 &= \frac{1}{4h_x^2}\left[\sigma_{11(2)} + \sigma_{11(3)} + \sigma_{11(6)} + \sigma_{11(7)}\right] \\
A_3 &= \frac{1}{4h_y^2}\left[\sigma_{22(1)} + \sigma_{22(2)} + \sigma_{22(3)} + \sigma_{22(4)}\right] \\
A_4 &= \frac{1}{4h_y^2}\left[\sigma_{22(5)} + \sigma_{22(6)} + \sigma_{22(7)} + \sigma_{22(8)}\right] \\
A_5 &= \frac{1}{4h_z^2}\left[\sigma_{33(1)} + \sigma_{33(2)} + \sigma_{33(5)} + \sigma_{33(6)}\right] \\
A_6 &= \frac{1}{4h_z^2}\left[\sigma_{33(3)} + \sigma_{33(4)} + \sigma_{33(7)} + \sigma_{33(8)}\right] \\
A_7 &= \frac{1}{4h_xh_y}\left[\sigma_{12(3)} + \sigma_{12(2)}\right] \\
A_8 &= -\frac{1}{4h_xh_y}\left[\sigma_{12(6)} + \sigma_{12(7)}\right] \\
A_9 &= \frac{1}{4h_xh_y}\left[\sigma_{12(5)} + \sigma_{12(8)}\right] \\
A_{10} &= -\frac{1}{4h_xh_y}\left[\sigma_{12(1)} + \sigma_{12(4)}\right] \\
A_{11} &= -\frac{1}{4h_xh_z}\left[\sigma_{13(2)} + \sigma_{13(6)}\right] \\
A_{12} &= \frac{1}{4h_xh_z}\left[\sigma_{13(3)} + \sigma_{13(7)}\right] \\
A_{13} &= -\frac{1}{4h_xh_z}\left[\sigma_{13(4)} + \sigma_{13(8)}\right] \\
A_{14} &= \frac{1}{4h_xh_z}\left[\sigma_{13(1)} + \sigma_{13(5)}\right] \\
A_{15} &= -\frac{1}{4h_yh_z}\left[\sigma_{23(1)} + \sigma_{23(2)}\right] \\
A_{16} &= \frac{1}{4h_yh_z}\left[\sigma_{23(3)} + \sigma_{23(4)}\right] \\
A_{17} &= -\frac{1}{4h_yh_z}\left[\sigma_{23(7)} + \sigma_{23(8)}\right] \\
A_{18} &= \frac{1}{4h_yh_z}\left[\sigma_{23(5)} + \sigma_{23(6)}\right] \qquad (2.56)
\end{aligned}
$$

$$(2.57)$$

where $\sigma_{mn(p)}$ is the mn-th element of matrix representation of the conductivity tensor defined at element p.

For each node of a cubic grid we obtain a linear equation given by (2.48) in the isotropic case and (2.55) in the anisotropic case. The unknown potentials at the n computational points are represented by $\mathbf{\Phi} \in \mathbb{R}^{n\times 1}$. The source terms represented by $\mathbf{I} \in \mathbb{R}^{n\times 1}$ are calculated in each of the n cubes utilizing equation

(2.49). Notice that in the linear equations (2.48) or (2.55) only the neighboring computational points are included. The system matrix $\mathbf{A} \in \mathbb{R}^{n \times n}$ is a sparse matrix, as each row has 19 non-zero elements. In matrix notation one can write:

$$\mathbf{A} \cdot \mathbf{\Phi} = \mathbf{I} \tag{2.58}$$

where $\mathbf{\Phi} = (\varphi_1, \ldots, \varphi_j, \ldots, \varphi_N)^T$ is a vector with the potential values at each computational point. $\mathbf{I}$ is a vector indicating the current source and sink. If the current source (sink) monopole is placed at the k-th (l-th) node of the computational grid, then $\mathbf{I}_k = I$ ($\mathbf{I}_l = -I$), else $\mathbf{I}_p = 0$ with $p \neq k, l$. $\mathbf{A} \in \mathbb{R}^{n \times n}$ is a stiffness matrix, with A_{ij} is the i-th coefficient if the j-th point is assigned as the center node.

The linear system (2.58) can be solved using direct or iterative techniques. In this dissertation an iterative method (successive over-relaxation) will be used.

2.4.2.7 Comparing the various numerical methods

The three methods BEM, FEM and FDM can all be used to solve the forward problem of EEG source analysis in a realistic head model.

A first difference between BEM and FEM or FDM is the domain in which the solutions are calculated. In the BEM the solutions are calculated on the boundaries between the homogeneous isotropic compartments while in the FEM and FDM the solution of the forward problem is calculated in the entire volume. Consequently, the FEM and FDM lead to a larger number of computational points than the BEM. Furthermore, the potential at an arbitrary point can be determined with FEM and FDM by interpolation of computational points in its vicinity, while for the BEM it is necessary to reapply the Barnard formula [13] and numerical integration.

Another important aspect is the computational efficiency. In the BEM, a full matrix needs to be inverted. Hence once the matrix is inverted, only a matrix multiplication is needed to obtain the scalp potentials. This limited computational load is an attractive feature when solving the inverse problem, where a large number of forward evaluations need to be performed.

For the FEM and the FDM, a direct inversion of the large sparse matrices found in (2.41) and (2.58) is not possible due to the dimension of the matrices. Typically at least 500,000 computational points are considered which leads to system matrices of 500,000 equations with 500,000 unknowns which cannot be solved in a direct manner with the computers now available. However matrices found in FEM and FDM can be inverted for a given source configuration or right-hand side term, utilizing iterative solvers such as the successive over-relaxation method, the conjugate gradient method [128], or algebraic multigrid methods [25, 76, 102, 151]. A disadvantage of the iterative solvers is that for each source configuration the solver has to be reapplied. The FEM and

FDM would be computationally inefficient when for each dipole an iterative solver would need to be used. To overcome this inefficiency the reciprocity theorem can be used, as will be explained in chapter 3 and appendix A. An alternative approach is transforming the inverse of the stiffness matrix so that only the electrode potentials at the nodes corresponding with the electrodes are calculated [152, 2].

When a large number of conducting compartments are introduced, a large number of boundaries need to be sampled for the BEM. This leads to a large full system matrix, thus a lower numerical efficiency. The FEM and FDM are sensitive to the conductivity of the different compartments. If the conductivity differs too much, then it may happen that the eigenvalues of the stiffness matrix become more separated. In FDM modeling, the heterogeneous nature of realistic head models will make the stiffness matrix less sparse and badly conditioned. Moreover, the incorporation of anisotropic conductivities will decrease the sparseness of the stiffness matrix. While in FEM, the stiffness matrix only becomes more ill-conditioned. This can lead to very slow convergence if iterative methods are used. However the skull has the lowest conductivity of all brain tissues and a solution can still be obtained, moreover this will not pose a problem to solve the system. In short, the spectrum of the stiffness matrix is narrow enough so the iterative system converges to a solution. In these methods it is possible to give each tetrahedron or cube a different conductivity. To obtain a fast convergence or a better condition number of the stiffness matrix, preconditioning should be used. Preconditioning transforms the system of equations $Ax = b$ into a preconditioned system $M^{-1}Ax = M^{-1}b$, which has the same solution as the original system. M is a preconditioning matrix or a preconditioner and its goal is to reduce the condition number (ratio of the largest eigenvalue to the smallest eigenvalue) of the stiffness matrix toward the optimal value 1. Basic preconditioning can be used in the form of Jacobi, Gauss-Seidel, Successive Over-Relaxation (SOR) and Symmetric Successive Over-Relaxation (SSOR). These are easily implemented as shown in Saad [128] or Datta [37]. More advanced methods use incomplete LU factorization and polynomial preconditioning [128, 104].

For the FDM in contrast with the BEM and FEM, the computational points lie fixed in the cube centers for the isotropic approach and at the cube corners for the anisotropic approach. In the FEM and BEM, the computational points, the vertices of the tetrahedrons and triangles, respectively, can be chosen more freely. Therefore, the FEM can better represent the irregular interfaces between the different compartments than the FDM, for the same amount of nodes. Moreover, in Pruis et al. [117] it was shown that FEM needed less computational points than FDM to obtain the same accuracy. However, the segmented medical images used to obtain the realistic volume conductor model are constructed out of cubic voxels. It is straightforward to generate a structured grid used in FDM from these segmented images. In the FEM and the BEM, additional tessellation algorithms [138] need to be used to obtain the tetrahedron elements and the surface triangles, respectively. However, recent

approaches in FEM with cubic elements have shown that shifting the nodes of the cubic elements to better represent the boundaries of the scalp and skull, yields a smaller error due to discretization [157].

Finally, it is known that the conductivities of some tissues in the human head are anisotropic such as the skull and the white matter tissue. Anisotropy can be introduced in the FEM [110] and in the FDM [129], but not in the BEM. Because of its simplicity and the ability to incorporate anisotropic conductivities, the FDM is used in this dissertation and, from now on, the focus will be on this method.

2.4.2.8 Solving the linear system of equations using Successive Over-relaxation

Properties of the system matrix If the linear system te be solved is rewritten from equations (2.48) and (2.55) in algebraic form as $\mathbf{A\Phi} = \mathbf{I}$, the system matrix $\mathbf{A} = \{a_{ij}\}$ has the following properties

Lemma 2.4.1. $\mathbf{A}$ *is a symmetric matrix.*

Proof. From the coefficients in the linear equations one can see that the coefficient connecting a computational point V_l to a neighbouring point V_k is identical to the coefficient connecting V_k to V_l, thus $\mathbf{A}$ is symmetric. □

Lemma 2.4.2. *The linear system of equations* $\mathbf{A}x = b$ *has infinite number solutions differing only in an additive constant, if* $\sum_{i=1}^{n} b_i = 0$.

Proof. For FDM in isotropic or anisotropic media, it can be shown from equation (2.48) or (2.55) that the sum of all entries in a row/column of $\mathbf{A}$ equals zero. Therefore, the vector $\mathbf{e} = [1, \ldots, 1]^T$ is an eigenvector with associated eigenvalue 0. The matrix ($\mathbf{A}$) of the FDM in both isotropic and anisotropic media has rank $n - 1$, with n the number of unknowns, and the eigenspace of the eigenvalue 0 is of dimension one. Note that for a singular problem to have a solution at all, the right-hand side $\mathbf{I}$ must be consistent, i.e. $\mathbf{I} \in \text{Range}(\mathbf{A})$, Range($\mathbf{A}$) being the range of A and defined as the space spanned by the independent eigenvectors of $\mathbf{A}$. The kernel of A, Kernel($\mathbf{A}$), is the set of vectors $\mathbf{a}$ that if multiplied by $\mathbf{A}$ returns zero. In this case the problem $\mathbf{A\Phi} = \mathbf{I}$ possesses an infinite set of solutions. An iterative method that converges from each initial guess toward an element of this solution set is said to be semi-convergent ([128]). In our case, $\mathbf{A}$ is symmetric, thus Range($\mathbf{A}$) = Kernel($\mathbf{A}$)$^{\perp}$ where $^{\perp}$ stands for the orthogonal complement. Since Kernel($\mathbf{A}$) is spanned by the vector $\mathbf{e} = (1, \ldots, 1)^T$ containing only ones as entries, a vector $\mathbf{v}$ lies in Range($\mathbf{A}$) if and only if

$$\mathbf{e}^T\mathbf{v} = \sum_{k=1}^{n} v_k = 0 \ . \tag{2.59}$$

□

From equations (2.48) and (2.55) it is easy to see that the right-hand side of our problem satisfies the above condition. The summation of the elements of the vector **I** in equation 2.58 results to zero because of the monopoles of the current source and sink. The vector, **I**, represent a dipole or a multipole. According to the definition given in equation 2.58 the sum of the elements are zero. Thus the problem $\mathbf{A\Phi} = \mathbf{I}$ possesses infinitely many solutions differing only in an additive constant.

Successive Over-relaxation (SOR) The SOR method is a representative of classical stationary methods. It is known to be a non-optimal choice as far as convergence is concerned, but has a very simple structure.

A linear system of equations $\mathbf{A\Phi} = \mathbf{I}$,

$$a_{i1}\varphi_1 + \cdots + a_{ii}\varphi_i + \cdots + a_{in}\varphi_n = I_i, \quad i = 1, \ldots, N,$$

can be rewritten as

$$\varphi_i = \frac{1}{a_{ii}} \left(I_i - \sum_{j=1, j\neq i}^{n} a_{ij}\varphi_j \right). \quad i = 1, \ldots, N,$$

Let $\varphi^{(k)}$ be an approximation to the solution after k iterations. The SOR method updates the unknowns in the following fashion. To compute $\varphi_i^{(k+1)}$ first an intermediate value

$$\bar{\varphi}_i^{(k+1)} = \frac{1}{a_{ii}} \left(I_i - \sum_{j=1}^{i-1} a_{ij}\varphi_j^{(k+1)} - \sum_{j=i+1}^{n} a_{ij}\varphi_j^{(k)} \right) \tag{2.60}$$

is determined. Here new values of $\varphi^{(k+1)}$ are used as soon as they are available. The new approximation then becomes

$$\varphi_i^{(k+1)} = \omega\bar{\varphi}_i^{(k+1)} + (1-\omega)\varphi_i^{(k)} = \varphi_i^{(k)} + \omega\left(\bar{\varphi}_i^{(k+1)} - \varphi_i^{(k)}\right) \quad . \tag{2.61}$$

The over-relaxation parameter ω is a weighting parameter used to put more weight onto the correction in order to improve convergence. According to the Young theorem, the optimal value for ω can be computed and can be shown to be equal to:

$$\omega_{opt} = \frac{2}{1 + \sqrt{1 - \rho\left(\mathbf{B}\right)^2}}, \tag{2.62}$$

where $\rho(\mathbf{B})$ is the spectral radius or the maximum of the absolute eigenvalues of the Jacobi iteration matrix. During the SOR procedure, the ω can be altered using this formula to obtain a faster convergence [128].

After j iterations, the node potentials, φ_i^j with $i = 1, \ldots, N$ (N is the number of computational points in the cubic grid) will be equal to $\mathbf{\Phi}^j = \left[\varphi_1^j, \ldots, \varphi_n^j\right]$. The iteration is terminated when the residual ($r_j = \left\|\mathbf{A}\mathbf{\Phi}^j - \mathbf{I}\right\|$) stops decreasing. An optimal extrapolation factor ω, which yields a minimum of iterations to satisfy the termination criterion, is dependent on the grid size. From tests, we have found that the extrapolation factor used in SOR with values $\omega = 1.93$, $\omega = 1.95$ and $\omega = 1.97$ for a grid size of 3, 2 and 1 mm, respectively, yields in general the smallest number of iterations. An implementation has been made in Matlab. If the computation grid of 195 by 195 by 195 elements (total number of 7414857 elements) are used, the calculation time for a grid size of 3, 2 and 1 mm takes typically 15 minutes, 2 hours and 6 hours respectively(Pentium 4, 2.6 GHz, 2 GBytes RAM). An implementation in C was also made, there the calculation times are 30 seconds, 2 minutes and 20 minutes.

2.4.3 The inverse problem

In this section we explain how the source parameters can be estimated using the electrode potentials measured at the scalp electrodes. This is known as the inverse problem and is basically an iterative procedure where the source parameters are adjusted until a cost function (indicating the difference between the measured electrode potentials and those caused by the estimated source) is minimal.

In von Helmholtz [148] it was shown that the potential distribution at the scalp can be a result of an infinite number of different source configurations. Therefore, the inverse problem has an infinite number of solutions. To impose unicity of the inverse problem, source models can be used. In this work we focus on dipole source models. Dipole sources are the building elements for more complex source models. Furthermore, the investigation of those simple models provides us with more insight on the effect of head model parameters. First, we will focus on the dipole estimation by means of minimization of a cost function in the least squares sense. Second, we will explain a dipole source estimation technique by means of signal subspace scanning.

In this section, $\mathbf{V} \in \mathbb{R}^{m \times n}$ denotes the electrode potentials measured or calculated (indicated by the subscript) at the m electrode positions over a period of t samples. Relating the notation in previous section, the electrode potentials calculated by a numerical method can be expressed as $\mathbf{V} = \{\varphi_k | k \text{ is an index associated with an electrode position}\}$.

2.4.3.1 Dipole source localization at one time instance ($n = 1$)

The parameters to be estimated in a dipole source localization problem are the three location parameter $\mathbf{r} = (x, y, z)^T \in \mathbb{R}^{3\times 1}$ and three component parameters $\mathbf{d} = (d_x, d_y, d_z)^T \in \mathbb{R}^{3\times 1}$, where ^{T} denotes the transpose operator. The potential values at l electrodes at the scalp caused by a dipole at location $\mathbf{r}$ and with components $\mathbf{d}$ can be calculated solving the forward problem and are represented by $\mathbf{V}_{model}$.

From equation 2.24 we could see that the potential values can be decomposed into 3 sets of potential values caused by dipoles at the same location $\mathbf{r}$ but with unitary dipole components oriented along the X-, Y- and Z-axis. Let $\mathbf{L} = (V_{model}(\mathbf{r}, \mathbf{e}_x)), V_{model}(\mathbf{r}, \mathbf{e}_y)), V_{model}(\mathbf{r}, \mathbf{e}_z))) \in \mathbb{R}^{m\times 3}$ denote the lead field matrix. Due to the linearity of the Maxwell equations, the potential values can be written as a linear combination:

$$\mathbf{V_{model}}(\mathbf{r}, \mathbf{d}) = \mathbf{L}(\mathbf{r}) \cdot \mathbf{d} \tag{2.63}$$

where $\mathbf{d}$ are the dipole components and $\mathbf{L}$ is the lead field matrix, which is dependent on the head model parameters, the electrode positions and the location of the dipole.

Given a set of electrode potentials $\mathbf{V}_{in} \in \mathbb{R}^{m\times 1}$, the inverse problem is solved by minimizing the relative residual energy (RRE):

$$RRE = \frac{\|\mathbf{V}_{in} - \mathbf{V}_{model}\|}{\|\mathbf{V}_{in}\|}, = \frac{\|\mathbf{V}_{in} - \mathbf{L}(\mathbf{r})\mathbf{d}\|}{\|\mathbf{V}_{in}\|}, \tag{2.64}$$

where $\|\cdot\|$ is the L_2-norm. During the optimization process the dipole parameters $\mathbf{r}$ and $\mathbf{d}$ are found so that the relative residual energy is at its global minimum. The relative residual energy is the amount of energy that cannot be explained by the dipole model.

In equation 2.64 six parameters have to be optimized. The number of parameters can be reduced by deriving the optimal dipole components $\mathbf{d}_{opt}$:

$$\mathbf{d}_{opt} = \mathbf{L}^{+}(\mathbf{r}) \cdot \mathbf{V}_{in} \tag{2.65}$$

where $\mathbf{L}^{+}(\mathbf{r})$ is the Moore-Penrose pseudo inverse of the lead field matrix. Substituting $\mathbf{d}_{opt}$ in equation 2.64 results in:

$$\begin{aligned} RRE &= \frac{\|\mathbf{V}_{in} - \mathbf{L}(\mathbf{r})\mathbf{d}_{opt}\|}{\|\mathbf{V}_{in}\|} \\ &= \frac{\|\mathbf{V}_{in} - \mathbf{L}(\mathbf{r})\mathbf{L}^{+}(\mathbf{r}) \cdot \mathbf{V}_{in}\|}{\|\mathbf{V}_{in}\|} \\ &= \frac{\|\left(\mathbf{I} - \mathbf{L}(\mathbf{r})\mathbf{L}^{+}(\mathbf{r})\right)\mathbf{V}_{in}\|}{\|\mathbf{V}_{in}\|}, \end{aligned} \tag{2.66}$$

where $\mathbf{I} \in \mathbb{R}^{m \times m}$ is the unity matrix and m is the number of electrodes. In this way, the location of the dipole $\mathbf{r}$ is the only remaining parameter to be optimized. The dipole orientation can be determined by substituting the estimated dipole location in equation 2.65.

2.4.3.2 Dipole estimation at multiple time instances ($n > 1$)

When estimating the sources over a period of time, stationary sources are assumed during that period of time. Therefore, the electrode potentials over a period of time $[t_0, t_1[$ can be written:

$$\mathbf{V}(t) = \mathbf{L}(\mathbf{r})\,\mathbf{e}(\phi, \theta)\,d(t) \tag{2.67}$$

where t is the time in the interval $[t_0, t_1[$, $\mathbf{e}(\phi, \theta)$ is the unitary dipole orientation and $d(t)$ is the time-varying magnitude of the dipole. At a specific sampling frequency the time dependent dipole intensities can be written in vector form as $\mathbf{t}_d \in \mathbb{R}^{1 \times n}$ Note that the time dependence of the electrode potentials translates to a time dependence of the dipole components, as stationary sources are assumed. In that case the RRE can be written as:

$$RRE = \frac{\|V_{in} - \mathbf{L}(\mathbf{r})\,\mathbf{e}(\phi, \theta)\mathbf{t}_d\|}{\|V_{in}\|} \tag{2.68}$$

$$= \frac{\left\| \left(\mathbf{I} - (\mathbf{L}(\mathbf{r})\mathbf{e}(\phi, \theta))\,(\mathbf{L}(\mathbf{r})\mathbf{e}(\phi, \theta))^{+} \right) \mathbf{V}_{in} \right\|}{\|\mathbf{V}_{in}\|} \tag{2.69}$$

Dipole estimation using the first component of the SVD The set of electrode potentials can decomposed using the singular value decomposition resulting:

$$\mathbf{V} = \mathbf{U}\mathbf{S}\mathbf{V}^T, \tag{2.70}$$

where $\mathbf{U}$ is the set of topographies, $\mathbf{S}$ are the singular values and $\mathbf{V}$ are the source signals. The matrix $\mathbf{S}$ is a diagonal matrix with the singlular values ordered from large to small. A large singular value indicates the dominance of the source in the EEG in terms of energy. Therefore, one can estimate the dominant source assuming that the other sources are due to noise contributions. By substituting $\mathbf{V}_{in}$ in equation 2.66 by the first column of $\mathbf{U}$, the relative residual energy can then be written as:

$$RRE = \frac{\|\mathbf{U}(:, 1) - \mathbf{L}(\mathbf{r}) \cdot \mathbf{d}\|}{\|\mathbf{U}(:, 1)\|} \tag{2.71}$$

where $\mathbf{U}(:,1)$ is the first column of the U matrix, which corresponds with the larges singular value. This technique is only valid if one and only one singular value is large compared with the other singular values.

2.4.3.3 Distributed sources

In this dissertation a single dipole is used to represent the focal electric activity. In the neurophysiological sense, the representation is reasonable. Alternatively, distributed sources can be used to represent sources that are not confined to a focal area. In this case more widespread activity is targeted. Distributed sources usually exist on multiple dipoles uniformly distributed in the brain compartment. Due to the linearity of the Poisson's equation, the potential can be written as a superposition of the potential caused by each individual dipole source. However, this leads to an underdetermined system, which has to be solved in the minimum norm sense and regularization techniques are needed [112, 134, 99].

2.5 Errors in EEG source localization

Dipole estimation errors (i.e. wrong estimate of neural sources in the brain for a given set of measured scalp potentials) can be due to two major groups of errors: data related errors (i.e. these are errors due to additive noise in the EEG signals) and model related errors (i.e. these are errors due to geometrical errors and errors in material properties such as conductivity).

2.5.1 Data related errors

The EEG is contaminated with measurement noise. During the acquisition of an EEG in a clinical environment different sources of noise contaminate the EEG: environment noise, instrumentation noise and biological noise. The major contributor to environment noise is the 50 or 60 Hz power-line activity, which is illustrated in figure 2.21(a). This activity can be suppressed by filtering. However, state-of-the-art acquisition systems use active shielding techniques to cancel the environment noise. Recently, EEG can be simultaneously measured during an MR scan. During the acquisition of the MR image the EEG is distorted due gradient switching of the MR scanner, which is illustrated in figure 2.21(d). These errors are called gradient switching artifacts [52]. Moreover, small movements of the electrodes due to blood volume pulse (BallistoCardioGraphic Artifacts or BCGa), respiration or movement of the patient inside the static field will also distort the EEG. An illustration of the BCGa is shown in figure 2.21(c). Advanced signal processing techniques can filter out these artifacts of the MR-scanner [52].

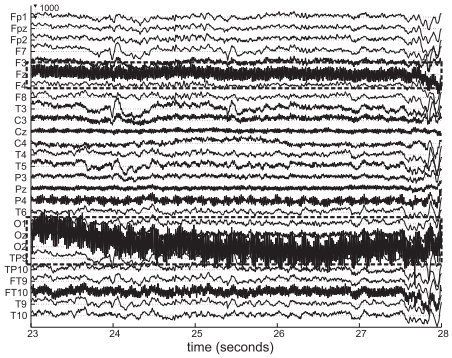

(a) Power line noise (50 Hz)

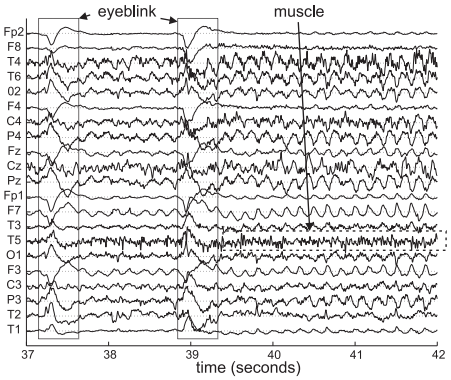

(b) Eye blink and muscle artifact

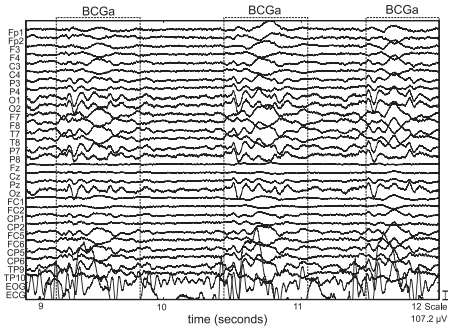

(c) BCGa in an MR scanner, which is synchronous with the heartbeat (see ECG channels)

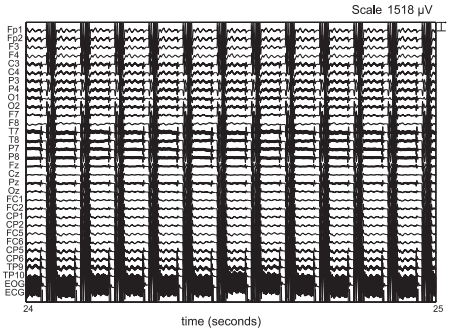

(d) Gradient artifact of EEG measured in an MR scanner

Figure 2.21: Illustrations of several noise contributors in the EEG. The noise contributors can cause dipole location errors in the EEG source analysis.

Typical example of instrumentation noise occurs in the quantization process during the conversion of an analog to a digital signal. Modern equipment uses 16 or 22 bit analog-to-digital converters, which generates noise smaller than $1.5\mu V$ or $71.5nV$. A typical EEG signal has a RMS value of approximately $50\mu V$ and higher.

Biological noise consists of signals produced by brain activity or non-brain activity that does not correspond to the focal activity we are looking for. One example is alpha activity (i.e. 8-12 Hz activity in the parietal channels). Other biological noise contributors are the electrocardiogram, eye movement or blink artifacts and electromyogram artifacts. The eyeblink artefact and muscle artefact are illustrated in figure 2.21(b).

2.5.2 Model related errors

To make the EEG source estimation feasible, some assumptions have to be made. These simplifications allow us to solve the forward problem or inverse problem in a reasonable amount of time and with respect to the available data at hand. In this case geometrical and conductivity parameters deviate from their real values.

However, these simplification contribute to the dipole position or orientation error. Here we discuss three types of modeling errors: source modeling errors, head modeling errors and conductivity errors.

2.5.2.1 Source modeling errors

As explained in section 2.3.1 dipolar sources are an adequate model to represent brain activity. However, this is only valid if the activity itself is limited to a focal region and stays focal over a period of time. If the actual source covers a large area over the surface of the brain, it will produce a widespread EEG pattern on the scalp that is similar to a single dipole deep inside the brain. Therefore, an inverse solution for a single dipolar source can produce a dipole that is several centimeters away from the actual distribution [35].

The solution to that problem is to use more complex source models. Two known approaches exist to extend the single dipole model. A first approach consists of placing sources in a grid in the brain compartment. Usually the grid as a resolution of 0.5 to 10 mm. Moreover, it was shown in section 2.16 the electrode potentials can be written as a superposition of the electrode potentials caused by 3 orthogonal dipoles at the same location. Thus, in each point in the cubic source grid, 3 orthogonal dipoles are placed. This approach results in more than 1000 dipoles. The inverse problem in this case is linear, since the only unknowns are the amplitudes of the dipoles in each point of the cubic grid. Given that the number of sensors in a clinical practice is of the order of 30 and in a experimental setup of the order of 100, the problem is highly underdetermined and regularization methods are required [8].

A second approach consists of limiting the number of parameters of the multidipolar sources to be less than the number of electrodes. In this case a few equivalent dipole sources of unknown location and moment are to be estimated with a nonlinear method. A fundamental problem with this approach is the number of sources, which has to be decided a priori. Furthermore, as the number of sources increases, the non-convexity of the cost function results in increased chances of trapping in undesirable local minima. These problems can be solved by scanning a region of interest that ranges from a single location to the whole brain volume for possible sources. An estimator for the contribution of each possible source location to the data can be derived using spatial filtering techniques (e.g. beamformers as in Sekihara et al. [134]) or signal classification indices (e.g. RAP-MUSIC as in Mosher and Leahy [103]).

2.5.2.2 Errors due to inaccurate geometry modeling

When a head model is used, which does not accurately represent the real head geometry, errors are induced. In Vanrumste et al. [146] and Huiskamp et al. [80] the importance was shown of using realistic head models instead of the more simplified spherical head models. Indeed, the real human head is not a sphere, but more complex. Not only the boundary of the head model should resemble the human head, but also the internal structure of the brain tissues. Cuffin [34] and Eshel et al. [43] showed that variation of skull and scalp thicknesses results in dipole estimation errors. In Vanrumste et al. [144] it was shown that a hole in the skull (e.g. occurring after brain surgery) yielded estimation errors near the hole. Moreover, it was also shown that omitting the ventricular system also resulted in localization errors in the regions near the omitted ventricular system. In Ramon et al. [121] it was shown that the scalp potentials are highly sensitive to the complexity of the head model. Moreover, the CSF plays an important role in the EEG source analysis both the layer at the boundary of the brain [120] as well as the ventricular system [143].

2.5.2.3 Errors due to inaccurate position of electrodes

The electrode positions are placed according to the standard 10-20 system. However, it can happen that these electrodes deviate from the standard position due to interpatient variability of head geometry or due to inaccurate placement of the electrodes on the scalp. Therefore, dipole estimation errors can occur. In Van Hoey et al. [140] it was shown that a one to one relationship existed between the dipole location error and the average displacement of the electrode positions. In other words, if the electrode positions used in the head model deviated on average 1 cm from the actual electrode positions, then the dipole location was shifted on average 1 cm from the real electrode position. This can be circumvented using fiducial markers on the electrodes that have a strong signal in the MR image acquisition, as electrodes themselves do not generate a signal on an MRI scan. Using image processing techniques the coordinates

of each marker can then be deduced and used as such in the head model [136]. Pohlmeier et al. [115] showed that the dipole location error diminishes when more electrodes are used, however they also suggested that there is an optimal number of electrodes as more electrodes will create an electrode-shunt effect which will decrease the accuracy.

2.5.2.4 Errors due to inaccurate modeling of conductivities of brain tissues

The skull conductivity has been subject to debate among researchers. In vivo measurements give very different from in vitro measurements. On top of that, the measurements are very patient specific. In Awada et al. [7], it was stated that the skull conductivity has a large influence on the forward problem. Pohlmeier et al. [115] showed by simulation studies that small inhomogeneities in the skull results in a dipole location error of up to 1 cm when these are not incorporated in the EEG source analysis.

It was believed that the conductivity ratio between skull and soft tissue (scalp and brain) was on average 80 [48]. Oostendorp et al. used a technique with realistic head models by which they passed a small current by means of 2 electrodes placed on the scalp. A potential distribution is then generated on the scalp. Because the potential values and the current source and sink are known, only the conductivities are unknown in the head model. Hence, equation 2.15 (or in general form equation (2.21)) can be solved for isotropic σ. Using this technique they could estimate the skull-to-soft tissue conductivity ratio to be 15 instead of 80 [109]. At the same time, Ferree et al. [44] did a similar study using spherical head models. Here, skull-to-soft tissue conductivity was calculated as 25. It was shown in Vanrumste et al. [144] that using a ratio of 80 instead of 16, could yield EEG source localization errors of an average of 3 cm up to 5 cm.

One can repeat the previous experiment for a large number of different electrode pairs and an image of the conductivity can be obtained. This technique is called electric impedance tomography (EIT). In short, EIT solves an inverse problem, by estimating the conductivities instead of the source parameters. Using this technique, the skull-to-soft tissue conductivity ratio was estimated to be around 20-25 [50, 31]. However in Gonçalves et al. [50], it was shown that the skull-to-soft tissue conductivity ratio could differ from patient to patient with a factor of up to 2.4. In Chen et al. [30] it was shown that this variability in the skull-to-soft tissue conductivity variability resulted in errors of 10 to 30 mm. In Gutiérrez et al. [55], maximum likelihood and maximum a posteriori techniques are used to simultaneously estimate the different conductivities. There the skull-to-soft tissue ratio was estimated to be 26.

Another study came to similar results using a different technique. In Lai et al. [90], the authors used intracranial and scalp electrodes to get an estimation of the skull-to-soft tissue ratio conductivity. From the scalp measures they

Table 2.1: The reference values of the absolute and relative conductivity of the compartments incorporated in the human head.

compartments	Geddes & Baker (1967)	Oostendorp (2000)	Hoekema (2001)	Gonçalves (2003)	Guttierrez (2004)	Lai (2005)
scalp	0.43	0.22	0.33	0.33	0.749	0.33
skull	0.006 - 0.015	0.015	0.032-0.080	0.0081	0.012	0.0132
cerebro-spinal fluid	-	-	-	-	1.79	-
brain	0.12 - 0.48	0.22	0.33	0.33	0.313	0.33
$\frac{\sigma_{scalp}}{\sigma_{skull}}$	80	15	10-40	20-50	26	25

estimated the cortical activity by means of a cortical imaging technique. The conductivity ratio was adjusted so that the intracranial measurements were consistent with the result of the imaging from the scalp technique. This resulted in a ratio of 25 with a standard deviation of 7. One has to note however that the study was performed on pediatric patients aged between 8 and 12. Their skull tissue normally contains a larger amount of ions and water and so may have a higher conductivity than the adults calcified cranial bones [90]. In a more experimental setting, the authors of Hoekema et al. [77] performed conductivity measures on the skull itself in patients undergoing epilepsy surgery. Here the authors estimated the skull conductivity to be between 0.032 and 0.080 S/m, which corresponds to a soft-tissue to skull conductivity of 10 to 40. An overview of the conductivities of brain tissues with a focus on the skull-to-soft tissue ratio can be found in table 2.1.

In the gray matter, scalp and cerebro-spinal fluid (CSF) the conductivity is equal in all directions. In this case, the conductivity of the tissues is isotropic. Thus the position dependent conductivity tensor becomes a position dependent scalar σ. The conductivity of CSF is quite accurately known to be 1.79 S/m [20].

2.5.3 Anisotropic conductivities

This dissertation is focused around EEG source localization in anisotropically conducting media. Therefore, the topic of anisotropic conductivities and the related source localization errors are dealt with in a separate section.

The skull forms a protective layer between the brain and the outside. Furthermore, it contains the structural integrity of the brain. Therefore, the skull is made of a hard structure. The hard structure acts as a low conductive medium and has a layered structure (see figure 2.22), which consists of 3 layers: a spongiform layer between two hard layers. Water, and also ionized particles, can move easily through the spongiform layer, but not through the hard layers [156]. This is illustrated in figure 2.23. At the skull, for example, the

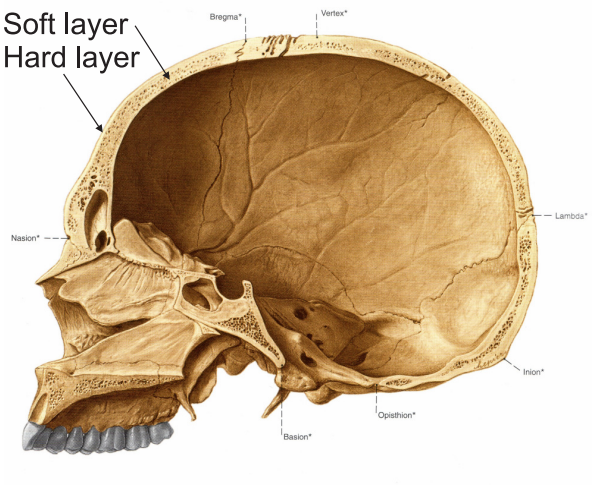

Figure 2.22: A sagittal view of the skull with the soft and hard layers of the skull. Some characteristic points at the skull are indicated. The inion and nasion are used in the clinical practice to place the electrodes on the scalp. Adopted from Putz and Pabst [119]

conductivity tangential to the surface is 10 times the conductivity perpendicular to the surface [126]. Wolters et al. stated that skull anisotropy has a smearing effect on the forward potential computation. Also Chauveau et al. [28] investigated the anisotropy of the skull by means of a resistor mesh model.

White matter consists of different nerve bundles (groups of axons) connecting cortical gray matter (mainly dendrites and cell bodies). Some important structures in the white matter consist of nerve bundles which are aligned parallel to each other (see figure 2.24a. The corpus callosum (see figure 2.24b) connects the two hemispheres of the brain. This structure consists of many parallel nerve bundles and is thus highly anisotropic. The *capsula interna* is another example of such a structure, which connects the nerve fibers coming from the center of

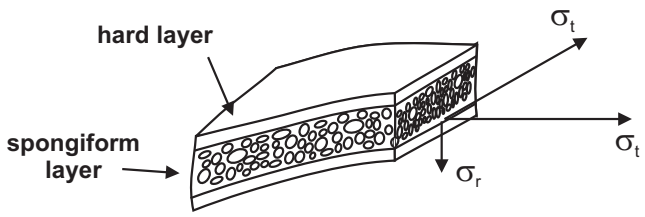

Figure 2.23: The anisotropic properties of the conductivity of skull. The skull consists of 3 layers: a spongiform layer between two hard layers. The conductivity tangentially to the skull surface is 10 times larger than the radial conductivity.

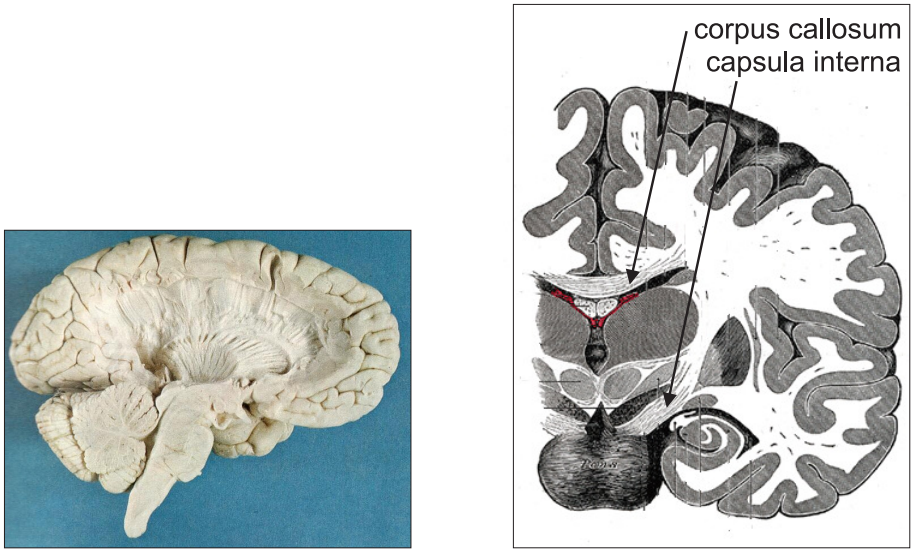

(a) (b)

Figure 2.24: (a) a cross-section of the brain, where white matter fibres are displayed. (b) a coronal slice of the brain with some important brain structures with parallel nerve fibres. Adopted from Gray [51].

the brain to regions in the cortical gray matter.

The nerve bundles consist of nerve fibers or axons (see figure 2.25). Water and ionized particles can move more easily along the nerve bundle than perpendicular to the nerve bundle. Therefore, the conductivity along the nerve bundle is measured to be 9 times higher than perpendicular to it [105, 48]. The nerve bundle direction can be estimated by a recent magnetic resonance technique: diffusion tensor magnetic resonance imaging (DT-MRI)[19]. This technique provides directional information on the diffusion of water. It is assumed that the conductivity is the highest in the direction in which the water diffuses most easily [139]. Authors [72, 60, 118] have shown that anisotropically conducting compartments should be incorporated in volume conductor models of the head whenever possible. We will elaborate further on this technique in chapter 4.

2.6 Summary and Contributions

In this chapter we discussed the EEG source analysis. First, we went into detail on the generating source of the EEG. The EEG that represents the activity originates from a superposition of synchronously active neurons. Moreover these neurons have to be alligned orthogonal to the cortex. With this in mind, the dipole source was proposed as a model for the EEG generator.

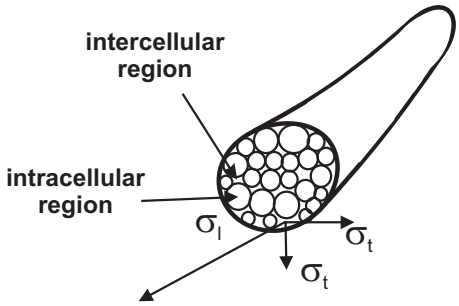

Figure 2.25: White matter consist of axons, grouped in bundles. The conductivity along the nerve bundle is 9 times larger than perpendicular to the nerve bundle.

Next, we discussed the EEG source estimation problem, which consists of a forward and inverse problem. Solving the forward problem yields the electrode potentials caused by a given dipole in a given head model. We discussed several techniques to solve the forward problem in a variety of head models. The inverse problem estimates the source parameters by iteratively solving the forward problem and comparing the results with a given set of electrode potentials.

Finally, a short overview of the influence of the different parameters in EEG source estimation was given. The literature search performed for this chapter resulted in a review paper [69] and two proceedings at an international conference [5, 30].

Chapter 3

Validation of FDM used to incorporate of anisotropic conductivities in EEG source estimation

Bashir : It's not our place to decide who lives and who dies. We're not gods.
Jack: Maybe not, but we are the next best thing!
—Star Trek Deep Space Nine (Episode 133), Statistical Probabilities

3.1 Introduction

In EEG source estimation, isotropic head models are often used. In reality however, the skull and brain tissues have anisotropic conductivities. The anisotropic conductivities can be incorporated in spherical or more realistic head models. Neglecting these anisotropic properties will generate errors. The aim of this chapter is twofold.

First, we will determine if the incorporation of anisotropy is relevant to improve the accuracy of the EEG source estimation. This is done using simulations in the spherical head model, which was explained in 2.4.2.3. A large error would justify the development and implementation of a numerical method that can incorporate anisotropy. We determined the dipole estimation errors when anisotropic conductivities are not taken into account. This was done doing simulation studies. We concluded that the errors due to not taking into account anisotropic conductivities of skull and white matter are not negligible and that anisotropic conductivities should be incorporated in the head model.

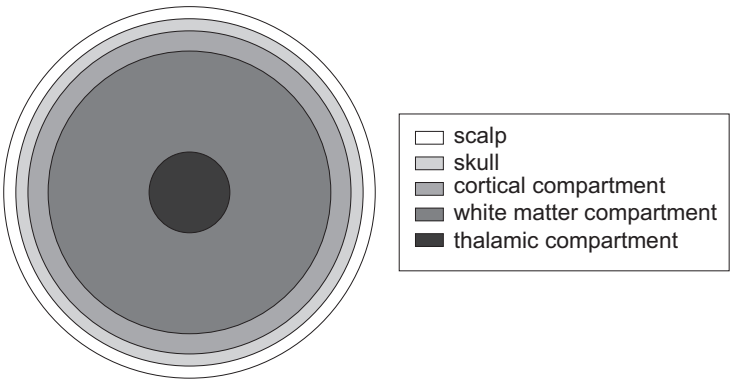

Figure 3.1: The 5 shell spherical head model. The different compartments are indicated by the different grayscale values. In the present study the skull and the white matter compartment can be set to isotropic or anisotropic conductivity. The other compartments are all set to isotropic conductivity.

Second, we will use the finite difference method (see section 2.4.2.6) that can incorporate anisotropic conductivities. The numerical method is applied in a discretized spherical head model and compared with the analytical solution by means of the differences in dipole estimation.

3.2 Dipole localization errors due to not incorporating anisotropic conductivities: simulation study in spherical head models

3.2.1 Rationale

Spherical head models enable us to use an analytical formula to solve the forward problem. Although the head models are very simplified, we use a spherical model since this enables us to perform fast studies to investigate the behavior of not incorporating or neglecting the anisotropic properties of the skull and/or brain tissues.

Before we can introduce a numerical technique to solve the forward problem in EEG source analysis, we have to assess the error due neglecting anisotropic head models. A simulation study in a spherical head model is suited for this, as an analytical formula exists to solve the forward problem in anisotropic media.

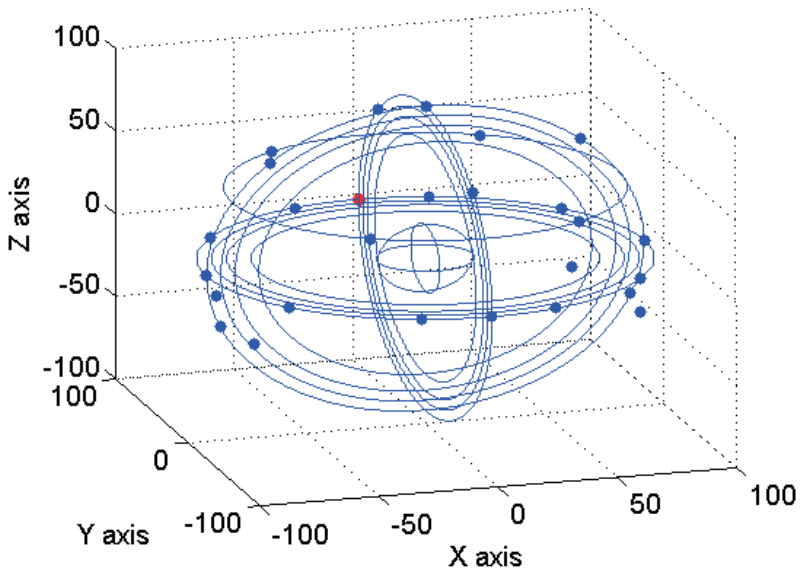

Figure 3.2: the 5 shell spherical head model and the placement of electrodes according to the international 10-20 system + 6 extra electrodes.

3.2.2 Simulation Setup

Here we use a 5 shell spherical head model (see figure 3.1): scalp shell (radius 92 mm), skull shell (radius 86 mm), cortical shell (radius 80 mm), white matter shell (radius 70 mm) and thalamic shell (radius 20 mm). The scalp shell, cortical shell and thalamic shell have an isotropic conductivity of 0.33 S/m. The skull shell and white matter shell can be made isotropic or anisotropic. The isotropic conductivity is 0.020 S/m and 0.33 S/m, respectively.

The values for the radial and tangential direction can be calculated from the isotropic conductivity by imposing the volume constraint [153]. The volume constraint is explained in appendix B. The anisotropic conductivity of the skull shell is 0.0043 S/m in the radial direction and 0.043 S/m in the tangential direction to the skull surface. The white matter has been modeled as follows: the nerve fibers start from the thalamic shell and go in the radial direction to the cortical sphere. Here the conductivity along the nerve fibers was set to be 9 times larger than the conductivity perpendicular to the nerve fiber. In this way the white matter sphere also has a radial and tangential conductivity of 1.42 S/m and 0.15 S/m respectively. The electrodes were placed according to the international 10-20 system, with 6 extra electrodes located at the temporal region, resulting in a total of 27 electrodes. The placement of the electrodes is also shown in figure 3.2.

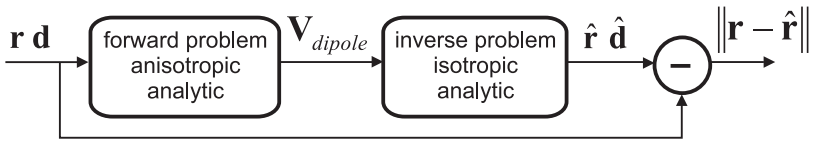

Figure 3.3: A flow chart of the simulation study where the dipole localization error due to the differences between the head models used in the forward problem and in the inverse problem is investigated.

First we investigated dipole localization errors due to assuming an isotropic head model instead of a head model with anisotropic conducting compartments. The setup of this simulation study is shown in figure 3.3, a setup which can easily be extended to other problems. The potentials at the electrodes are calculated by using the analytical expression for a given dipole in the brain compartments in a 5 shell spherical head model with skull or white matter compartment being anisotropic. Next, for the set of potential values at the 27 electrodes, the dipole parameters were estimated for a 5 shell spherical head model but with the initial anisotropic conducting compartment set to isotropic. The dipole localization errors were then inspected.

3.2.3 Results

3.2.3.1 Skull Anisotropy

Figure 3.4 shows the dipole localization error as an arrow. The start of the arrow denotes the position of the original dipole and the tip points to the estimated dipole location. We can see that the estimated dipoles are shifted towards the center. The average dipole localization error for all test dipoles and the three orientations in the cortical shell is 20.16 mm with a maximum error of 27.23 mm. In the thalamic shell the average dipole localization error is 4.14 mm, with a maximum of 6.67 mm.

3.2.3.2 White matter anisotropy

Figure 3.5 shows the dipole localization error when white matter anisotropy is neglected. The dipoles are estimated away from the center. The dipole localization error in the cortical sphere is on average 4.23 mm with a maximum of 11.08 mm. In the thalamic sphere this error increases to an average of 17.05 mm; with a maximum of 26.34 mm.

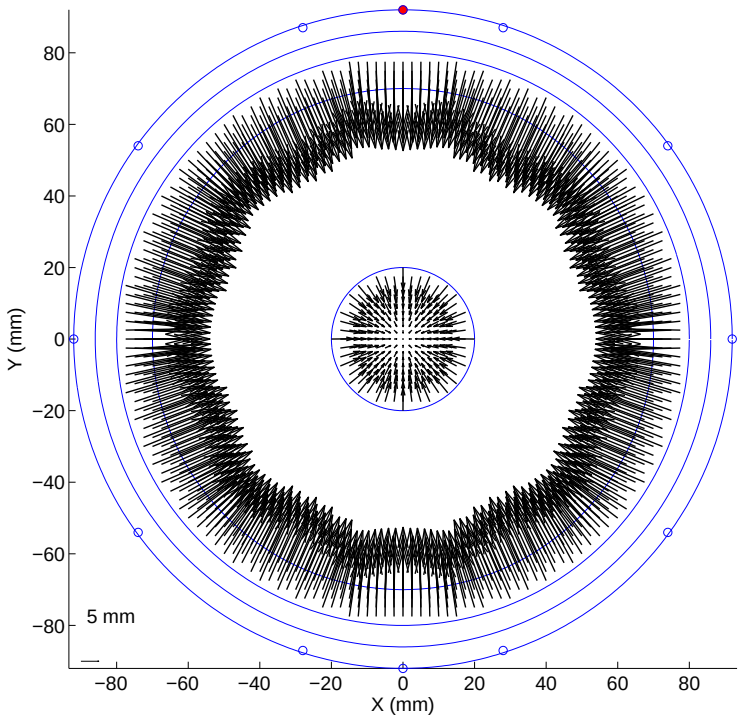

Figure 3.4: The dipole localization error when the conductivity of the skull compartment was assumed to be isotropic, while the original test dipole was set in a head model with an anisotropically conducting skull compartment. The other compartments were kept isotropic. The arrows represent the dipole localization error in an axial (XY) plane. The tail is the original position, the tip is the fit position. The original dipoles were oriented along the X axis. The horizontal line in the bottom left corner represents a distance of 5 mm.

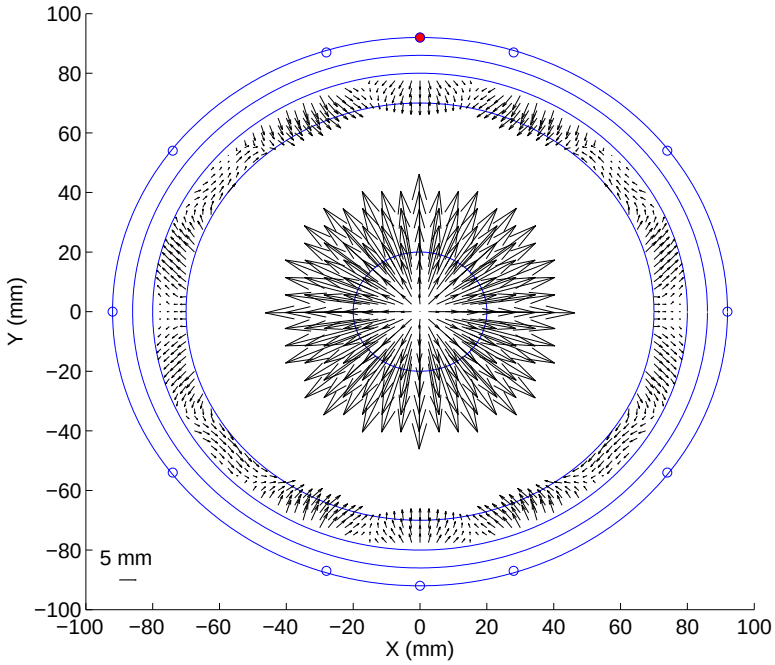

Figure 3.5: The dipole localization error when the conductivity of the white matter was assumed to be isotropic, while the original test dipoles were set in a head model with anisotropically conducting white matter compartment. The other compartments were kept isotropic. The arrows represent the dipole localization error in an axial (XY) plane. The tail is the original position, the tip is the fitted position. The original dipoles were oriented along the X axis. The horizontal line in the bottom left corner represents a distance of 5 mm.

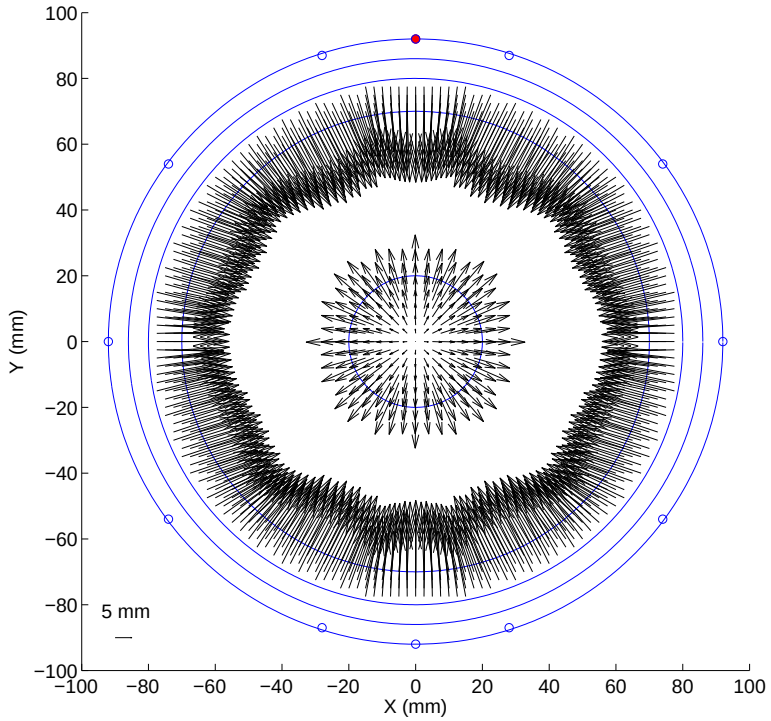

Figure 3.6: The dipole localization error when the conductivity of the skull compartment and white matter compartment were assumed to be isotropic, while the original test dipoles were set in a head model with an anisotropically conducting skull and white matter compartments. The arrows represent the dipole localization error in an axial (XY) plane. The tail is the original position, the tip is the fit position. The original dipoles were oriented along the X axis. The horizontal line in the bottom left corner represents a distance of 5 mm.

3.2.3.3 Skull and white matter anisotropy

In figure 3.6 we can see the dipole localization error when skull and white matter anisotropy are neglected. The dipoles, located in the thalamic shell, are estimated away from the center. The dipoles in the cortical shell are estimated toward the center of the head. In the cortical shell the dipole localization error is on average 22.54 mm and has a maximum of 32.33 mm. In the thalamic region the error is on average 7.62 mm and has a maximum of 13.82 mm.

3.2.4 Discussion and Conclusions

We investigated the influence of not incorporating an anisotropic compartment in the spherical head model and quantified the influence in terms of the dipole location error. From figure 3.7 we can appreciate that the errors due to using a more simplified head model (with isotropic conductivities) instead of a more realistic one (with anisotropic conductivities) for most of the test dipoles are larger than 15 mm. Errors may rise up to 30 mm, which is unacceptable for EEG source analysis. It is therefore necessary to incorporate anisotropic information for a more accurate localization of the dipole.

The skull remains a difficult obstacle to perform EEG dipole localization. Therefore, a correct modeling of the skull is needed. In this study we showed that a correct modeling of the anisotropic conductivities is also important, especially for the cortical focal activity (see figure 3.7). Although white matter fibers are not directed in the radial direction in a real human head, this study suggests that the anisotropic conductivity of white matter fibers should also be incorporated.

The localization was done in a spherical head model, which is also a simplification of the head model. More realistic head models can be constructed which accurately represent the actual geometry of the human head. However, these realistic head models require numerical techniques. The results from this part of this chapter will be used as a reference for the next part of this chapter, where a numerical technique based on finite differences that can incorporate anisotropic conductivities is compared to the analytical formula.

3.3 Validation of the finite difference method with anisotropic conductivities

3.3.1 Aim of the study

In the previous paragraph, because the geometry consisted of concentric spheres an analytical formula can be used, which calculates the electrode potentials in a fast way. However, in reality the human head is not spherical. It has a irregular shape and the inside is heterogeneous. Studies have shown the importance

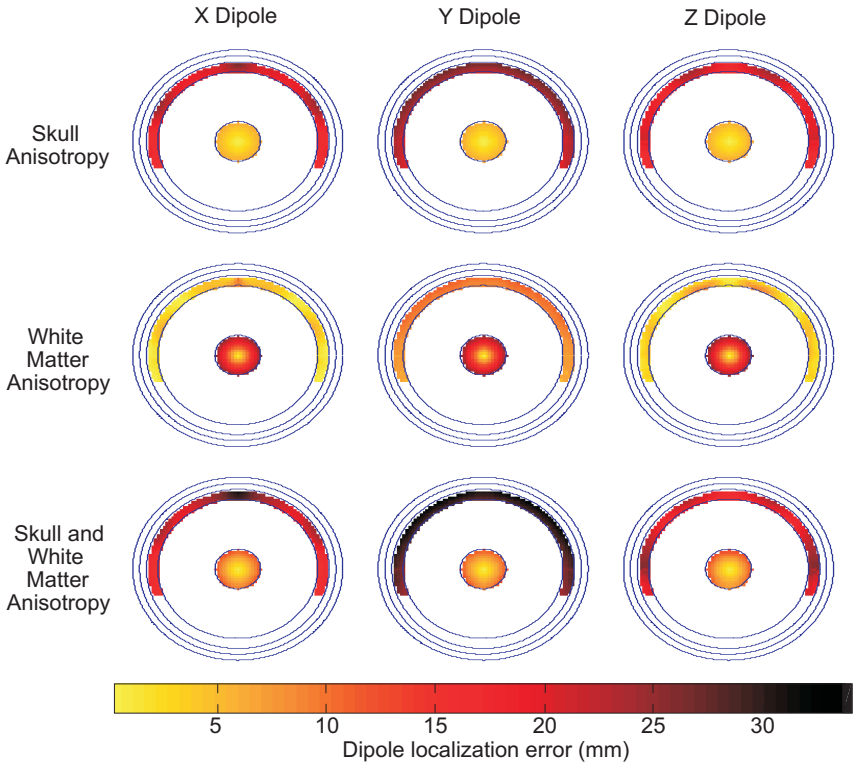

(a)

Figure 3.7: The dipole localization in coronal planes (XZ) of the 5 shell spherical head model. Coronal planes are arranged column wise according to dipole orientation and row-wise according to compartments for which anisotropy was neglected. The dipole localization error is shown as a color, according to the color bar below.

of correctly modeling the geometry of the human head [80, 146]. However, calculating the forward problem in a realistic head model requires numerical methods, which locally solves the forward problem in small elementary volumes or surfaces. In this study, we used the aFDM, introduced in 2.4.2.6.3, to compare it with the analytical formula. As an error measure we used the difference between the dipole location in a spherical head model calculated with the analytical formula and the dipole location in a spherical head model calculated with the aFDM.

3.3.2 Solving the forward problem using forward differences

Numerical methods use a computational grid or lattice to solve the forward problem. For FDM the head is tessellated in a cubic grid, where each cube has the same size. A conductivity tensor was assigned to each cubic element, depending to which compartment it belongs (air, scalp, skull, cortical gray matter, white matter and thalamic gray matter). The modelling of the air is done by putting the matrix reprentation of the conductivity tensor to a zero matrix. In this way, we create a natural boundary around the head model. In this study we used four kinds of compartments : scalp, skull, white matter and gray matter. The scalp and gray matter compartments are considered isotropic throughout this study. For isotropic tissues the conductivity tensor becomes a scalar. However, for anisotropic conducting tissues, the conductivity tensor can vary for different positions in the anisotropic compartment.

In the multi shell spherical head model the conductivity tensor in the skull and white matter compartment is a diagonal matrix. If we assume that the local coordinate system is oriented along the radial and tangential direction, then the conductivity tensor at an element j can be written as follows:

$$\mathbf{\Sigma}^j_{sph} = \begin{pmatrix} \sigma^j_r & 0 & 0 \\ 0 & \sigma^j_t & 0 \\ 0 & 0 & \sigma^j_t \end{pmatrix},$$

where σ^j_t and σ^j_r are the conductivities in the tangential and radial direction at element j, respectively. The matrix representation has to be transformed to a global cartesian coordinate system of the head, equal for all elements. Therefore a rotation matrix has to be applied. The matrix representation of the conductivity tensor at element j in the cartesian system of the head is then given by $\mathbf{\Sigma}^j_{head} = \mathbf{T_j}\mathbf{\Sigma}^j_{sph}\mathbf{T_j}^T$, where T_j is a rotation transfer matrix at element j from the local coordinate system to the global coordinate system [75].

The radial σ_r and tangential conductivities σ_t are calculated using the volume constraint, which is explained in appendix B. This states that the volume of the anisotropic conductivity ellipsoid is equal to the volume of the isotropic conductivity sphere. For the isotropic conductivities we use $\sigma^{brain}_{isotropic} = 0.33\ S/m$

for the brain compartment, $\sigma_{isotropic}^{skull} = \sigma_{isotropic}^{brain}/16 = 0.020\ S/m$ for the skull compartment and $\sigma_{isotropic}^{scalp} = 0.33\ S/m$ for the scalp [50, 44]. For the skull we use a radial conductivity of $\sigma_r^{skull} = 0.004309\ S/m$ and a tangential conductivity of $\sigma_t^{skull} = 10\sigma_r^{skull} = 0.04309\ S/m$. In the white matter compartment we modeled the white matter anisotropy as nerve fibers that originate at the edge of the inner gray matter compartment and go radial to the edge of the outer gray matter compartment. Here we use a radial conductivity of $\sigma_r^{brain} = 1.4278\ S/m$ and a tangential conductivity of $\sigma_t^{brain} = 0.15864\ S/m$.

A finite difference method which can handle these properties has been presented by Saleheen and Kwong [130] and introduced in 2.4.2.6.3. The method differs from the traditional finite difference method (see section 2.4.2.6.2, which puts the computational points at the center of the elements, in that it calculates the potential values at the nodes of the elements.

Basically, the method states that in a 3D cubic lattice, the potential value at point 0 can be written as a linear combination of potential values at 18 neighbors according to figure 2.19 and 2.55. Thus, Poisson's equation (2.21) can be approximated in a finite difference calculation scheme as follows:

$$\sum_{i=1}^{18} A_i \varphi_i - \left(\sum_{i=1}^{18} A_i \right) \varphi_0 = I\delta(\mathbf{r} - \mathbf{r}_k) - I\delta(\mathbf{r} - \mathbf{r}_l), \tag{3.1}$$

where φ_i is the discrete potential value at node i. A_i are the coefficients depending on the conductivity tensor of the elements and the internode distance. These coefficients are given in Saleheen and Kwong [130] and are shown in equations 2.57. The dipole source is characterized by the right hand side of the equation. The current injected or removed is denoted by I and the location of the current source and sink is denoted by $\mathbf{r}_k$ and $\mathbf{r}_l$, respectively. Equation 3.1 can be represented as a stencil, where the central node (node 0) can be placed at an arbitrary node of the head model at location $\mathbf{r}$.

For each computational point a linear equation can be written as in equation 3, and for all computational points we obtain a set of linear equations which can be written as follows: $\mathbf{A} \cdot \mathbf{\Phi} = \mathbf{I}$. The matrix $\mathbf{A} \in \mathbb{R}^{n \times n}$ is the stiffness matrix and it is dependent of the isotropic or anisotropic conductivities at the elements. $\mathbf{I} \in \mathbb{R}^{n \times 1}$ is the array who denotes the current source and sink. The current source and current sink at k and l is indicated by $\mathbf{I}(k) = I$ and $\mathbf{I}(l) = -I$, respectively. All remaining elements are zero. n is the number of computational points. Furthermore, the stiffness matrix A is sparse as for each row there are at most 18 off-diagonal non-zero elements . We wish to solve this system for $\mathbf{\Phi} \in \mathbb{R}^{n \times 1}$.

3.3.3 Successive Over-Relaxation

To solve this large sparse linear system, iterative methods need to be used. We have utilized successive OverRelaxation (SOR) [15]. The SOR is a method for solving a linear system of equations and is derived from an extrapolation to the Gauss-Seidel method. This extrapolation takes the form of a weighted average between the previous iterate, $\varphi_i^{(k-1)}$, and the computed Gauss-Seidel iterate successively for each component:

$$\varphi_i^{(k)} = \omega\bar{\varphi}_i^{(k)} + (1-\omega)\varphi_i^{(k-1)}, \tag{3.2}$$

where $\bar{\varphi}_i$ is the Gauss-Seidel iterate, and ω is the extrapolation factor. After j iterations, the node potentials, $\varphi_i^{(j)}, \forall 1 \leq i \leq n$, will be equal to $\mathbf{\Phi}^{(j)} = (\varphi_0^{(j)}, \varphi_1^{(j)}, \ldots, \varphi_N^{(j)})$. The iteration is terminated when the residual ($r^{(j)} = \left\|\mathbf{A}\mathbf{\Phi}^{(j)} - \mathbf{I}\right\|$) stops decreasing. An optimal extrapolation factor ω_{opt}, which yields a minimum of iterations to satisfy the termination criterium, is dependent on the grid size.

3.3.4 Reciprocity

Since the solution is non-linear with repect to the dipole location, the forward calculation has to be done during the minimization of the cost function of the invers problem. During a dipole source reconstruction, it would be too time-consuming to solve the forward problem for each dipole position and orientation utilizing successive over-relaxation. Therefore, the reciprocity theorem is used to reduce the number of forward calculations. Reciprocity was introduced in EEG source analysis by Rush and Driscoll [127]. Reciprocity describes the relation of mutual dependence of the input and the output of the linear system: the voltage between two electrodes at the surface due to a current source and current sink infinitesimally close to each other (dipole configuration), equals the voltage between these two points due to a unit current at the initial electrodes [95]. The use of reciprocity in solving the forward problem using finite differences was validated by Vanrumste et al. [145]. By solving only one forward calculation numerically, by introducing current monopoles at an electrode pair, and storing the obtained node potentials or lead field (which is the gradient of the potential field) in a data structure, one can obtain the potential difference at the electrode pair for every dipole position and orientation as follows:

$$U_{AB}(\mathbf{r}, \mathbf{d}) = \frac{\mathbf{d}^T \cdot \nabla V(\mathbf{r})}{I_{AB}}, \tag{3.3}$$

with U_{AB} the potential difference between the scalp electrodes A and B generated by the dipole at position $\mathbf{r}$ and with moment $\mathbf{d}$. I_{AB} is a fictive unit current which enters at electrode A and leaves at electrode B. When $\mathbf{r}$ does not coincide with a node, then $\nabla V(\mathbf{r})$ is obtained with tri-linear interpolation.

If l scalp electrodes are used to measure the EEG, $l-1$ electrode pairs can be found with linearly independent potential differences. Therefore $l-1$ numerical forward calculations are performed and stored. The $l-1$ potential differences at the $l-1$ electrode pairs are then transformed into l average referenced potentials at the l electrodes. Together with the anisotropic finite difference with reciprocity method (AFDRM) we will use this to perform simulations, described further on. For the remainder of this dissertation, we will call the finite difference incorporated with anisotropic conductivities in combination with reciprocity, the *Anisotropic Finite Differences with Reciprocity Method* (AFDRM).

3.3.5 Inverse problem

The inverse problem was solved via a minimization the RRE:

$$RRE = \frac{\|\mathbf{V}_{in} - \mathbf{V}_{model}(\mathbf{r}, \mathbf{d})}{\|\mathbf{V}_{in}\|} + C(\mathbf{r}) \tag{3.4}$$

where $\mathbf{V}_{in}$ are the electrode potentials used as input in the source estimation and $\mathbf{V}_{model}(\mathbf{r}, \mathbf{d})$ are those solved by the forward problem due to a dipole source at location $\mathbf{r}$ and with moment $\mathbf{d}$. $C(\mathbf{r})$ is a penalty term which is small when the dipole location is inside the brain compartments (white and gray matter) and large otherwise. The minimization is done by a Nelder-Mead simplex method, which can find the global minimum if the cost function is smooth. Hence, the method succeeds in finding the correct dipole parameters, when the electrode potentials obtained by a dipole in an isotropic head model and the same head model is used for the dipole estimation.

3.3.6 Simulation setup

In this paragraph we will discuss the methodology that was used to compare the numerical method, AFDRM, with the analytical method in the 5 shell spherical head model.

For the AFDRM method we divided the 5 compartment spherical head model into cubic grids of 3,2 and 1 mm. By using a fine grid we can assume that the dipole localization errors due to electrode mislocation is negligible, hence there will always be a lattice point at an electrode location. test dipoles were placed in the gray matter inner sphere, white matter sphere and gray matter outer sphere, distributed along the axial (XY), sagittal (YZ) and coronal (XZ) plane. The X, Y and Z axis are oriented along the left-right, back-front and bottom-top direction of the head model, respectively. The distance between the test dipoles was 5 mm. In the XY plane there were 777 test dipoles and in the XZ and YZ plane there were 586 dipoles. We did not consider test dipoles that were inferior to the most inferior electrode position. For each location, we also

considered 3 orientations according to the Cartesian coordinate system: X-, Y-, Z-orientation. The total number of test dipoles is $(777 + 2 * 586) * 3 = 5847$, for each head model.

The radial σ_r and tangential conductivities σ_t are calculated using the volume constraint, which is explained in appendix B. The volume constraint states that the volume of the anisotropic conductivity ellipsoid should be equal to the volume of the isotropic conductivity sphere. For the isotropic conductivity values we use $\sigma_{isotropic}^{brain} = 0.33\ S/m$ for the brain compartment, $\sigma_{isotropic}^{skull} = \sigma_{isotropic}^{brain}/16 = 0.020\ S/m$ for the skull compartment and $\sigma_{isotropic}^{scalp} = 0.33\ S/m$ for the scalp [50, 44]. For the skull we use a radial conductivity of $\sigma_r^{skull} = 0.004309\ S/m$ and a tangential conductivity of $\sigma_t^{skull} = 10\sigma_r^{skull} = 0.04309\ S/m$. In the white matter compartment we modeled the white matter anisotropy as nerve fibers that originate at the edge of the inner gray matter compartment and go radial to the edge of the outer gray matter compartment. Here we use a radial conductivity of $\sigma_r^{brain} = 1.4278\ S/m$ and a tangential conductivity of $\sigma_t^{brain} = 0.15864\ S/m$.

3.3.6.1 Dipole localization errors due to using AFDRM in a spherical head model with isotropic conducting compartments

First, we want to validate the numerical method AFDRM, described in 2.4.2.6.3 in isotropic media. Consider a dipole at location $\mathbf{r}$ and with orientation $\mathbf{d}$. We calculated the electrode potentials $\mathbf{V_{dipole}}$ in an isotropic head model by the analytical expression. Using $\mathbf{V_{dipole}}$ we solve the inverse problem in the isotropic head model, but we use the numerical method instead of the analytical expression. We obtain an estimated dipole location $\hat{\mathbf{r}}$ and orientation $\hat{\mathbf{d}}$, and we can calculate the Euclidean norm between the original and the estimated dipole. By doing this simulation we can investigate how accurate the numerical method is compared to the analytical expression.

By using the isotropic 5-shell spherical model in both the forward and the inverse problem, we can validate the numerical method discussed in 2.4.2.6.3 in isotropic media. We calculated the dipole localization error for different grid sizes.

3.3.6.2 Dipole localization errors due to using AFDRM in a 5 shell spherical head model with skull or white matter being anisotropic conducting compartments

In this part, we want to validate the aforementioned numerical method, AFDRM, in the 5 shell spherical head model with skull or white matter compartments set to anisotropic conductivity values. The flow chart of the simulation study can be derived from figure 3.9: the potentials at the electrodes were calculated by using the analytical expression for a given dipole in the brain

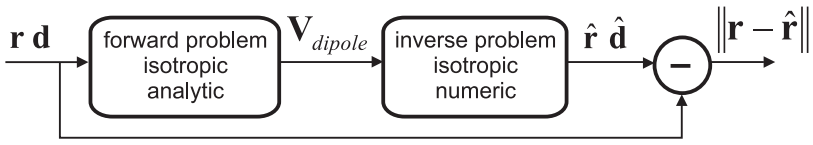

Figure 3.8: A flow chart of the simulation study where the dipole localization error is investigated due to the discretization error in isotropic head models. A dipole is used to perform one forward calculation in an isotropic head model with the analytical formula. The resulting electrode potentials are then used to estimate the dipole parameters in a isotropic head model using the numerical method, AFDRM.

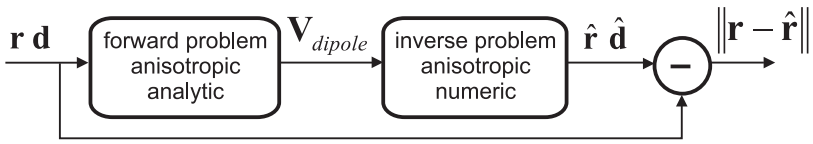

Figure 3.9: A flowchart of the simulation study where the dipole localization error is investigated due to the discretization error in isotropic head models. A dipole is used to perform one forward calculation in an anisotropic head model with the analytical formula. The resulting electrode potentials are then used to estimate the dipole parameters in a anisotropic head model using the numerical method, AFDRM.

compartments in a 5 shell spherical head model with skull or white matter compartments set to anisotropically conducting values and all other compartments set to isotropic. Next, using the AFDRM the inverse problem was solved for the set of potentials in a 5 shell spherical head model with the initial anisotropically compartment set to anisotropic conducting values. The dipole localization errors were then inspected and compared with the localization error when anisotropic conductivities of the skull or white matter is neglected. In the latter, the test dipole configuration described above was used so that the results are obtained from test dipoles of the same simulation setup.

3.3.6.3 Error measures

Applying the above simulations to one dipole at location $\mathbf{r}$ with components $\mathbf{d}$, will result in an estimated dipole at location $\hat{\mathbf{r}}$ with components $\hat{\mathbf{d}}$. The dipole location error due to discretization (using the numerical method instead of the analytical formula) can then be written as the euclidean distance:

$$d(\mathbf{r}, \hat{\mathbf{d}}) = \|\mathbf{r} - \hat{\mathbf{r}}\| \tag{3.5}$$

3.3.7 Results

3.3.7.1 Dipole localization errors due to using AFDRM in a 5 shell spherical head model with isotropic conducting compartments

The results of the first simulation study are summarized in table 3.1, figure 3.10 and figure 3.11. Each row in figure 3.10 represents the dipole localization error for a given grid size. We distinguish a 1, 2 and 3 mm grid. The three columns represent the errors for a fixed dipole orientation. The mean localization errors of all dipoles (see table 3.1) are 1.43 mm, 0.78 mm, 0.48 mm for 3 mm, 2 mm and 1 mm grid size respectively. The color indicates the dipole localization error. We can see that at a 3 mm grid size, the dipole localization errors are greater then a 2 mm grid size, which has greater dipole localization errors as a 1 mm grid size. From table 3.1 the maximum error in a 3 mm cubic grid was larger than 10 mm, while in a 1 mm cubic grid the largest error was no more than 4 mm. These large errors are mostly situated near the edges of the brain compartment, as is shown in 3.10.

Figure 3.11 shows the histogram of the dipole localization error for (a) 1 mm grid size, (b) 2 mm grid size and (c) 3 mm grid size. The finer the grid, the more the distribution is skewed to the left. This means that the dipole location error in a finer grid is smaller. Note that for a 1 mm grid size there is no larger dipole localization error than 3 mm.

Other studies obtain mean localization errors of 3.4 mm and 2.2 mm, for a 3 and 2 mm grid size in a spherical head model [145]. By using AFDRM, we can obtain a smaller mean localization error of 1.43 mm, 0.78 mm and 0.48 mm for a 3mm, 2mm and 1 mm grid size respectively. The reason for the better accuracy, is probably due to the fact that the calculation is done on the nodes between the elements, instead of the center of the elements (like the traditional FDM).

3.3.7.2 Dipole localization errors due to using AFDRM in a 5 shell spherical head model with skull or white matter being anisotropic conducting compartments

Figure 3.12 shows the dipole localization error when only skull anisotropy is incorporated in the AFDRM and spherical head model, and this for dipole orientations along the Cartesian axes and different grid sizes. Table 3.2 summarizes the dipole location errors. We obtain a mean dipole localization error of 9.229 mm for a 3 mm grid size (standard deviation: 3.905 mm, maximum: 21.765 mm), 6.086 mm for a 2 mm grid size (standarddeviation: 2.765 mm, maximum: 16.541 mm) and 2.551 mm for a 1 mm grid size (standard deviation: 1.192 mm, maximum: 6.793 mm). For a 3 mm grid size we see large dipole localization errors, which are located near the interface of the white matter

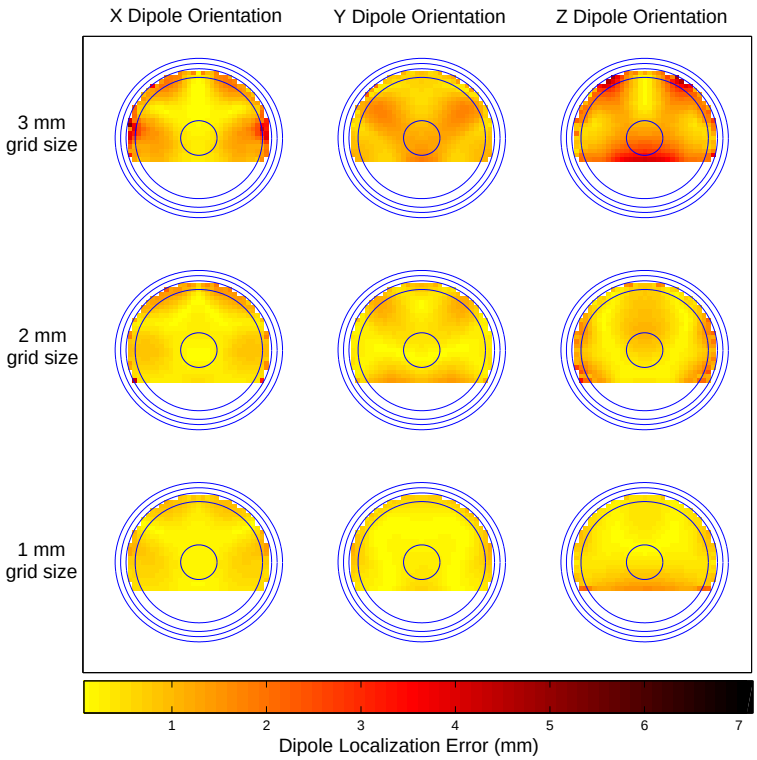

Figure 3.10: The dipole localization error mapped on the XZ planes for AFDRM in an isotropic spherical head model. The first, second and third column are the dipole localization errors of all dipoles oriented along the X axis, Y axis and Z axis, respectively. The upper, middle and bottom row represent grid sizes of 3 mm, 2 mm and 1 mm, respectively.

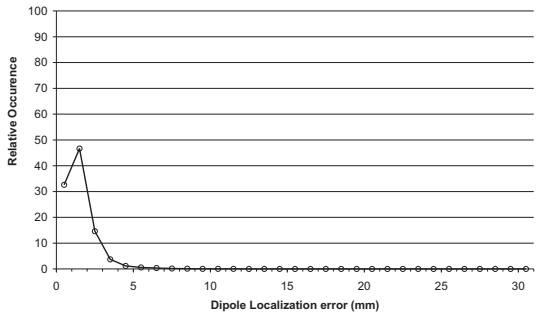

(a)

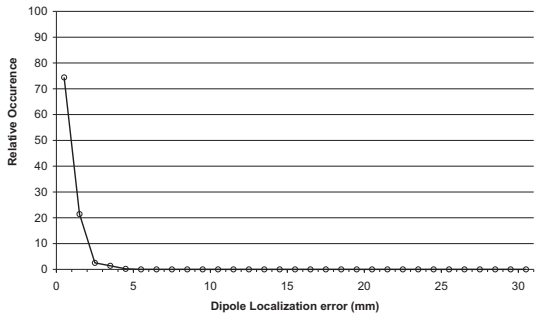

(b)

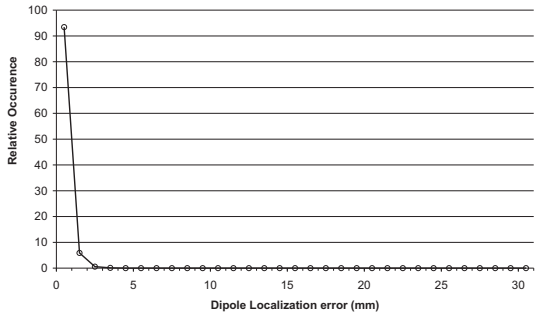

(c)

Figure 3.11: The histogram of the dipole localization error in the isotropic 5-spherical head model using AFDRM at a grid size of (a) 3 mm, (b) 2 mm and (c) 1 mm. The dipole localization error is shown on the X axis in mm. The Y axis indicates the percentage of dipoles which belongs to a range of dipole localization error indicated by the bins.

Dipole Orientation	mean	standard deviation	maximum	minimum
resolution of the cubic grid : 3 mm				
X	1.0444	0.8302	5.2001	0.0133
Y	1.3351	1.0116	8.2438	0
Z	1.8566	1.0609	11.6861	0.0067
total	1.4269	1.0334	11.6861	0
resolution of the cubic grid : 2 mm				
X	0.73883	0.47164	4.2093	0.022135
Y	0.78455	0.77757	4.8591	0.021664
Z	0.80921	0.52187	4.6955	0
total	0.77753	0.60597	4.8591	0
resolution of the cubic grid : 1 mm				
X	0.46736	0.24567	1.4562	0.017365
Y	0.46966	0.33159	1.9061	0.008766
Z	0.49904	0.43434	3.8836	0.012705
total	0.47868	0.34615	3.8836	0.008766

Table 3.1: Dipole estimation error due to discretization when using the AFDRM in a isotropic spherical head model. The error is expressed in mm. The first column indicates the selection of dipole with a specific orientation (along X,Y or Z direction) or all dipoles (indicated as total).

shell and the gray matter outer shell. As the grid size decreases, the dipole localization errors decrease.

The histogram of the dipole localization error is given in figure 3.13. We can appreciate that the distribution of the errors shifts to the left, when moving from a coarse to a fine grid. Important to note is that at a 1 mm grid size the dipole localization error has an upper boundary equal to 7 mm. To place these results in a broader context, we also repeated the histogram of the dipole localization error due using isotropic instead of an anisotropic compartment (see figure 3.13 (d)). Here the results from the first part of this chapter 3.2 were used as a reference. However, the simulation was redone to the same dipoles as in the simulation.

Figure 3.14 shows the dipole localization error when only white matter anisotropy is incorporated in the AFDRM and spherical head model, and this for dipole orientations along the three cartesian axes and different grid sizes. We obtain a mean dipole localization error of 3.078 mm for a 3 mm grid size (standard deviation: 3.171 mm, maximum: 34.142 mm), 1.695 mm for a 2 mm grid size (standard deviation: 1.434 mm, maximum: 12.047 mm) and 1.044 mm for a 1 mm grid size (standard deviation: 1.107 mm, maximum: 11.606 mm). These results are summarized in table 3.3 The dipole localization errors are smaller than the ones when only skull anisotropy is incorporated in the AFDRM. At a 3 mm grid size the dipole localization is worst at the basal part

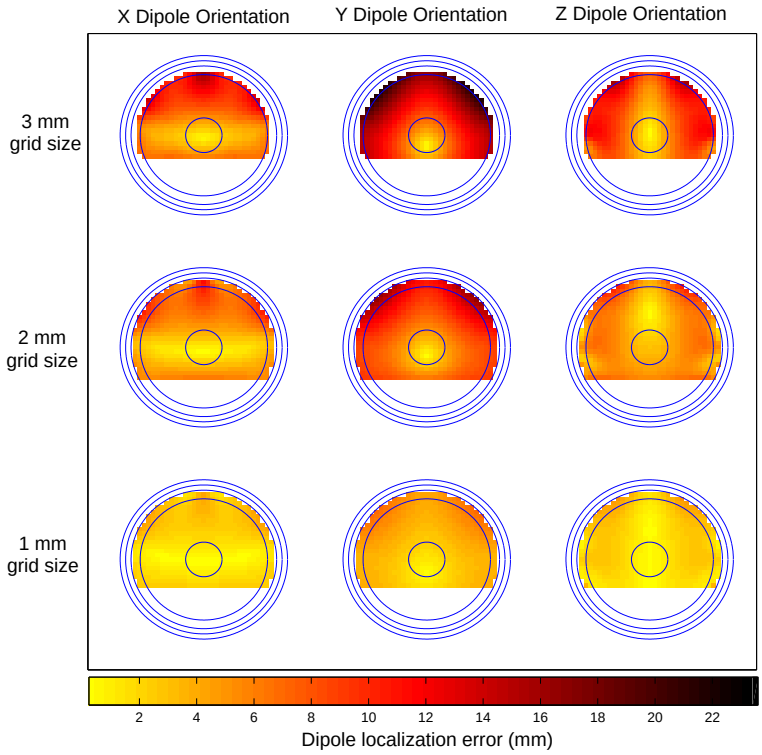

Figure 3.12: The dipole localization error for an anisotorpically conducting skull layer is shown. The color bar shows the distance from the original dipole to the estimated dipole in mm. The rows show the dipole localization error at a same grid size, while the columns show the dipole localization error when the original dipole orientation is considered fixed.

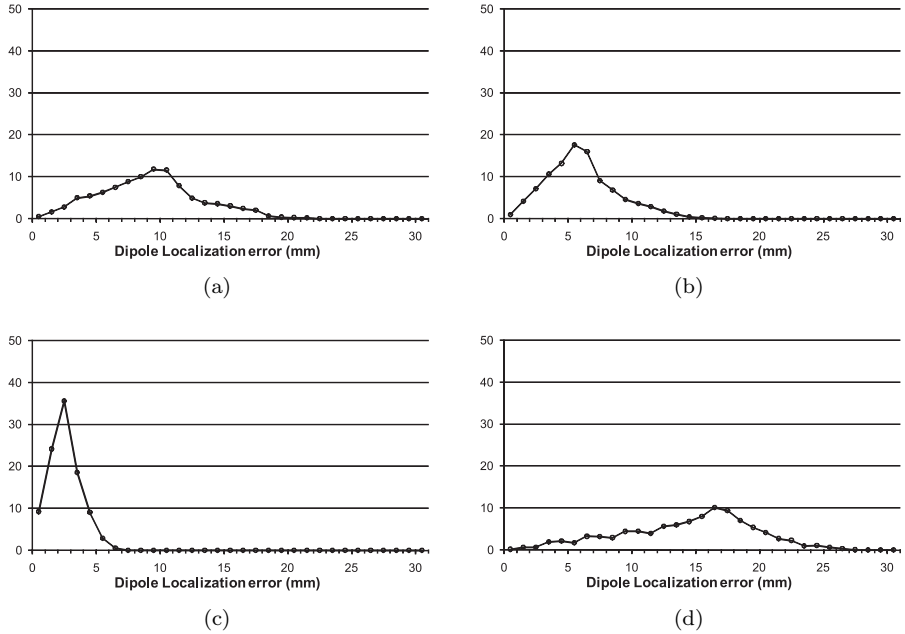

Figure 3.13: The histogram of the dipole localization errors for using AFDRM in a 5 shell spherical head model with a skull anisotropic conducting compartment is shown at a grid size of (a) 3 mm, (b) 2mm and (c) 1 mm, respectively. The dipole localization error is denoted in the X axis in mm. The Y axis indicates the percentage of dipoles which belongs to a range of dipole localization error indicated by the bin. To place these results in a broader context, we also showed (d) the histogram of the dipole localization errors due to using an isotropic instead of an anistropic skull compartment.

Dipole Orientation	mean	standard deviation	maximum	minimum
resolution of the cubic grid : 3 mm				
X	8.1562	3.5399	18.9942	0.62284
Y	9.7125	3.856	21.765	0.62477
Z	9.8194	4.0781	19.8436	0.2575
total	9.2294	3.905	21.765	0.2575
resolution of the cubic grid : 2 mm				
X	5.4779	2.6432	14.6548	0.14975
Y	6.2032	2.7731	16.5408	0.21969
Z	6.5775	2.7651	13.6852	0.15533
total	6.0862	2.7653	16.5408	0.14975
resolution of the cubic grid : 1 mm				
X	2.2508	1.0897	5.8161	0.2315
Y	2.6754	1.1707	6.793	0.023478
Z	2.7281	1.2525	5.3978	0.050511
total	2.5514	1.1919	6.793	0.023478

Table 3.2: Dipole estimation error due to discretization when using the AFDRM in a spherical head model with an anisotropic conducting skull compartment. The error is expressed in mm. The first column indicates the selection of dipole with a specific orientation (along X,Y or Z direction) or all dipoles (indicated as total).

of the brain, below the center. The histogram of the dipole localization error is shown in figure 3.15. We can see that the anisotropy is modelled very adequately. Moreover, the upper boundary of the dipole localization error at a 1 mm grid size is 6 mm.

From figure 3.14 and table 3.3 we can appreciate the large error at the bottom of the white matter compartment in the third column (original dipole has an orientation along the Z axis). As the electrodes are mainly situated in the upper half of the spherical head model, they only measure one half of the dipolar electric field caused by the dipole in that region. Moreover, due to the illposedness of the inverse problem, large errors occur at places that have poor spatial sampling of the electrodes.

As shown in figure 3.16 the dipole localization error when assuming anisotropic compartments is bigger than the dipole localization error when assuming isotropic compartments. In the anisotropic head models, there is not only a discretization of the potential values, like in the isotropic head models, but there is also a discretization of the conductivity tensors. In a numerical head model, an element belonging to an anisotropic compartment has a fixed matrix representation of the conductivity tensors. The conductivity tensors are dependent on the direction of the anisotropy, which is dependent on the vectors tangential to the skull surface for the skull anisotropy. These vectors are only calculated on discrete places in the skull layer. In reality the vectors can be written as

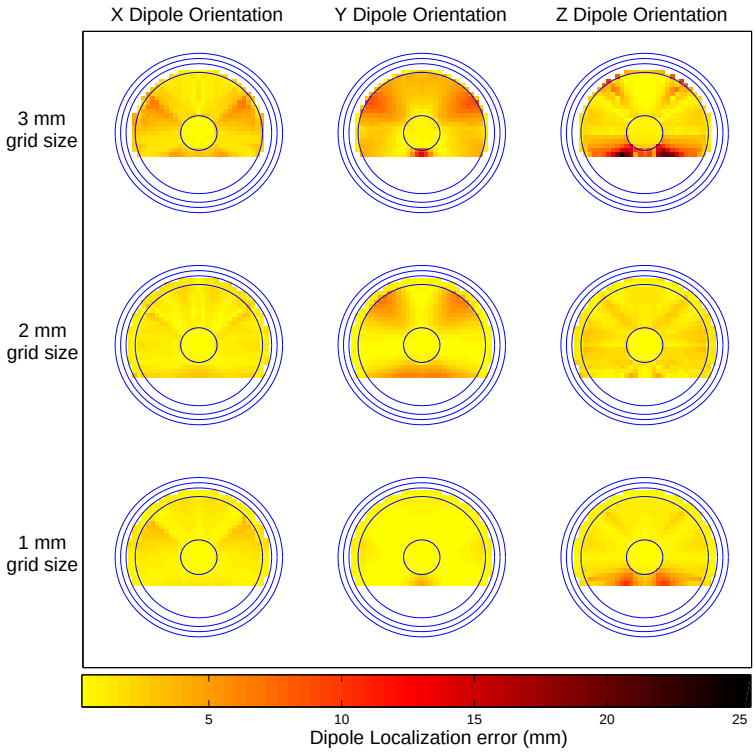

Figure 3.14: The dipole localization error if the white matter layer is anisotropic is shown at different grid sizes. The color denotes the distance between the original dipole and the estimated dipole in mm. The rows show the dipole localization error at a same grid size, while the columns show the dipole localization error when the original dipole orientation is considered fixed.

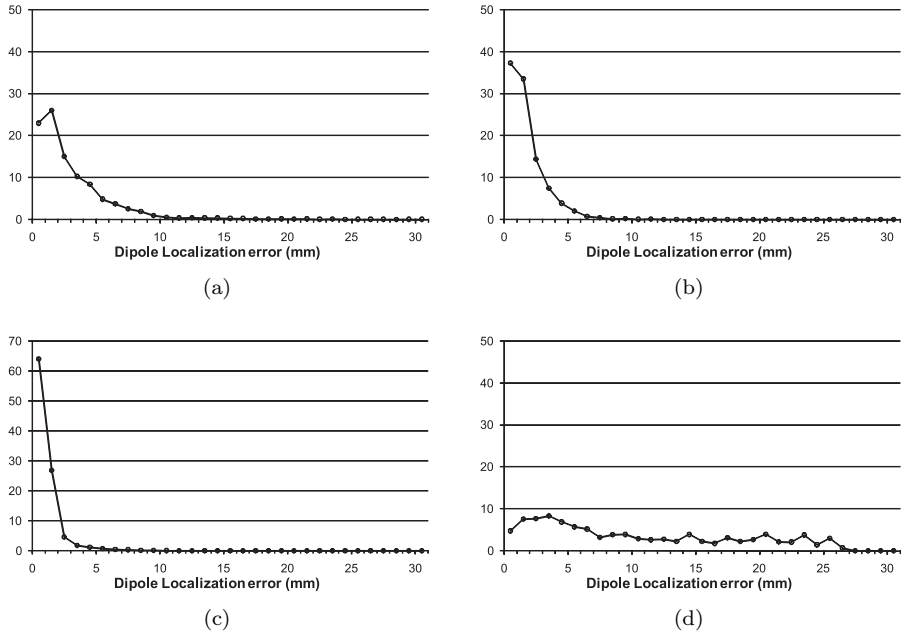

Figure 3.15: The histogram of the dipole localization errors for using AFDRM in a 5 shell spherical head model with white matter anisotropic conducting compartment is shown at a grid size of (a) 3 mm, (b) 2mm and (c) 1 mm, respectively. The dipole localization error is denoted in the X axis in mm. The Y axis indicates the percentage of dipoles which belongs to a range of dipole localization error indicated by the bin. To place these results in a broader context, we also (d) repeated the histogram of the dipole localization errors due to using an isotropic instead of an anistropic white matter compartment. Here the results from the first part of this chapter 3.2 were used as a reference.

Dipole Orientation	mean	standard deviation	maximum	minimum
resolution of the cubic grid : 3 mm				
X	2.3627	1.7038	9.8343	0.040344
Y	2.6185	2.4492	16.9984	0.064512
Z	4.2522	4.379	34.1415	0.04224
total	3.0778	3.1711	34.1415	0.040344
resolution of the cubic grid : 2 mm				
X	1.5581	1.207	7.3888	0
Y	1.7454	1.601	11.3254	0
Z	1.7803	1.4562	12.047	0
total	1.6946	1.4338	12.047	0
resolution of the cubic grid : 1 mm				
X	0.94259	0.6123	3.5759	0.008382
Y	0.89426	0.83761	5.5383	0.019556
Z	1.2955	1.5823	11.6095	0.025203
total	1.0441	1.1068	11.6095	0.008382

Table 3.3: Dipole estimation error due to discretization when using the FDM in a spherical head model with an anisotropic conducting white matter compartment. The error is expressed in mm. The first column indicates the selection of dipole with a specific orientation (along X,Y or Z direction) or all dipoles (indicated as total).

continuous functions.

3.4 Summary and Conclusions

In a first instance, we investigated the influence of the anisotropic conductivities of brain tissues on EEG dipole analysis. Neglecting the skull anisotropy and white matter anisotropy, yield mean dipole localization errors of 13.73 mm and 11.21 mm, respectively. These errors are not negligible and the anisotropic conductivities have to be considered in the forward problem.

A validation of the AFDRM has been performed in isotropically conducting media. We found that the mean dipole localization errors are very small: a 3 mm grid yields 1.48 mm, a 2 mm grid 0.78 mm and a 1 mm grid 0.48 mm. The error due to the discretization is thus very small ($\sim$ grid spacing/2) and acceptable to do EEG dipole analysis. From this study we can conclude that the method works for isotropically conducting head models.

The next step was to incorporate anisotropic data. In this case we also compared the analytical head model with the numerical head model, both with the anisotropic skull layer of with the anisotropic white matter layer by means of the dipole localization error. For a grid size larger than 1 mm, the mean dipole localization is bigger than 3 mm. This means that the above AFDRM method

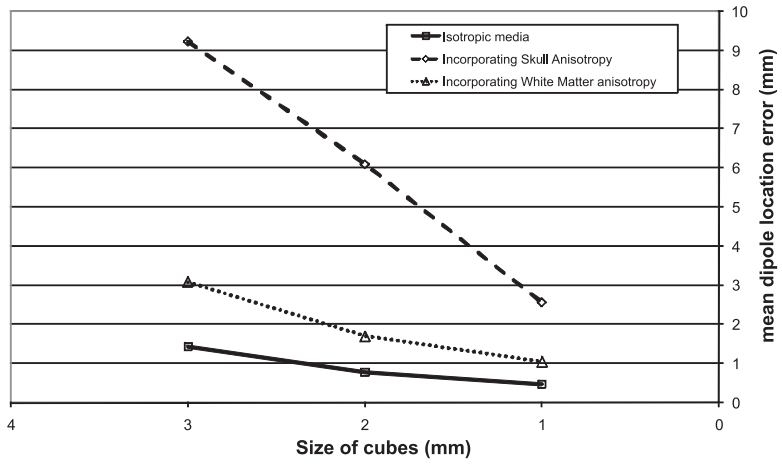

Figure 3.16: The mean dipole location error versus the size of the cubes in the cubic grid. We see that the smaller the cubes (the finer the computational grid), the smaller the discretization error is. The discretization of the anisotropic conductivity tensors also introduces an error as the error due to discretization of the anisotropic head model is larger than the one due to discretization in the isotropic head model.

cannot adequately model the skull anisotropy if the grid size is bigger than 1 mm. In order to model the anisotropy adequately, we must consider the grid size of the lattice of the AFDRM to be 1 mm or less.

The results shown in this study indicate that AFDRM can be used for realistic head models. One way to do this is by dividing the head in cubes of a specific grid size. The smaller the grid size, the smaller the dipole localization error due to using AFDRM, but the larger the memory and computational needs. The latter is not an issue anymore, as 64-bit computing in a cluster environment enables the increase of the computational possibilities. Once the head model is made, the inverse problem can be solved. With the use of reciprocity, the number of forward calculations, needed to solve the inverse problem, can be reduced very significantly. On a PC (3 GHz, 2 GBytes RAM), one forward calculation using the SOR lasted approximately 20 minutes, whereas using reciprocity the forward calculation lasted less than a second.

These results were presented in a publication in an A1 journal [64], a publication in an A2 journal [60], an abstract in a A1 journal [57] and several proceedings at international [61, 62] and national conferences [56, 63, 58, 59].

Chapter 4

Construction of a realistic head model with anisotropic conductivities using magnetic resonance imaging

The most exciting phrase to hear in science, the one that heralds new discoveries, is not Eureka! (I found it) but rather, "hmm... that's funny..."
—Isaac Asimov

4.1 Introduction

In the previous chapter we developed a numerical method that can incorporate anisotropic conductivities. This was validated using a spherical head model with a spherically symmetric anisotropic conductivity profile. The human head however is not spherical and the anisotropic conductivity profile is not known a priori. In this chapter we will discuss a methodology to measure the geometry of the human head using magnetic resonance images. A similar technique will be used to measure the direction dependence of the brain tissues. This is done using diffusion weighted imaging, which measures the amount of free diffusion of water in brain tissues along different directions. From this information, the anisotropic conductivity profile can be constructed.

In the first part of this chapter, we will discuss the construction of the head model and the acquisition of the magnetic resonance images. The second part of the chapter will investigate in a realistic head model how the modeling of the anisotropy in white matter will affect the dipole estimation. Moreover,

the effect of neglecting the anisotropic properties of the conductivity of several brain tissues will be investigated.

4.2 Introduction to Magnetic Resonance Imaging

4.2.1 Magnetic Resonance Imaging

Magnetic resonance imaging (MRI) is a well-known medical imaging technique to study the structural anatomy or functional behavior of the human body. MRI is a non-invasive procedure that uses the behavior of different soft tissues in magnetic fields to visualize contrast differences. The MR scan results in a set of images. Each image represents a slice of the human head. An example of such an image can be seen in figure 4.1. Specific tissue types can be deduced from that image. Taking into account some a priori knowledge of anatomy of the head, one can distinguish the scalp, soft bone of the skull, cerebro-spinal fluid (CSF), white and gray matter. From these images the anatomical information can be derived using segmentation techniques.

An elementary volume of the image is a *pixel*, which depicts the MR signal measured at a specific coordinate. In a traditional T1 MR scan, the pixel becomes more white, if the tissue contains more fat. Most tissues contain fat and are thus visible in the image. However, the hard parts of the bone are difficult to see on a T1 MR scan. By stacking these image slices a 3D volume can be obtained. Hence, the elementary volume is a *voxel* (derived from volume pixel). The voxel has a specific dimension, depending on the MR scan. In a Siemens Trio 3 tesla MR scanner of the radiology department of the Ghent University Hospital, a commonly used MR scan (T1 MPRAGE) results in a three dimensional image with a voxel size of 0.98 mm $\times$ 0.98 mm $\times$ 0.98 mm.

From the image 4.1 we can see that the soft tissue of the brain consists of 2 parts. First, the gray matter contains the neuron structures. The gray matter at the outside of the brain (also known as *cortex*) is responsible for the processing of the information and execution of complicated motoric and cognitive tasks, such as movement, reading, interpretation, etc... The white matter (the soft tissue between the gray matter structures) contains neuron fibers that connect several regions of the brain. The white matter is thus responsible for the communication between the brain regions. Among others the *corpus callosum* (see also figure 2.4) is the largest interconnection between the left and right half of the brain. This structure can be seen as a hook-shaped light gray structure at the center of the image in figure 4.1 and consists of many nerve fibers lying parallel and packed closely together.

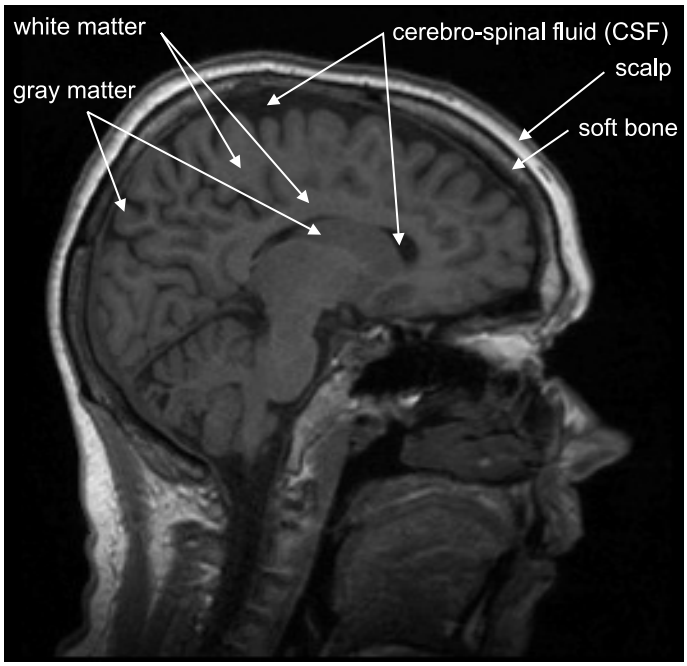

Figure 4.1: A sagittal plane of an MR image.

4.2.2 Diffusion weighted imaging

A recent MRI technique also enables us to visualize neuron fibers in the brain. *Diffusion weighted Magnetic Resonance Imaging* (DW-MRI) measures the free diffusion length of water molecules inside the brain [19]. Water molecules diffuse more easily along the nerve fibers than orthogonal to the nerve fiber. This diffusion is more explicit at the corpus callosum, where many nerve fibers are lying parallel to each other. Using a special MR sequence, the diffusion can be measured. One Diffusion Weighted Image (DWI) measures the diffusion length in one particular direction. The total diffusion in an orthogonal basis can be expressed by means of a second order tensor. To construct the order diffusion tensor in each voxel, one needs at least 6 images in different directions and a reference image [16, 18]. The whole process of deriving the diffusion tensor from diffusion weighted imaging is also called *Diffusion Tensor Magnetic Resonance Imaging* (DT-MRI) [91]. From this tensor information we can calculate the fibers that are most likely to actually be present in the brain. This is illustrated in figure 4.2.

The degree of anisotropy can be quantified using several measures. The most common measure is the fractional anisotropy (FA). Let d_1,d_2 and d_3 be the

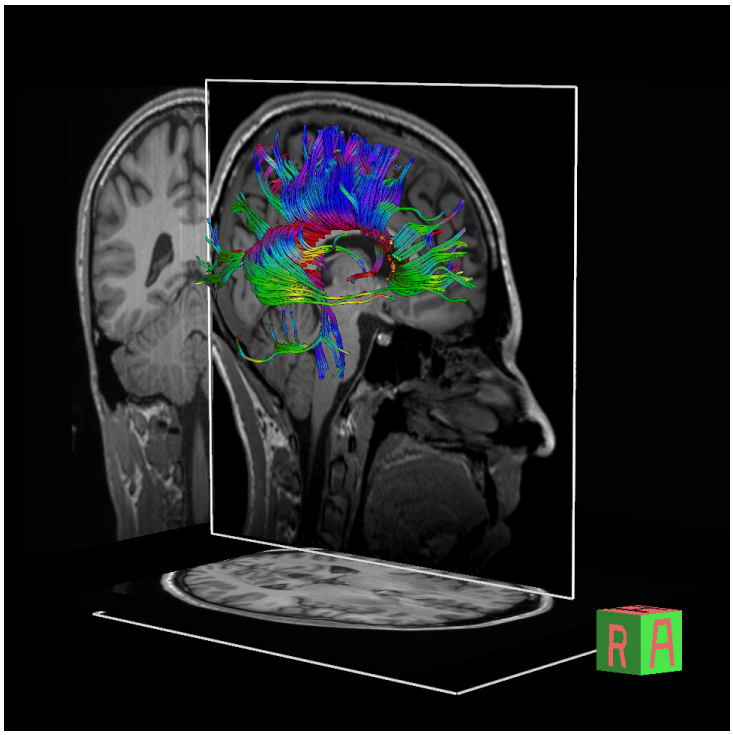

Figure 4.2: A visualization of the neuron fibers fused with an MR image of the brain. Here only the fibers from the corpus callosum are drawn.

eigenvalues of the diffusion tensor at a specific voxel:

$$FA = \sqrt{\frac{3}{2}} \frac{\sqrt{(d_1 - \bar{d})^2 + (d_2 - \bar{d})^2 + (d_3 - \bar{d})^2}}{\sqrt{d_1^2 + d_2^2 + d_3^2}} \tag{4.1}$$

where $\bar{d}$ is the mean diffusivity or $\bar{d} = (d_1 + d_2 + d_3)/3$. The FA is 0 in the isotropic case and 1 in the hypothetical case that the diffusion is directed only in 1 direction and zero in the other directions [17].

In our introduction we stated that, for the skull, the tangential conductivity is factor 10 larger than the normal conductivity. Furthermore, in white matter, the conductivity along a nerve bundle was set to be 9 times larger then the conductivity along the two directions perpendicular to the nerve bundle. Therefore, a more intuitive measure was constructed. We define the anisotropic ratio (AR) of the white matter as:

$$AR = \frac{d_1}{mean\,(d_2, d_3)}, \tag{4.2}$$

where d_1 is the largest eigenvalue and d_2 , d_3 the two smallest eigenvalues of the diffusion tensor at a specific voxel (see figure 4.8). As diffusion weighted images do not image the diffusion in the skull, the measure is only used for white matter voxels. The above measures only depicts the anisotropy in prolate tensors or cigar-shaped tensors. It has been shown however that over 90% of the fibers in white matter are prolate.

4.3 Aim of the study

The remainder of this chapter will consist of two parts. First, a realistic head model is constructed. We will focus on the construction of the anisotropic conductivities of the skull and white matter. The anisotropic conductivity tensor of an element belonging to the skull will be derived using traditional image processing and the geometry of the skull. For the derivation of the white matter, the diffusion weighted images will be used. Here, two approaches exist as will be discussed. The second part of the chapter will consist of two simulation studies. A first simulation study will compare the two approaches to derive the anisotropic conductivities of white matter using the DW-MRI. A second simulation will discuss the importance of also incorporating the conductivity tensor in gray matter regions.

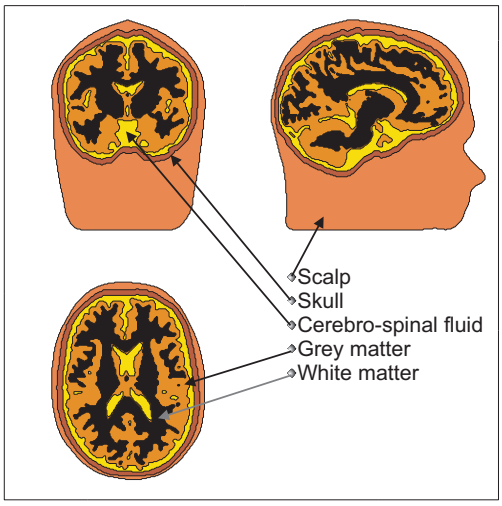

Figure 4.3: The coronal, sagittal and axial plane of the head model. The different compartments are indicated: scalp, skull, cerebro-spinal fluid, gray matter and white matter. The test dipoles were placed in each voxel of the gray.

4.4 Construction of the realistic head model with anisotropic conductivities

4.4.1 Construction of compartments

In our study we used a realistic head model that was derived from segmented T1 weighted MRI images. The MRI images were obtained on a 3 Tesla MRI scanner (Siemens Trio, Erlangen, Germany) using a 3 dimensional MP RAGE sequence with a repetition time (TR) of 1550 ms and an echo time (TE) of 2.48ms (bandwidth = 210 Hz per pixel). The image consisted of $256 \times 256 \times 176$ matrix of isotropic voxels of 0.9 mm $\times$ 0.9 mm $\times$ 0.9 mm. SPM5 was used to segment the white matter, gray matter and cerebro-spinal fluid [47]. The segmentation results in three values for each voxel, each indicating its probability of belonging to white matter, gray matter or cerebro-spinal fluid (CSF). The voxels are then assigned to the compartment for which the voxel had the highest probability. A median filtering was applied to exclude isolated voxels that had outlier probabilities. This procedure allowed us to classify each voxel to a compartment. Note that the gray matter compartment consisted of a cortical part and a center part. The skull compartment was constructed by a dilation operation of the brain compartment and was on average 6 mm thick. The scalp compartment was obtained by subsequently applying an opening, closing and hole filling operation on the thresholded MR image. This way we

could make a distinction between head and air. The skull, CSF and brain compartments were then added to the head model. Figure 4.3 shows an axial, sagittal and coronal plane of the head model. The conductivities of the CSF and scalp remain isotropic through the remainder of this dissertation and were set to $1.0\,S/m$ and $0.33\,S/m$, respectively.

4.5 Anisotropic conductivity of the skull

As mentioned in 2.5.3, the skull has an anisotropic conductivity. The conductivity tangential to the surface of a skull segment is 10 times larger than the normal conductivity . The tangential and normal direction can be derived using the geometry of the skull surface.

A T1 MR image using the MPRAGE sequence was used to segment the 3D image in a white matter, gray matter and cerebro-spinal fluid (CSF) compartment, using SPM5 [47]. Results are shown in panel (a) of figure 4.4. The ensemble of the white matter, gray matter and CSF was set to be the brain compartment. As skull has no signal on a T1 MR image and is difficult to segment, a dilated image of the brain was used as the skull (see panel (b) in figure 4.4). Using the geometry of the skull, the normal direction was found as follows.

The skull compartment was dilated with an 6 neighborhood structural element. The dilation was only performed on the outward surface of the skull. The dilated image is subtracted with the original image, resulting in a thin outline around the skull surface (see panel (c) in figure 4.4). In a voxel of the skull VOX_i^{skull}, the nearest 8 voxels of the subtracted dilated image were chosen and the point of gravity of these voxels was calculated, indicated as POG. The vector pointing from the voxel of the skull VOX_i^{skull} to the point of gravity POG was chosen to represent the normal direction of the skull segment. These normals are shown in panel (d) of figure 4.4.

The normalized normal $\mathbf{n}_i$ at the i-th voxel from the skull, was then used to construct two vectors $\mathbf{t}_{i(1)}$ and $\mathbf{t}_{i(2)}$ orthogonal to the normal. When the skull was set to be anisotropic conducting, the conductivity along the tangential directions, $\mathbf{t}_{i(1)}$ and $\mathbf{t}_{i(2)}$, was set to be 10 times larger than the normal conductivity (along the normal direction, $\mathbf{n}_i$) at the i-th voxel of the skull [126]. Let σ_n and σ_t be the normal conductivity and tangential conductivity at the i-th voxel. A tensor at each voxel can be constructed, which can be represented as an ellipsoid as shown in 4.5.

Using the volume constraint we can determine the conductivity values along the normal and tangential directions. This constraint states that the isotropic conductivity of the skull should be the geometric mean of the conductivity values along the normal and tangential directions [156]. The isotropic conductivity is known to be variable among patients and in time, but can be measured by Electric Impedance Tomography (EIT) techniques. We started from a a isotropic

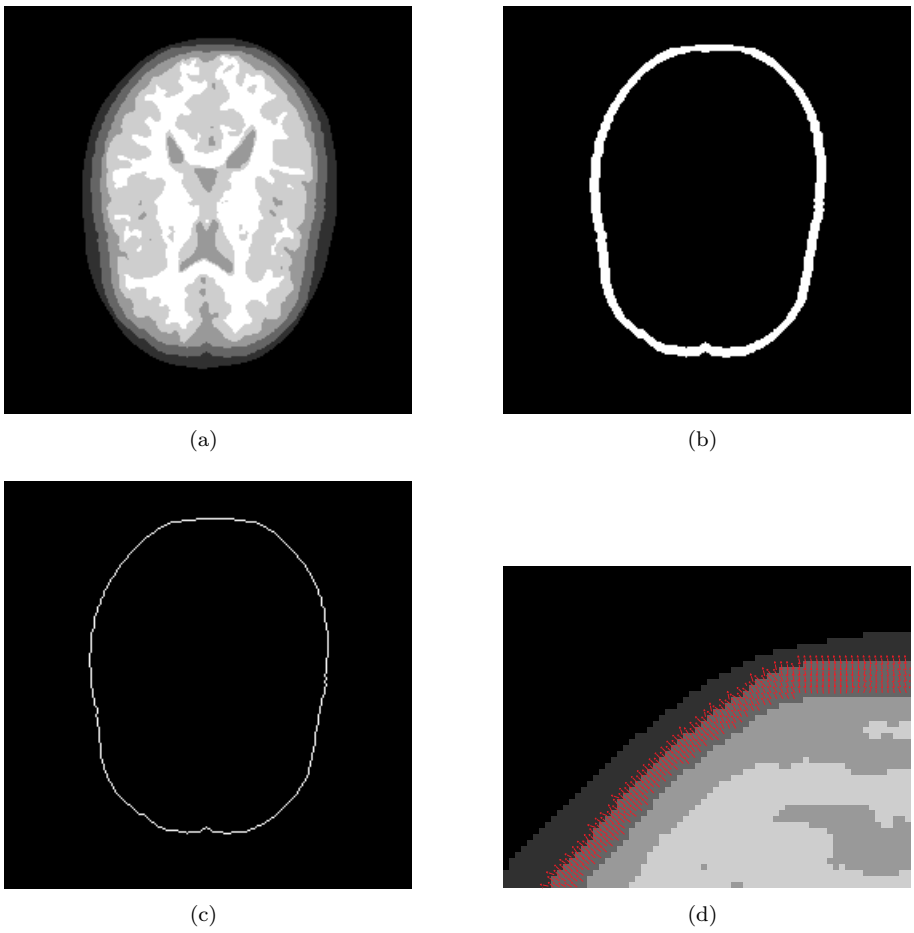

(a) (b)

(c) (d)

Figure 4.4: An overview of the construction of the anisotropic conductivity of the skull. Panel (a) shows the an axial slice of the head model constructed using T1 MR images. Panel (b) shows the skull compartment at the same slice. Panel (c) shows the dilated image subtracted with the original skull image. The dilation was only performed on the outward surface. Panel (d) shows the outward normals at each voxel.

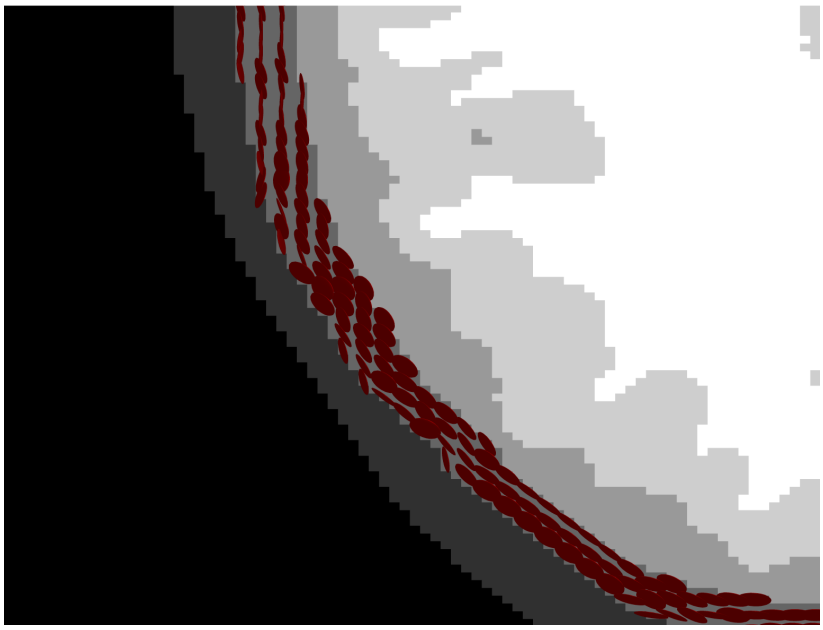

Figure 4.5: An illustration of the conductivity tensors at the skull. The different gray-scales denote the compartments of the head model. The diffusion tensors are represented as ellipsoids in red.

skull conductivity of $\sigma^{skull}_{isotropic} = \sigma^{brain}_{isotropic}/16 = 0.33/16 = 0.020$ S/m.

Using the relations above, we can calculate the conductivity values in the normal and tangential directions, $\sigma_n = 0.0043$ S/m and $\sigma_t = 0.043$ S/m. The calculation is shown in appendix B.

4.6 Anisotropic conductivity of white matter

4.6.1 Acquisition of the diffusion tensor using diffusion weighted magnetic resonance imaging (DW-MRI)

The anisotropic conductivities were derived from diffusion weighted images (DWIs). All diffusion weighted images were acquired with a 3 tesla MRI scanner (Siemens Trio, Erlangen, Germany) equipped with an 8-element head coil. Diffusion weighted imaging was performed in 60 directions with an echoplanar spin echo sequence with a band width of 1300 Hz per pixel. A total of 60 slices was acquired with a repetition time (TR) of 10400 ms and an echo time of 105 ms. To minimize the influence of eddy currents, a twice-refocused spin echo (TRSE) preparation was used with b-factors of 0 and 1000 s/mm^2

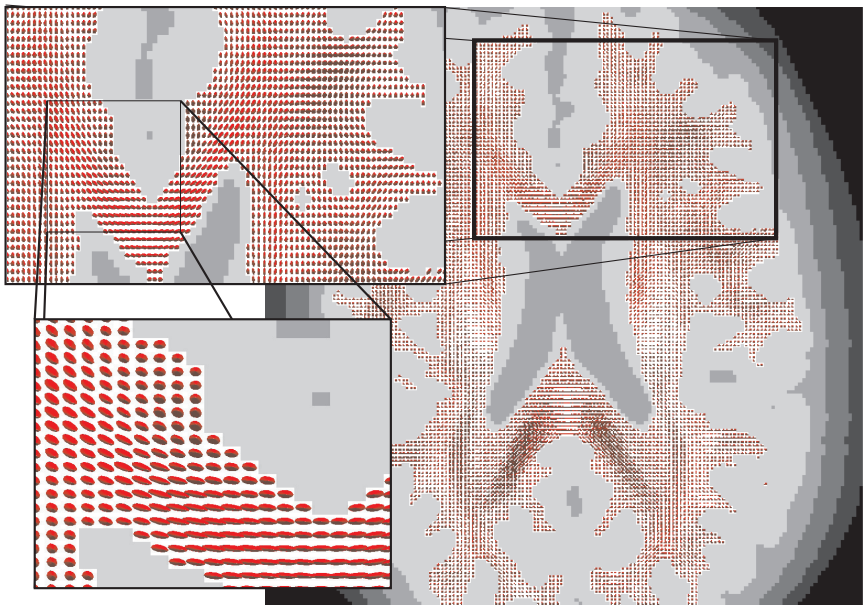

Figure 4.6: An illustration of the diffusion ellipsoids in white matter is shown. We can notice that the diffusion ellipsoids in the corpus callosum (left bottom panel) are very prolate, meaning that the diffusion is mainly in one direction. Indeed the parallel nerve bundles of the corpus callosum connect the left and right hemisphere. In the white matter near the gray matter cortex the diffusion ellipsoids are more spheroids, which indicate that the anisotropy is less than in the corpus callosum.

[122]. The results consisted a of $128 \times 128 \times 60$ matrix of isotropic voxels of $2\,\text{mm} \times 2\,\text{mm} \times 2\,\text{mm}$.

The DWIs were aligned and smoothed with a 3D scalar partial-differential-equation filter [29]. The RESTORE technique corrects for physiological noise such as cardiac pulsation [27]. An altered version of the RESTORE method was used to robustly estimate the diffusion tensors: first the original non-smoothed DWIs were used to identify outliers in the data and then these outliers were rejected during the final tensor fitting of the smoothed DWIs. A registration was done between the T1 MR image (source) and the DWIs (target) by applying a affine transformation (linear transformation) on the T1 MR image to register with the DWIs. Note that the DWIs were not transformed as a transformation of these images causes a change in the diffusion tensor. This change of basis can be taken into account, but this was beyond the scope of this dissertation.

An accurate solution of the forward problem with anisotropic conductivities of white matter requires a fine grid of $1\,\text{mm} \times 1\,\text{mm} \times 1\,\text{mm}$ voxels [64]. The T1 volume and the diffusion tensor images were therefore linearly interpolated to a $1\,\text{mm} \times 1\,\text{mm} \times 1\,\text{mm}$ cubic grid. Figure 4.6 illustrates a T1 MR image with

the diffusion ellipsoids in each white matter voxel. From the 3D segmented images we extract a grid with the same resolution (1 mm×1 mm×1 mm). This grid is used to solve the forward problem. The total head model consisted of 4499621 cubic voxels. However for solving the forward problem, the potentials were calculated in the nodes between the elements. The calculation grid of the AFDRM consisted of 4599754 nodes. By consequence, the system of linear equations, which had to be solved in section 2.4.2.8, had more than 4599754 equations with as many unknowns, as the calculation is done on the node points and not on the elements.

4.6.2 From diffusion tensor to conductivity tensor

The T1 MR (MPRAGE) images, which are used to construct the geometry of the human head, do not provide information about the direction of the nerve fibers in a voxel. Therefore we use diffusion weighted MR imaging to determine the direction of the nerve bundles in white matter. The DW-MRI image was made using a 2 mm ×2 mm ×2 mm grid. Therefore, the T1 MR (MPRAGE) image was coregistered with the DW-MRI. The T1 MR image was then interpolated to a cubic grid of 1 mm ×1 mm ×1 mm voxel size. From the diffusion weighted images one can estimate a diffusion tensor in each voxel of the white matter. By construction the tensor $\mathbf{D} \in \mathbb{R}^{3\times3}$ is symmetric, full rank. Therefore, it can be represented as an ellipsoid and can be written as:

$$\mathbf{D} \cdot \mathbf{v} = \Delta \cdot \mathbf{v}, \tag{4.3}$$

where $\mathbf{v} \in \mathbb{R}^{3\times3}$ is a matrix where each column, $\mathbf{v}_i$, is an eigenvector and form an orthonormal basis. $\Delta \in \mathbb{R}^{3\times3}$ is a diagonal matrix, where $d_i = (\Delta)_{ii}$ is the eigenvalue associated with eigenvector $\mathbf{v}_i$. $\mathbf{v}_i$ are the unitary vectors pointing in the direction of the principal axes and d_i are the magnitudes of the principal axes of the diffusion ellipsoid. To derive a diffusion tensor in each voxel of the 1 mm ×1 mm ×1 mm T1 MR image a linear interpolation of the neighboring matrix representations of the diffusion tensors was used.

Nicholson [105] determined the conductivity along a nerve bundle to be nine times larger than perpendicular to the bundle. In this case, the fractional anisotropy is 0.8715 and equal in every voxel. However, when we take a closer look to the FA, we can appreciate that the ratio is not a fixed but a variable value. The FA in an axial plane is plotted in figure 4.7. We can see that the anisotropic ratio is not constant over the axial slice. At the corpus callosum we can see a very large FA of on 0.7 to 0.9 average 8 - 10, which would indicate a strongly anisotropic diffusion is present. Indeed, the corpus callosum consists of a large number of nerves bundled parallel to each other. In other parts of the white matter, the bundles separate along different directions yielding a lower FA. When a nerve bundle exits the corpus callosum, the bundle splits up in two or more directions to the cortical areas. In this case, the diffusion is less prominent in one direction. The largest eigenvalue will decrease, while

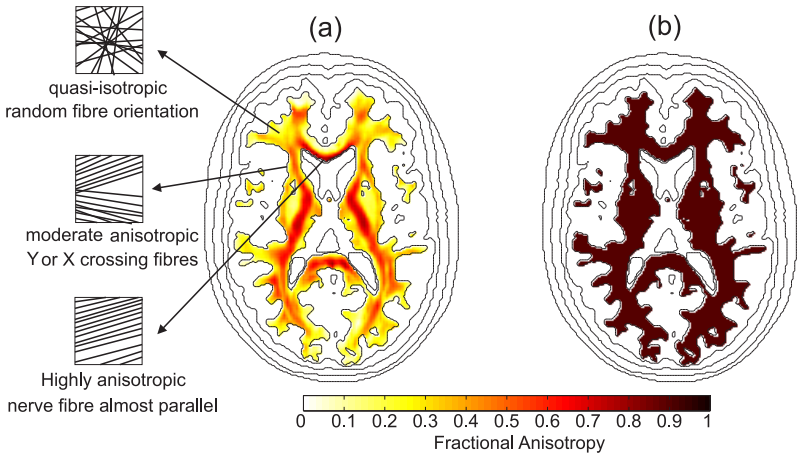

Figure 4.7: (a) The color coded fractional anisotropy (FA) in an axial slice. Black indicates a region of high FA (high anisotropy), white indicates a low FA (near isotropic). An illustration of three possible nerve bundle configurations is shown. The arrows indicate in which regions of anisotropic ratio they might occur. (b) The FA when the diffusion along the nerve bundle is nine times larger than perpendicular to the nerve bundle. In this case, the fractional anisotropy is equal at every white matter voxel.

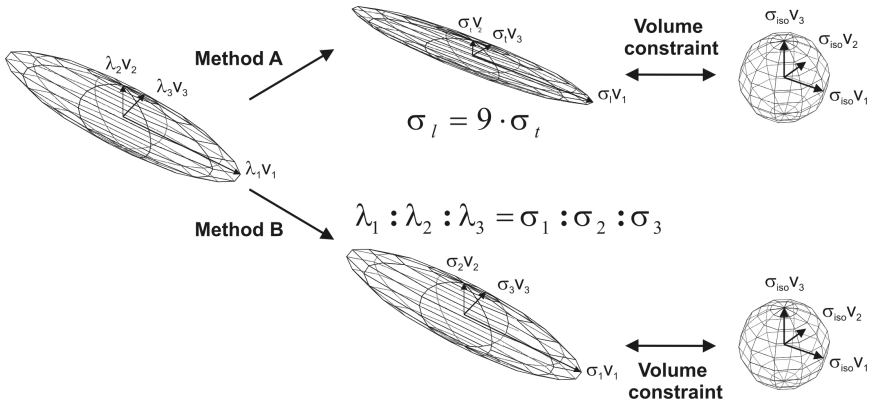

Figure 4.8: Schematic of the methods A and B. Method A shows the derivation of the conductivity tensor from the diffusion tensor when using a fixed anisotropic ratio of 9:1. The resulting ellipsoid is then related to the isotropic conductivity sphere using the volume constraint. Method B shows the linear relationship between the eigenvalues of the diffusion and conductivity ellipsoid. The resulting ellipsoid is identical to the diffusion ellipsoid up to an unknown scaling factor, which can be derived using the volume constraint with the isotropic conductivity sphere of white matter.

the other eigenvalues will increase in value. This translates into a less anisotropic diffusion tensor, as Wolters et al. [153] also have observed in their direct measurements. Near the gray matter, the nerve bundles split up again into smaller nerve bundles to make connections with local cortical gray matter areas. Moreover, cortical gray matter areas are connected to neighboring cortical gray matter areas. Therefore, the diffusion tensor shows almost equal diffusivity along 3 orthogonal directions. Hence, the tissue becomes almost isotropic ($FA \cong 0$).

4.6.3 The more realistic model A: proportional anisotropic ratio

Basser et al. [19] were the first to propose that the conductivity tensor and diffusion tensor might share eigenvectors . Sen and Torquato [135] described the relationship between a general transport tensor and the underlying microscopic structure of the medium using a perturbation expansion in the statistical correlations of the microstructure. The presented framework was applied for white matter anisotropy by Tuch et al. [139], Haueisen et al. [72] and Wolters [156].

In Tuch et al. [139] it was shown that the diffusion tensor was strongly linearly related to the conductivity tensor. A more thorough validation was done by Oh et al. [108]. This approach was also mentioned in studies in Wolters

et al. [150], Wolters [156]. Although, being different processes, diffusion and conductivity are governed by the same transport equations. Like the diffusion of water, carriers of charged particles will propagate preferably along the nerve fibers. We have shown above that the diffusion has a variable anisotropic ratio throughout the white and gray matter. Now, we assume that the same anisotropy will be valid for the conductivity tensor. There is a linear relationship between the conductivity tensor eigenvalues, σ_i, and the diffusion tensor eigenvalue, d_i, which can be written as:

$$\sigma_i = \frac{\sigma_e}{d_e} d_i, \tag{4.4}$$

where σ_e and d_e denote the extracellular conductivity and diffusivity [139]. This linear approximation of the relationship between the eigenvalues of the conductivity tensor and diffusion tensor assumes the intracellular conductivity to be negligible. Haueisen et al. [72] also used equation 4.4 to relate the conductivity and the diffusion tensor. Here σ_e/d_e was empirically defined as $0.736\, S{\cdot}s/mm^3$. Below, we will derive the scaling factor using the volume constraint. This constraint states that the volume of the ellipsoid derived from the conductivity tensor and the volume of the sphere derived from the isotropic conductivity tensor is equal. A more detailed explanation can be given in appendix B. Although, there is no physical theory behind it, for large resolution DWI, it is a model best suited for large resolution DW-MR images. Other models are more applicable to smaller resolution DW-MR images and have theoretical foundation (e.g. transport equation model in Tuch et al. [139])

Let $\mathbf{D} \in \mathbb{R}^{3\times 3}$ be the matrix representation of the diffusion tensor in a voxel belonging to white matter. We can decompose $\mathbf{D}$ into its eigenvalues according to equation 4.3. The linear relationship between the eigenvalues of the conductivity tensor and diffusion tensor in white matter can be expressed as:

$$\frac{d_1}{\sigma_1} = \frac{d_2}{\sigma_2} = \frac{d_3}{\sigma_3}, \tag{4.5}$$

where d_1, d_2 and d_3 are the eigenvalues of the matrix representation of the diffusion tensor at a voxel derived from the diffusion weighted images. $\sigma_1, \sigma_2, \sigma_3$ are the unknown eigenvalues of the matrix representation of the conductivity tensor at the same voxel. This system with 3 unknowns and 2 equations can be solved by applying the volume constraint (see appendix B) on the anisotropic conductivity ellipsoid using the isotropic conductivity sphere in white matter:

$$\frac{4}{3}\pi \left(\sigma_{isotropic}^{brain}\right)^3 = \frac{4}{3}\pi\sigma_1\sigma_2\sigma_3 \tag{4.6}$$

where $\sigma_1, \sigma_2, \sigma_3$ are the unknown eigenvalues of the conductivity tensor and $\sigma_{isotropic}^{brain}$ is the isotropic conductivity of brain tissue which was set to 16 times

larger than the isotropic skull conductivity. In our study, $\sigma_{isotropic}^{brain}$ is 0.33 S/m [44, 50].

4.6.4 The simplified model B: fixed anisotropic ratio

Nicholson [105] determined the conductivity along a nerve bundle to be nine times larger than perpendicular to the bundle. However, Wolters et al. [153] performed measurements of the maximal ratio of largest to smallest diffusion tensor eigenvalue, which was much lower than the ratio of 1:9. Therefore, they considered a wide range of anisotropic conductivity ratios for the white matter compartment and performed various simulations and visualizations to investigate the impact of white matter anisotropy. In our study, we used the anisotropic conductivity ratio of 1:9 (see figure 4.8 method A). Using the eigenvectors from the diffusion tensor in each voxel we can set the white matter to have an anisotropic conductivity. In a voxel belonging to white matter, the conductivity along the largest eigenvector σ_1 is set 9 times larger than the one along the perpendicular eigenvectors σ_2, σ_3:

$$\begin{aligned} \sigma_1 &= 9 \cdot \sigma_2, \\ \sigma_2 &= \sigma_3, \end{aligned} \tag{4.7}$$

where σ_1 is the conductivity along the largest eigenvector $\mathbf{v}_1$ of the diffusion tensor. σ_2 and σ_3 are the conductivity along the perpendicular eigenvectors $\mathbf{v}_2$ and $\mathbf{v}_3$, respectively. Equations 4.7 contain one remaining unknown which can be solved using the volume constraint (see appendix B):

$$\frac{4}{3}\pi(\sigma_{isotropic}^{brain})^3 = \frac{4}{3}\pi\sigma_1\sigma_2\sigma_3. \tag{4.8}$$

The isotropic conductivity $\sigma_{isotropic}^{brain}$ is set to $0.33 S/m$ as mentioned in the previous paragraph 4.6.3 [44, 50].

Both approaches, A and B, result in eigenvectors with conductivity values, indicating the conductivity along the direction of that eigenvector. If we define a local Cartesian basis with the axes along the eigenvectors, the tensor can be represented by a diagonal matrix. For solving the forward problem, the tensors have to be represented in the global Cartesian basis of the head model. This can be done by a rotation of the Cartesian tensor:

$$\mathbf{\Sigma} = \mathbf{T} \cdot \begin{bmatrix} \sigma_1 & 0 & 0 \\ 0 & \sigma_2 & 0 \\ 0 & 0 & \sigma_3 \end{bmatrix} \cdot \mathbf{T}', \tag{4.9}$$

where $\sigma_1, \sigma_2, \sigma_3$ are the conductivity eigenvalues and $\mathbf{T}$ is the rotation matrix composed by putting the eigenvectors in the columns.

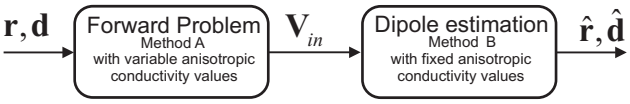

Figure 4.9: A flow chart of the simulation setup used to compare the more realistic approach A with the simplified approach B. First a dipole $(\mathbf{r}, \mathbf{d})$ is placed in a head model with variable anisotropic conductivity values (approach A) and the forward problem is solved. This results in a set of electrode potentials according to the forward model, V_{in}. This set of electrode potentials is then used to estimate the source in a head model where a fixed ratio for the anisotropic conductivity was assumed (approach B) by solving the inverse problem. This results in the estimated dipole parameters $\left(\hat{\mathbf{r}}, \hat{\mathbf{d}}\right)$.

4.7 Influence of different modeling approaches of the anisotropic conductivities of white matter

4.7.1 Aim of the study

In section 4.6, a realistic and a simplified approaches to model the anisotropic conductivity of the white matter are discussed. Due to using the simplified approach dipole estimation errors are made. In our opinion, the simplified approach is an overestimation of the anisotropic conductivity of the white matter, while the realistic approach takes into account the variable anisotropy throughout the white matter.

4.7.2 Simulation Setup

Dipole location and orientation errors are investigated when a simplified head model (model B) is assumed instead of a more realistic head model (model A). A similar methodology was followed in [144, 153, 53, 120]. Simulation studies were performed, which consisted of two steps (see figure 4.9).

First, one forward calculation was performed to obtain the electrode potentials, $\mathbf{V}_{in} \in \mathbb{R}^{m \times 1}$, caused by a dipole in the more realistic head model. The dipole was positioned at $\mathbf{r}$ and had the components $\mathbf{d}$, where $\mathbf{r}, \mathbf{d} \in \mathbb{R}^{3 \times 1}$:

$$\mathbf{V}_{in} = \mathbf{L}_{\mathbf{A}}(\mathbf{r}) \cdot \mathbf{d}. \tag{4.10}$$

where $\mathbf{L}_{\mathbf{A}}$ is the lead-field matrix in the more realistic head model (model A).

Next, from the electrode potentials $\mathbf{V}_{in}$, the dipole was estimated in the simplified head model. This was done by minimizing the following cost function:

$$RRE = \frac{\|\mathbf{V}_{in} - \mathbf{U}_{model}(\mathbf{r}, \mathbf{d})\|_2^2}{\|\mathbf{V}_{in}\|_2^2} + C(\mathbf{r}), \tag{4.11}$$

$\mathbf{U}_{model}$ is the set of electrode potentials caused by a dipole in the simplified head model:

$$\mathbf{U}_{model} = \mathbf{L}_{\mathbf{B}}(\mathbf{r}) \cdot \mathbf{d}, \tag{4.12}$$

where $\mathbf{L}_{\mathbf{B}}(\mathbf{r})$ is the lead-field matrix of the simplified head model (model B). Note that the dipole estimation process is an inverse problem in which the forward problem needs to be solved iteratively. This is contrary to the first step of the simulation, where only one forward calculation was done to obtain a set of electrode potentials. Moreover, the forward calculation was solved in a more realistic head model, whereas the forward calculations in the inverse problem are solved in a simplified head model. Thus the error due to the use of a simplified model during solving the inverse problem is investigated.

The starting point of the Nelder-Mead optimization was chosen to be the position $\mathbf{r}$ and the component $\mathbf{d}$ of the original dipole [116]. The set of dipole parameters, $\hat{\mathbf{r}}$ and $\hat{\mathbf{d}}$, which minimizes the cost function (see equation 4.11), are the estimated dipole parameters in the simplified head model.

We evaluate the dipole location error using the Euclidean distance between the original dipole location $\mathbf{r}$ and the estimated dipole location $\mathbf{d}$:

$$DLE = \|\hat{\mathbf{r}} - \mathbf{r}\|. \tag{4.13}$$

The angle between the vector components of the original dipole $\mathbf{d}$ and estimated dipole $\hat{\mathbf{d}}$ can be calculated by using the cosine rule:

$$\angle\left(\hat{\mathbf{d}}, \mathbf{d}\right) = \arccos\left(\frac{\hat{\mathbf{d}}^T\mathbf{d}}{\|\hat{\mathbf{d}}\|\,\|\mathbf{d}\|}\right), \tag{4.14}$$

where $\mathbf{d}^T$ means the transpose of vector $\mathbf{d}$.

4.7.3 Test dipoles

In the above simulation (see figure 4.9) the test dipole placed in the more realistic head model (model A) represents the actual source, while the resulting source parameters are the parameter estimates when a simplified head model (model B) is used. We want to evaluate the estimation errors (i) with respect to the location of the test dipole in the head model and (ii) with respect to the orientation of the dipole at a specific location.

Study I: Estimation errors with respect to the location of the test dipole.
The test dipoles were located in three planes: an axial, coronal and sagittal plane (see figure 4.3). In those 3 planes a uniform square grid was placed with distance of 1 mm between each node. The nodes of the square grid were chosen to be the locations of the dipole sources. Moreover, as brain activity can originate from gray matter only, only the nodes situated in the gray matter were considered. As a dipole can be decomposed into 3 orthogonal dipoles along the main axes, for each dipole location three orthogonal orientations were considered: along left-right (X orientation), along back-front (Y orientation) and along bottom-top (Z orientation). Note that the simulation is done for each test dipole at a time.

Due to the uniform grid the number of test dipoles was 23983. All of these were situated in gray matter, because brain activity which can be measured by the EEG can only originate from the gray matter. Moreover, the dipoles were placed in the cortical gray matter as well as in the gray matter of the deep structures. For each simulation the dipole location and orientation errors between the original test dipole and the estimated dipole were calculated.

Study II: Estimation errors with respect to the orientation of the test dipole. In this study, the location of the test dipoles was chosen at two specific sites. A first location $\mathbf{r}_1$ was chosen near the edge of the gray matter cortex, near a region of the white matter where the anisotropic ratio was low (AR was on average 1). A second location $\mathbf{r}_2$ was chosen in the gray matter near the center of the head model and near a region of the white matter where the anisotropic ratio was moderate (AR was on average 3). The location of the test dipole is indicated in figures 4.13 by a red star. The colors indicate the anisotropic ratio in the more realistic head model. The blue arrow in figure 4.13 indicates the principal direction (largest eigenvector) of the diffusion tensor in a voxel of the white matter. In the simplified approach, this direction is chosen to construct the conductivity tensor, which sets the conductivity along the largest eigenvector to be 9 times larger to the orthogonal eigenvectors. Thus in the simplified approach all the voxels of the white matter have an anisotropic ratio of 9.

The orientation of the test dipole at location $\mathbf{r}_1$ and $\mathbf{r}_2$ is chosen from a set of uniformly distributed orientations indicated by an azimuth (in radians) $\theta \in]-\pi, \pi]$ and an elevation (in radians) $\phi \in]-\pi/2, \pi/2]$. The magnitude of the dipole was chosen to be one, thus we have unitary dipole components. θ is the angle between the projection of the dipole component onto the axial plane and the left-right orientation. ϕ is the angle between the dipole component and the XY-plane. The total number of orientations for each location was 2456. In this way, we can visualize the dipole location error and orientation error in function of the orientation of the test dipole. Moreover, we can compare the errors with the orientation of the principal conductivity direction (largest eigenvector), as it is along this direction that the conductivity is overestimated when the simplified approach (or approach B) is used (the anisotropic ratio of

the conductivity in white matter is set to 9 but should be less).

4.7.4 Results

Study I:Estimation errors with respect to the location of the test dipole in the head model

Figure 4.10 shows the estimation error on the dipole location between the test dipoles and the estimated dipole. The error is depicted as a color code and ranges from 0 to 18 mm. We observe that the large errors (≥ 5 mm) occur near the center of the brain and also near the edges between white and gray matter. This is due to the fact that in these regions of interest a large anisotropic ratio was assumed (model A), while a more realistic lower anisotropic ratio (model B) was used to calculate the electrode potentials. A large error (≥ 10 mm) was also observed in the basal part of the brain. This is mainly due to the absence of electrodes in the basal part of the brain (cerebellum). From figure 4.12 we can appreciate that there is almost no error above 10 mm. A maximum error of 17.7 mm was found in gray matter regions.

Concerning the errors on the dipole orientation, we can appreciate from figure 4.11 that the errors with a large magnitude (≥ 30 degrees) are concentrated near the center of the brain and are mainly situated near white matter boundaries. For the similar reason of the location error, this is due to the fact that the electrode potentials are largely influenced by anisotropy when the test dipole is placed in a highly anisotropic conducting region. At the center of the brain we noted errors of over 60 degrees. From figure 4.12 we can see that on average 60 % of the errors in the orientation are above 10 degrees. The mean orientation error was 11.6 degrees. The maximum orientation error was 60.9 degrees.

Study II: Estimation errors with respect to the orientation of the test dipole.

Figure 4.13 shows the dipole location estimates as black dots for each orientation of the test dipole for the location $\mathbf{r}_1$ and $\mathbf{r}_2$, respectively. The locations of the test dipoles are shown as a red star. The arrows show the orientation of the largest eigenvector of the diffusion tensor of each white matter voxel. From figure 4.13a we can see that when the simulation was done for a test dipole at location $\mathbf{r}_1$ the estimated locations in the simplified head model is more situated toward the center. Whereas, when the simulation was done with a test dipole at location $\mathbf{r}_2$, the estimated locations are near the original test dipole location. We can also note that due to a different orientation of the original dipole, the estimated location is also different.

Figures 4.14 and 4.15 show the dipole location and orientation error in function of the azimuth and elevation of the dipole orientation when the study II was done at location $\mathbf{r}_1$ and $\mathbf{r}_2$ respectively. Note that the figures should be seen on the surface of a sphere and should be seen as an orientation distribution function of the dipole location and orientation error with respect to the orientation of the

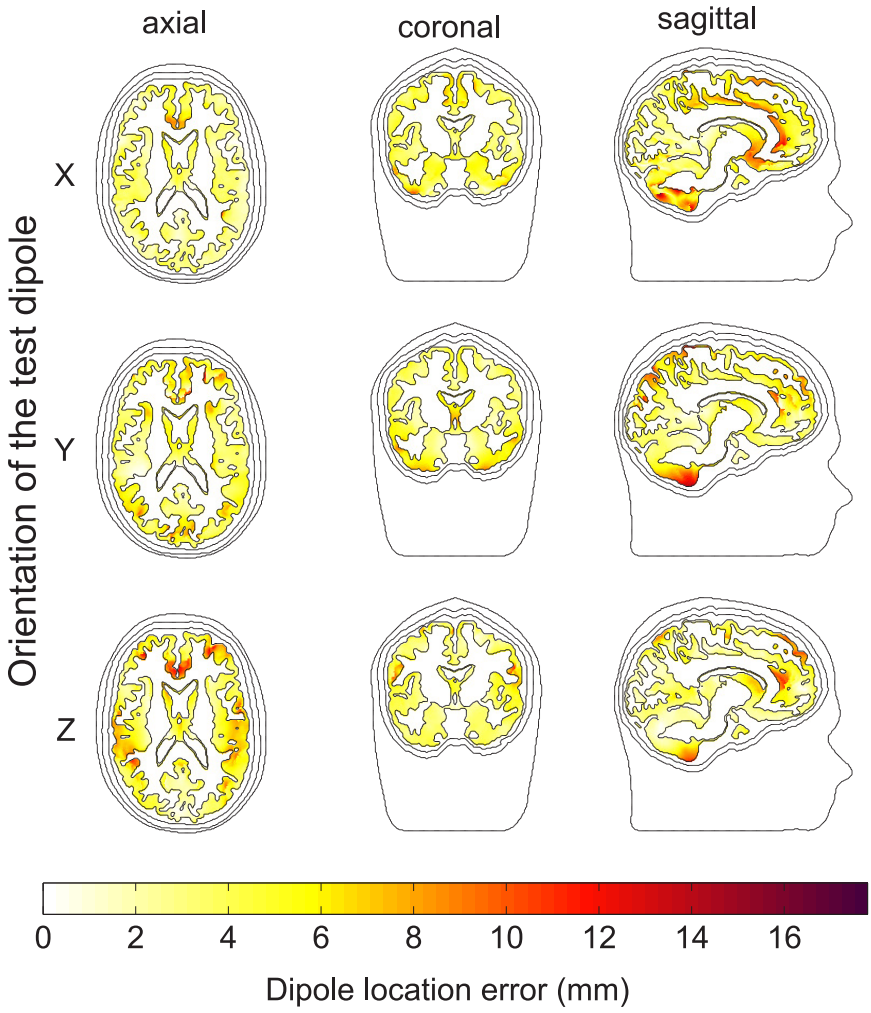

Figure 4.10: Dipole location errors when using a head model in the inverse problem where anisotropic conductivity was derived using method A while the electrode potentials were calculated in a head model where anisotropic conductivity was derived using method B. The range of the errors is given in the color bar below. The columns illustrate the axial, coronal and sagittal planes, respectively. The rows (a), (b) and (c) show the errors for the test dipoles oriented along the X-, Y-, and Z-direction, respectively.

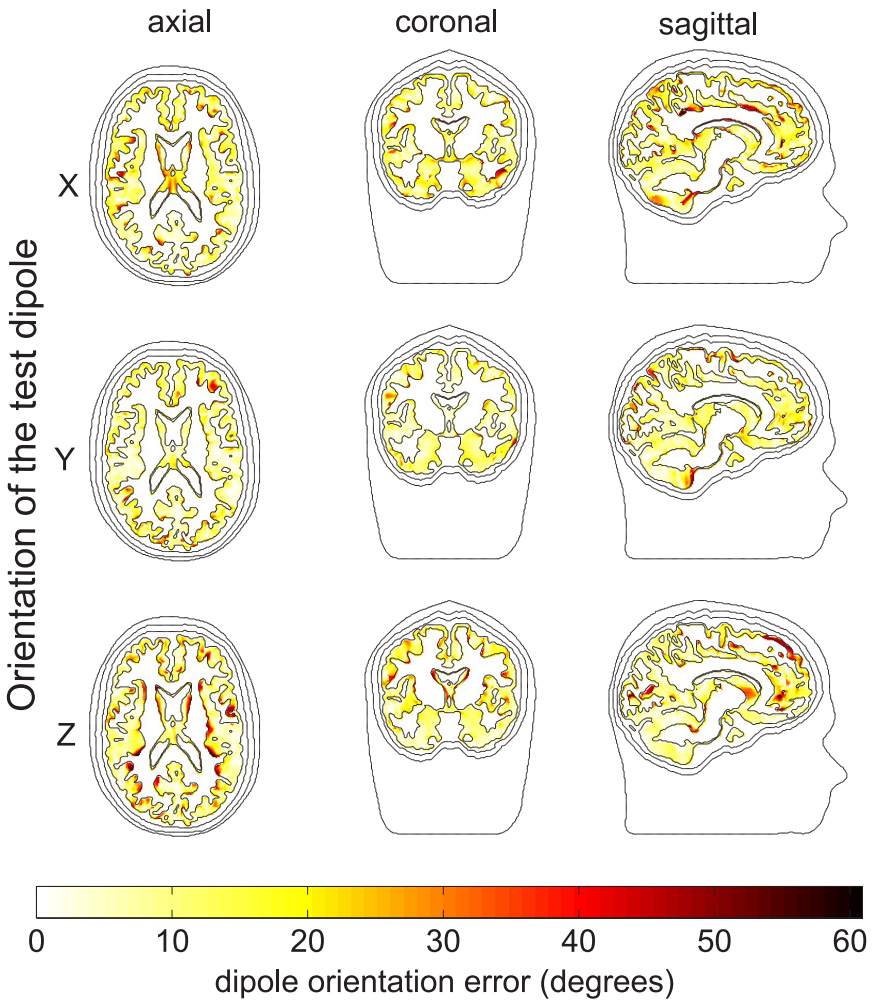

Figure 4.11: Dipole orientation errors when using a head model in the inverse problem where anisotropic conductivity was derived using method A while the electrode potentials were calculated in a head model where anisotropic conductivity was derived using method B. The range of the error is given in the color bar below. The columns illustrate the axial, coronal and sagittal planes, respectively. The rows (a), (b) and (c) show the errors for the test dipoles oriented along the X-, Y-, and Z-direction, respectively.

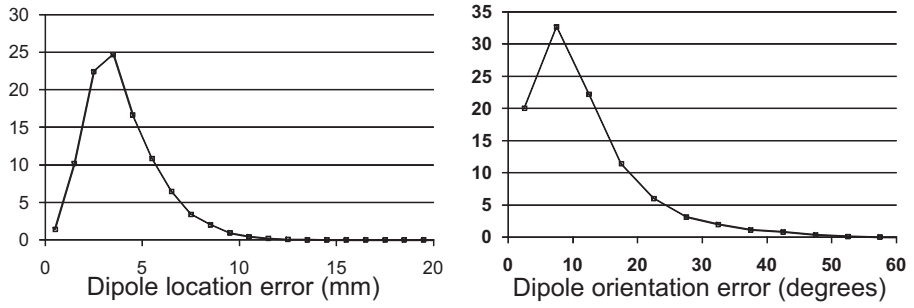

Figure 4.12: Histogram of the dipole location (a) and orientation (b) errors for all test dipoles found in the simulations described in section 4.7.2. The X-axes depicts (a) the dipole location error in mm and (b) the dipole orientation error in degrees (°). The bin sizes were 1 mm and 5 degrees (°) respectively.

test dipole. The black dots are the azimuth and elevation of the orientation of the anisotropy of nearby white matter voxels. The orientation of the anisotropy was calculated as the orientation of the largest eigenvector. Moreover, a pattern is visible that is repetitive and symmetric. For example, in figure 4.14 the location error is large when the azimuth is $\theta = 0$ and the elevation $\phi = \pi/4$. At the other side of the sphere ($\theta = \pi$ and $\phi = -\pi/4$) we also note the large errors.

4.7.5 Discussion and Conclusion

The results of this study show that using the simplified model (model B) instead of the more realistic model (model A) for the anisotropic conductivity profile of the white matter, introduces dipole location and orientation errors in the EEG inverse problem. The dipole location errors due to using a different model are moderate (≤ 10 mm), however the dipole orientation errors are considerable. It was already known that the anisotropic conductivity of the skull had a large influence on the potentials, calculated by the forward problem [153, 96]. Haueisen et al. stated the importance of white matter anisotropy [72], with regard to the dipole magnitude and orientation. The results from our study suggest that an accurate modeling is required for accurate source estimation.

We also found that a highly anisotropic white matter, surrounding a dipole source, has a big effect on the solution of the forward problem. In more detail we see in figure 4.11 that the large errors (red or black colored regions) are associated with simulations where test dipoles were placed in a moderate anisotropic region (AR=3 near gray matter boundary) and the forward problem was calculated using model A. Afterward, the electrode potentials were used

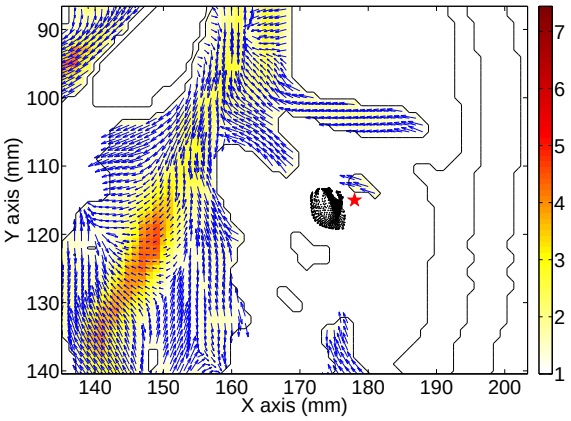

(a)

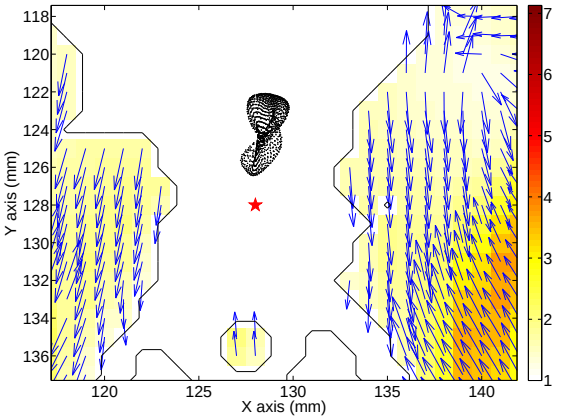

(b)

Figure 4.13: Test dipole location and dipole location estimations when the simulation was done for test dipoles at location (a) $\mathbf{r}_1$ and (b) $\mathbf{r}_2$ and the components of the test dipoles were chosen from a set of components uniformely distributed from a sphere around the dipole location. The red star in both figures denote the original dipole location. The location of the dipole estimates are indicated by black dots. The voxels of the white matter are coloured according to the fractional anisotropy and the blue arrow indicates the largest eigenvector of the tensor of that voxel.

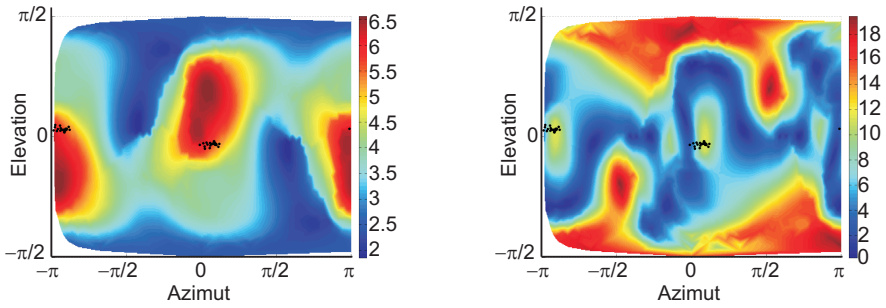

(a) (b)

Figure 4.14: The location error (a) and orientation error (b) as a function of the dipole orientation represented by a azimuth and elevation when simulation II was performed with a source at the cortex of teh brain ($\mathbf{r}_1$). The azimuth is ranged in radians from $-\pi$ to π and the elevation from $-\pi/2$ to $\pi/2$. The color code denotes the location error and orientation error. The black dots denote the orientation of the anisotropy in the nearest white matter voxels.

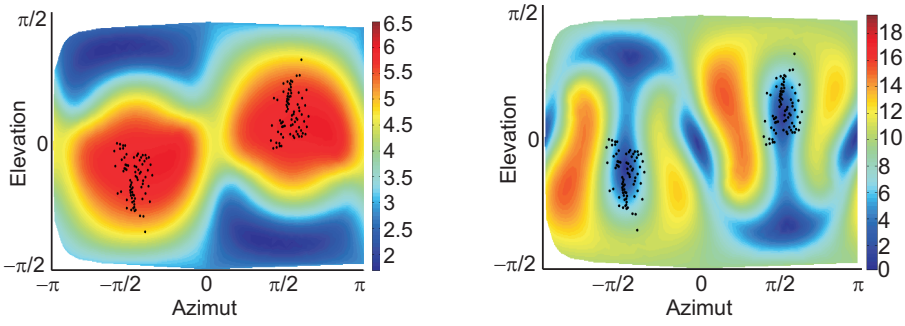

(a) (b)

Figure 4.15: The location error (a) and orientation error (b) as a function of the dipole orientation represented by a azimuth and elevation when simulation II was performed with a source near the center of the brain ($\mathbf{r}_2$). The azimuth is ranged in radians from $-\pi$ to π and the elevation from $-\pi/2$ to $\pi/2$. The color code denotes the location error and orientation error. The black dots denote the orientation of the anisotropy in the nearest white matter voxels.

to estimate the dipole in a head model where, according to model B, the anisotropy of the region was fixed to a high anisotropic ratio (AR=9). Similar results were observed in Güllmar et al. [53]. There a relative difference measure was used to quantify discrepancies in the forward solution in a rabbit head model.

From figures 4.13, 4.14 and 4.15 we can see that when the dipole is estimated in the simplified head model, the estimates are displaced in the direction of the anisotropy when the orientation of the test dipoles is situated along the orientation of the anisotropy. In other words, the dipole location errors are mainly large when the orientation of the test dipoles are similar to the orientation of the anisotropy in the nearby white matter voxels. On the contrary, the orientation error is small when the orientation of the test dipole is similar to the orientation of the anisotropy in the neighboring white matter voxels. Thus it seems that the location and orientation error is dependent on the orientation of the test dipole relative to the orientation of the anisotropy. Similar studies did observe the effect of anisotropic material on the dipole reconstruction, but did not see a dependence of the test dipole orientation relative to the orientation of the anisotropy. These studies only considered dipoles to be in 3 orthogonal directions [53]. Moreover, performing study II for a reasonable amount of possible locations and orientations would be very time consuming.

From figure 4.15b we can see that the orientation error is very small when the orientation of the test dipole is similar to the orientation of the anisotropy (angle difference is approximately 0° or 180°). In addition, the error is very small when the orientation of the test dipole and the orientation of the anisotropy is approximately perpendicular (angle difference is approximately 90°). A similar study with magnetic measurements came to similar results [92]. They suggested that at these orientations of the test dipole relative to the orientation of the anisotropy, the electrical field becomes rotational invariant around the direction of the anisotropy. However, these findings cannot be seen in figure 4.14a or b. Therefore, more similar studies on the influence of the dipole location and orientation in the near vicinity of the anisotropic white matter will be more thoroughly investigated in the future.

4.8 Influence of the anisotropic conductivities of gray matter

4.8.1 Aim of the study

Diffusion weighted images are used to quantify the anisotropy in white matter. The use of noise suppression techniques and the 60 directions provides us a reliable estimate of the diffusion tensor in each voxel. However, these diffusion images also provide an indication of anisotropic ratio in the gray matter region.

Therefore, using the model explained in 4.6.2 an anisotropic conductivity tensor can be derived in gray matter regions.

The rationale behind this study is that due to misclassification during the segmentation or partial volume effects, white matter voxels are assigned to the gray matter compartment. However, these white matter voxels can contain highly anisotropic conductivity, but are set to isotropic, assuming the gray matter has an isotropic conductivity. In figure 4.16 we can see the FA as a color code. In the figure, the color ranged from 0 till 0.5 to visualize where the gray matter has a high FA. Mostly the FA is very low (~ 1), which means that gray matter is mostly isotropic. However, near the boundaries between white and gray matter compartments, some voxels have a high FA but are assigned to the gray matter. Near the corpus callosum, there are voxels that are assigned to gray matter due to the partial volume effect, but that have a reasonably high anisotropic ratio.

4.8.2 Simulation setup

The construction of the head model was similar as explained in the previous study (see 4.7). However, the voxels that were assigned to the gray matter compartment could be set to having an anisotropic conductivity which was derived from the diffusion weighted images. The absolute value of anisotropic conductivities was calculated using the volume constraint (see appendix B). The isotropic gray matter conductivity in the volume constraint was set to $0,33$ S/m. The skull and white matter had an anisotropic conductivity according to section 4.5 and 4.6. A more simplified head model was also constructed with the same geometry and conductivities, except for the gray matter conductivity that was set to having an isotropic conductivity. The isotropic conductivity of the gray matter was again set to $0,33$ S/m.

The forward problem is calculated using the AFDRM method where anisotropic conductivities can be incorporated according to the realistic approach discussed in 4.6.2. In an XY-, YZ- and XZ-plane, we placed 3 dipoles (along the X-, Y- and Z-axis) in each voxel belonging to the white and gray matter of the brain. For each dipole the forward problem was solved in a head model with anisotropically conducting skull, white and gray matter compartments. This resulted in a set of electrode potentials.

The electrode potentials were then used to solve the inverse problem in a head model where the conductivity of gray matter was set to be isotropic. The obtained estimate of the dipole location $\hat{\mathbf{r}}$ and orientation $\hat{\mathbf{d}}$ was used to evaluate the dipole location error (or location shift) and orientation error due to not incorporating the anisotropic conductivities of gray matter. By taking the Euclidean distance between the estimated dipole and the original dipole, the dipole localization error due to neglecting the anisotropic conductivity of gray matter was investigated. The angle between the estimated and original dipole, denotes the dipole orientation error due to not taking into account anisotropic

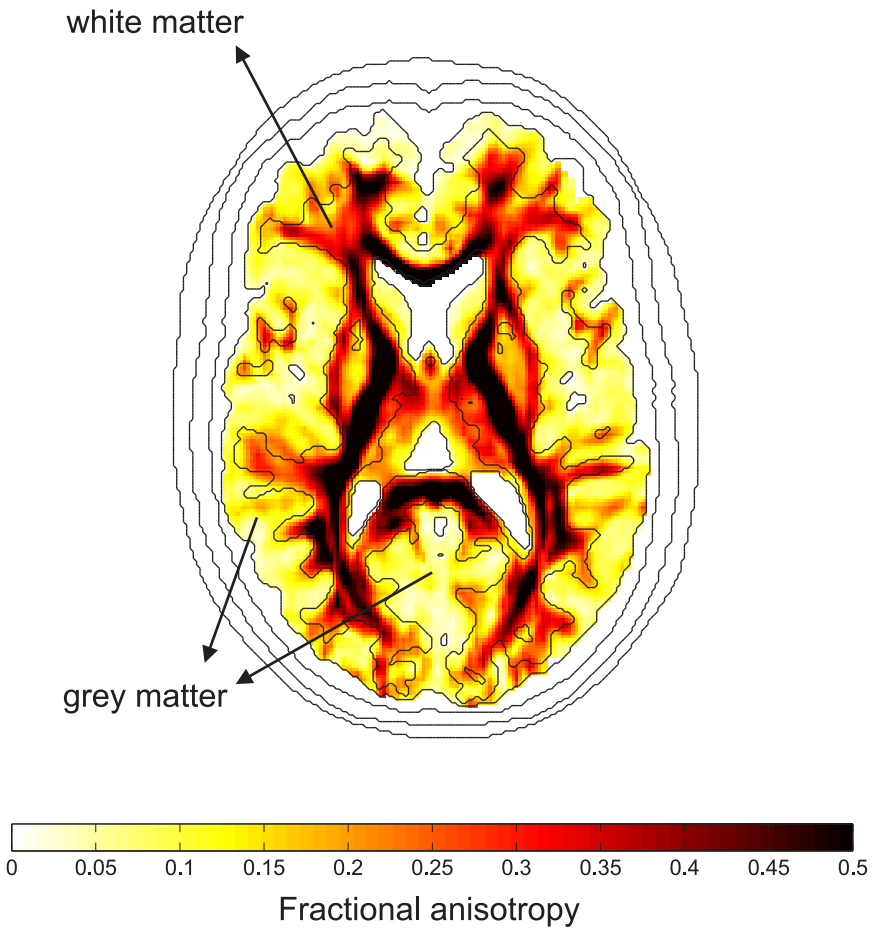

Figure 4.16: The anisotropic ratio as a color code of the white and gray matter. The black lines denote the interfaces between scalp, skull, CSF, white and gray matter. The color code was ranged from an FA till 0.5 for the sake of visibility. We can see that there is in some gray matter regions an anisotropic conductivity tensor can be defined, although the FA is not high.

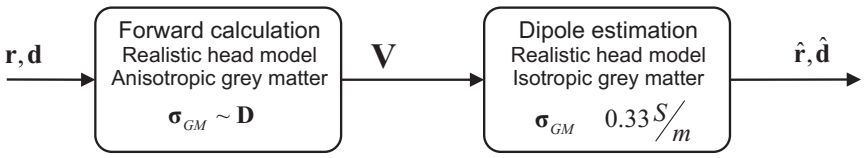

Figure 4.17: A flow chart of the simulation setup. A dipole with location **r** and moment **d** is used to for one forward calculation in a head model with anisotropic gray matter. The resulting electrode potentials are then used to estimate the source in an head model with gray matter anisotropic.

gray matter anisotropy. A schematic of the simulation setup is shown in figure 4.17.

4.8.3 Results

Figure 4.18 and 4.19 show the dipole location error and orientation error, respectively. The dipole location error ranged between 0 and 10 mm, approximately. Table 4.1 summarizes the average, standard deviation, maximum and minimum errors for not incorporating gray matter anisotropy. From the table we can see that the dipole location error is very small. The largest error was found at the bottom part of the cerebellum. However, these large errors can be due to the absence of the electrode coverage, i.e. poor spatial sampling of the electrodes in the bottom part of the head. Indeed, the voxels of the bottom part of the cerebellum were lower inferior then the most inferior electrode. These errors will increase the mean error. Thus, this suggests that neglecting the anisotropy of gray matter does not have a large influence on the dipole location.

The dipole orientation error was ranged between 0 and 40 degrees. In the gray matter, the largest errors was found were at those regions where the anisotropic ratio in the anisotropic head model of the forward calculation was large. Indeed, the incorporation of the anisotropic conductivity changes the potential field caused by a dipole in such a region very locally. This local change in the potential field also affects the global potential field measured at the surface of the scalp. This will be explained in the next chapter.

4.8.4 Discussion and conclusions

Using DW-MRI, we can define a anisotropic conductivity tensor in voxels belonging to gray matter. Furthermore, voxels with a high anisotropic ratio which can originate from the white matter, can be assigned to the gray matter due to segmentation errors or partial volume effects. In this study we determined the dipole estimation error due to not incorporating the anisotropic conductivity

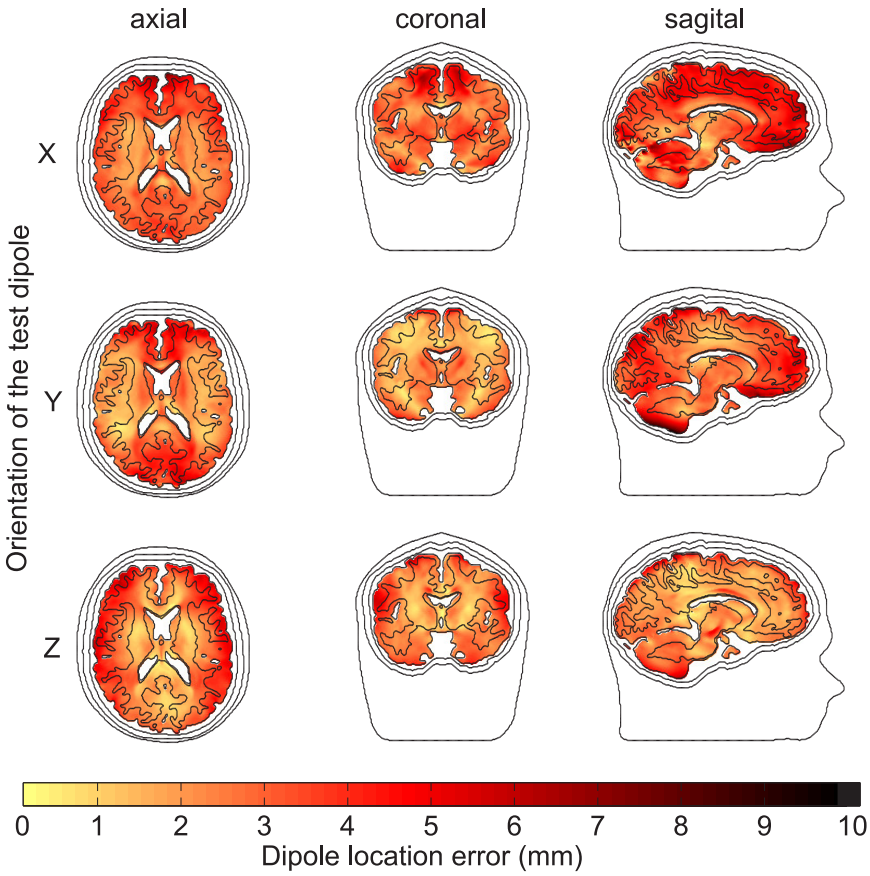

Figure 4.18: The dipole location error due to not incorporating anisotropic conductivities of gray matter. A axial, coronal and sagittal plane is shown in the columns. Each row depicts an orientation of the test dipole. The location error ranged from 0 to on average 10 mm. The largest error was found at the bottom of the brain, below the cerebellum.

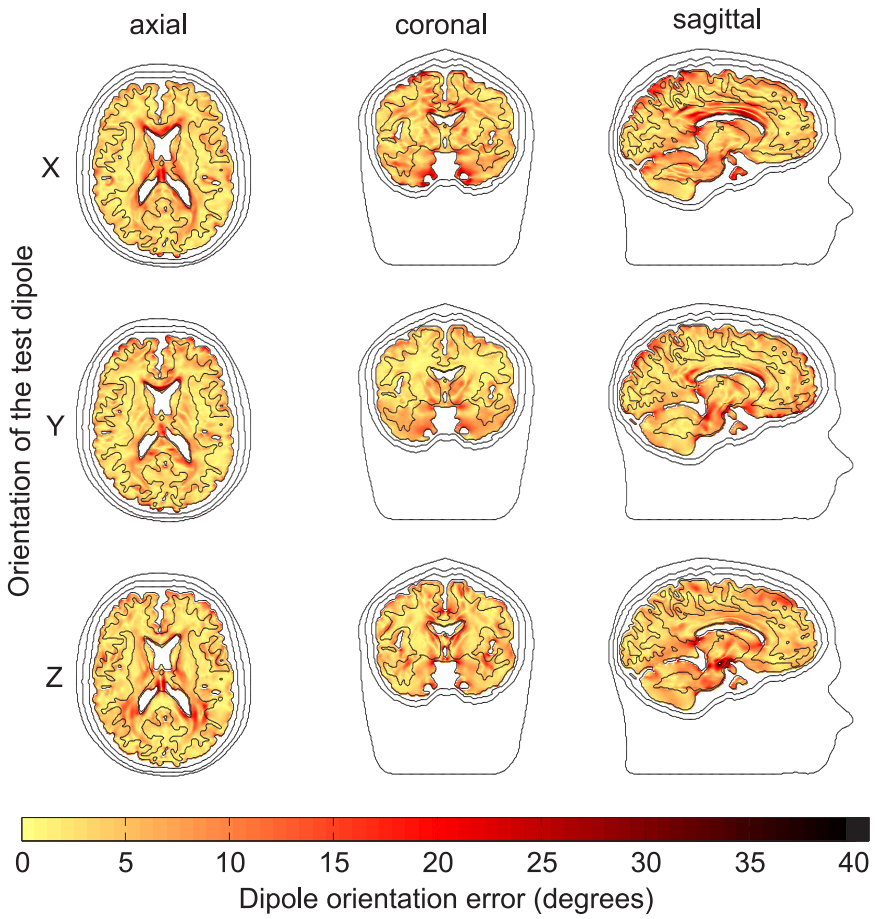

Figure 4.19: The dipole orientation error due to not incorporating anisotropic conductivities of gray matter. A axial, coronal and sagittal plane is shown in the columns. Each row depicts an orientation of the test dipole. The error ranged from 0 to 40 degrees. The largest errors in the gray matter were found at regions where the anisotropic ratio was high, but an isotropic conductivity was assumed in the dipole estimation.

location of the test dipole	mean	standard deviation	maximum	minimum
Dipole location error (mm)				
gray matter	2.9202	1.2037	9.6441	0.1062
White matter	2.6101	1.0675	8.7640	0.1307
total	2.7879	1.1578	9.6441	0.1062
Dipole orientation error (degrees)				
gray matter	5.0683	3.7919	34.4631	0.0000
White matter	4.9368	3.6392	40.2443	0.0197
total	5.0122	3.7281	40.2443	0.0000

Table 4.1: The dipole location (in mm) and orientation error (in degrees) due to not incorporating the anisotropic conductivities of gray matter. The columns in both tables indicate (from left to right) the average, standard deviation, maximum and minimum value of the dipole location and orientation error, respectively. The rows indicate the set of test dipoles according to their location: the test dipole located at the gray matter, white matter or both (indicated as total).

of gray matter. The mean dipole location errors and orientation errors are low: 2.7 mm and 5.01 degrees, respectively. However, we can notice large errors in the dipole location near the edges of the brain. The orientation error was very large at regions where a high anisotropic ratio was neglected. Examples of these regions are interfaces between the corpus callosum and the CSF.

4.9 Summary and contributions

In this chapter we discussed a formalism to incorporate an anisotropic conductivity profile into the skull and white matter compartment. Magnetic resonance images and diffusion weighted magnetic resonance images can be used to derive the anisotropic properties of the skull and white matter compartment. This approach enables us to model many tissue types. Using segmented T1 MR images and DW-MR image we can construct a head model with anisotropic conductivities which we can use in the EEG source analysis.

However, we found that the modeling of the white matter is an important factor in the EEG source estimation procedure. Two approaches to derive the conductivity tensors were discussed: a realistic one and a more simplified one. The simplified approach states that the conductivity along the largest principal direction is 9 times larger than the principal directions orthogonal to it. The realistic approach states that the principal directions of the diffusion tensor and the conductivity are the same, while preserving the ratios between the diffusion and conductivity along each principal direction. By using the simplified approach instead of the realistic one dipole estimation errors are made. We found that the dipole location error was large ($\geq$ 5 mm)at gray matter regions

at the center of the brain and near the edges of white and gray matter. Indeed, near those places the simplified approach causes an overestimation of the anisotropy compared with the realistic approach. The mean location error was approximately $4,0$ mm with a maximum of 17.7 mm.

Large orientation errors were found in the gray matter regions at the center of the brain and near the interfaces with the white matter compartment. Again, this is due to the fact that the electrode potentials are largely influenced by anisotropy when the test dipole is placed in or near a highly anisotropic conducting region. At the center of the brain we noted errors of over 60 degrees. On average 60 % of the errors in the orientation are above 10 degrees. The mean orientation error was 11.6 degrees. The maximum orientation error was $60,9$ degrees. The closer the dipole source is to a region with a large difference in FA, the larger the dipole estimation errors.

Therefore, a qualitative study was done to investigate the influence of the dipole orientation of the test dipole on using the simplified approach in the source estimation. Depending on the orientation errors from approximately 2 to 7 mm were found. Moreover, we found that the location error is larger if the test dipole is oriented along the largest principal direction of the nearest white matter voxels. Thus it seems that the location and orientation is dependent on the orientation of the test dipole relative to the orientation of the anisotropy using the simplified approach.

The results from this study and from Güllmar et al. show that a local characterization of the anisotropy is crucial for the accuracy of the forward problem [53]. Indeed, putting the anisotropic ratio of white matter to the same fixed ratio within that compartment will result in inaccuracies in the forward solution and thus also in the inverse problem. Characterizing the anisotropic conductivity tensor at the voxel level is required for accurate source localization.

In the second half of this chapter, we discussed the influence of not incorporating anisotropic conductivities in gray matter. Using DW-MRI, a conductivity tensor can also be derived in voxels belonging to gray matter. Although these regions have a very low anisotropic ratio ($FA \sim 0.1$), we wanted to investigate whether the anisotropic ratio of these gray matter voxels can be neglected. Due to segmentation errors or partial volume effects, voxels with a larger FA (e.g. white matter structures) can be assigned to be in the gray matter compartment. This mainly happens near the boundaries of the white matter. The mean dipole location errors and orientation errors are low: 2.7 mm and 5.01 degrees, respectively. However, we can notice large errors in the dipole location near the edges of the brain. The orientation error was very large at regions with a large FA, as in these regions the anisotropic conductivities was neglected. Examples of these regions are interfaces between the corpus callosum and the CSF.

This work resulted in an A1 publication [70] and an A2 publication [68] in the context of an international conference where an oral presentation was given.

Chapter 5

Dipole estimation errors due to neglecting anisotropic conductivities in EEG source analysis

There are sadistic scientists who hurry to hunt down errors instead of establishing the truth
—Marie Curie

5.1 Introduction

In the previous chapters we saw how anisotropic conductivities can be incorporated in realistic head models. Nowadays, isotropic head models are often used. In reality the skull and brain tissues are anisotropic conducting. In this chapter, we want to investigate the influence of neglecting these anisotropic conductivities of the skull and brain tissue compartments on the dipole estimation.

In a first part, we will investigate the effect of neglecting anisotropic conductivities on the dipole estimation. This is done by simulation studies where compartments are set to isotropic, knowing that the electrode potentials are derived from an anisotropic head.

In a second part, we will investigate what happens to the electrode potentials at the scalp surface for anisotropically conducting compartments. In this way, we want to learn more about the physics behind the influence of anisotropically conducting compartments.

In section 2.5 possible causes of dipole estimation errors were discussed. In the third part of this chapter we will focus on the estimation error due to neglecting anisotropy in the presence of noise. In this case, we combine two types of error: (i) a systematical error due to neglecting anisotropy and (ii) a random error due to noise. In a first simulation, the effect of neglecting anisotropic conductivities will be discussed. There we will compare the errors made by neglecting the anisotropic conductivity properties of several brain tissues. In a second simulation, the systematical error of the anisotropic conductivities and the random error due to noise will be investigated. In this case, we want to determine to which level of noise the incorporation of anisotropic conductivities can make EEG source localization more accurate.

5.2 Dipole location and orientation errors due to neglecting anisotropic conductivities in skull and brain tissues

In this study we want to determine the dipole location and orientation error due to not incorporating the anisotropic conductivities of the skull and/or brain compartment. In reality the electrode potentials are generated by sources in the brain and the skull and brain tissues (more specific the white matter) are anisotropic. If we want to estimate the source in a head model with isotropic conductivities a location and an orientation error occurs. By determining these errors we want to investigate the error we make if assume the head model to be isotropic.

Brain matter and skull have an anisotropic conductivity. We can use the geometrical properties of the skull to determine the normal and tangential direction in each cubic element of the skull compartment. The normal direction is the direction perpendicular to the skull surface. The tangential direction is the direction along the skull. DW-MR imaging can be used to determine the anisotropic conductivity of the soft tissues of the brain. These anisotropic properties can be used to construct the head model. The AFDRM is used to solve the forward problem in the head model which is introduced in 2.4.2.6.3 and 3.3.4.

5.2.1 Simulation setup

The construction of the head model was done in a similar way as in chapter 4, but we briefly repeat it in the following.

5.2.1.1 Construction of the head model

The head model consists of compartments which are derived from segmenting the T1 MR image. A DW-MRI image was also performed and the T1 MR

image was coregistered with the DW-MRI image. The T1 MR image was measured using an MPRAGE sequence in a 3 Tesla Siemens Trio MR scanner and had a dimension of 128 by 128 by 104 consisting of voxels of 2 mm $\times$2 mm $\times$2 mm. The image was resized and zero padded to have voxels of 1 mm $\times$1 mm $\times$1 mm with a dimension of 255 by 255 by 255. From this image the segmentation was preformed using SPM5 [47]. The diffusion tensors were also linearly interpolated to an 3D array of 255 by 255 by 255, so that each voxel of the resized image contained one diffusion tensor.

In this simulation we constructed 4 head models. A summary of the anisotropic properties is given in table 5.1.

5.2.1.2 Incorporating anisotropic conductivities

In this paragraph the determination of the anisotropic conductivities of the skull and brain tissues is given. This is a brief summary of the methodology followed in chapter 4. In the head model we can incorporate two types of anisotropy: skull and brain tissues. Hence we can construct 4 head models by making combinations of the conductivity anisotropy given by table 5.1.

Anisotropic conductivities of the skull

From the segmented T1 MR images the skull compartment was made by a dilation of the brain and the CSF compartment. The dilation was made so that the average thickness of the skull was about 6 mm. In each voxel of the skull the normal, $\mathbf{n}$ and two tangential directions, $\mathbf{t}_1$ and $\mathbf{t}_2$, were derived. Then the conductivity along the skull was set 10 times larger than the normal direction. Using the volume constraint, the absolute values of the conductivity along $\mathbf{n}$,$\mathbf{t}_1$ and $\mathbf{t}_2$ are calculated. An explanation and the derivation of the values of these conductivities are given in appendix B. The matrix representation of the conductivity tensor $\mathbf{\Sigma}_{skull}$ with respect to the basis ($\mathbf{n}$,$\mathbf{t}_1$,$\mathbf{t}_2$) becomes:

$$\mathbf{\Sigma}'_{skull} = \begin{bmatrix} \sigma_n & 0 & 0 \\ 0 & \sigma_t & 0 \\ 0 & 0 & \sigma_t \end{bmatrix}. \tag{5.1}$$

Model	Scalp	Skull	CSF	White matter	Gray matter
1	I	A	I	A	A
2	I	A	I	I	I
3	I	I	I	A	A
4	I	I	I	I	I

Table 5.1: Summarization of the conductivity parameters of the head models used in the simulations."I" and "A" denote the compartment was set to have an isotropic or anisotropic conductivity, respectively.

where σ_n,σ_t and σ_t is the conductivity along the directions given by the unitary vectors $\mathbf{n}$,$\mathbf{t}_1$ and $\mathbf{t}_2$ respectively. The matrix representation of the conductivity tensor is then transformed to the basis of the head model by:

$$\mathbf{\Sigma} = \mathbf{T} \cdot \begin{bmatrix} \sigma_n & 0 & 0 \\ 0 & \sigma_t & 0 \\ 0 & 0 & \sigma_t \end{bmatrix} \cdot \mathbf{T}', \tag{5.2}$$

where σ_n, σ_t are the conductivity eigenvalues and $\mathbf{T}$ is the rotation matrix composed by putting the vectors $\mathbf{n}$,$\mathbf{t}_1$ and $\mathbf{t}_2$ in the columns. Here, $\sigma_n = 0.004309\ S/m$ and $\sigma_t = 10 \cdot \sigma_n = 0.04309\ S/m$.

Anisotropic conductivities of brain tissues (white and gray matter)

We derived the conductivity tensor in each voxel of the white and gray matter using the realistic approach given in section 4.6.3 in chapter 4. The realistic approach assumes that the conductivity tensor and diffusion tensor share the same principal direction (or eigenvectors of the matrix representation). The linear relationship between the eigenvalues of the conductivity tensor and diffusion tensor in white matter is expressed as:

$$\frac{d_1}{\sigma_1} = \frac{d_2}{\sigma_2} = \frac{d_3}{\sigma_3}, \tag{5.3}$$

where d_1, d_2 and d_3 are the eigenvalues of the matrix representation of the diffusion tensor at a voxel derived from the diffusion weighted images. $\sigma_1, \sigma_2, \sigma_3$ are the unknown eigenvalues of the matrix representation of the conductivity tensor at the same voxel. We can see that the conductivity tensor is merely a scaling of the diffusion tensor. The scaling factor is derived using the volume constraint as explained in 4.6.3 and appendix B.

5.2.1.3 Simulation

We want to investigate the dipole estimation errors due to not taking into account the conductivity of skull and brain tissues. Therefore, we constructed 3 anisotropic head models, model i, each one with a lead-field matrix $\mathbf{L}^i_{anisotropic}$, with $i \in 1, 2, 3$. Furthermore, an isotropic head model (model 4) with a lead-field matrix $\mathbf{L}^4_{isotropic}$ was constructed where all the compartments had isotropic conductivities. To investigate how large the error on the dipole location and/or orientation due to using a more simplified head model, one has to compare head models.

The comparison can be done by following a simulation according to figure 5.1. We can do this by first setting a dipole in the more complex head model (e.g. with anisotropic conductivity) and solve the forward problem. We obtain the electrode potentials $\mathbf{V}_{electrodes} \in \mathbb{R}^{m \times 1}$ caused by a dipole with location $\mathbf{r}$ and

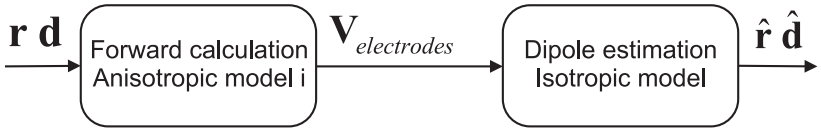

Figure 5.1: A flowchart of the simulation. A dipole is put in an head model according to model i with $i = 1, \ldots, 3$, given in table 5.1 and one forward calculation was done. The resulting electrode potentials are then used to estimate the dipole parameters in an isotropic head model (model 4 in table 5.1). This way, we estimate the source in a simplified head model, when the electrode potentials are obtained by a more realistic one.

components $\mathbf{d}$ with $\mathbf{r}, \mathbf{d} \in \mathbb{R}^{3\times 1}$:

$$\mathbf{V}_{electrodes} = \mathbf{L}^{i}_{anisotropic}(\mathbf{r}) \cdot \mathbf{d}. \tag{5.4}$$

where $\mathbf{L}^{i}_{anisotropic}$ is the lead-field matrix of a head model (referred below as model i and $i = 1, \ldots, 3$) where one or more compartments have anisotropic conductivities. As brain activity can neurophysiological speaking only occur in gray matter, we only considered the test dipole to be in gray matter.

Using these electrode potentials $\mathbf{V}_{electrodes}$, we can estimate a dipole in a head model where all compartments have isotropic conductivity by solving the inverse problem. The starting point of the Nelder-Mead optimization was chosen to be the same as the test dipole. In our experience the cost function was smooth enough to obtain a global optimum. Estimating a single dipolar source results in a simple cost function which is smooth in the vicinity of the original test dipole. We obtain an estimate of the dipole location $\hat{\mathbf{r}}$ and components $\hat{\mathbf{d}}$, which is different from the original dipole location $\mathbf{r}$ and components $\mathbf{d}$ due to the simplified head model. In this way, we can investigate the dipole estimation error due to changes of head model parameters. Table 5.2 summarizes the simulations performed in this section.

Simulation	Forward Calculation	Inverse problem
A	Model 1	Model 4
B	Model 2	Model 4
C	Model 3	Model 4

Table 5.2: Summarization of the simulations performed in this section. The head models used in the forward calculation and the inverse problem have an anisotropic conductivity according to table 5.1

Simulation A: Dipole estimation errors due to omitting anisotropic conductivity from the skull and brain tissue (white and gray matter)

In a first simulation we want to investigate the dipole localization errors when the skull and brain tissue (white and gray matter) compartments are assumed

to be isotropic conducting. First, we simulated the electrode potentials originated a dipole source in an anisotropic head model where the skull and brain tissue compartments were set to have an anisotropic conductivity. In other words, $V_{electrode}$ are calculated by solving the forward problem in head model 1 in table 5.1. We used the resulting set of electrode potentials to estimate the source in an isotropic head model, where the skull and brain tissues were isotropic conducting. Here, the inverse problem is solved in an isotropic head (model 4 in table 5.1) given $V_{electrodes}$. The result is an estimate of the dipole location $\hat{\mathbf{r}}$ and orientation $\hat{\mathbf{d}}$. In this way, we can investigate the dipole localization error due to neglecting the anisotropic properties of the conductivity in a realistic head model.

Simulation B: Dipole estimation errors due to omitting anisotropic conductivity from the skull

In a second simulation, we use the same setting as the first one, but in the forward calculation we used an anisotropic head model where only the skull compartment was set to have an anisotropic conductivity (head model 2 in table 5.1). The inverse problem was solved using an isotropic head model (head model 4 in table 5.1). Using this setup, the dipole location and orientation error can be evaluated due to neglecting only the anisotropic properties of the conductivity of the skull compartment.

Simulation C: Dipole estimation errors due to omitting anisotropic conductivity of brain tissues (white and gray matter)

A third simulation was performed to calculate the dipole location and orientation errors due to neglecting the anisotropic conductivity properties of brain tissues. The compartments belonging to brain tissues are white and gray matter. Therefore, a head model with only the white matter and gray matter compartment set to anisotropic conducting, was used in the forward calculation (Model 3 in 5.1). The calculated electrode potentials were then used in the inverse problem with an isotropic head model (Model 4 in table 5.1).

5.2.1.4 Test dipoles and error measures

Each simulation summarized in table 5.2 are repeated for a set of test dipoles constructed as follows: three planes (coronal, sagittal and axial) were chosen. The locations of the test dipoles were set in each voxel of the gray matter region. Moreover, three orientations were considered: X direction (left-right), Y direction (front-back) and the Z direction (bottom-top). Hence, nine sets of dipoles were constructed according to a plane and an orientation. The total number of dipoles was 23983.

Each test dipole at a position $\mathbf{r}$ with orientation $\mathbf{d}$ was subjected to the simulations. This resulted in an estimated dipole at location $\hat{\mathbf{r}}$ with orientation $\hat{\mathbf{d}}$. Due to neglecting anisotropy a location and orientation error is made. The dipole location error (DLE) is the Euclidean distance between the location of

the estimated dipole and the one of the test dipole. The orientation error (DOE) is the angle between the orientation of the estimated dipole and the one of the original test dipole:

$$DLE = \|\mathbf{r} - \hat{\mathbf{r}}\|, \tag{5.5}$$

$$DOE = \angle(\mathbf{d}, \hat{\mathbf{d}}). \tag{5.6}$$

5.2.2 Results

Simulation A: Dipole estimation errors due to omitting anisotropic conductivity from the skull and brain tissue (white and gray matter)

Dipole location errors due to setting the conductivity to isotropic instead of anisotropic of different compartments are shown in figure 5.2(a). In figure 5.2(a) we see the dipole location error as a color coded map when both the skull and brain tissues (white and gray matter) are not taken into account. The error is very large ($\geq$ 2 cm) near the boundary of the brain tissues. Figures 5.3 shows the distribution of the dipole localization for test dipoles placed in gray matter. The total of the dipole localization errors from all planes and each with the original dipole along a main axis was ranged in bins of 1 mm width. We can see that the distribution has a symmetrical shape around 10 mm. In the gray matter regions, the average dipole location error was 10.0 mm. This discrepancy is mainly due to the fact that the dipole localization at the edge of the brain compartment is larger and the gray matter regions are mainly situated at the boundary of the brain. An maximum error of more than 25 mm is observed in the lower part of the cerebellum, mainly due to the lack of electrodes in the basal part of the brain.

The dipole orientation errors due to omitting anisotropic conductivity from the skull and brain tissue is shown in figure 5.4(a). We can see large errors ($\geq$ 30 degrees) at the fasciculi and the corpus callosum, which would indicate a large influence of the anisotropic conductivities on the orientation when the source originates in high anisotropic regions. A large error is also seen at the basal part of the brain, mainly due to the lack of electrodes at the basal part of the brain. Figures 5.5 show the distribution of the orientation errors from all test dipoles. Here we can see that 80% or more of the orientation errors are below 10 degrees. In fact, the average orientation error due to neglecting skull and brain tissue anisotropy is $6,4$ degrees. A maximum error was found of $61,9$ degrees.

Simulation B: Dipole localization errors due to omitting anisotropic conductivity of the skull compartment

Figure 5.2(b) shows the dipole location error when only the skull compartment is set to isotropic conductivities in stead of anisotropic conductivities. We see similar errors if skull and brain tissues were neglected: the simulations with test dipoles situated at the edge of the brain resulted in larger location errors.

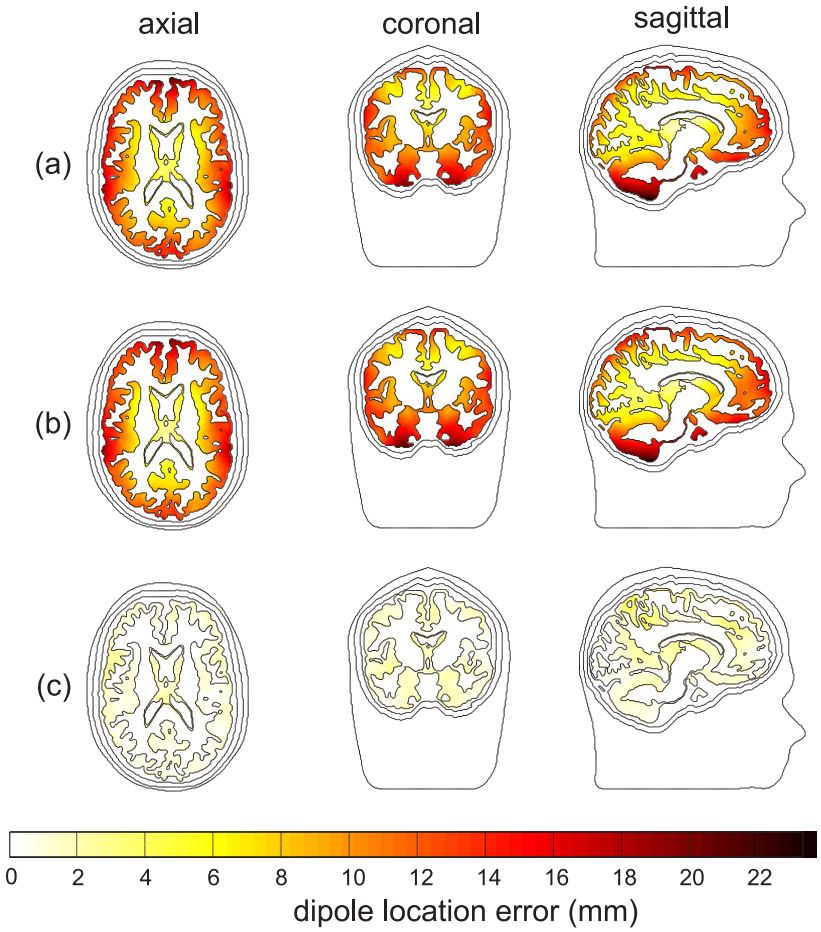

Figure 5.2: Dipole location errors when the (a) skull and white matter compartments, (b) skull compartment only and (c) white and gray matter compartments are set to isotropic gray matter compartment is set to isotropic in an axial, coronal and sagital plane.

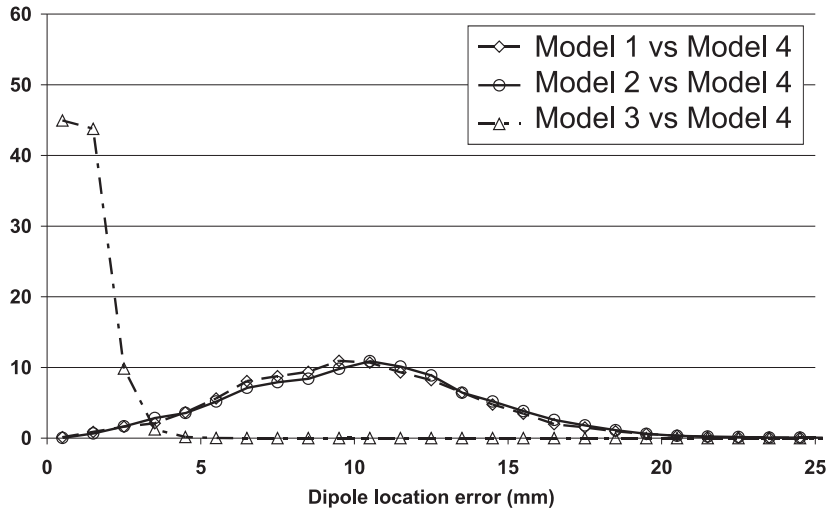

Figure 5.3: Histogram of the dipole location error when model 1,2 or 3 is used to solve the one-time forward calculation and model 4 (isotropic head model) is used to solve the inverse problem.

From figure 5.3(a) and (b) we can appreciate that the errors have a similar distribution as the results from previous simulation. The mean location error was 10.2 mm. A maximum error of 35 mm was found at the basal part, due to lack of electrode positions at the lower half of the head model.

With respect to the dipole orientation, large estimation errors were seen (≥ 30 degrees) at the corpus callosum and other neural pathways, where the anisotropic ratio was high. These errors are in accordance with the previous simulation. Also here, the large part of the dipole orientation errors are below 10 degrees as seen in figure 5.5.

Simulation C: Dipole localization errors due to omitting anisotropic conductivity of the brain compartment

From figure 5.2(c) we can see that the dipole location error is much lower, than the previous simulations. Moreover, it is difficult to determine where the large errors are situated. For test dipoles situated in white and gray matter compartments the dipole location error is mostly below 5 mm (see figure 5.3(a) and (b)). A mean error was found of 1.1 mm and the maximum error was approximately 8.4 mm. The large errors were situated at the corpus callosum and other parts, where the anisotropic conductivity ratio was high. The regions were assumed to be isotropic conducting in the source estimation procedure.

The dipole orientation errors had similar proportions than those of the previous simulations. Most test dipoles had a orientation error of less then 10 degrees (see figure 5.5). The mean orientation error was $3,6$ degrees. However, a maximum orientation error was found over 40 degrees in regions that are highly

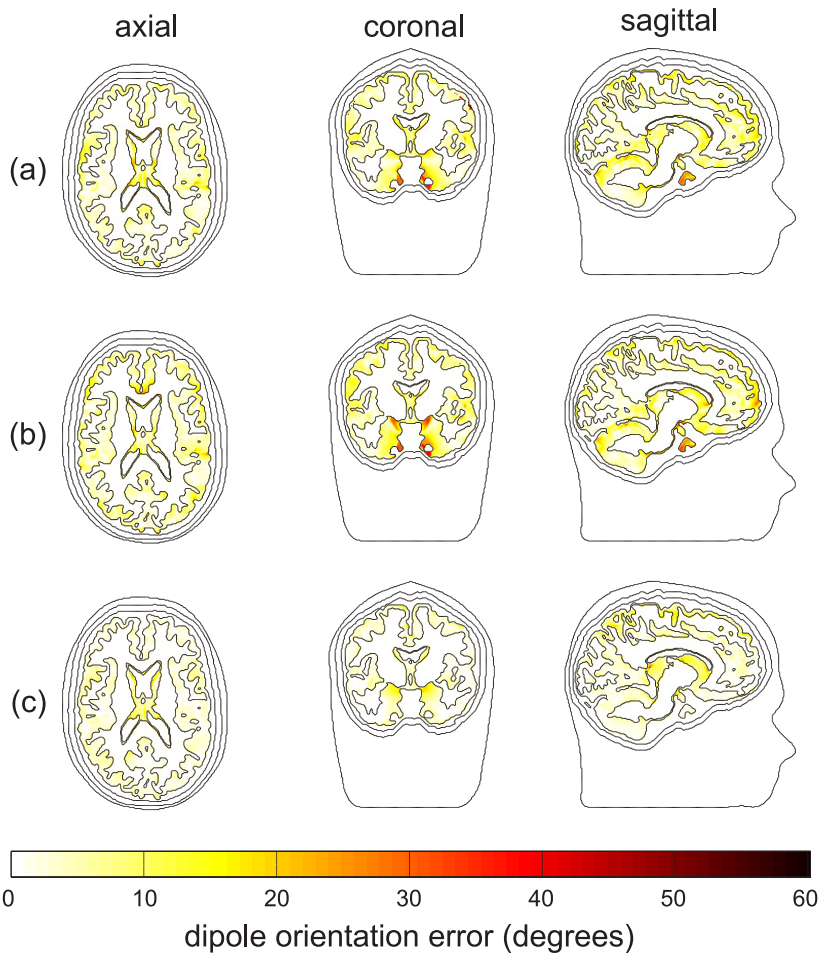

Figure 5.4: Dipole orientation errors when the (a) skull and white matter compartments, (b) skull compartment only and (c) white and gray matter compartments are set to isotropic gray matter compartment is set to isotropic in an axial, coronal and sagittal plane.

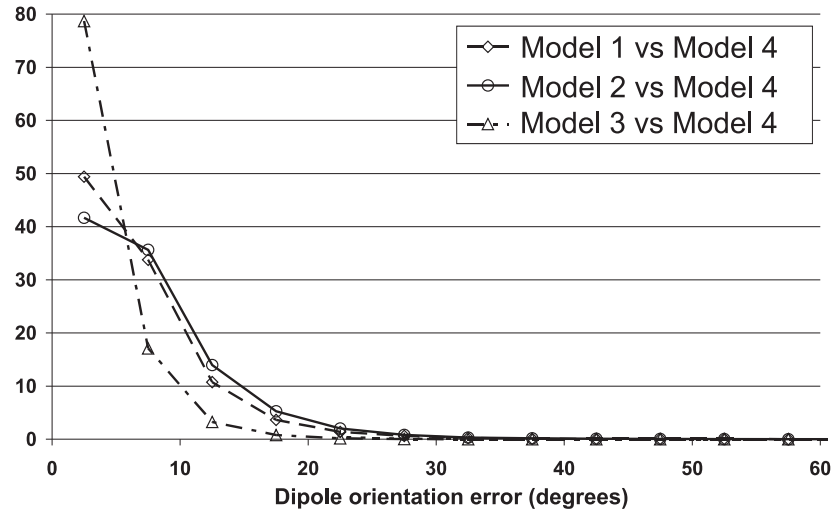

Figure 5.5: Histogram of the dipole location error when model 1,2 or 3 is used to solve the one-time forward calculation and model 4 (isotropic head model) is used to solve the inverse problem.

anisotropic.

5.2.3 Discussion

The results suggest that the anisotropic conductivity of the skull plays an important role in EEG source analysis. Not incorporating the anisotropic conductivities of the skull results in errors of on average 10 mm and in worst case an error of 25 mm. These results are in concordance with results found in the literature. However, most studies investigate the effect on the forward problem [153, 53, 72]. Few studies are performed in which the dipole is estimated by solving the inverse problem in an isotropic head model, knowing that the given electrode potentials are generated from an anisotropic head model, as was done here [156, 96, 3]. In Haueisen et al. [72] it was found that small superficial sources would lead to small errors. However, this study was done using only 7 dipoles positioned at various depths on a specific region of the brain. An investigation over the whole brain was not done. Moreover, the skull was not modeled as an anisotropic conductor, but as a layered conductor, where each layer was isotropic.

In Wolters et al. [153] and Güllmar et al. [53] it was concluded that a high anisotropic region had a large effect on forward problem. The deeper a source lies, the more it is surrounded by anisotropic tissue, the larger the influence of the anisotropy on the resulting electric field. Therefore, the presence of anisotropic conducting tissues compromises the forward potential computation. By consequence, it has a large effect on the inverse problem [153]. However, they

used a high anisotropic ratio (AR=10) to model their white matter anisotropy. In our case, the white matter is modeled according to in our opinion a more realistic approach given in section 4.6. There it was also stated that the AR in large parts of the white matter is approximately 2, which is much lower than 10.

5.3 Influence of anisotropic conductivities on the forward problem: a qualitative analysis

In the previous part, we can notice the location errors and orientation errors due to neglecting the anisotropic conductivities of skull and brain tissues. In this section, we will try to find an explanation of these errors. Therefore, two sources, both placed in the gray matter, are depicted and the forward problem is solved in each head model as given in table 5.1. The sources were placed (i) in the gray matter in the fronto-temporal region and (ii) in the cingular cortex.

Due to a change in conductivity properties of the compartments of the different models, the three-dimensional potential field caused by a dipole source will change. In this study we will investigate how neglecting the anisotropic properties of the skull and brain tissues will affect the potential field.

5.3.1 Simulation I: fronto-temporal source

Figure 5.6 shows the equipotential lines caused by a source in the fronto-temporal region. In panel (a) and (b) we see the potential field in head model 1 and 4 according to 5.1. In figure 5.6(a) we can notice the larger number of equipotential lines along the skull than in figure 5.6(b). This indicates a rapid decrease in the potential. Hence, an anisotropic skull has a more pronounced shielding effect than an isotropic skull.

Figures 5.7 shows the potential field caused by a dipolar source in the fronto-temporal region at the surface of the scalp (left column) and the brain (right column). The first and second row indicate the potential field in an anisotropic head model (model 1 in table 5.1) and an isotropic head model (model 4 in table 5.1). The third row indicates the difference of the potential field in an anisotropic head model and the isotropic head model. At the scalp, we can notice that the difference of the electrode potentials is of the same magnitude as the electrode potentials at the surface in both isotropic and anisotropic cases. This suggests that for a superficial dipolar source, the potential field is strongly influenced by the anisotropic conductivities. The smaller potential values at the surface of the scalp in the anisotropic head model as opposed to those in the isotropic head model suggests that the anisotropic conductivity acts as a shielding and smears the potential field. The potentials at consecutive

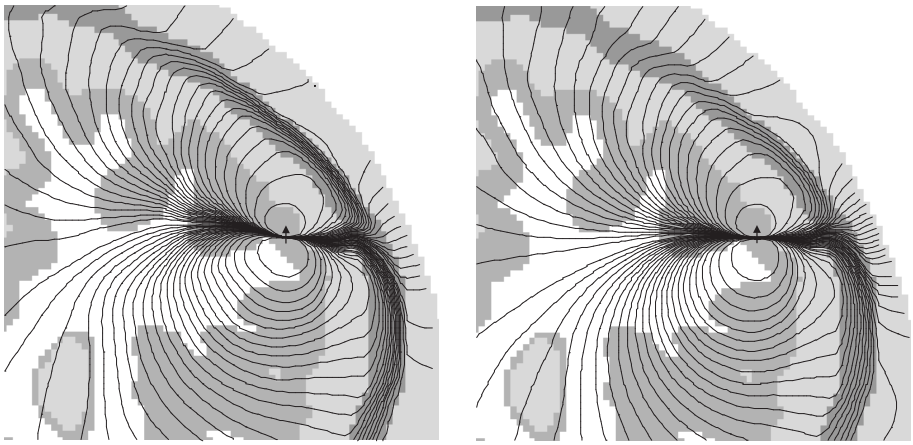

(a) (b)

Figure 5.6: The equipotential lines of the potential field caused by fronto-temporal dipole source along the Z axis. The Z axis is the vertical direction in the figure. The potential field was calculated in 2 realistic head models: (a) with skull and soft tissues anisotropic conducting and (b) with all compartments isotropic conducting. These head models correspond with head model 1 and 4 in table 5.1, respectively.

boundary points of the scalp (indicated by the dashed line in figure 5.7(a) and (c)) are shown as one dimensional signal in figure 5.8. In this figure, we can see that the normalized potentials at the boundary points are more smeared in the anisotropic head model (model 1) compared to the the isotropic head model (model 4). Due to this smearing the dipoles are estimated deeper if anisotropic conductivities are neglected.

At the surface of brain (second column in figure 5.7) we see that the difference is very local. The magnitude of the difference is a factor 10 lower than the electrode potentials at the surface of the brain. However, the local change in the potential field at the brain surface is smeared due to the anisotropic conductivities of the skull.

Hence, making the skull anisotropic causes an extra smearing and shielding effect. This causes a change in the topographies, which causes the dipole estimation errors when anisotropic conductivities in the EEG source analysis is not incorporated. The dipole estimate when neglecting the anisotropic conductivities can be determined in the same simulation setup as given in figure 5.1 and are shown in figure 5.9. We can see that when the anisotropic conductivities are neglected the dipole is estimated deeper than the actual dipole. The shift in the location and orientation due to neglecting anisotropic conductivities was 11.9 mm and 5.6 degrees.

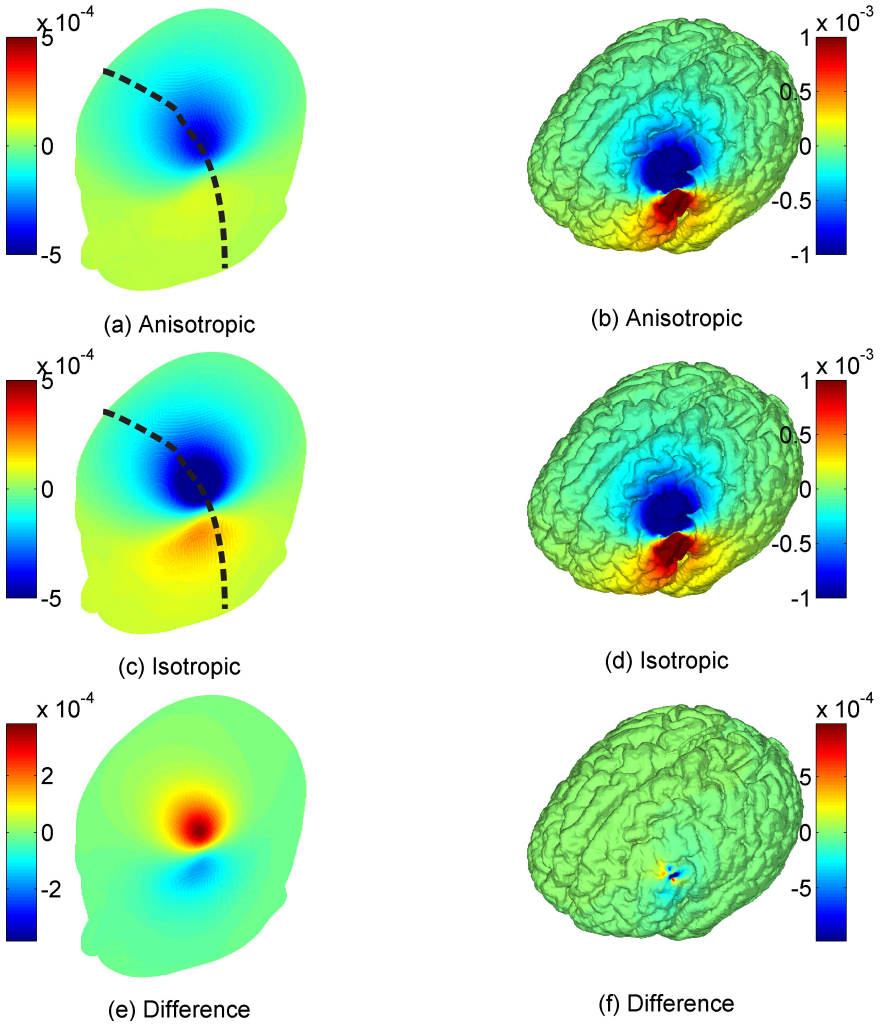

Figure 5.7: The potential distribution at the surface of the scalp (first column) and the brain (second column) due to a superficial fronto-temporal source. The values are in V.The dashed line in panel (a) and (c) indicate the potential measurement points at the boundary surface used in figure 5.8

5.3.2 Simulation II: Medial source in the cingular cortex

The second source was placed in the cingular cortex, near the corpus callosum, to see the effect of the highly anisotropic white matter on the potential field caused by a dipole. Similar conclusions can be drawn from the previous paragraph. Figure 5.10 shows the equipotential lines caused by a source in the cingular cortex. Also here we can notice the more pronounced shielding effect

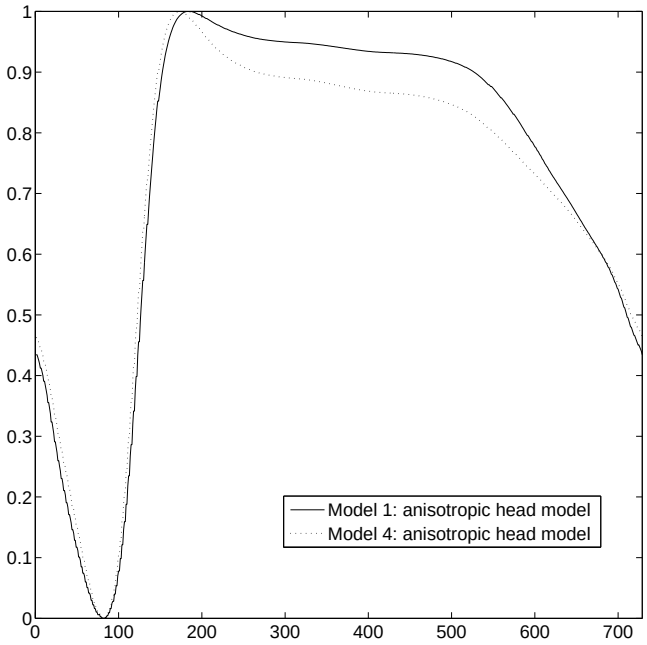

Figure 5.8: The normalized potential at consecutive measurement boundary nodes obtained by calculating the forward problem in model 1 (solid line) and model 4 (dashed line). These boundary surface points are also indicated in figure 5.7 by the dashed line in panel (a) and (c).

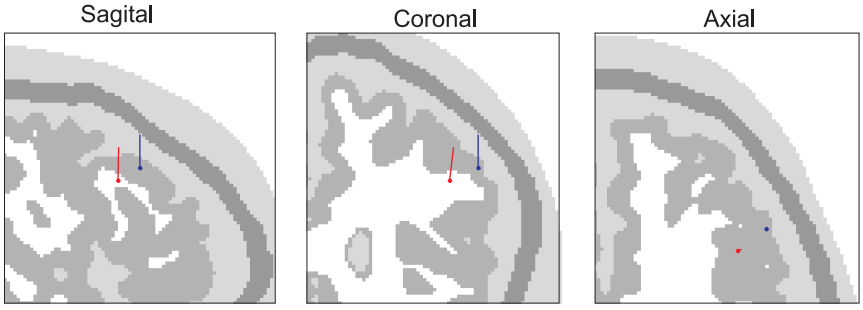

Figure 5.9: An sagital, axial and coronal slice of the original test dipole (blue) and the estimated dipole when anisotropic conductivities are neglected.

when the skull is modeled as an anisotropic conductor. The equipotential lines are very close to each other, indicating a steep potential fall in the skull.

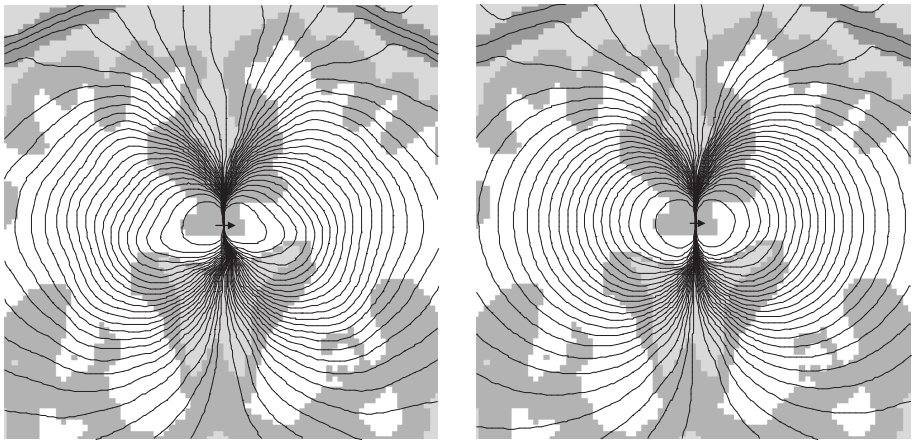

(a) (b)

Figure 5.10: The equipotential lines of the potential field caused by fronto-temporal dipole source along the Z axis. The Z axis is the vertical direction in the figure. The potential field was calculated in 2 realistic head models: (a) with skull and soft tissues anisotropical conducting and (b) with all compartments isotropic conducting. These head model correspond with headmodel 1 and 4 in table 5.1, respectively.

If we compare panels (a) and (b) in figure 5.6 we can see some changes in the potential field which are very pronounced near the dipolar source. Together with previous results, this suggest that the local potential field is considerably affected by the anisotropic conductivities. This can be beneficial for the study of stimulation in brain regions in the treatment for epilepsy or Parkinson's disease.

Figure 5.11 shows the potential distribution at the surface of the scalp (first column) and the brain (second column). The setup is explained in the previous section for figure 5.7. At the scalp the difference in the potential distribution (panel (e)) at the scalp is approximately a factor 2 smaller than the potential distribution at the scalp in the isotropic (figure 5.11(a)) and anisotropic head model (figure 5.11(b)). This suggests that a deeper source will have less effect at the surface of the scalp, although it has a large effect near the source as seen in figures 5.10.

In figure 5.12, the normalized potential is plotted for consecutive boundary nodes. A dipole in this region will create a similartopography in both anisotorpic or isotropic head models. Although the topographies at the scalp are attenuate, there is no smearing of the potential distribution. At this region, we expect the dipole estimation errors to be low, as the dipole estimation procedure is sensitive to a scaling of the electrode potentials, but rather sensitive to a change in topography. The shift in the location and orientation when anisotropic conductivities are neglected at the position in this simulation were

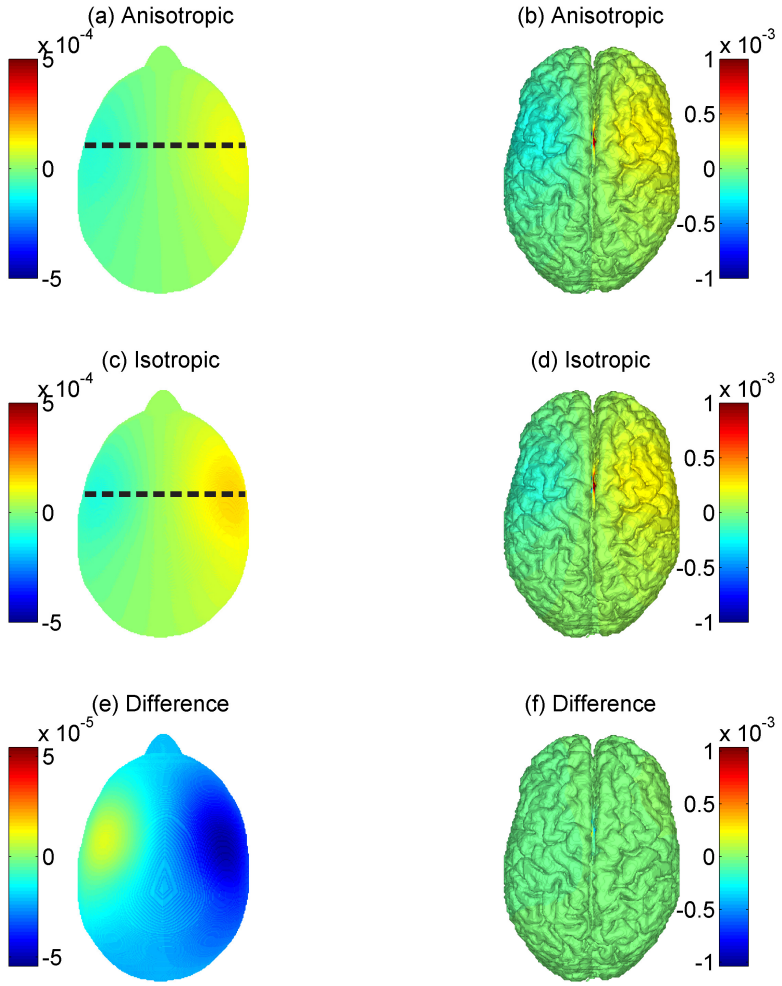

Figure 5.11: The potential distribution at the surface of the scalp (first column) and the brain (second column) due to a deep source at the cingular cortex. The values are in V. The dashed line in panel (a) and (c) indicate the potential measurement points at the boundary surface used in figure 5.12

very low.

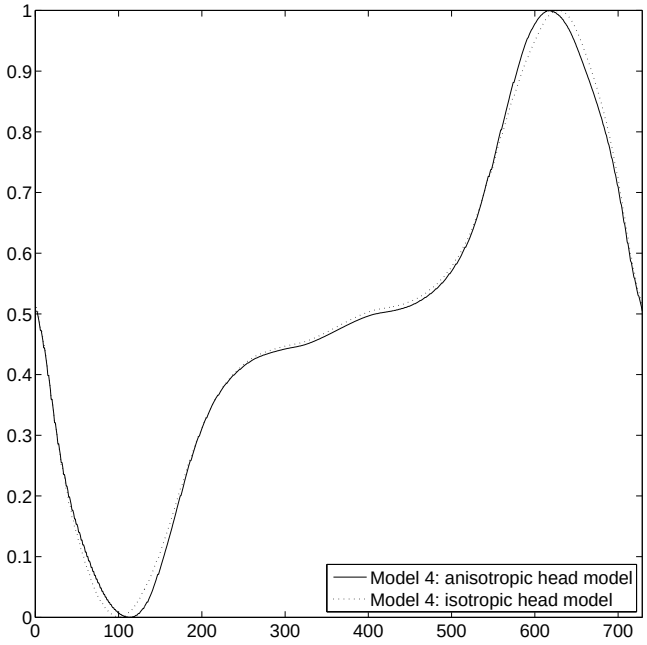

Figure 5.12: The normalized potential at consecutive measurement boundary nodes obtained by calculating the forward problem in model 1 (solid line) and model 4 (dashed line). These boundary surface points are also indicated in figure 5.11 by the dashed line in panel (a) and (c).

5.4 Dipole localization errors due to not incorporating anisotropic conductivities in the presence of noise

5.4.1 Aim of the study

Assume simulation are done according to figure 5.1 when the head model used in the dipole estimation and the forward calculation are the same. The dipole estimation error should be zero, as the head models are exactly the same and no additive noise is introduced to the electrode potentials. However, when noise is introduced in to the electrode potentials, the dipole estimation may deviate from its original position. This is an estimation error due to the noise. The additive noise can be quantified.

5.4.1.1 Noise level

The noise level gives an idea of the amount of noise that occurs in the EEG signal applied to perform EEG source analysis. The noise level can be written as:

$$nl = \frac{U^b_{RMS}}{U_{RMS}} \tag{5.7}$$

where U^b_{RMS} and U_{RMS} is the root-mean-square (RMS) value of the background EEG and the fragment of EEG applied to perform EEG source analysis, respectively. To have an idea of the signal contribution the RMS value U_{RMS} is calculated for the average referenced epoch of EEG, applied to solve the inverse problem. This epoch consists of s time samples and l electrode potentials. The RMS value becomes:

$$U_{RMS} = \sqrt{\frac{1}{l \cdot s} \sum_{j=1}^{s} \sum_{i=1}^{l} U^2_{ij}}, \tag{5.8}$$

where U_{ij} is the potential at electrode i and time sample j.

To have an idea of the noise contribution, we can calculate the RMS value of the average referenced EEG prior to the event we want to perform EEG source analysis on. The RMS vlue of the background EEG then becomes:

$$U^b_{RMS} = \sqrt{\frac{1}{l \cdot s} \sum_{j=1}^{s} \sum_{i=1}^{l} U^2_{ij,b}}, \tag{5.9}$$

where $U_{ij,b}$ is the potential at electrode i and time sample j in a typical epoch representing the background noise.

Depending on the neurological phenomenon on which we want to perform EEG source analysis, the noise level may vary. In chapter 6 the noise level is calculated for a fragment of real data, where an patient suffering from epilepsy is monitored. A patient suffering from epilepsy have a typical EEG, that consists of ictal events (during a epileptic seizure) and inter-ictal episodes. The interictal episodes contain so-called *spikes*, which are believed to occur from the same onset zone as the epileptic seizure originates. A video/EEG monitoring is done to investigate the patient in the clinical setup. Although the environment is built to minimize the noise contributors, the patient still has the possibility to move. In these circumstances, a noise level from 0.2 to 1 was measured from a EEG registration, where the spikes were marked by a experienced neurologist.

During event related tasks, the EEG can also be measured to investigate the brain functionality during a specific task (reading, visual interpretation,...). During these tests, the conditions are well defined and the experiment is performed inside a cage of Faraday to eliminate external noise contributions. Moreover, the test subject has to remain as still as possible. The task is repeated several times of an amount of trials. The EEG measured over the different trials are then averaged to eliminate sources in the brain, which are uncorrelated with the task at hand. In these circumstances the noise level can be made lower than 0.1.

5.4.1.2 Systematical errors vs errors due to noise

For a dipole placed in an anisotropic head model at position $\mathbf{r}$ and moment $\mathbf{d}$, a systematical error occurs when only errors due to ommitting the anisotropic conductivity are considered. This results in a dipole shift $\|\Delta\mathbf{r}_{anisotropy}\| = \mathbf{r} - \hat{\mathbf{r}}_{anisotropy}$ (in mm). When the inverse problem is solved in the same head model as the one-time forward calculation to obtain the electrode potentials and the electrode potentials are inferred with noise, then an error due to noise occurs. The amount of noise can be determined by the noise level. The larger the noise level, the larger the amount of inferred noise. This results in a dipole shift for each inference of noise. Hence, the mean dipole shift can then be written as $E\left(\|\mathbf{r}_{noise}\|\right) = E\left(\left\|\mathbf{r} - \hat{\mathbf{r}}^i_{noise}\right\|\right)$, where $\hat{\mathbf{r}}^i_{noise}$ is the i-th estimate of the dipole location with an inference of the noise.

When noise is added to the electrode potentials from the forward calculation in the simulation, a random error is introduced. This will result in a mean dipole shift $E(\|\Delta\mathbf{r}_{noise+anisotropy}\|) = E(\|\mathbf{r} - \hat{\mathbf{r}}_{noise+anisotropy}\|)$ (in mm). When the noise level increases, so does the random error due to noise. At a specific point the error due to neglecting anisotropy will be negligible compared to the error due to noise. This point is reached when the error due to noise only is similar to the error due to anisotropy and noise, $E(\|\Delta\mathbf{r}_{noise+anisotropy}\|) \approx E(\|\Delta\mathbf{r}_{noise}\|)$.

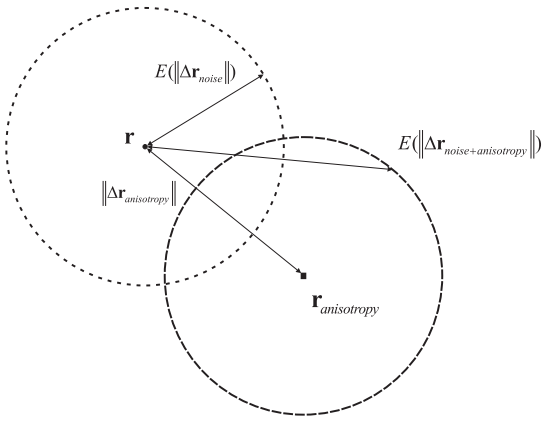

Figure 5.13: An illustration of the several errors due to noise and anisotropy. The dotted sphere around the location of the test dipole indicates the expected value of the dipole location error when only noise is inferred on the measurement potentials. The dashed sphere indicates the expected value of the dipole location error when noise and the anisotropic conductivities are negelected. When the noise level increases, so will the radii of the spheres. Hence, at a certain noise level, the spheres will be similar and thus the error due to noise only and the error due to noise and negecting anisotropic conductivities will also be similar.

5.4.2 Materials

In this study we want to investigate the dipole estimation errors in the presence of noisy EEG signals. Here noise is added to the electrode potentials calculated by the solving the forward problem in one of the anisotropic head models caused by a dipole at position $\mathbf{r}$ and moment $\mathbf{d}$. The noise is sampled from a 20 second fragment of background EEG. Nowadays, the quality of the instrument and the experiment is very high and the instrumentation and environment noise are reduced to minimal. Background EEG is EEG originating from brain activity not related to the signal of our interest. The background EEG of a duration of approximately 2 second ($\sim$ 600 samples) is chosen from a fragment of EEG where no significant brain activity was detected (see figure 5.14).

5.4.3 Simulation Setup

5.4.3.1 Simulation Overview

A flow chart of the simulation is illustrated in figure 5.15. We started from a dipole at a specific position $\mathbf{r}$ and with an orientation $\mathbf{d}$. We studied the effects on the dipole estimation due to neglecting anisotropy in the presence of noise in a time window of 1 and 20 samples.

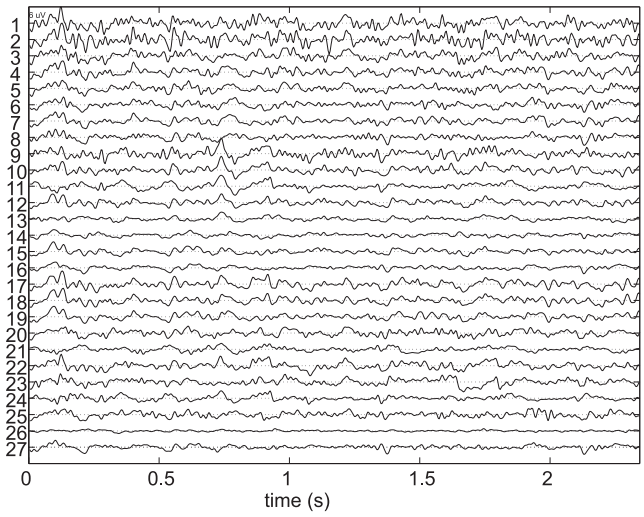

Figure 5.14: A EEG fragment containing background activity of approximately 2 seconds.

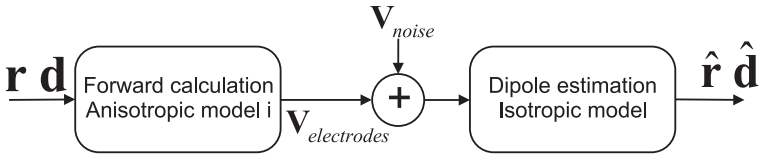

Figure 5.15: A flow chart of the simulation setup investigating the effect of not incorporating anisotropic conductivities in the noiseless case. First a dipole $(\mathbf{r}, \mathbf{d})$ is placed in a head model with anisotropic conductivities according to a model according to table 5.1 and the forward problem is solved. The resulting electrode potentials $\mathbf{V}_{electrodes}$ are inferred with additive noise. This set of electrode potentials is then used to estimate the dipole in an isotropic head model. This results in the estimated dipole parameters $\left(\hat{\mathbf{r}}, \hat{\mathbf{d}}\right)$.

Simulation using a single time instance

When a single time instance was modeled, the electrode potentials $\mathbf{V}_{electrodes} \in \mathbb{R}^{27\times 1}$ were calculated by:

$$\mathbf{V}_{electrodes} = \mathbf{L}^{i}_{anisotropic}(\mathbf{r})\mathbf{d} \tag{5.10}$$

where $\mathbf{L}^{i}_{anisotropic}$ is the lead-field matrix of a head model (referred below as model i where $i = 1, \ldots, 3$ in table 5.1). These are the lead-field matrices of the head models where one or more compartments have anisotropic conductivities.

Next a set of electrode potentials $\mathbf{V}_{background} \in \mathbb{R}^{27\times 1}$ of 1 time sample is chosen from the full background EEG fragment, illustrated in figure 5.14 and added to the electrode potentials. The amplitude of the background fragment is scaled according to the noise value:

$$\mathbf{V}_{noise} = nl \cdot U^{RMS}_{electrodes} \cdot \frac{\mathbf{V}_{background}}{U^{RMS}_{background}} \tag{5.11}$$

where $U^{RMS}_{electrodes}$ is the RMS value of the $\mathbf{V}_{electrodes}$ and $U^{RMS}_{background}$ is the RMS value of the fragment of the background EEG. nl is the predefined noise level, which can be adjusted to control the amount of noise in the EEG. In this way, the noise level indicates the amount of noise in the EEG signal. Let $\mathbf{V}_{total} \in \mathbb{R}^{27\times 1}$ be the set of electrode potentials with the added noise:

$$\mathbf{V}_{total} = \mathbf{V}_{electrodes} + \mathbf{V}_{noise}. \tag{5.12}$$

The resulting electrode potentials $\mathbf{V}_{total}$ are then used the estimate a dipole in the isotropic realistic head model (model 4 in table 5.1). The dipole estimation is done in the traditional way and the RRE can be written as :

$$RRE = \frac{\left\| \left(\mathbf{I} - \mathbf{L}^{4}_{isotropic}(\mathbf{r})\mathbf{L}^{4}_{isotropic}(\mathbf{r})^{+} \right) \mathbf{V}_{total} \right\|}{\|\mathbf{V}_{total}\|} \tag{5.13}$$

where $\mathbf{I} \in \mathbb{R}^{27\times 27}$ is the identity matrix and $\mathbf{L}^{4}_{isotropic}(\mathbf{r})$ is the lead-field matrix due to a dipole in the isotropic head model (model 4) at location $\mathbf{r}$. Here $\|.\|$ denotes the Euclidean norm between two one dimensional signals.

Minimizing the cost function will yield a dipole location $\hat{\mathbf{r}}$. Hence, for one noise inference the dipole location error is $\|\mathbf{r} - \hat{\mathbf{r}}\|$. When the simulation is repeated for 1000 inferences of noise, a mean dipole location can be calculated as $E\left(\|\mathbf{r} - \hat{\mathbf{r}}\|\right)$.

Simulation using a time window of 20 samples

When a time window of 20 samples was used, then the electrode potentials, $\mathbf{V}_{electrodes} \in \mathbb{R}^{27\times 20}$, are simulated using a dipole at position $\mathbf{r}$ and moment $\mathbf{d}(t) = \mathbf{e}_d \times s(t)$, with $t = 1, \ldots, 20$ (in samples). $\mathbf{e}_d \in \mathbb{R}^{3\times 1}$ is a unitary vector

indicating the orientation of the dipole. The values of the time series $s(t)$ are chosen to be uniformly distributed between 0 and 1. Thus one can write:

$$\mathbf{V}_{electrodes} = \mathbf{L}^{i}_{anisotropic}(\mathbf{r})\mathbf{e}_d s(t) \tag{5.14}$$

Then $\mathbf{V}_{background} \in \mathbb{R}^{27\times 20}$ are 20 consecutive time samples from the full fragment of background EEG. $\mathbf{V}_{background}$ is then scaled in the same way as in equation 5.11. The after addition, $V_{total} \in \mathbb{R}^{27\times 20}$ is then a fragment of noisy electrode potentials which are used in solving the inverse problem in an isotropic head model (model 4 in table 5.1).

When a 20 sample time window is used, the dipole estimation is done on the first component of the SVD decomposition of $\mathbf{V}_{total}$ as explained in section 2.4.3.2. In this case the RRE can be written as:

$$RRE = \frac{\left\|(\mathbf{I} - \mathbf{L^4_{isotropic}}(\mathbf{r})\mathbf{L^4_{isotropic}}(\mathbf{r})^{+})\mathbf{U}_1\right\|}{\|\mathbf{U}_1\|} \tag{5.15}$$

where $\mathbf{I} \in \mathbb{R}^{27\times 27}$ is the identity matrix. $\mathbf{U}_1$ denotes the first column of the topographies in the SVD decomposition of $\mathbf{V}_{total}$.

Minimizing expression for the RRE will result in an estimated dipole location $\hat{\mathbf{r}}$. Hence, we can calculate the mean dipole location error, $E\left(\|\mathbf{r} - \hat{\mathbf{r}}\|\right)$, due to neglecting anisotropic conductivities in the presence of noise.

The error due to noise only

The error due to only noise are calculated by using the same anisotropic head model (with skull and white matter anisotropic conducting compartments) as used in the forward calculation. These results can act as a reference. In the cost function *RRE* in the above paragraphs the lead field matrix of the same head model used in the forward calculation, $\mathbf{L^i_{anisotropic}}(\mathbf{r})$, is used.

5.4.3.2 Test dipoles

The above simulations are repeated for many instances of noise and for many dipole positions. A three dimensional grid was constructed in the gray matter compartment with a grid size of 10 mm. Location of the grid points were chosen as dipole location. This resulted in 51 dipole locations. For each dipole location and for each inference of $\mathbf{V}_{noise}$, the dipole orientation was sampled uniformly along the unit sphere. For each dipole position $\mathbf{r}_j$, 1000 instances of $\mathbf{V}_{noise}$ are generated by randomly sampling over the EEG fragment of 600 samples. Hence, the dipole orientation $\mathbf{d}^i_j = \mathbf{e}(\theta_i, \phi_i)$ with $i = 1, \ldots, 1000$ where θ_i and ϕ are uniformly chosen between $[0, 2\pi[$ and $[-\pi, \pi[$, respectively. Hence, the total number of dipoles used in a simulation was 51×1000.

For each dipole at location $\mathbf{r}_j$, the simulation was done over 1000 instances of $\mathbf{V}_{noise}$ and $\mathbf{d}^i_j$, this resulted in an estimated dipole location and orientation.

Solving the inverse problem with the 1000 noisy electrode potentials results 1000 estimated dipoles with location $\hat{\mathbf{r}}_j^i$ and orientation $\hat{\mathbf{d}}_j^i$ with $i = 1, \ldots, 1000$ and $j = 1, \ldots, 51$. Hence, a mean dipole location error can be calculated as follows

$$E(DLE) = \frac{\sum_{i=1}^{51} \sum_{i=1}^{1000} \left\| \mathbf{r}_j - \hat{\mathbf{r}}_j^i \right\|}{51 * 1000} \tag{5.16}$$

Moreover, The simulations are also repeated for 10 noise level values ranging from 0 to 1. The resulting $E(DLE)$ for each noise level is plotted in a graph. 3 graphs are made corresponding to the model used for in the forward calculation: model 1, 2 and 3 in table 5.1. In each graph 4 curves are plotted: the simulation using 1 time sample and 20 time sample and for each simulation the $E(DLE)$ due to noise only and due to neglecting anisotropy and noise as a function of the noise level.

5.4.4 Results

Figures 5.16, 5.17 and 5.18 show the mean of the location error due to noise only (dashed line) and due to noise and neglecting anisotropy (solid line). When no noise is present, the noise level is 0 and the error due to noise is also zero. However, when anisotropy is neglected then a systematical error is still present in the noiseless case. When the anisotropic conductivities of the skull and brain tissues a mean dipole location error of 10 mm can be observed. Similar results were found when neglecting the anisotropic conductivities of the skull. When only the anisotropy of the brain tissues are not incorporated, a dipole location error was made of 1.3 mm. These results are in concordance with the results found in the first part of this chapter.

When anisotropic conductivities of the skull and brain tissues are neglected and noise is added to the electrode potentials at a low noise level (≤ 0.2), then the error due to noise and using a simplified head model is about 5 till 10 mm larger than the location error due to noise only, regardless of on how many time samples the source estimation was performed. Hence, at these noise levels, the localization can be made more accurate by incorporating anisotropic conductivities. However, at higher noise levels (≥ 0.5) and the source estimation is performed on one time sample, then the error due to noise only and the error due noise and using an simplified head model have a difference of less than 3 mm. Hence at a noise level of 0.4 and higher, incorporating anisotropic conductivities will not increase much the accuracy.

When the source estimation is performed on a fragment of 20 time samples using the first component of the SVD, then even at higher noise levels the accuracy of the source estimation can be improved by incorporating anisotropic conductivities. At a noise level of 0.7, the error due to neglecting anisotropy and noise is 5 mm larger than the error due to noise only. When the noise level is higher than 0.9, the difference between the error due to noise and due

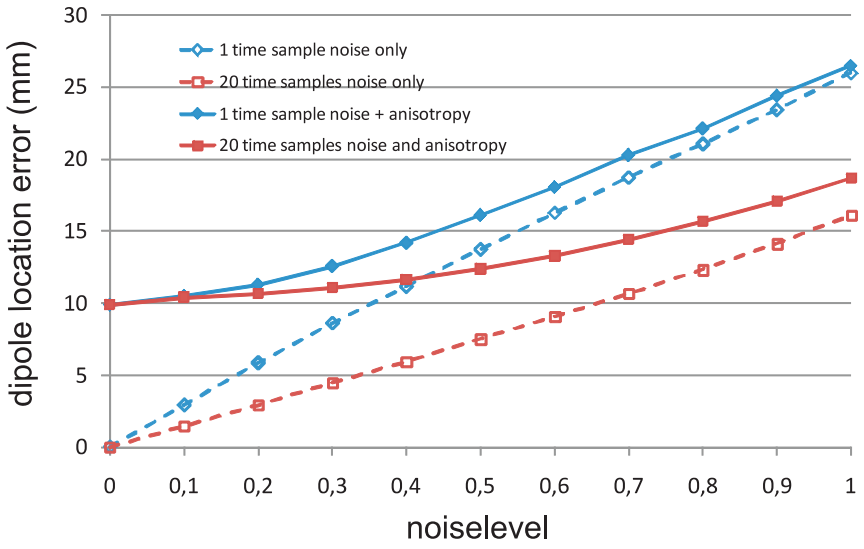

Figure 5.16: The dipole location error in function of the noise level when only noise is inferred (dashed line) and when noise is inferred and skull and brain tissues are set to isotropic conducting (solid line). The time samples indicated shows the number of time samples used when solving the inverse problem.

to neglecting anisotropy and noise becomes smaller than 3 mm. At that noise level, the incorporation of anisotropic conductivities will not improve much the accuracy of the dipole location estimate.

When only skull anisotropy is neglected, we see a similar result as the previous paragraph. The results from the previous paragraphs can thus be repeated here. This suggests that the anisotropic skull has an important influence on the dipole estimate, even using noisy EEG.

While if only the brain tissues are anisotropic, the systematical error (due to neglecting the anisotropic properties of brain tissues) is already very small, as seen in figure 5.18 when looking at the point where the noise level is equal to zero. From a noise level of 0.1 the error due to anisotropy and noise is similar than the error due to noise only. This suggests that the when a very small amount of noise occurs, the error is mainly due to the noise and the error due to neglecting anisotropy is negligible. The same holds when the anisotropy of gray matter is not incorporated. At a noise level of 0.2 the error due to noise is similar to the error due to noise and neglecting anisotropy. This suggests that the error in the source estimation is mainly due to the noise of the EEG. Therefore, the incorporation of anisotropic conductivity of the white and/or gray matter is not necessary, even if the noise level is low.

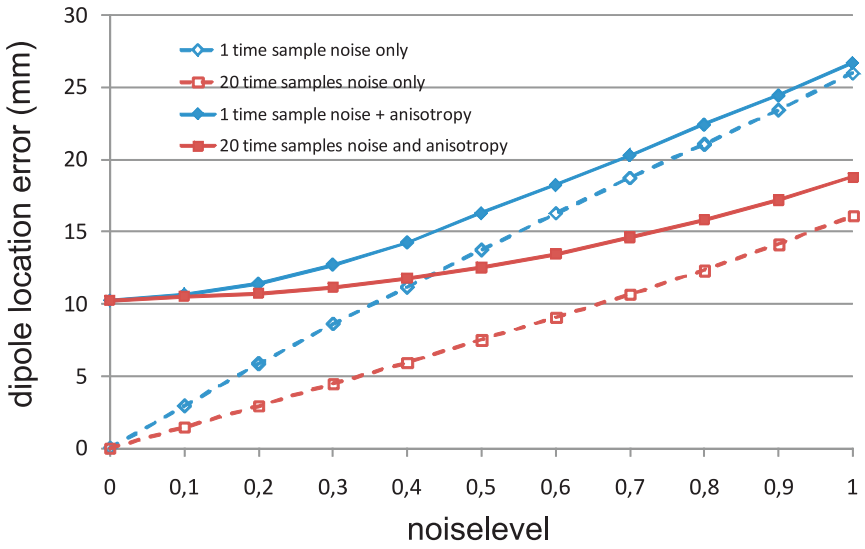

Figure 5.17: The dipole location error in function of the noise level when only noise is inferred (dashed line) and when noise is inferred and the skull compartment is set to isotropic conducting (solid line). The time samples indicated shows the number of time samples used when solving the inverse problem.

5.5 Summary and conclusions

The aim of this chapter was to study the effect of neglecting anisotropic conductivities in realistic head models. Neglecting the anisotropic conductivities of the skull and brain tissues can causes dipole location errors in the gray matter regions of on average 10 mm. A maximum dipole location error of 25 mm found at the lower part of the cerebellum. The dipole location errors are largest at the edge of the brain compartment. A similar magnitude of errors were found if only the anisotropic properties of the skull are neglected. Indeed the distribution of the dipole location error for test dipole in the gray and white matter when neglecting the anisotropic conductivity of the skull and brain tissues and when neglecting the anisotropic conductivity of the skull only are similar. These histograms indicate that 50% of the dipole location errors are larger than 10 mm. Neglecting the anisotropic conductivities of the brain tissues causes small estimation errors. Here the mean dipole location error was 1.1 mm for the test dipoles put in gray matter. The maximum error was approximately 8.4 mm.

Concerning the dipole orientation error, the errors are very small. In all simulations, the dipole orientation error of 80% of the test dipoles are below 10 degrees. The mean dipole orientation error was 6.4 degrees. However, large dipole orientation errors were found when neglecting the anisotropic conductivities of the skull and brain tissues at the bottom part of the brain. There a

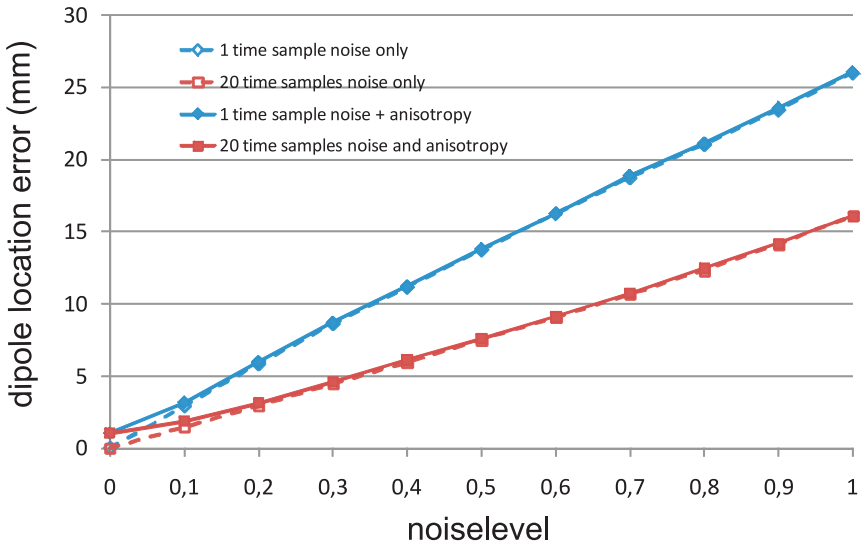

Figure 5.18: The dipole location errorin function of the noise level when only noise is inferred (dashed line) and when noise is inferred and the white matter compartment is set to isotropic conducting (solid line). The time samples indicated shows the number of time samples used when solving the inverse problem.

maximum error of 61.9 degrees was found.

In the second part, a qualitative study of the influence of the anisotropic conductivities was done using simulation study. We found that setting the conductivity of the skull to anisotropic, causes a shielding effect. Therefore, the potential values in an anisotropic skull are more attenuated compared to the isotropic skull. Setting the conductivity of the brain compartments to anisotropic causes very local changes in the potential field. These local changes can affect the dipole estimation, mainly if the dipole is close to anisotropic regions with a high FA. These local changes in the potential field can be interesting for studies on deep-brainstimulation

When anisotropic conductivities of the skull and brain tissues are neglected and noise is added to the electrode potentials at a low noise level ($\leq$ 0.4), then the error due to noise and using a simplified head model is about 5 till 10 mm larger than the location error due to noise only, regardless of on how many time samples the source estimation was performed. Hence, at these noise levels, the localization can be made more accurate by incorporating anisotropic conductivities.

However, at higher noise levels ($\geq$ 0.7) and the source estimation is performed on one time sample, then the error due to noise only and the error due noise and using an simplified head model are similar. In that case, incorporating anisotropic conductivities will not increase much the accuracy. However, when

the source estimation is performed on a fragment of 20 time samples using the first component of the SVD, then even at higher noise levels the accuracy of the source estimation can be improved by incorporating anisotropy.

A similar reasoning can be made if only the anisotropic conductivities of the skull and noise is added. However when only the conductivities of the brain tissues are neglected in the presence of noise, then the error due to noise and due to neglecting anisotropy almost coïncide with the error due to noise only. Only in the noiseless case and at very low noise levels (≤ 0.1) and a very accurate source estimation is wanted, then incorporating white matter anisotropy can be beneficial for the accuracy of the source estimation. However, if the amount of noise is reasonable, the incorporation of anisotropic conductivities of the brain compartments is not necessary. These results suggest that the anisotropic conductivity of the skull is the most important influence on the source estimation and the need for an adequate characterization of the skull.

Although these results suggest that the anisotropic conductivities of the brain are not necessary to incorporate in the head model, they are dependent on the model used to approximate the white and gray matter anisotropy. In our case, we presented a model which is best suited for low resolution DW-MR images. Nowadays, advanced MR techniques within a 7 Tesla scanner are emerging which enables to acquire high resolution DW-MR images.

The results shown in this chapter led to several proceedings presented in international conferences [65, 67]. An article describing these results is in preparation.

Chapter 6

Example of an application in epilepsy

It is the tension between creativity and skepticism that has produced the stunning and unexpected findings of science
—Carl Sagan

6.1 Introduction

In this chapter we want to show an application in which EEG source analysis with the AFDRM method can be used. The application in mind is epilepsy, which will be explained later. Although this is a example, this setup can be used to validate the AFDRM method. Collecting the data is a time consuming process, which was beyond the scope of this dissertation. At the end of this chapter we will provide a methodology that enables us to validate the method.

6.2 Background

Epilepsy is a neurological disorder, which involves the abnormal synchronous electrical activity of a focal or large brain area. This activity is often called an epileptic discharge. The most common examination for the diagnosis of epilepsy is the EEG. Patients with epilepsy can have special features in their EEG. The EEG measured during an epileptic seizure is called the *ictal EEG*. An illustration af an ictal EEG is shown in figure 6.1. The amplitude is higher than when no seizure occurs.

The EEG of a patient between the epileptic seizures is called the *interictal EEG*. Examples of interictal epileptic EEG features include a spike with a time duration of 20 to 70 ms, a sharp wave with a time duration of 70 to 200 ms and

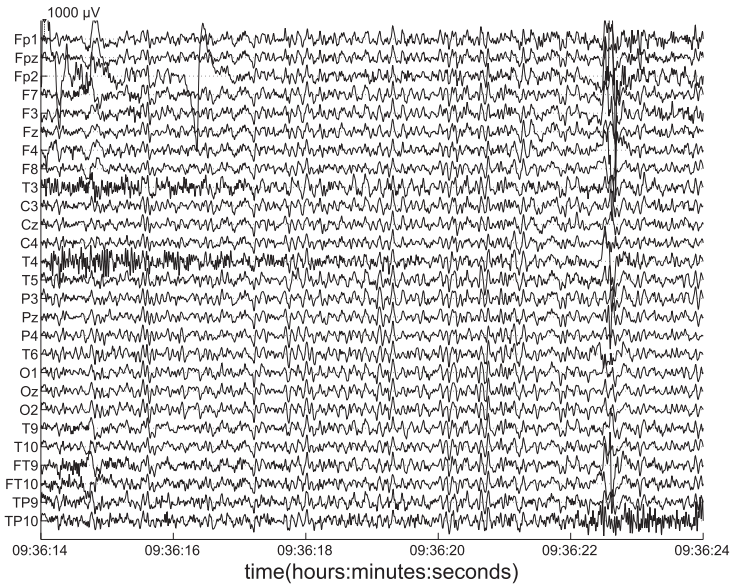

Figure 6.1: An fragment of an epileptic seizure of 10 seconds.

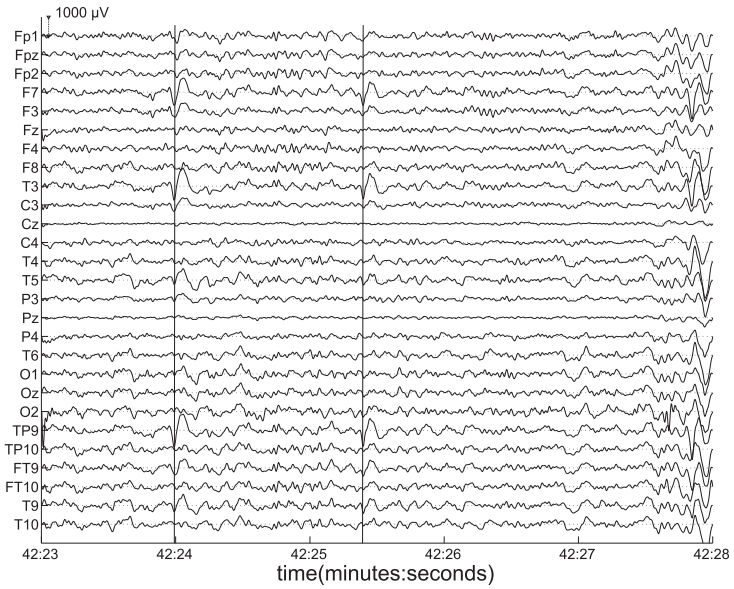

Figure 6.2: A fragment of interictal EEG of 5 seconds. Two spikes occur very short after each other. The spikes are marked with a black vertical line.

a spike-wave-complex, consisting of a spike followed by a wave. It is believed that the brain areas generating the interictal EEG are the same as the ones generating the ictal EEG [79]. An example of a spike is shown in figure 6.2.

In most cases epilepsy can be treated by anti-epileptic drugs. In 30% of the cases the epileptic seizures cannot be controlled. This is called refractory epilepsy. Those patients can be treated with resective surgery, however the epileptogenic zone (the area causing the epilepsy) should be focal and very clear. Furthermore, it is clear that the resective surgery should not lead to a neurological deficit. To detect the epileptogenic zone and to decide whether surgery can be performed, a presurgical evaluation is needed. In this evaluation several techniques are performed on the patient. If these techniques yield the same conclusion on the epileptogenic focus, then a surgery can take place.

The presurgical evaluation usually starts with a long-term (3 to 5 days) Video/EEG monitoring. The analysis of the seizure on video and EEG, both presented on a split-screen, is of major importance to localize the epileptogenic zone [23]. Neuroimaging techniques, such as computed tomography (CT) and MRI, may detect structural abnormalities in the brain at the epileptogenic site. Positron Emission Tomography (PET) provides information on cerebral blood flow and oxygen and glucose metabolism. Areas of glucose hypometabolism are often associated with epileptogenic zones [142]. Single Photon emission computed tomography (SPECT) can be used to evaluate regional blood flow changes which may suggest for an epileptogenic zone [142]. Neuropsychological tests investigate the higher cognitive functionality of the brain, such as speech and memory. These tests may also reveal a dysfunction of certain brain areas.

When these investigations indicate the same epileptogenic zone, and when no major neurological deficit is expected from a surgical procedure, a multidisciplinary team decides to perform surgery and remove the area responsible for the epileptic seizures. On the other hand, when these investigations are not congruent, a long-term invasive EEG monitoring may be considered. Rigid or flexible depth electrodes are surgically implanted in the brain through a hole in the skull. These electrodes have a variable amount of contact points which can be used to measure the activity. The invasive electrodes are placed near areas that have a high probability of being the epileptogenic zone. When by inspecting the invasive recordings, an epileptogenic zone can be distinguished, resective surgery may be performed.

Both surface EEG and the EEG measured at the scalp can be used to perform a localization of the generating electrical source. The dipole model can be used to represent the focal epileptogenic zone. EEG source estimation can thus be considered as an additional noninvasive examination in the presurgical evaluation of epilepsy. This additional noninvasive technique is introduced in the hope that further invasive recordings can be reduced in the future [24].

Depth electrodes can be used to validate the source estimation procedure retrospectively. The depth electrodes are inserted at regions which are candidates for the epileptic onset zone. As the depth electrode measures very locally, the

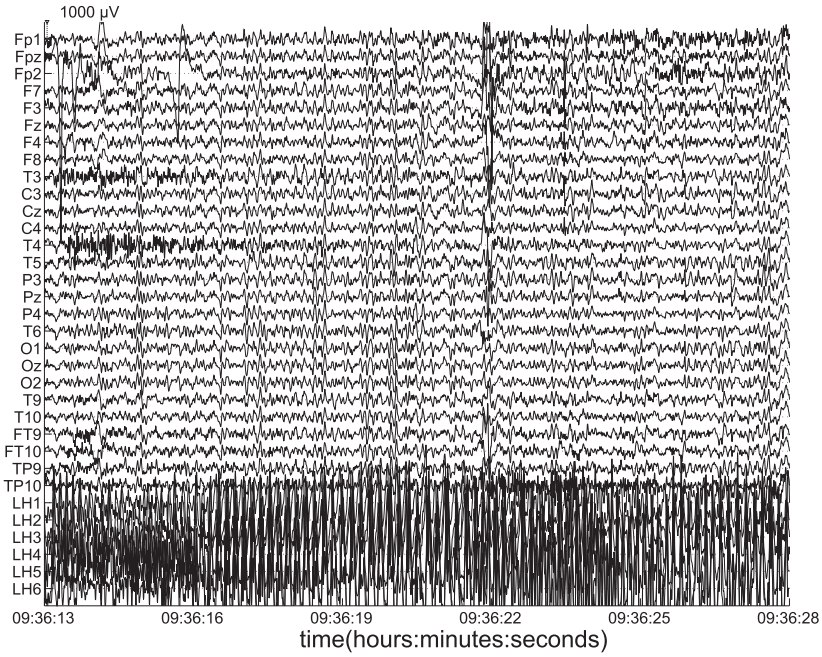

Figure 6.3: A fragment of a seizure of 15 seconds. The EEG measured at the depth electrodes implanted in the left hippocampus (LH) are also shown. We can see some rythmic activity of the depth electrode.

seizure can be measured with a very good time resolution. In figure 6.3 an illustration is shown of a simultaneous surface and depth EEG registration. During a seizure, the depth electrodes have a rhythmic activity. The same fragment as in figure 6.1, was depicted. The six lower electrodes are depth electrodes implanted in the left hippocampus. Hence, the position of the electrode where the seizure occurs first, pinpoints the onset zone.

6.3 Patient Information

A patient from the database of the reference center of epilepsy of the department of neurology of the Ghent University Hospital (Ghent, Belgium) was chosen. The patient had a favorable outcome and had a resective surgery. Since then, the patient has been seizure free. The recordings and the MR images used in the presurgical evaluation are a unique dataset as the patient had to undergo the complete presurgical evaluation. A female patient of age 51 was chosen from an extensive database who had a history of temporal lobe epilepsy, with seizures of approximately 30-60 seconds. The MR image revealed sclerosis of the hippocampus. However, a localization from the EEG was not conclusive

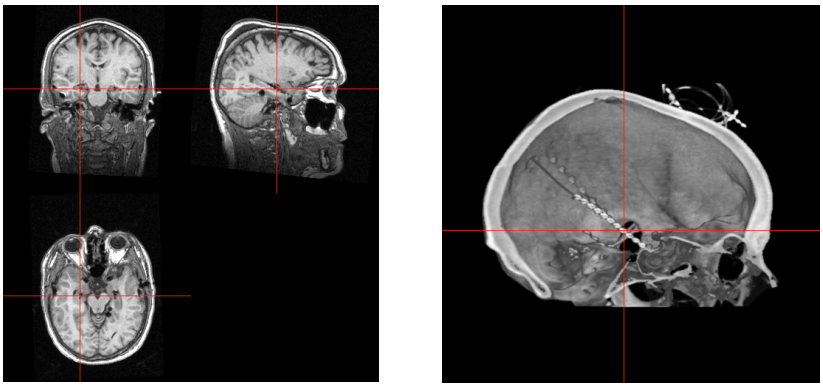

(a) (b)

Figure 6.4: (a) A MR image of the patient with the implanted depth electrodes. A coronal, sagittal and axial slice are shown. The red line intersect at the electrode (LH4) where the seizure onset started. (b) A 3D rendered image of a computed tomography (CT) image from the patient with the implanted depth electrodes.

as the seizures was not unilateralized. Therefore the patient was submitted to an intracranial EEG registration. The patient had depth electrodes in the left and right hippocampus (amygdalo-occipital electrodes). Furthermore, grid electrodes (electrodes fixated on a plastic patch) were inserted in the left and right temperobasal area. During the intracranial investigation, several seizures were recorded and analysed. The seizures started with rhythmic spiking at the electrode (LH4) which was inserted in the left hippocampus. An MR image was taken while the depth electrodes were implanted, from which we could determine the exact location of the electrode LH4 and thus the seizure onset (see figure 6.3a).

Based on the good localization of the depth electrode, the patient underwent a selective amgydalo-hippocampectomy and has been seizure free since one year and three months. An invasive recording was done as an ictal seizure localization was not lateralized. A post-operative MR image was made to image the resection of the hippocampus.

6.4 Estimation of epileptic activity using the AFDRM method

6.4.1 Materials

The EEG fragment of 2 seconds shown in figure 6.2 was used to estimate a dipolar source. The EEG was recorded using a video/EEG monitoring system of Micromed (Italy). The sampling frequency was 256 Hz.

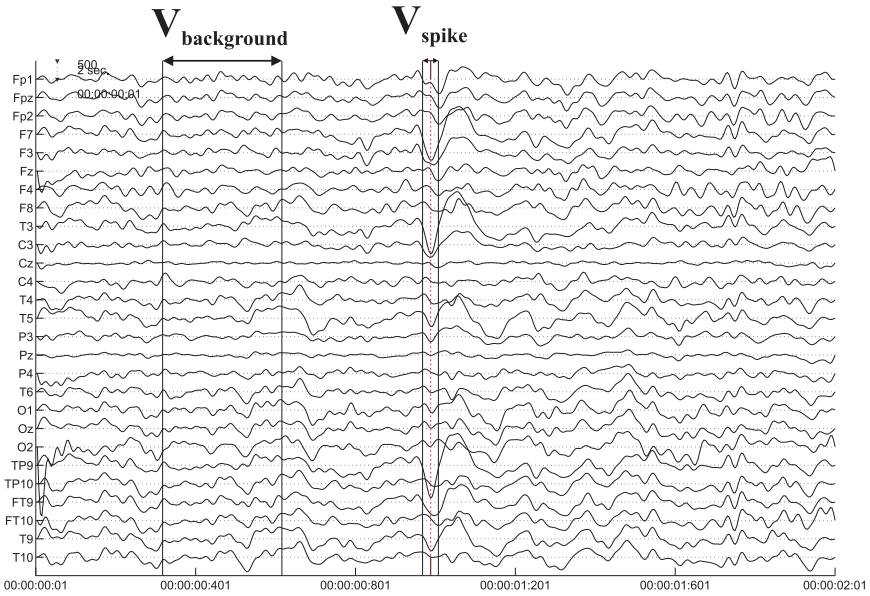

Figure 6.5: The EEG fragment of 2 seconds containing a spike, indicated by a red dashed line. The fragment of the background and the signal for the calculation of the noise level is also shown between two black lines.

The noise level was calculated as follows. The fragment was filtered between 0.05 and 40 Hz and the potentials at each electrode were average referenced. A window of 30 ms (8 samples), shown in figure 6.5 as $\mathbf{V}_{spike}$, around the tip of the spike was used to calculate the RMS value of the EEG signal, U_{RMS}. The RMS value of the background, U^b_{RMS}, is calculated using a background fragment prior to the spike of approximately 250 ms (100 samples) (see figure 6.5). This gives us an idea of the noise contribution to the EEG. The noise level according to equation 5.7 yields 0.42. In section 5.4 it was shown that incorporating anisotropic conductivities of the skull and brain tissues at that noise level, does provide a more accurate estimation of the source estimation.

The scalp EEG of the patient was recorded during a video/EEG monitoring. During a seizure, the EEG is contaminated with noise. Therefore, we use an epileptic spike to perform source estimation. Spikes are believed to originate from the same focal zone as the onset of a seizure [79]. An EEG fragment of 0.3 seconds was used to perform source localization (see figure 6.6). The fragment had a sampling rate of 256 Hz was filtered with a bandpass filter between 0.05 Hz and 45 Hz to eliminate noise.

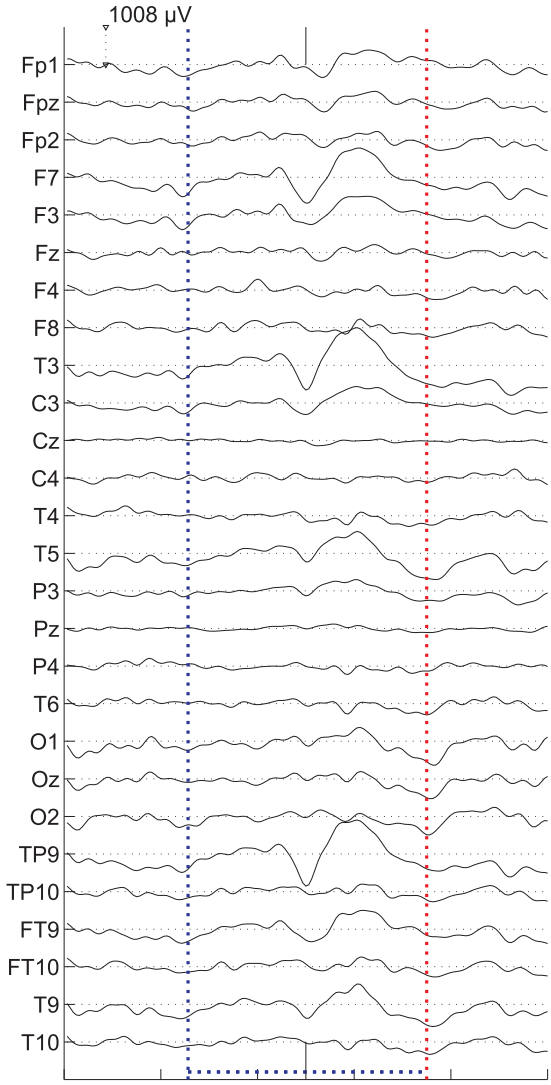

Figure 6.6: The fragment containing an epileptic spike is shown. The spike is shown between the bars. The time window between the bars is 0.3 seconds.

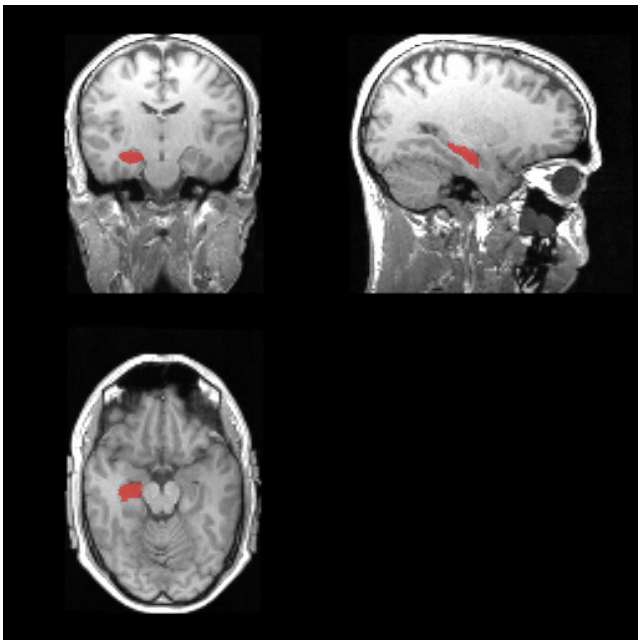

Figure 6.7: The MR image of the head model with the segmented hippocampus structure in red.

6.4.2 Using the MR image of the head model to estimate the sources

As a diffusion weighted image of the patient was not available, a source estimation was done using the head model as constructed and used in chapters 4 and 5. The head model was constructed using segmentation techniques The left hippocampus was the brain structure where the seizure originated. Therefore, we asked a neuroradiologist to segment the hippocampus on the MR image of the head model. Therefore, we can visualize the dipole estimates with the hippocampus structure in an MR image.

6.4.3 EEG source analysis: constraining the search space to the gray matter

As generators of the EEG are mainly situated in the gray matter where the neurons are concentrated, we want to constrain the source estimation to the gray matter. However, due to the irregularity and the high non-convexity of the boundary of the gray matter compartment, the source estimation using a classical optimization like Nelder-Mead simplex method can be easily be trapped in local minima. Therefore we solved the inverse problem using space mapping (SM) techniques, which were introduced in the field of EEG in Crevecoeur et al.

[32, 33]. These techniques are explained in appendix C. Here a coarse and a fine model are used. The three shell spherical is used as a coarse model and the realistic head model as the fine model. The three shell spherical head model is fitted in the realistic head model as the geometric link between the coarse and the fine model. In our case, the Hybrid Aggressive Space Mapping (HASM) technique with the Trust Region Aggressive Space Mapping (TRASM) is used. The trust region is defined as the gray matter compartment.

6.5 Results

In figure 6.8 the dipole source estimated from the spike fragment is shown. The red structure is a three dimensional visualization of the segmented hippocampus. The cyan dipole is the estimate in a isotropic head model, while the green dipole is the estimate using an anisotropic head model. We can see that the estimate in an anisotropic head model is closer to the hippocampus. The distance between the location of the dipoles in isotropic and anisotropic head model is 8.9 mm.

6.6 Limitations of the study

Although this study suggests that incorporating the anisotropic conductivities improves the accuracy of the EEG source estimation, some limitation have to be kept in mind. Due to the absence of a DW-MRI image of the patient, a true head model from the MR image of patient could not be made. Therefore, a mapping was made from the MR image of the patient with the implanted electrodes and the MR image of the head model. Because of another geometry, dipole location errors will occur. A better accuracy would have been obtained if the geometry of the head model is as close as possible to the actual geometry of the head model.

Another limitation that is to be considered are the electrode positions. The exact electrode positions were not known as an MR image with fiducial markers at the electrodes was not available. It is known that an average mislocation of the electrode position of 10 mm, will result in a dipole location error of 10 mm [140]. Hence, if the electrode positions are exactly known with respect to the head model, a better localization accuracy can be obtained.

The EEG fragment used in the EEG source estimation containing the spike had a noise level of approximately 0.4. The noise level can be reduced if advanced signal processing techniques can be used prior to the source estimation. Also combining several spike waveforms would reduce the noise in the spike waveform considerably.

Finally, this patient is a single case study and a thorough validation study should consist of multple patients. Moreover, the collection of the dataset

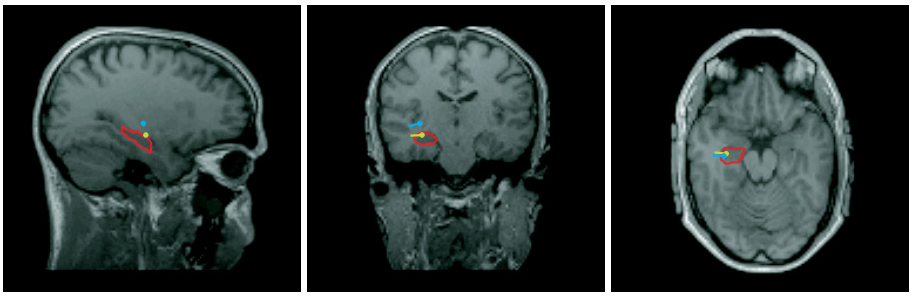

(a)

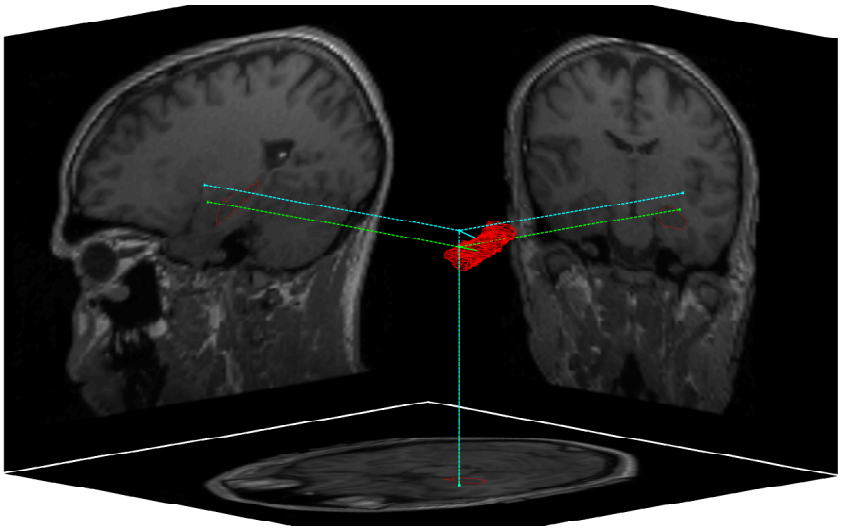

(b)

Figure 6.8: Figure (a) shows three projections of the dipole estimates in a sagital, coronal and axial slice and figure (b) shows a three three dimensional representation of the head model with the dipole estimates. The region of interest (ROI) depicted in red indicates the manually segmented hippocampus, which was resected and rendered the patient seizure free. The cyan dipole is the location of the estimate in an isotropic head model. The green dipole is the location of the estimate using an anisotropic head model. The 3D coordinates are also projected on the slices, this is indicated by the dotted line.

usually takes more than a year as the patient is first subjected to the simplest investigations first. If a solution for the patient is obtained for the patient at early investigation, a more complex or invasive investigation is thus not needed.

6.7 Future work

In the ideal case for a thorough validation study a dataset should include a T1 MR image where the head model can be constructed from. Moreover, an exact location of the electrodes at the scalp surface should be known. Therefore, little spheres filled with vitamins can be glued on the electrodes. In an MR scan these littles spheres will light up, which can be used to pinpoint the exact positions of the electrodes on the MR image.

From chapter 5 we saw that the incorporation of anisotropic conductivities of brain tissues is not necessary for an accurate source localization. Hence, a DW-MRI of a 2 mm by 2mm by 2 mm resolution is not necessary. However, this could change of higher resolutin DW-MRI images are taken. If this is possible, than other approaches that model the anisotropic conductivities will be more accurate instead of the volume constraint.

The incorporation of anisotropic conductivity of the skull is important for an accurate source localization. We want to note that if one wants to study the electric field caused by stimulation in the brain, the anisotropic conductivities of the brain tissues might be useful to incorporate. As the skull does not have a signal on a MRI scan, an alternative is needed. A computed tomography (CT) scan images very accurately the skull. If a CT image can be fused with a MRI scan, then the skull can be accurately modeled. It has been shown in Cuffin [34],Marin et al. [96] and in Vanrumste et al. [144] that the skull has a large effect on the EEG source analysis. Knowing the exact geometry of the skull and the exact location of the electrodes is known together with the soft tissues of the head using the MR image, an accurate head model can be constructed.

Furthermore, when an invasive recording is performed, the MR image with the implanted electrodes can be used to determine the seizure onset zone. Moreover, a CT image with implanted electrodes fused with the MR image with the implanted electrodes offers an accurate localization of the depth electrodes.

During the video/EEG recording and the invasive recordings, epileptic seizures and spikes can be recorded. These epileptic phenomena can be correlated with the location of these implanted electrodes. Therefore, we can accurately depict the ictal onset zone based on the MR images of the implanted electrodes. An alternative investigation that can provide useful information in pinpointing the seizure onset zone is ictal SPECT. In this investigation the patient is injected with a radioactive tracer as early as possible in the seizure onset. After the seizure the image shows the activation during that seizure, which depicts the onset zone with a propagation of activity.

Finally, if resective surgery was done, using an post operative MR image coregistered on the pre-operative MR image we draw regions of interest that depict the exact amount of removed brain tissue. The outcome of the surgery is actually known on a long term basis. The patient can be seizure free early after the resective surgery. However, it is not uncommon that patients start having seizures again.

This collection of data requires a good collaboration several instances of the Ghent University Hospital. Moreover, in order to have complete dataset, the patient should undergo the full investigations of the presurgical evaluation. The first steps in defining the protocol in the collection of the data sets have been made.

6.8 Summary and Contributions

In this chapter we applied our method in a prospective study in which we used realistic data measured during a video/EEG monitoring session at the Reference center of Epilepsy at the Department of Neurology of the Ghent University Hospital. The data used in the source estimation represented a spike, which is a characteristic phenomenon in interictal EEG (i.e. EEG measured between epileptic seizures).

Using a two-level approach to solve the inverse problem, a search space could be constrained to the gray matter compartment. A spike is believed to be generated by synchronously active neurons and it is plausible that the origin is located in the gray matter. However, it possible that dipoles are situated in the white matter. An estimation was done in the isotropic head model and the anisotropic head model with both skull and brain tissues anisotropic conducting. We found that the estimate of the dipole location in the realistic head model with anisotropic conductivities is 8.9 mm closer than the dipole location estimated in the isotropic head model. This study suggests that the anisotropic head model increases the accuracy with approximately 9 mm, which is in concordance with the results shown in section 5.2 and section 5.4 taking into account the noise level of 0.42 (see section 6.4.1).

This large error may contributed to the volume constraint which decreases the conductivity perpendicular to the skull $\sigma_n = 0.0043\,S/m$ while in the isotropic case $\sigma_{isotropic}^{skull} = 0.02\,S/m$. Therefore future investigations and data is needed to investigate this validity of this model and to determine if other models are more plausible.

Chapter 7

General conclusions and further research

hic opus, hic labor est
—Vergilius, "Aeneis, book VI"

In this chapter a global overview and a general conclusion is given of this dissertation.

EEG source analysis consists of two subproblems, a forward problem calculates the electrode potentials at the scalp by a dipolar source, while the inverse problem estimates the source parameters which best represent a given set of electrode potentials. The forward problem requires a head model, which represents the human head and which is subdivided into compartments according to the tissue types. An important parameter of these tissue types is the conductivity, which is often modelled as isotropic (i.e. the conductivity is equal in all directions). In reality the conductivity of these tissue types are anisotropic. The main topic of the dissertation is the incorporation of anisotropic conductivities for EEG source analysis. Throughout the dissertation we discussed how we can incorporate the anisotropic conductivities of the skull and white matter in the EEG source estimation problem and the effect of not taking into account these anisotropic properties on the source estimation.

7.1 General conclusions

Errors due to not neglecting anisotropic conductivities: study in a spherical head model
In chapter 3 we started with a simple study in a spherical head model in which the skull and white matter conductivity could be set to anisotropic or isotropic. Neglecting the anisotropic conductivities of the skull and white matter yielded

location errors of on average 22.36 mm in the cortical shell and 7.32 mm in the thalamic shell. Maximum error of 32.33 mm were found. The magnitude of these errors (order of centimeter) are unacceptable for an accurate EEG source analysis. This suggest that if anisotropic conductivities are not incorporated an error of more than 15 mm exists on the dipole estimate. Therefore, it was concluded that anisotropic conductivities have to be incorporated. Realistic head models are a more accurate representation of the human head, but require numerical methods. This study expresses the need for a numerical method which can incorporate anisotropic conductivities to solve the forward problem.

Validation of the numerical method to use with realistic head model
In this thesis the finite difference method was chosen because of its ease of use and implementation. The anisotropic finite difference with reciprocity method (AFDRM), numerical technique that can incorporate, was introduced in chapter 2 and validated in chapter 3. In the isotropic case, the mean location error due to discretization was 1.78 mm, 0.73 mm and 0.48 mm in a cubic grid of size 3 mm, 2 mm and 1 mm, respectively, which is an improvement compared to traditional FDM. When anisotropic conductivities of the skull are incorporated, the mean location error due to using the AFDRM was 9.2 mm, 6.1 mm and 2.6 mm in a cubic grid of grid size 3 mm, 2 mm and 1 mm, respectively. When the anisotropic conductivities of the white matter are incorporated, a mean location error was found of 3.1 mm, 1.6 mm and 1.0 mm when the grid size was 3 mm, 2 mm and 1 mm, respectively. The finer the cubic grid, the smaller the location error due to discretization. From the result, we could conclude that a cubic grid of 1 mm or less is needed to minimize the errors due to discretization when the AFDRM is used.

Construction of the head model: different approaches to model the white matter
In chapter 4 we discussed the construction of a realistic head model and the application of the AFDRM in the realistic head model. The focus was on the construction of the anisotropic conductivities of skull and white matter. For the skull, a segmented MRI image can be used to derive a tangential and normal direction in each voxel. Then the conductivity along the tangential direction was set to 10 times larger than the normal direction. Deriving the anisotropic conductivity of the white matter was done using a technique called diffusion weighted magnetic resonance imaging (DW-MRI). A diffusion tensor can be derived. The conductivity tensor can be derived from the diffusion tensor using two possible approaches. A simplified approach states that the conductivity along the largest principal diffusion direction is 9 times larger than the orthogonal directions. However, we have demonstrated that the fractional anisotropy in white matter is not fixed and mostly smaller than 9. Hence, using the simplified approach to model an anisotropic conductivities of white matter might be an overestimation of the anisotropy. Therefore, a more realistic

approach was discussed, where the diffusion along each principle direction is scaled to obtain the conductivity tensor.

We compared both approaches by means of the dipole location and orientation error of the estimates in a realistic head model. We found that using the dipole location error due to using the realistic approach was relatively small; a mean error of $4,04$ mm was found with a maximum error of 17.7 mm. Concerning the errors on the dipole orientation, we found that the errors with a large magnitude ($\geq$ 30 degrees) are concentrated near the center of the brain and are mainly situated near white matter boundaries. Similarly as for the location error, this is due to the fact that the electrode potentials are largely influenced by anisotropy when the test dipole is placed near a highly anisotropically conducting region. Moreover, more than 60% of the dipole estimation errors were above 10 degrees.

Although only two approaches to model the white matter anisotropy are presented here and compared, there are more approaches which have been more founded by a theory. Due to the low resolution of the DW-MRI, these models are not valid as the low resolution causes a homogenization of the anisotropy. A higher resolution DWI-MR could cause a more heterogeneous distribution in the FA values and thus the anisotropy of each voxel. It has yet to be established whether this has an effect on the dipole estimation. Moreover, it has yet to be established which approach to model the anisotropic conductivities of white matter is more valid.

Construction of the head model: errors due to neglecting anisotropic conductivities of gray matter

Next we investigated the dipole location and orientation error due to neglecting gray matter errors. DW-MRI also images the diffusion in gray matter regions, therefore the anisotropic conductivity tensor can also be derived in these regions. Neglecting the anisotropic conductivities of gray matter results in dipole location errors on average 2.7 mm with a maximum of 9.8 mm. The orientation error was found to be on average 5.05 degrees and had a maximum of 40 degrees. The largest orientation errors were found in places where the gray matter region was highly anisotropic. Although gray matter can be considered isotropic, due to segmentation errors and the partial volume effect, some highly anisotropic regions can be assigned to the gray matter compartment while in fact these regions belong to white matter.

If DW-MRI are present, one might just use them to constuct the anisotropic conductivities. However, modelling a compartment as anisotropic while it is in reality isotropic also introduces an error. An accurate model thus greatly depends on an accurate segmentation of the MR images and accurate measurements of the anisotropic properties of the white matter.

Error due to not incorporating anisotropic conductivities: study in a realistic head model

In chapter 5 we used the AFDRM to study the effects of not incorporating the anisotropic conductivities of the skull and brain (white and gray matter) in EEG source analysis. The chapter consists of 3 parts. First, we determined the dipole location and orientation error when anisotropic conductivities of the skull and/or brain tissues are neglected. The results showed that when the anisotropic conductivities of the skull or both the skull and brain tissues are not taken into account an average dipole location of 10 mm error can occur. With respect to the dipole orientation, large estimation errors were seen ($\geq$ 30 degrees) at the corpus callosum and other neural pathways, where the anisotropic ratio was high. When only the anisotropic conductivities of the brain tissues are neglected, a mean location error was found of 1.1 mm. The dipole orientation error was found to be very low ($\leq$ 10 degrees).

Second, the influence of making the skull or brain tissues anisotropically conducting on the potential field distribution is inspected visually. A frontotemporal source and a source near the highly-anisotropic region were placed in each of the head model and the potential field caused by each source is calculated. Making the skull more anisotropic causes an extra electrostatic shielding effect. Furthermore, making the brain tissues anisotropically conducting changes the potential field in the vicinity of the dipole source. This effect is very noticeable near regions with a high anisotropic ratio (such as the corpus callosum).

In the third part of the study we investigated the dipole location error when not taking into account the anisotropic conductivities in the presence of noise. For this purpose, we applied background noise on the electrode potentials. The electrode potentials are caused by a dipole source in a head model with anisotropic conductivities. The noisy electrode potentials are used to estimate the dipole source in a isotropic head model. The amount of noise could be quantified by the noise level. The location error due to neglecting anisotropy and noise was compared to the one due to noise only. It was found that incorporating the anisotropy of the skull will improve the accuracy of the EEG source analysis, however due to noise the incorporation of the brain tissues shows a small improvement of the accuracy of the EEG source estimation. Although these results suggest that the anisotropic conductivities of the brain are not necessary to incorporate in the head model, they are dependent on the model used to approximate the white and gray matter anisotropy. Depending on the model of anisotropy and the resolution of the DW-MRI, these results can change significantly. In our case, we presented a model which is best suited for low resolution DW-MR images. Nowadays, advanced MR techniques within a 7 Tesla scanner are emerging which enables to acquire high resolution DW-MR images. When a high resolution DW-MRI (e.g. 1 mm by 1 mm by 1mm or even 0.5 mm by 0.5 mm by 0.5 mm) is available, other approaches might be more valid [139].

Moreover, the incorporation of the anisotropic conductivities of the brain tissues could be useful for the simulation of the potential field to study the effects of deep brain stimulation. In therapeutic applications for epilepsy or parkin-

son's desease, neurologists and neurophysiologists are interested in which regions in the brain are actually stimulated.

Example of an application
An example of an application using the AFDRM is shown in chapter 6. The application in mind is epilepsy and is demonstrated by means of a prospective study using a data set obtained from an extensive database of the Reference Center of Refractory Epilepsy of the Department of Neurology and the Department of Radiology of the Ghent University Hospital (Ghent, Belgium). The patient was monitored with a video/EEG monitoring with both scalp and with implanted depth electrodes. An MR image was taken from the patient with the implanted depth electrodes, therefore, we could pinpoint the onset zone of the epileptic seizures. Surgery was performed, which removed the hippocampus from the patient and rendered the patient seizure free. As DW-MRI images were not available, the left hippocampus was aligned on an MR image by a neuroradiologist. The patient had a resective surgery where the left hippocampus was removed and rendered the patient seizure free since. A spike was picked from a dataset and was used to estimate the source in an head model with isotropic conductivities and with the skull and brain tissues anisotropically conducting. It is believed that spikes and epileptic seizures originate from the same onset zone. The dipole estimate in the anisotropic head model was closer to the manually segmented hippocampus than the one using the isotropic head model. Although this study is very preliminary and needs further investigation, it suggests that using the anisotropic head model the accuracy of the EEG source estimation increases. In this chapter we wanted to show how the AFDRM can be used in the clinical practice and how a thorough validation study can be performed.

7.2 Future work

Validation
As discussed in chapter 6 a thorough validation study has yet to be performed. In the same chapter we discussed how we can do this and which data has to be collected. These datasets can be very extensive for each patient. Unfortunately, the collection of these extensive data sets is time consuming and requires a factor of luck that the patient has to undergo the full presurgical evaluation with the invasive recordings.

As a side project of the validation study, one could determine the necessity for individually patient-based head models. For the EEG source analysis, we can use one generic head model for each patient or an individually made head model for each patient. By determining the difference in location and orientation of the estimated dipoles we can determine if it is important to model the head individually for each patient or a standard head model can be used for application of EEG source analysis in epilepsy.

Not only is the head model an important parameter of the EEG source analysis, so is the source model. In this dissertation we limited ourselves to a single dipole model. For complex brain activity this model is insufficient and more complex models (multiple dipoles or distributed dipoles) have to be used. This requires a complex cost function in the source estimation and thus makes the EEG source analysis very complex. The feasibility of estimating a complex source model in a complex head model has yet to be investigated. Performing such a complex source analysis may come at the cost of the smoothness of the cost function and thus other minimization techniques have to be used to obtain the global minimum [33].

The source estimation procedure is also dependent on the number of electrodes used. The more electrodes are used, the lesser the ill-posedness of the problem becomes. Although the problem will always remain ill-posed, using more electrodes improves the accuracy of the source estimation up to a certain point. Depending on the noise level of the measured EEG, an upper limit of the amount of electrodes can be found above which the improvement of the source estimation compared to the upper boundary is negligible.

Applicability in other domains

EEG source analysis can also be used in other applications than epilepsy. Event Related Potentials (ERPs) is an EEG signal waveform associated with a specific task or stimulus and allows us to study the functionality of the brain. A task or a stimulus causes an activation pattern in time at distinct brain regions. EEG source analysis can be used to determine these brain regions as well in space as in time. As the signal-to-noise ratio is very low in ERPs, anisotropic conductivities should be included for an accurate source estimation. However, this needs to be thoroughly validated yet.

The threedimensional AFDRM modeling enables us to model many tissue types. Many patients have an MR scan which is abnormal due to the presence of tumors or due to absence of some brain regions by a previous surgical operation. Using advanced segmentation techniques these abnormalities can be incorporated in the head model. In neonatal studies, for example, the skull has a more cartilage structure at the fontanelles. An accurate source estimation depends on an accurate modeling of the skull. Hence, these fontanelles can be modelled as holes in the skull which can be done by the technique presented here. Numerical techniques based on the surfaces of large structures (e.g. BEM) are less suited to perform EEG source analysis in such complex head models.

Improvements to the model

A major unknown parameter of the head models is the absolute value of the conductivities. A lot of effort has been done in measuring or calculating the conductivity of the different tissues of the human head. However, a large inter-patient variability on the conductivity values exist. Electric Impedance

Tomography (EIT) has shown a lot of promise in determining these conductivity values. The problem of EIT is similar to the problem of EEG source estimation. The electrode potentials measured at the scalp in EIT are caused by a known source, which usually consists of injecting a current at an electrode pair. In this case, the unknowns are the conductivity values at the brain tissues. Unfortunately, analog to the EEG source estimation problem, EIT is an ill-posed problem. Determining the anisotropic conductivity values, makes the EIT problem even more ill-posed.

The volume constraint is only a model to construct the anisotropic conductivities of brain tissues, which is best suited when only a DW-MRI scan with resolution $2\,mm$ by $2\,mm$ by $2\,mm$ is available. Advanced MR techniques in 3 and 7 Tesla scanners are emerging, enabling us the possibility of higher resolution DW-MRI and higher Signal-to-Noise Ratio. In this case, the resolution could be $1\,mm$ by $1\,mm$ by $1\,mm$ or even $0.5\,mm$ by $0.5\,mm$ by $0.5\,mm$. When such a fine resolution is used, other models to determine the conductivity tensor from diffusion tensor images might be better suited.

Multimodality

In the diagnosis of neurological disorders or the study of brain functionality, a broad range of investigations or medical imaging techniques exist next to EEG source analysis. Medical imaging techniques can be subdivided into 2 types. Structural imaging techniques only image the anatomical or tissue type related information inside the human head. Examples of such techniques are MRI, DW-MRI and EIT. Functional imaging techniques highlight the metabolic or oxigen related changes due to the manifestation of a neurological disorder or an task or stimulus. Examples of these imaging techniques are nuclear imaging techniques, like PET and SPECT, and functional MRI, which images the blood oxygenation level at a high spatial resolution. EEG source analysis can also be a functional imaging technique based on the electrophysiological activation in the brain. Combining all these channels of information together could provide us with more insight in how the brain works or how a particular neurological disorder manifests.

In this dissertation we combined several structural imaging techniques (MRI, DW-MRI) to increase the accuracy of a functional imaging technique (EEG). It is well known that the EEG source analysis has a low spatial resolution due to the noise in the EEG. The EEG source analysis can be made more accurate if other modalities are incorporated. Other functional modalities can act as priori information which can be incorporated in the EEG source analysis. The very high time resolution of the EEG enables us to track the source estimations in time. The timing information of the source estimations can reveal connectivity patterns between brain regions. These brain regions can be pinpointed by functional MRI (fMRI), a technique that measures the functionality of the brain. Ultimately, these connectivity patterns can be made more robust by including the anatomical connections, derived by fiber tracking using DW-MRI.

In the clinical practice in epilepsy, there is still a discussion whether spikes and seizures originate from the same onset zone. The technique presented in this dissertation is a tool to confirm of refute this hypothesis. Functional magnetic resonance imaging is a recent MR technique that images consumption of oxygen in brain area's due to an event, triggered by an condition (e.g. spikes). It involves a statistical processing of triggered events, such as spikes. However, this technique is not feasible to image the activity of a epileptic seizure, as the patient has to be inside an MR scanner and the decreased consumption of oxygen is only visible in a small time period of time (order of seconds).

Ictal SPECT has been shown to have high diagnostic value in epilepsy [142]. Here a radiopharmacon is injected at start of the seizure and perfuses in brain regions with high activity. The radiopharmacon remains in the activated region even when the seizure has ended. Due to the long half-life of the radiopharmacon, it is still possible to visualize the activated regions when the patient has rested from the seizure. To relate the ictal SPECT activity with the fMRI activity would be difficult as they are both based on different physiological processes and have different time resolutions. However, both modalities can be used as a prior in the EEG source estimation procedure. Hence by comparing the source estimations in space and in time when both modalities are used as a priori information, one can relate the activity of a seizure with the one of a spike.

Ideally, both prevouis modalities, fMRI and SPECT, in combination with EEG source analysis as described in this dissertation can be used in the presurgical evaluation of patients suffering from epilepsy. If all the information is combined into a tool that can determine the origin of brain activity, neurologists and psychologists could diagnose and precribe treatment in a more reliable and accurate way. This could be useful in the diagnosis of, for instance, epileptic seizures or spikes but also other neurologic disorders could benefit from it.

Appendix A

Reciprocal Approaches

In the literature one finds two approaches to solve the forward problem. In the conventional approach, the transfer-coefficients making up the leadfield matrix **L** in equation (2.24) are obtained by calculating the surface potentials from dipole sources via Poisson's equation. The calculations are made for each dipole position within the head model and the potentials at the electrode positions are recorded.

In the reciprocal approach introduced in Rush and Driscoll [127], Helmholtz' principle of reciprocity is used. The electric field that results at the dipole location within the brain due to current injection and withdrawal at the surface electrode sites is first calculated. The forward transfer-coefficients are obtained from the scalar product of this electric field and the dipole moment. Calculations are thus performed for each electrode position rather than for each dipole position. This speeds up the time necessary to do the forward calculations since the number of electrodes is much smaller than the number of possible dipoles.

A.1 The general idea of reciprocity

Consider a resistor circuit, with two clamps AB and r_x as illustrated in figure A.1. The clamp AB represents a pair of scalp electrodes. The clamp r_x is located in the brain region.

First a current I_{r_x} at clamp r_x is introduced. This source will generate a potential $U_{AB}(I_{r_x})$ at AB as illustrated in figure A.1(a). Next, current I_{AB} at AB is set. This will give rise to a potential difference $V_{r_x}(I_{AB})$ at r_x illustrated in figure 13(b). The reciprocity theorem in circuit analysis states:

$$U_{AB}\ I_{AB} = V_{r_x}\ I_{r_x}. \tag{A.1}$$

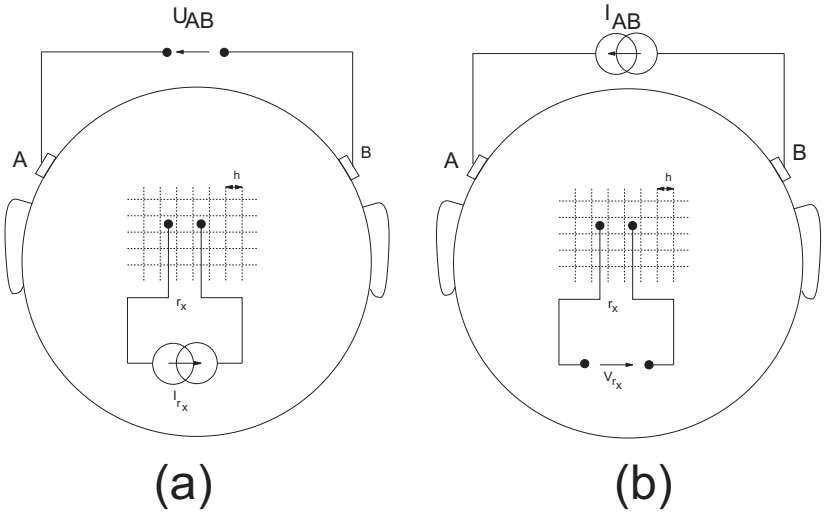

Figure A.1: A schematic representation of the reciprocity theorem. A resistor network where a current source is introduced in the brain and the potential difference is measured at an electrode pair, and visa versa: (a) a current source I_{r_x} is introduced and the potential U_{AB} is measured, and (b) a current source I_{AB} is introduced and a potential V_{r_x} is measured.

A.2 Mathematical treatment

A mathematical treatment for a digitized volume conductor model is developed in this section. Consider a digitized volume conductor model with n computational points or nodes. At each of the nodes the potential V_i with $i = 1 \dots n$ is calculated for given sources which are the current monopoles I_i with $i = 1 \dots n$. Poisson's equation can then be transformed to a linear equation at each node, as illustrated for the FEM and FDM in subsections 2.4.2.5 and 2.4.2.6. This set of linear equations can be written in matrix notation. The system matrix then becomes $\mathbf{A} \in \mathbb{R}^{n \times n}$ and has the following properties: it is sparse, symmetric and regular. One can write:

$$\mathbf{A}.\mathbf{V} = \mathbf{I},$$

with $\mathbf{V} = [V_1 \dots V_n]^T \in \mathbb{R}^{n \times 1}$ and $\mathbf{I} = [I_1 \dots I_n]^T \in \mathbb{R}^{n \times 1}$ and with ^{T} the transpose operator. The desired potential difference $V_k - V_l$ between nodes k and l can be obtained for a current source I_f at node f and a current sink I_g at node g with $I_f = -I_g$. All other sources are zero. Cramer's solution for a linear system then becomes:

$$V_k = \frac{I_f[(-1)^{k+f+1} A_{fk} - (-1)^{k+g+1} A_{gk}]}{\det \mathbf{A}}, \tag{A.2}$$

$$V_l = \frac{I_f[(-1)^{l+f+1}A_{fl} - (-1)^{l+g+1}A_{gl}]}{\det \mathbf{A}}, \tag{A.3}$$

with $A_{*\circ}$ the minor for row $*$ and column $\circ$.

On the other hand the potential V_f and V_g for a current source I_k and current sink I_l with $I_k = -I_l$, are:

$$V_f = \frac{I_k[(-1)^{f+k+1}A_{kf} - (-1)^{f+l+1}A_{lf}]}{\det \mathbf{A}}, \tag{A.4}$$

$$V_g = \frac{I_k[(-1)^{g+k+1}A_{kg} - (-1)^{g+l+1}A_{lg}]}{\det \mathbf{A}}. \tag{A.5}$$

Furthermore, $A_{*\circ}$ is equal to $A_{\circ *}$ due to the fact that $\mathbf{A}$ is symmetric. Hence, (eqn.(A.2) – eqn.(A.3))/I_f equals (eqn.(A.4) – eqn.(A.5))/I_k. Subsequently the reciprocity theorem is deduced:

$$I_k(V_k - V_l) = I_f(V_f - V_g).$$

A.3 Reciprocity for a dipole source with random orientation

Considering equation (A.1), a dipole can be represented as two current monopoles, a current source and sink, providing I_{r_x} and $-I_{r_x}$, separated by a distance $2h$. The dipole is oriented from the negative to the positive current monopole and is assumed to be along the x-axis of the resistor network with node spacing h. The magnitude of the dipole moment is then $2hI_{r_x}$. The centre $\mathbf{r}$ of the two monopoles can then be seen as the dipole position. The scalp electrodes are located sufficiently far from the sources compared with the distance $2h$ between the sources so that we can assume a dipole field. Equation (A.1) can be rewritten as:

$$U_{AB} = \frac{V_{r_x}\, I_{r_x}}{I_{AB}}. \tag{A.6}$$

The forward problem in EEG source analysis gives the potential U_{AB} for a current dipole located at $\mathbf{r}$ and oriented along the x-axis. Rewriting equation(A.6) with $d_x = 2hI_{r_x}$ and

$$\frac{\partial V}{\partial x} \approx \frac{[V_{I_{AB}}(\mathbf{r} + h\mathbf{e}_x) - V_{I_{AB}}(\mathbf{r} - h\mathbf{e}_x)]}{2h},$$

gives:

$$U_{AB} = \frac{d_x \frac{\partial V}{\partial x}}{I_{AB}}. \tag{A.7}$$

In a similar way, U_{AB} can be calculated for a dipole located at $\mathbf{r}$ oriented along the y-axis and the z-axis.

Consider a dipole at position $\mathbf{r}$ and with dipole components $\mathbf{d} = (d_x, d_y, d_z)^T \in \mathbb{R}^{3\times 1}$. The potential U_{AB} reads:

$$U_{AB}(\mathbf{r}, \mathbf{d}) = \frac{\mathbf{d}^T \cdot \nabla V(\mathbf{r})}{I_{AB}}, \tag{A.8}$$

with $\nabla V(\mathbf{r}) = (\partial V(\mathbf{r})/\partial x, \partial V(\mathbf{r})/\partial y, \partial V(\mathbf{r})/\partial z)^T \in \mathbb{R}^{3\times 1}$.

The flowchart in figure A.2 shows the consecutive steps that are necessary in the reciprocity approach in conjunction with FDM.

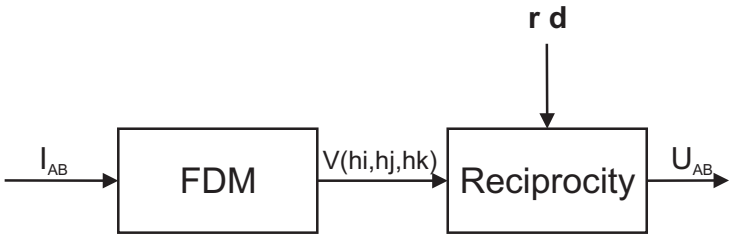

Figure A.2: The consecutive steps when applying reciprocity in conjunction with FDM is shown. First a current dipole I_{AB} is set on the electrode pair AB. Using FDM the potential field is calculated in each point $V(ih, jh, kh)$. With the dipole parameters and the potential field, the reciprocity theorem can be applied. This results in a potential difference at the electrode pair AB.

- A fictive current I_{AB} of arbitrary value is introduced which enters the head at electrode A and leaves the head at electrode B.
- Utilizing the FDM the potentials $V(hi, hj, hk)$ can be calculated with h the internode spacing and i, j, k the node numbers along the Cartesian axes. Figure A.3 illustrates the equipotential lines and current density vectors $\mathbf{J} = -\sigma\nabla V$ in the brain region, with $\nabla V = (\partial V/\partial x, \partial V/\partial y, \partial V/\partial z)^T$. The partial derivative $\partial V/\partial x$ is approximated by $[V(h(i+1), hj, hk) - V(h(i-1), hj, hk)]/2h$. The partial derivatives $\partial V/\partial y, \partial V/\partial z$ are obtained in a similar way.
- U_{AB} the potential difference between the scalp electrodes A and B generated by the dipole at position $\mathbf{r}$ and dipole moment $\mathbf{d}$ is obtained by applying eqn. (A.8). When $\mathbf{r}$ does not coincide with a node, then $\nabla V(\mathbf{r})$ is obtained with tri-linear interpolation [116].

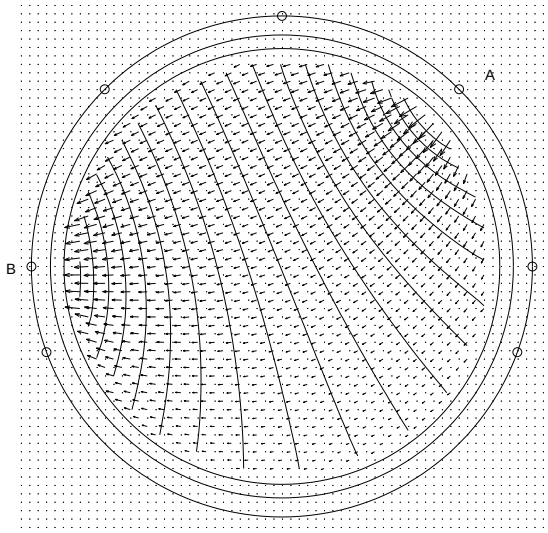

Figure A.3: The equipotential lines and the current density vectors caused by a current source and current sink at two electrodes.

By solving only one forward calculation numerically, by introducing current monopoles at electrodes A and B, and storing the obtained node potentials in a data structure, U_{AB} is obtained for every dipole position and orientation.

If N scalp electrodes are used to measure the EEG, $N-1$ electrode pairs can be found with linear independent potential differences. Therefore $N-1$ numerical forward calculations are performed and stored in data structures. In addition, the $N-1$ potential differences at the $N-1$ electrode pairs are transformed in N average referenced potentials at the N electrodes.

Reciprocity has been applied in the literature in conjunction with BEM [45], FEM [149] and FDM [88, 89, 144, 145, 64].

Appendix B

Volume Constraint

B.1 Introduction

Diffusion is the transporation of water molecules, while conductivity is the transportation of charged particles. Although two different processes, they can be written according to the same transport equation [139]. Using the two approaches given in 4.5 and 4.6, a set of equation relates the eigenvalues of the conductivity tensors and diffustion tensors. However, the system of equations is underdetermined and the conductivity eigenvalues are unknown up to a scaling factor. One way to determine the scaling factor is by relating the anisotropic conductivity tensor with the isotropic values. These isotropic values have been measured in Gonçalves et al. [50], Ferree et al. [44] and Lai et al. [90].

In this section, we will discuss a model to relate the conductivity with the isotropic conductivity. Therefore, we can derive the conductivity tensor using the diffusion tensor, calculated from the diffusion weighted images. First, the representation of the diffusion of conductivity tensor in ellipsiods will be discussed.

B.2 Representation of the diffusion tensor as ellipsoids

The anisotropic conductivity can be represented as ellipsoids. The radii of the ellipsoid denote the conductivity int each direction. For example, in the scalp we model the conductivity as isotropic: The conductivity in each direction is the same (e.g. at the scalp the conductivity is $\sigma_{scalp} = 0.33\ S/m$) and this can be represented by a perfect sphere (see figure B.1a). If there is one direction in which the conductivity is higher than the other two, then a cigar-shaped

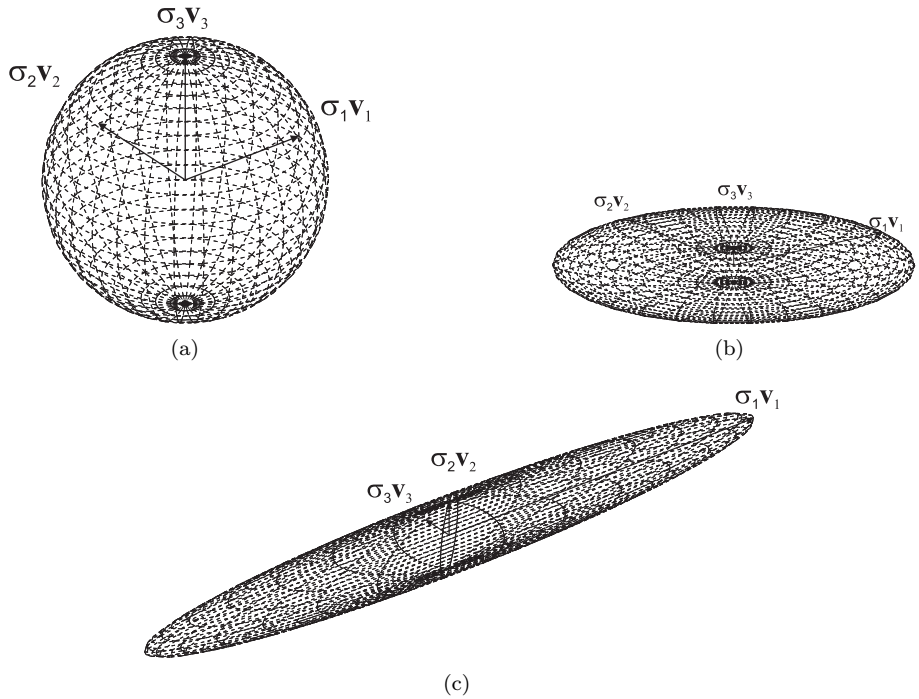

Figure B.1: An illustration of the representation of a tensor as an ellipsoid. (a) shows an sphere, the conductivity of diffusion is equal in all direction. (b) shows an oblique ellipsoid, the conductivity of diffusion is large in two directions as opposed to the third direction. (c) shows an cigar-shpaed ellipsoid, the conductivity or diffusion is large in 1 direction as opposed to the other orthogonal directions.

ellipsoid occurs (see figure B.1c). With 2 principle directions the ellipsoid has an oblique shape (see figure B.1b).

B.3 Deriving the conductivity tensor from the diffusion tensor using the volume constraint

The *volume constraint* [150] states that the volume of the isotropic conducting sphere must be equal to the anisotropic conducting ellipsoids:

$$\frac{4}{3}\pi\sigma_{isotropic}^3 = \frac{4}{3}\pi\sigma_1\sigma_2\sigma_3. \tag{B.1}$$

The constraint can be used to model the anisotropic conductivity, if the isotropic conductivity is known. These isotropic conductivities have been measured

using Electric Impedance Tomography [44, 50]. Maxwell [97] showed that a current at the center of the medium in a homogeneous anisotropic infinite medium, has equipotential lines with an ellipsoidal shape. Each equipotential line is associated with a constant charge density ρ. In isotropic media, the equipotential lines are spheres. Although a proof of the validity of this assumption does not exist, we believe it is a sound model for anisotropy.

B.3.1 Skull

For the skull we model the conductivity as an oblique ellipsoid, which means that 2 of the principal directions are the same. These directions correspond to the tangential direction on the surface. Together with the fact that the tangential conductivity σt is modelled 10 times larger than the normal conductivity σn we obtain the following system of equations:

$$\frac{4}{3}\pi\sigma_{isotropic}^3 = \frac{4}{3}\pi\sigma_t^2\sigma_n \tag{B.2}$$

$$10\sigma_{rad} = \sigma_{tang} \tag{B.3}$$

where $\sigma_{isotropic}$ is 0.020 S/m for the skull compartment. Using these equations, we can solve σ_t and σ_r yielding the conductivity in the tangential and radial direction respectively. Solving the equations yields a radial conductivity of $\sigma_n^{skull} = 0.004309\ S/m$ and a tangential conductivity of $\sigma_t^{skull} = 10\sigma_n^{skull} = 0.04309\ S/m$

B.3.2 White Matter: simplified approach

In the simplified approach the conductivity along the nerve fibre σ_l is 9 times larger than the conductivity perpendicular to the nerve fibre σ_p. Note that the conducitivity tensor can then be written as:

$$\mathbf{\Sigma} = \begin{bmatrix} \sigma_l & 0 & 0 \\ 0 & \sigma_p & 0 \\ 0 & 0 & \sigma_p \end{bmatrix}. \tag{B.4}$$

For white matter anisotropy we modelled that they spread in the radial direction. We obtain the following equations:

$$\frac{4}{3}\pi\sigma_{isotropic}^3 = \frac{4}{3}\pi\sigma_p^2\sigma_l \tag{B.5}$$

$$9\sigma_p = \sigma_l \tag{B.6}$$

where $\sigma_{isotropic}$ is $0.33 S/m$ for the brain compartment. Solving these equations yield σ_t and σ_r or the conductivity in the transversal direction (tangential direction) and in the longitudinal direction of the nerve fiber (radial direction),

respectively. The results are a radial conductivity of $\sigma_r^{whitematter} = 1.4278\ S/m$ and a tangential conductivity of $\sigma_t^{whitematter} = 0.15864\ S/m$.

B.3.3 White Matter and gray matter: more realistic approach

In the realistic approach, the eigenvalues of the conductivity tensor are related those of the diffusion tensor. The ratio between the diffusion eigenvalues and the conductivity values associated with the same eigenvectors are constant and dependent on the volume constraint. If we denote the eigenvalues of the diffusion tensor as d_1, d_2, d_3 and the conductivity values as $\sigma_1, \sigma_2, \sigma_3$, we can write:

$$\frac{4}{3}\pi\sigma_{isotropic}^3 = \frac{4}{3}\pi\sigma_1\sigma_2\sigma_3 \tag{B.7}$$

$$\frac{d_1}{\sigma_1} = \frac{d_2}{\sigma_2} \tag{B.8}$$

$$\frac{d_1}{\sigma_1} = \frac{d_3}{\sigma_3} \tag{B.9}$$

where $\sigma_{isotropic}$ is $0.33 S/m$ for the brain compartment. Solving these equations yield σ_1, σ_2 and σ_3 or the conductivity along the three principle directions of the diffusion. As the diffusion tensor is variable throughout the white and gray matter, so will the conductivity tensor. Therefore, the absolute values of the conductivity along the principal directions is position dependent and has to be calculated each time.

Appendix C

Solving EEG inverse problem using space mapping techniques

C.1 Introduction

The EEG inverse problem can be solved in a non-parametric way and parametric way. The non-parametric way supposes a current distribution along the human brain and is solved by minimizing a properly chosen regularized cost function [112]. The parametric way of solving the EEG inverse problem is the reconstruction of one or a limited number of multiple electrical dipoles [103]. This paper focusses on the parametric way of solving the EEG inverse problem since epileptic foci may be represented by dipoles [40].

The inverse problem is solved by minimizing the least squares cost between the electrode potentials of the patient $\mathbf{V}_{in}$ and the simulated electrode potentials $\mathbf{V}_{model}$ due to a dipole source at location $\mathbf{r}$ with orientation $\mathbf{d}$. For a given dipole position $\mathbf{r}$, the optimal components in the least-squares sense $\mathbf{d}_{opt}$ are found from the best approximated solution of the overdetermined system of linear equations (2.24):

$$\mathbf{d}_{opt} = \mathbf{L}^{+} \cdot \mathbf{V}_{in} \tag{C.1}$$

with $\mathbf{L}^{+} = (\mathbf{L}^{T}\mathbf{L})^{-1}\mathbf{L}^{T}$ being the Moore-Penrose pseudo-inverse of the leadfield matrix $\mathbf{L}$. The EEG cost function is defined as follows:

$$RRE(\mathbf{r}) = \frac{\|\mathbf{V}_{in} - \mathbf{L}(\mathbf{r})\mathbf{L}(\mathbf{r})^{+} \cdot \mathbf{V}_{in}\|}{\|\mathbf{V}_{in}\|} \tag{C.2}$$

and is also called the relative residual energy (RRE). $\|\cdot\|$ is the L_2-norm. The result is a dipole estimate at location $\hat{\mathbf{r}}$:

$$(\hat{\mathbf{r}}, \hat{\mathbf{d}}) = \arg \min_{\mathbf{r}\in\Omega_{cc}, \mathbf{d}\in]0,2\pi]} RRE(\mathbf{r}) \tag{C.3}$$

The RRE is minimized in the cerebral cortex, with the following location region in the head Ω_{cc}, of the patient's head. This is *a priori* known information since the information is coregistered with the MR images.

C.2 Traditional one-level inverse EEG procedures

The EEG inverse problem is typically solved by traditional optimization methods, which use only one forward model in the inverse procedure. The widely-used Nelder-Mead Simplex method [36], simulated annealing [86], genetic algorithm [82], etc. are typical methods. These approaches are highly time-consuming and unsuitable for the rapid evaluation of the location and orientation of neural sources. Indeed, many evaluations are needed in the forward model. Further, when assuming a well-defined search region, difficulties occur concerning convergence. Much more start values are needed for solving the inverse problem when using the NMS method for solving the inverse problem.

Another possibility for solving the EEG inverse problem is the use of artificial neural networks (ANNs). Such methods are very fast but are not robust to noise [141].

C.3 Space Mapping techniques

The space mapping (SM) technique, introduced by Bandler et al. [11], is used for optimization of engineering models which involve complex and expensive function evaluations. The technique has been succesfully applied in the field of microwaves for component and system modelling, for a review see Bandler et al. [12]. The SM technique assumes that two different models of the same physical system are available. The technique aims at combining the computational efficiency of a coarse model with the accuracy of a fine model. We want to optimize a costfunction (in our case the RRE) in the accurate but computationally-intensive fine model. Recently, SM techniques have be introduced to the field of EEG source estimation. Due to their fast convergen and their robustness to noise, they have proven to be very useful in the optimization procedure when solving the inverse problem [33].

In space mapping techniques, we use two volume conductor models (a fine and a coarse head model) for solving the forward problem. The coarse head model

is a 3-shell concentric spherical head model, where the forward problem can be solved usint an analytical formula. The fine head model is the realistic head model, where the AFDRM is used to solve the forward problem. The leadfield matrix in the coarse and the fine head model due to a dipole at position $\mathbf{r}_i$ can be indicated as $\mathbf{L}_c(\mathbf{r}_i)$ and $\mathbf{L}_f(\mathbf{r}_i)$, respectively.A geometrical link between the two head models has to be set. This is done by performing a least-squares fit of the spherical head model on the realistic head model.

Let $\mathbf{f}(\mathbf{r}_f) : \Omega_f \rightarrow \mathbb{R}^m$ and $\mathbf{c}(\mathbf{r_c})\Omega_f \rightarrow \mathbb{R}^m$ be functions that model the EEG signals in the fine and coarse model respectively, located at a location $\mathbf{r}_f$ and $\mathbf{r}_c$. Ω_f and Ω_c are the parameter spaces (in our case the space spanned by the dipole location parameters) of the fine and coarse model. It is possible to express:

$$\mathbf{f}(\mathbf{r}_f) = \mathbf{L}_f(\mathbf{r}_f)\mathbf{L}_f(\mathbf{r}_f)^+\mathbf{V}_{in} \tag{C.4}$$

$$\mathbf{c}(\mathbf{r}_c) = \mathbf{L}_c(\mathbf{r}_c)\mathbf{L}_c(\mathbf{r}_c)^+\mathbf{V}_{in} \tag{C.5}$$

when considering one dipole at location $\mathbf{r}_f$ because the optimal dipole orientation can be found by the least-squares estimate $\mathbf{d}_f = \mathbf{L}_f(\mathbf{r}_f)^+\mathbf{V}_{in}$. $\mathbf{L}_f(\mathbf{r}_f)^+$ is the Moore-penrose pseudo-inverse of the leadfield matrix of the fine head model and $\mathbf{V}_{in}$ are the measured electrode potentials at the scalp of the patient.

Initially, the dipole location $\mathbf{r}$ is estimated in the fine model by minimizing the relative residual energy as in equation C.3:

$$RRE_F(\mathbf{f}(\mathbf{r}_f)) = \frac{\|\mathbf{V}_{in} - \mathbf{f}(\mathbf{r}_f)\|}{\|\mathbf{V}_{in}\|}. \tag{C.6}$$

Hence, finding the optimal dipole location can be written as:

$$\hat{\mathbf{r}}_f = \arg \min_{\mathbf{r}_f \in \Omega_f} RRE_F(\mathbf{f}(\mathbf{r}_f)) \tag{C.7}$$

The non-convexity of the head model increases the chance of getting trapped into local minima. Moreover, if one restricts the search space to only the cortical gray matter, many start values are needed to obtain a global minimum.

Similar for the coarse head model, the cost function to be optimized to solve the inverse problem can be written as:

$$RRE_C(\mathbf{c}(\mathbf{r}_c)) = \frac{\|\mathbf{V}_{in} - \mathbf{c}(\mathbf{r}_c)\|}{\|\mathbf{V}_{in}\|}. \tag{C.8}$$

Due to simplicity of the coarse model (the 3 shell spherical head model) the global minimum $\hat{\mathbf{r}}_c$ of RRE_C

$$\hat{\mathbf{r}}_c = \arg \min_{\mathbf{r}_c \in \Omega_c} RRE_C(\mathbf{c}(\mathbf{r}_c)) \tag{C.9}$$

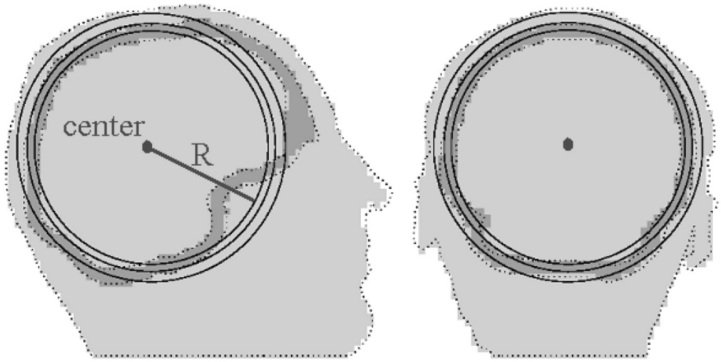

Figure C.1: An illustration of the geometrical link between the coarse model and the fine model

can be calculated in a computational efficient way. Moreover, the convex search space reduces the possibility of getting trapped in local minima. Therfore, the coarse model $\mathbf{c}(\mathbf{r}_c)$ will be used as the basis for generating successive surrgates for the fine one. A suitable surrogate model is obtained by constructing a mapping between the parameters spaces of the two models. Let a parameter mapping $\mathbf{p} : \Omega_f \rightarrow \Omega_c$ be an approximation of the form:

$$\mathbf{f}(\mathbf{r}_f) \approx \mathbf{c}(\mathbf{p}(\mathbf{r}_f)). \tag{C.10}$$

Finding the parameter mapping $\mathbf{r}_c = \mathbf{p}(\mathbf{r}_f)$, the so called parameter extraction (PE) is a very important subproblem of the SM technique. We extract the parameters of the coarse model to match the fine model:

$$\mathbf{p}(\mathbf{r}_f) = \arg \min_{\mathbf{r}_c \in \Omega_c} \|\mathbf{f}(\mathbf{r}_f) - \mathbf{c}(\mathbf{r}_c)\| . \tag{C.11}$$

If the approximation C.10 is valid, then the composite function $\mathbf{c}(\mathbf{p}(\mathbf{r}_f))$, is applicable for a surrogate of $\mathbf{f}$. Hence, the optimum of $\mathbf{c}(\mathbf{p}(\mathbf{r}_f))$ can be expected close to the optimum of $\mathbf{f}(\mathbf{r}_f)$. For evaluating $\mathbf{p}(\mathbf{r}_f)$ in equation C.11, one evaluation in the fine model has to be evaluated.

Fitting the inner shell of the spherical head model between the brain and skull compartments in the realistic head model makes the geometric link between the parameters of the two volume conductor models (see figure C.1). The center and radius of the three layers of the coarse model are determined that way using a least squares approximation. In order to apply SM, we assure that $\Omega_c \subset \Omega_f$. Indeed, the first iterate $\mathbf{r}_f^{(1)} = \hat{\mathbf{r}}_c$ in the fine model for every $\hat{\mathbf{r}}_c$ has to be possible. The PE (see equation C.11) can be written as

$$\mathbf{p}(\mathbf{r}_f) = \arg \min_{\mathbf{r}_c \in \Omega_c} \|\mathbf{f}(\mathbf{r}_f) - \mathbf{c}(\mathbf{r}_c)\| \tag{C.12}$$

$$= \arg \min_{\mathbf{r}_c \in \Omega_c} \left\| (\mathbf{I}_m - \mathbf{L}_c(\mathbf{r}_c)\mathbf{L}_c(\mathbf{r}_c)^+)\mathbf{f}(\mathbf{r}_f) \right\| \tag{C.13}$$

where $\mathbf{I}_m$ is the identity matrix. Here, $\mathbf{c}(\mathbf{r}_c) = \mathbf{L}_c(\mathbf{r}_c)\mathbf{L}_c(\mathbf{r}_c)^+\mathbf{f}(\mathbf{r}_f)$, which is the coarse model with the fine model $\mathbf{f}(\mathbf{r}_f)$ as $\mathbf{V}_{in}$.

C.3.1 Agressive Space Mapping (ASM)

The Agressive Space Mapping (ASM) technique intends to solve the nonlinear equations

$$\mathbf{e}(\mathbf{r}_f) = 0 \tag{C.14}$$

with the error-function $\mathbf{e} : \Omega_f \rightarrow \Omega_c : \mathbf{e}(\mathbf{r}_f) = \mathbf{p}(\mathbf{r}_f) - \hat{\mathbf{r}}_c$ for $\mathbf{r}_f$ by means of quasi-Newton iterations using the classical Broyden formula [26]. This is an iterative procedure that updates $\mathbf{r}_f$ to obtain the solution. The first iteration $\mathbf{r}_f^{(1)}$ is equal to $\hat{\mathbf{r}}_c$. Let $\mathbf{r}_f^{(k)}$ be the k-th iteration in the solution of equation C.14. The next iteration can be written as:

$$\mathbf{r}_f^{(k+1)} = \mathbf{r}_f^{(k)} + \mathbf{h}^{(k)} \tag{C.15}$$

where the step $\mathbf{h}^{(k)}$ is obtained from

$$\mathbf{B}^{(k)}\mathbf{h}^{(k)} = -\mathbf{e}(\mathbf{x}_f^{(k)}). \tag{C.16}$$

$\mathbf{B}^{(k)} \in \mathbb{R}^{m \times m}$ is the approximation of the mapping Jacobian (see Bandler et al. [12], for further details). An initial approximation to $\mathbf{B}$ can be taken as the identity matrix. $\mathbf{B}^{(k)}$ can be updated using Broyden's rank one formula:

$$\mathbf{B}^{(k+1)} = \mathbf{B}^{(k)} + \frac{\mathbf{e}^{(k)}}{\mathbf{h}^{(k)T}\mathbf{h}^{(k)}}\mathbf{h}^{(k)T} \tag{C.17}$$

where $\mathbf{e}^{(k)} = \mathbf{e}(\mathbf{x}_f^{(k)})$. It becomes clear that the algorithm stops when $\left\|\mathbf{e}^{(k)}\right\|$ becomes sufficiently small.

C.3.2 Trust Region Aggressive Space Mapping

In Bakr et al. [9] a Trust Region Aggressive Space Mapping (TRASM) was used. The step $\mathbf{h}^{(k)}$ in equation C.15 is solved according to

$$\left(\mathbf{B}^{(k)T}\mathbf{B}^{(k)} + \lambda\mathbf{I}\right)\mathbf{h}^{(k)} = -\mathbf{e}(\mathbf{r}_f^{(k)}) \tag{C.18}$$

with λ a parameter which is chosen so that the step satisfied $\left\|\mathbf{h}^{(k)}\right\| \leq \delta$, where δ is the size of the trust region. Hence we can choose the step so that the

update $\mathbf{r}_f^{(k+1)}$ remains in a specified region. In our case λ is chosen in such a way that $\mathbf{r}_f^{(k+1)}$ remains in the gray matter region.

C.3.3 Hybrid Aggressive Space Mapping (HASM)

The HASM enables switching between direct optimization in the traditional way and TRASM. If TRASM is not converging to a minimum then the algorithm switches to direct optimization in the fine model and vice versa. Fur further details we refer to Bakr et al. [10].

References

[1] "IP-NEUROFEM: A C++ class structured code for fast high-resolution finite element method based EEG and MEG source analysis", URL `http://www.neurofem.com`.

[2] Z. Akalin-Acar and N. Gençer, "An advanced boundary element method (bem) implementation for the forward problem of electromagnetic source imaging", *Physics in Medicine and Biology*, 49:5011–5028, 2004.

[3] A. Anwander, C.H. Wolters, M. Dümpelmann, and T. Knösche, "Influence of realistic skull and white matter anisotropy on the inverse problem in EEG/MEG-source localization", *Proceedings of the International Conference on Biomagnetism (BioMag2002)*, 2002.

[4] J.P. Ary, S.A. Klein, and D.H. Fender, "Location of sources of evoked scalp potentials: Corrections for skull and scalp thicknesses", *IEEE Transactions on Biomedical Engineering*, 28(6):447–452, June 1981.

[5] S. Assecondi, H. Hallez, Y. D'Asseler, and I. Lemahieu, "Comparison of different auto-solid angle approximations in bem for eeg dipole source localization", In *Proceedings of the Joint Meeting of the 6th International Symposium on Noninvasive Functional Source Imaging of the Brain and Heart and the International Conference on Functional Biomedical Imaging (NFSI-ICFBI 2007)*, pages 70–73, 12–14 October 2007.

[6] K.A. Awada, D.R. Jackson, J.T. Williams, D.R. Wilton, S.B. Baumann, and A.C. Papanicolaou, "Computational aspects of finite element modeling in eeg source localization", *IEEE Transactions on biomedical engineering*, 44:736–752, 1997.

[7] K.A. Awada, D.R. Jackson, S.B. Baumann, J.T. Williams, D.R. Wilton, P.W. Fink, and B.R. Prasky, "Effect of conductivity uncertainties and modeling errors on EEG source localization using a 2D-model", *IEEE Transactions on Biomedical Engineering*, 45 (9):1135–1145, 1998.

[8] S. Baillet, J. C. Mosher, and R. M. Leahy, "Electromagnetic brain mapping", *IEEE Signal Processing Magazine*, November:14–30, 2001.

[9] M. H. Bakr, J. W. Bandler, R. M. Biernacki, S. H. Chen, and K. Madsen, "A trust region aggressive space mapping algorithm for em optimization", *IEEE Transactions on Microwave Theory and Techniques*, 46:2412–2425, 1998.

[10] M. H. Bakr, J. W. Bandler, N. K. Georgieva, and K. Madsen, "A hybrid aggressive space mapping algorithm for em optimization", *IEEE Transactions on Microwave Theory and Techniques*, 47:2440–2449, 1999.

[11] J. W. Bandler, R. M. Biernacki, S. H. Chen, P. A. Grobelny, and R. H. Hemmers, "Space mapping technique for electromagnetic optimization", *IEEE Transactions on Microwave Theory and Techniques*, 42:2536–2544, 1994.

[12] J. W. Bandler, Q. S. Cheng, A. S. Dakroury, M. H. Mohamed, M. H. Bakr, K. Madsen, and J. Søndergaard, "Space mapping: The state of the art", *IEEE Transaction on Microwave Theory and Techniques*, 52: 337–361, 2004.

[13] A. C. L. Barnard, I. M. Duck, and M. S. Lynn, "The application of electromagnetic theory to electrocardiography: I. derivation of the integral equations", *Biophysics Journal*, 7:443–462, 1967.

[14] A.C.L. Barnard, I.M. Duck, M.S. Lynn, and W.P. Timlake, "The application of electromagnetic theory to electrocardiology ii: Numerical solution to the integral equations.", *Biophysical Journal*, 7:463–491, 1967.

[15] R. Barrett, M. Berry, T. F. Chan, J. Demmel, J. Donato, J. Dongarra, V. Eijkhout, R. Pozo, C. Romine, and H. Van der Vorst, *Templates for the Solution of Linear Systems: Building Blocks for Iterative Methods, 2nd Edition*. SIAM, Philadelphia, PA, 1994.

[16] P. J. Basser and D. K. Jones, "Diffusion-tensor MRI: theory, experimental design and data analysis - a technical review", *Nuclear Magnetic Resonance in Biomedicine*, 15:456–467, 2002.

[17] P.J. Basser and C. Pierpaoli, "Microstructural and physiological features of tissues elucidated by quantitative-diffusion-tensor MRI", *Journal of Magnetic Resonance B*, 111(3):209–219, June 1996.

[18] P.J. Basser, J. Mattiello, and D. Le Bihan, "Estimation of the effective self-diffusion tensor from the NMR spin echo", *Journal of Magnetic Resonance B*, 103:247–254, 1994.

[19] P.J. Basser, J. Mattiello, and D. LeBihan, "MR diffusion tensor spectroscopy and imaging", *Biophysical Journal*, 66:259–267, January 1994.

[20] S.B. Baumann, D.R. Wozny, S.K. Kelly, and F.M. Meno, "The electrical conductivity of human cerebrospinal fluid at body temperature", *IEEE Transactions on Biomedical Engineering*, 44(3):220–223, 1997.

[21] P. Berg and M. Scherg, "A fast method for forward computation of multiple-shell spherical head models", *Electroencephalography and Clinical Neurophysiology*, 90:58–64, 1994.

[22] H. Berger, "Über das elektroenkephalogramm des menschen", *Archiv für Psychiatrie und Nervenkrankheiten*, 87:527–570, 1929.

[23] P. Boon, T. Vandekerckhove, E. Achten, E. Thierry, L. Goossens, K. Vonck, M. D'have, G. Van Hoey, B. Vanrumste, B. Legros, L. Defreyne, and J. De Reuck, "Epilepsy surgery in Belgium, the experience in Gent", *Acta Neurologica Belgica*, 99(4):256–265, December 1999.

[24] P. Boon, M. D'Havé, B. Vanrumste, G. Van Hoey, K. Vonck, P. Van Walleghem, J. Caemaert, E. Achten, and J. De Reuck, "Ictal source localization in presurgical patients with refractory epilepsy.", *J Clin Neurophysiol*, 19(5):461–468, October 2002.

[25] William L. Briggs, *A multigrid tutorial*. SIAM, 1987.

[26] C. G. Broyden, "A class of methods for solving nonlinear simultaneaous equations", *Mathematics of Computation*, 19:577–593, 1965.

[27] L.-C. Chang, D. K. Jones, and C. Pierpaoli, "RESTORE: robust estimation of tensors by outlier rejection.", *Magnetic Resonance in Medicine*, 53(5):1088–1095, May 2005.

[28] N. Chauveau, X. Franceries, B. Doyon, B. Rigaud, J. P. Morucci, and P. Celsis, "Effects of skull thickness, anisotropy, and inhomogeneity on forward EEG/ERP computations using a spherical three-dimensional resistor mesh model", *Human Brain Mapping*, 21(2):86 – 97, 2003.

[29] B. Chen and E. W. Hsu, "Noise removal in magnetic resonance diffusion tensor imaging.", *Magnetic Resonance in Medicine*, 54(2):393–401, August 2005.

[30] F. Chen, H. Hallez, P. Van Hese, Y. D'Asseler, and I. Lemahieu, "Dipole estimation errors due to skull conductivity perturbations: Simulation study in spherical head models", In *Proceedings of the Joint Meeting of the 6th International Symposium on Noninvasive Functional Source Imaging of the Brain and Heart and the International Conference on Functional Biomedical Imaging (NFSI-ICFBI 2007)*, pages 86–89, 12–14 October 2007.

[31] M. Clerc, J.-M. Badier, G. Adde, J. Kybic, and T. Papadopoulo, "Boundary element formulation for electric impedance tomography", In *ESAIM: Proceedings*, volume 14, pages 63–71, 2005.

[32] G. Crevecoeur, H. Hallez, P. Van Hese, Y. D'Asseler, L. Dupre, and R. Van de Walle, "Influence of noise on EEG source analysis using space mapping techniques", *International Journal of Applications in Electromagnetics and Mechanics*, 25:383–387, 2007.

[33] G. Crevecoeur, H. Hallez, P. Van Hese, Y. D'Asseler, L. Dupre, and R. Van de Walle, "EEG source analysis using space mapping techniques", *Journal of Computational and Applied Mathematics*, 215:339–347, 2008.

[34] B. N. Cuffin, "Effects of local variations in skull and scalp thickness on EEG's and MEG's", *IEEE Transactions on Biomedical Engineering*, 40 (1):42–48, January 1993.

[35] B.N. Cuffin, "EEG dipole source localization", *IEEE Engineering in Medicine and Biology*, 17(5):118–122, 1998, ISSN 0739-5175, doi: 10.1109/51.715495.

[36] N. Cuffin, "A method for localizing eeg sources in realistic head models", *IEEE Transactions on Biomedical Engineering*, 42(1):68–71, 1995.

[37] B. N. Datta, *Numerical Linear Algebra and Applications*. Brooks/Cole Publishing Company, 1995.

[38] J. C. de Munck, "A linear discretization of the volume conductor boundary integral equation using analytically integrated elements", *IEEE Transactions on Biomedical Engineering*, 39 (9):986 – 990, 1992.

[39] J. C. de Munck, "The potential distribution in a layered anisotropic spheroidal volume conductor", *Journal of Applied Physics*, 64(2):464–470, July 1988.

[40] J. C. de Munck and M. J. Peters, "A fast method to compute the potential in the multiphere model", *IEEE Transactions on Biomedical Engineering*, 40(11):1166–1174, November 1993.

[41] J. C. de Munck, B. W. Van Dijk, and H. Spekreijse, "Mathematical dipoles are adequate to describe realistic generators of human brain activity", *IEEE Transactions on Biomedical Engineering*, 35(11):960–965, November 1988.

[42] J. J. Ermer, J. C. Mosher, S. Baillet, and R. M. Leahy, "Rapidly recomputable EEG forward models for realistic head shapes", *Physics in Medicine and Biology*, 46(4):1265–1281, 2001.

[43] Y. Eshel, S. Witman, M. Rosenfeld, and Abboud S., "Correlation between skull thickness asymmetry and scalp potential estimated by a numerical model of the head", *IEEE Transactions on Biomedical Engineering*, 42 (3):242–249, March 1995.

[44] T. C. Ferree, K. J. Eriksen, and D. M. Tucker, "Regional head tissue conductivity estimation for improved EEG analysis", *Biomedical Engineering, IEEE Transactions on*, 47(12):1584–1592, Dec. 2000, doi: 10.1109/10.887939.

[45] S. Finke, R. M. Gulrajani, and J. Gotman, "Conventional and reciprocal approaches to the inverse dipole localization problem of electroencephalography", *IEEE Transactions on Biomedical Engineering*, 50 (6): 657–666, 2003.

[46] E. Frank, "Electric potential produced by two point current sources in a homogeneous conducting sphere", *Jounal of Applied Physics*, 23(11): 1225–1228, November 1952.

[47] Karl J. Friston, editor, *Statistical Parametric Mapping: The Analysis of Functional Brain Images*. Academic Press Inc.,U.S., 2006.

[48] L. A. Geddes and L. E. Baker, "The specific resistance of biological material–a compendium of data for the biomedical engineer and physiologist.", *Medical and Biological Engineering*, 5(3):271–293, May 1967.

[49] D. B. Geselowitz, "On bioelectric potentials in an inhomogeneous volume conductor", *Biophysics Jounal*, 7:1–11, 1967.

[50] S. I. Gonçalves, J. C. de Munck, J. P. A. Verbunt, F. Bijma, R. M. Heethaar, and F. Lopes da Silva, "In vivo measurement of the brain and skull resistivities using an EIT-based method and realistic models for the head", *IEEE Transactions on Biomedical Engineering*, 50(6):754–767, June 2003.

[51] H. Gray, *Gray's Anatomy*. Longman Group Ltd., 1973.

[52] F. Grouiller, L. Vercueil, A. Krainik, C. Segebarth, P. Kahane, and O. David, "A comparative study of different artefact removal algorithms for EEG signals acquired during functional MRI", *Neuroimage*, 38(1): 124–137, October 2007.

[53] D. Güllmar, J. Haueisen, M. Eiselt, F. Giessler, L. Flemming, A. Anwander, T. R. Knösche, C. H. Wolters, M. Dümpelmann, D. S Tuch, and J. R. Reichenbach, "Influence of anisotropic conductivity on EEG source reconstruction: investigations in a rabbit model", *IEEE Transactions on Biomedical Engineering*, 53(9):1841–1850, September 2006.

[54] R. M. Gulrajani, *Bioelectricity and Biomagnetism*. John Wiley & Sons, Inc, New York, 1998.

[55] D. Gutiérrez, A. Nehorai, and C. H. Muravchik, "Estimating brain conductivities and dipole source signals with eeg arrays.", *IEEE Transactions on Biomedican Engineering*, 51(12):2113–2122, December 2004.

[56] H. Hallez, P. Van Hese, P. Boon, I. Lemahieu, and R. Van de Walle, "Incorporation of anisotropy in realistic head models for EEG source localisation", In *Abstracts of the 4th FTW PhD symposium*, Gent, December 2003.

[57] H. Hallez, P. Van Hese, P. Claeys, I. Lemahieu, and R. Van de Walle, "The influence of anisotropic electrical properties of brain tissues on EEG source localisation", *Epilepsia*, 45:177, June 2004.

[58] H. Hallez, B. Vanrumste, P. Van Hese, P. Boon, and Y. D'Asseler, "Can FDM be used to incorporate anisotropy in EEG dipole source localisation?", In *Abstracts of the 5th FTW PhD symposium*, Gent, 12 2004.

[59] H. Hallez, B. Vanrumste, P. Van Hese, P. Boon, Y. D'Asseler, and R. Van de Walle, "Can finite difference methode be used to incorporate anistropy in eeg dipole source localisation?", In *Abstract book of the 4th Belgian day on Biomedical Engineering*, page 31, Brussel, 10 2004.

[60] H. Hallez, P. Van Hese, B. Vanrumste, P. Boon, Y. D'Asseler, I. Lemahieu, and R. Van de Walle, "Dipole localization errors due to not incorporating compartments with anisotropic conductivities: Simulation study in a spherical head model", *International Journal of Bioelectromagnetism*, 7:134–137, 2005.

[61] H. Hallez, P. Van Hese, B. Vanrumste, P. Boon, Y. D'Asseler, I. Lemahieu, and R. Van de Walle, "Dipole localization errors due to not incorporating compartments with anisotropic conductivities: Simulation study in a spherical head model", In *Abstract book of the 5th International Symposium on Noninvasive Functional Source Imaging within the Human Brain and Heart*, page 21, Minneapolis, 5 2005.

[62] H. Hallez, P. Van Hese, B. Vanrumste, P. Boon, Y. D'Asseler, I. Lemahieu, and R. Van de Walle, "The anisotropic versus the isotropic head model in the presence of noise", In *Proceedings of the 3rd European Medical and Biological Engineering Conference*, page 6 pp on CDrom, Prague, 11 2005.

[63] H. Hallez, B. Vanrumste, P. Van Hese, P. Boon, Y. D'Asseler, and I. Lemahieu, "Dipole localization errors due to not incorporating compartments with anisotropic conductivities: Simulation study in a spherical head model", In *Sixth FirW PhD Symposium*, page on CD, 11 2005.

[64] H. Hallez, B. Vanrumste, P. Van Hese, Y. D'Asseler, I. Lemahieu, and R. Van de Walle, "A finite difference method with reciprocity used to incorporate anisotropy in electroencephalogram dipole source localization", *Physics in Medicine and Biology*, 50:3787–3806, 2005.

[65] H. Hallez, B. Vanrumste, S. Delputte, P. Van Hese, Y. D'Asseler, R. Van de Walle, and I. Lemahieu, "Dipole localization errors due to not incorporating anisotropic conductivities in realistic headmodels", In *Proceedings of the IEEE/EMBS Benelux symposium, Belgian Day on Biomedical Engineering*, page 91, Brussel, 12 2006.

[66] H. Hallez, A. Vergult, R. Phlypo, P. Van Hese, W. De Clercq, Y. D'Asseler, R. Van de Walle, B. Vanrumste, W. Van Paesschen, S. Van Huffel, and I. Lemahieu, "Muscle and eye movement artifact removal prior to EEG source localization", *Proceedings of the 28th Annual International Conference of the IEEE Engineering in Medicine and Biology Society (EMBS)*, 1:1001–1005, 2006.

[67] H. Hallez, B. Vanrumste, S. Delputte, P. Van Hese, S. Assecondi, Y. D'Asseler, and I. Lemahieu, "Dipole estimation errors in EEG source localization due to not incorporating anisotropic conductivities of white matter in realistic head models", In *Proceedings of the joint meeting of the 6th International Symposium on Noninvasive Functional Source Imaging of the Brain and Heart and the International Conference on Functional Biomedical Imaging*, pages 90–93, 2007.

[68] H. Hallez, B. Vanrumste, S. Delputte, P. Van Hese, Y D'Asseler, and I Lemahieu, "Importance of including anisotropic conductivities of grey matter in eeg source localization", *International Journal of Bioelectromagnetism*, 9:105–106, 2007.

[69] H. Hallez, B. Vanrumste, R. Grech, J. Muscat, Wim De Clercq, A. Vergult, Y. D'Asseler, K. P. Camilleri, S. G. Fabri, S. Van Huffel, and I. Lemahieu, "Review on solving the forward problem in eeg source analysis", *Journal of Neuroengineering and Rehabilitation*, 4(46), 2007.

[70] H. Hallez, B. Vanrumste, P. Van Hese, S. Delputte, and I. Lemahieu, "Dipole estimation errors due to differences in modeling anisotropic conductivities in realistic head models for EEG source analysis", *Physics in Medicine and Biology*, 53(7):1877–1894, 2008.

[71] J. Hara, T. Musha, and W. R. Shankle, "Approximating dipoles from human EEG activity: The effect of dipole source configuration on dipolarity using single dipole models", *IEEE Transacions in Biomedical Engineering*, 46(2):125–129, February 1999.

[72] J. Haueisen, D. S. Tuch, C. Ramon, P. H. Schimpf, V. J. Wedeen, J. S. George, and J. W. Belliveau, "The influence of brain tissue anisotropy on human EEG and MEG", *NeuroImage*, 15:159–166, 2002.

[73] B. He, T. Musha, Y. Okamoto, S. Homma, Y. Nakajima, and T. Sato, "Electric dipole tracing in the brain by means of the boundary element method and its accuracy", *IEEE Transactions on Biomedical Engineering*, 34(6):406–414, 1987.

[74] B. He, D. Yao, and J. Lian, "High-resolution eeg: on the cortical equivalent dipole layer imaging", *Clinical Neurophysiology*, 113(2):227–35, 2002.

[75] F.A. Hinchey, *Vectors and Tensors for Engineers and Scientists*. Wiley, John & Sons, Incorporated, December 1976, ISBN: 0470151943.

[76] R. Hoekema, K. Venner, J. Struijk, and J. Holsheimer, "Multigrid solution of the potential field in modeling electrical nerve stimulation", *Computers and Biomedical Research*, 31:348–362, 1998.

[77] R. Hoekema, G. H. Wieneke, F. S. S. Leijten, C. W. M. van Veelen, P. C. van Rijen, G. J. M. Huiskamp, J. Ansems, and A. C. van Huffelen, "Measurement of the conductivity of skull, temporarily removed during epilepsy surgery.", *Brain Topography*, 16(1):29–38, 2003.

[78] M. A. Huerta and G. Gonzalez, "The surface potentials produced by electric sources in stratified spherical and prolate spheroidal volume conductors", *International Journal of Electronics*, 54(5):657–671, 1983.

[79] J. R. Hughes, "The significance of the interictal spike discharge: a review", *Journal of Clinical Neurophysiology*, 6:207–226, 1989.

[80] G. J. Huiskamp, M. Vroeijenstijn, R. van Dijk, G. Wieneke, and A.C. van Huffelen, "The need for correct realistic geometry in the inverse EEG problem", *IEEE Transactions on Biomedical Engineering*, 46(11):1281–1287, November 1999.

[81] J. D. Jackson, *Classical Electrodynamics*. John Wiley & Sons, 1998.

[82] T. Jiang, A. Luo, X. Li, and F. Kruggel, "A comparative study of global optimization approaches to MEG source localization", *International Journal of Computational Mathematics*, 80:305–324, 2003.

[83] C. R. Johnson, "Numerical methods for bio-electric field problems", In Joseph D Bronzino, editor, *The biomedical engineering handbook*, chapter 12. CRC press, IEEE press, 1995.

[84] D. Johnston and S. M.-S. Wu, *Foundations of Cellular Neurophysiology*. the MIT Press, Massachusetts Institute of Technology, 1994.

[85] F. Kariotou, "Electroencephalography in ellipsoidal geometry", *Journal of Mathematical Analysis and Applications*, 290:324–42, 2004.

[86] D. Khosla, M. Singh, and M. Don, "Spatio-temporal EEG source localization using simulated annealing", *IEEE Transactions on Biomedical Engineering*, 44:1075–1091, 1997.

[87] L. G. Kiloh, A. J. Mc Comas, J. W. Osselton, and Upton A. R. M., *Clinical Electroencephalography*. Butterworths, 1981.

[88] P. Laarne, H. Eskola, J. Hyttinen, V. Suikho, and J. Malmivuo, "Validation of a detailed computer model for the electric fields in the brain", *Journal of Medical Engineering and Technology*, 19(2):84–87, March 1995.

[89] P. Laarne, J. Hyttinen, S. Dodel, J. Malmivuo, and H. Eskola, "Accuracy of two dipolar inverse algorithms applying reciprocity for forward calculation", *Computers and Biomedical Research*, 33(3):172–185, 2000.

[90] Y. Lai, W. van Drongelen, L. Ding, K. E. Hecox, V. L. Towle, D. M. Frim, and B. He, "Estimation of in vivo human brain-to-skull conductivity ratio from simultaneous extra- and intra-cranial electrical potential recordings.", *Clinical Neurophysiology*, 116(2):456–465, February 2005.

[91] D. Le Bihan and P. van Zijl, "From the diffusion coefficient to the diffusion tensor", *NMR in Biomedicine*, 15:431–434, 2002.

[92] M. Liehr and J. Haueisen, "Experimentally observed influence of anisotropic compartments in a volume conductor on magnetic field distribution generated by artificial current dipoles", *International Journal of Bioelectromagnetism*, 7(1):131–133, 2005.

[93] J.K. Mai, J. Assheuer, and G. Panixos, *Atlas of the Human Brain*. Academic Press, San Diego, 1998.

[94] M. Malik, K. F. Smits, and F. W. Lindemans, "Effects of anisotropic myocardial conductivity in model of defibrillation current density distribution.", *Medical and Biological Engineering and Computing*, 32(4 Suppl): S34–S40, July 1994.

[95] J. Malmivuo and R. Plonsey, *Bioelectromagnetism: Principles and Applications of Bioelectric and Biomagnetic Fields*. Oxford University Press, New York, 1995.

[96] G. Marin, C. Guerin, S. Baillet, L. Garnero, and G. Meunier, "Influence of skull anisotropy for the forward and inverse problem in EEG: simulation studies using FEM on realistic head models.", *Human Brain Mapping*, 6 (4):250–269, 1998.

[97] J. C. Maxwell, *A Treatise on electricity & magnetism*. Dover Publications Inc., 1954.

[98] P. Meijs and M. J. Peters, "The EEG and MEG using a model of eccentric spheres to describe the human head", *IEEE Transactions on Biomedical Engineering*, 34:913–920, 1987.

[99] C. M. Michel, M. M. Murray, G. Lantz, S. Gonzalez, and R. Spinelli L. Grave de Peralta, "EEG source imaging", *Clinical Neurophysiology*, 115 (10):2195–2222, 2004.

[100] A. R. Mitchell and D. F. Griffiths, *The Finite Difference Method in Partial Differential Equations*. John Wiley & Sons, 1980.

[101] M. Mohr, *The simulation of Bioelectric Fields: the Forward and Inverse Problem in Electro-encephalographic Source Analysis*, PhD thesis, Universität Erlangen-Nürnberg, 2004.

[102] M. Mohr and B. Vanrumste, "Comparing iterative solvers for linear systems associated with the finite difference discretisation of the forward problem in electroencaphalographic source analysis", *Medical and Biological Engineering and Computing*, 41(1):75–84, 2003.

[103] J. C. Mosher and R. M. Leahy, "Source localization using recursively applied and projected (RAP) MUSIC", *IEEE Transactions on Signal Processing*, 47:332–340, 1999.

[104] L. A. Neilson, M. Kovalyov, and Z. J. Koles, "A computationally efficient method for accurately solving the EEG forward problem in a finely discretized head model.", *Clinical Neurophysiology*, 116(10):2302–2314, October 2005.

[105] P. W. Nicholson, "Specific impedance of cerebral white matter.", *Experimental Neurolphysiology*, 13(4):386–401, December 1965.

[106] E. Niedermeyer and F. Lopez da Silva, "Epileptic seizure disorders", In E. Niedermeyer and F. Lopes da Silva, editors, *Electroencephalography: Basic Principles, Clinical Applications and Related Fields*, chapter 28, pages 461–564. Williams and Wilkins, Baltimore, Maryland, 3rd edition, 1993.

[107] Ernst Niedermeyer and Fernando Lopez Da Silva, *Electroencephalography: Basic Principles, Clinical Applications, and Related Fields*. Lippincott Williams & Wilkins, 5 edition, 2004.

[108] S. H. Oh, S. Y. Lee, M. H. Cho, T.-S. Kim, and I. H. Kim, "Electrical conductivity estimation from diffusion tensor and T2: a silk yarn study", In *Proceedings of the International Society of Magnetic Resonance in Medicine*, 2006.

[109] T.F. Oostendorp, J. Delbeke, and D.F. Stegeman, "The conductivity of the human skull: results of in vivo and in vitro measurements", *IEEE Transactions on Biomedican Engineering*, 47(11):1487–1492, November 2000.

[110] Niels Ottosen and Hans Peterson, *Introduction to the finite element method*. Prentice hall, 1992.

[111] M. Panizo, A. Castellanos, and J. Rivas, "Finite-difference operators in inhomogeneouw anisotropic media", *Journal of Applied Physics*, 48(3): 1054–1057, March 1977.

[112] R. D. Pascual-Marqui, "Review of methods for solving the EEG inverse problem", *International journal of bioelectromagnetism*, 1:75–86, 1999.

[113] R. Plonsey, *Bioelectric Phenomena*. McGraw-Hill, New York, 1969.

[114] R. Plonsey and D. B. Heppner, "Considerations of quasistationarity in electrophysiological systems", *Bulletin of Mathematical Biophysics*, 29 (4):657–664, 1967.

[115] R. Pohlmeier, H. Buchner, G. Knoll, A. Rienacker, R. Beckmann, and J. Pesch, "The influence of skull - conductivity misspecification on inverse source localisation in realistically shaped finite element models", *Brain Topography*, 9(3):157–162, 1997.

[116] W.H. Press, S.A. Teukolsky, W.T. Vetterling, and B.P. Flannery, *Numerical Recipes in C*. Cambridge University Press, Cambridge, 1995, pp. 430-443.

[117] G. W. Pruis, B. H. Gilding, and M. J. Peters, "A comparison of different numerical methods for solving the forward problem in eeg and meg.", *Physiol Meas*, 14 Suppl 4A:A1–A9, Nov 1993.

[118] A. Pursula, J. Nenonen, E. Somersalo, E.J. Ilmoniemi, and T. Katila, "Bioelectromagnetic calculations in anisotropic volume conducters", *Proceedings of Biomag2000*, pages 659–662, August 2000.

[119] R. Putz and R. Pabst, editors, *Sobotta, Atlas der Anatomie des Menschen*. Urban & Fischer, München, 1999.

[120] C. Ramon, J. Haueisen, and P. H. Schimpf, "Influence of head models on neuromagnetic fields and inverse source localizations.", *BioMedical Engineering Online*, 5:55, 2006.

[121] C. Ramon, P.H. Schimpf, and J. Haueisen, "Influence of head models on EEG simulations and inverse source localizations", *Biomedical Engineering Online*, 5:10, 2006.

[122] T. G. Reese, O. Heid, R. M. Weisskoff, and V. J. Wedeen, "Reduction of eddy-current-induced distortion in diffusion MRI using a twice-refocused spin echo.", *Magnetic Resonance in Medicine*, 49(1):177–182, Jan 2003, doi: 10.1002/mrm.10308, URL `http://dx.doi.org/10.1002/mrm.10308`.

[123] Rojansky, *Electromagnetic fields and waves*. Dover, 1971.

[124] B. J. Roth, M. Balish, A. Gorbach, and S. Sato, "How well does a three-sphere model predict positions of dipoles in a realistically shaped head?", *Electroencephalography and clinical Neurophysiology*, 87:175–184, 1993.

[125] B. J. Roth, D. Ko, I. R. von Albertini-Carletti, D. Scaffidi, and Susumu Sato, "Dipole localization in patients with epilepsy using the realistic shaped head model", *Electroencephalography and clinical Neurophysiology*, 102(3):160–166, March 1997.

[126] S. Rush and D. A. Driscoll, "Current distribution in the brain from surface electrodes", *Anesthetics and Analgesia*, 47:717–723, 1968.

[127] S. Rush and D.A. Driscoll, "EEG electrode sensitivity - an application of reciprocity", *IEEE Transactions on Biomedical Engineering*, 16(1): 15–22, 1969.

[128] Y. Saad, *Iterative methods for sparse linear systems*. SIAM, Philadelphia, 2nd edition edition, 2003.

[129] H. I. Saleheen and T. N. Kwong, "New finite difference formulations for general inhomogeneous anisotropic bioelectric problems", *IEEE Transactions on Biomedical Engineering*, 44(9):800–809, September 1997.

[130] H. I. Saleheen and T. N. Kwong, "A new three-dimensional finite-difference bidomain formulation for inhomogeneous anisotropic cardiac tissues", *IEEE Transactions on Biomedical Engineering*, 45(1):15–24, 1998.

[131] Y. Salu, L. G. Cohen, D. Rose, S. Sato, C. Kufta, and M. Hallett, "An improved method for localizing electric brain dipoles", *IEEE Transactions on Biomedical Engineering*, 37:699–705, 7 1990.

[132] J. Sarvas, "Basic mathematical and electromagnetic concepts of the biomagnetic inverse problem", *Physics in Medicine and Biology*, 32(1):11–22, 1987.

[133] P. H. Schimpf, C. Ramon, and J. Haueisen, "Dipole models for the EEG and MEG", *IEEE Transactions on Biomedical Engineering*, 49(5):409–418, 2002.

[134] K. Sekihara, K.E. Hild, and S.S. Nagarajan, "A novel adaptive beamformer for MEG source reconstruction effective when large background brain activities exist", *IEEE Transactions on Biomedical Engineering*, 53 (9):1755–1764, September 2006.

[135] A.K. Sen and S. Torquato, "Effective conductivity of anisotropic two-phase composite media", *Physical Review B*, 39(7):4504–4515, 1989.

[136] J. Sijbers, B. Vanrumste, G. Van Hoey, P. Boon, M. Verhoye, A. Van der Linden, and D. Van Dyck, "Automatic localisation of EEG electrode markers within 3D MR data", *Magnetic Resonance Imaging*, 18:485–488, 2000.

[137] E. J. Speckmann and C. E. Elger, "Introduction to the neurophysiology, basis of the EEG and DC potentials", In E. Niedermeyer and F. Lopes da Silva, editors, *Electroencephalography, Basic Principles, Clinical Applications and Related Fields*, chapter 1, pages 1–13. Urban and Schwarzenberg, 2nd edition, 1987.

[138] J. F Thompson, B. K. Soni, and N. P. Weatherrill, *Handbook of grid generation*. CRC Press, 1998.

[139] D. S. Tuch, V. J. Wedeen, A. M. Dale, J. S. George, and J. W. Belliveau, "Conductivity tensor mapping of the human brain using diffusion tensor MRI", *Proceedings in National Academie of Science*, 98(20):11697–11701, September 2001.

[140] G. Van Hoey, Vanrumste B., M. D'Havé, R. Van de Walle, I. Lemahieu, and P. Boon, "Influence of measurement noise and electrode mislocation on EEG dipole-source localisation", *Medical & Biological Engineering & Computing*, 38:287–296, 2000.

[141] G. Van Hoey, J. De Clercq, B. Vanrumste, R. Van de Walle, M. D'Have, I. Lemahieu, and P. Boon, "EEG dipole localization using artificial neural networks", *Physics in Medicine and Biology*, 45:997–1011, 2000.

[142] W. Van Paesschen, P. Dupont, S. Sunaert, K. Goffin, and K. Van Laere, "The use of spect and pet in routine clinical practice in epilepsy.", *Current Opinions in Neurology*, 20(2):194–202, April 2007.

[143] B. Vanrumste, G. Van Hoey, R. Van de Walle, M. D'Havé, I. Lemahieu, and P. Boon, "The influence of the ventricular system in EEG dipole analysis", In *Abstract Book of the 10th World Congress of the International Society for Brain Electromagnetic Topography*, 1999.

[144] B. Vanrumste, G. Van Hoey, R. Van de Walle, M. D'Have, I. Lemahieu, and P. Boon, "Dipole location errors in electroencephalogram source analysis due to volume conductor model errors", *Medical & Biological Engineering & Computing*, 38:528–534, 2000.

[145] B. Vanrumste, G. Van Hoey, R. Van de Walle, M. D'Havé, I. Lemahieu, and P. Boon, "The validation of the finite difference method and reciprocity for solving the inverse problem in EEG dipole source analysis", *Brain Topography*, 14(2):83–92, 2001.

[146] B. Vanrumste, G. Van Hoey, R. Van de Walle, M. D'Havé, I. Lemahieu, and P. Boon, "The performance of the spherical head model compared to the realistic head model in dipole localization with noisy EEG", *Medical Engineering and Physics*, 24(6):403–418, 2002.

[147] F. Vatta, P. Bruno, and P. Inchingolo, "Multiregion bicentric-spheres models of the head for the simulation of bioelectric phenomena", *IEEE Transactions in Biomedical Engineering*, 52(3):382–389, 2005.

[148] H. L. F. von Helmholtz, "Ueber einige Gesetze der Verteilung elektrischer Ströme in körperlichen Leitern mit Anwendung auf die tierisch elektrischen Versuche", *Ann. Physik und Chemie*, 89:211–233,354–377, 1853.

[149] D. Weinstein, L. Zhukov, and C. Johnson, "Lead-field bases for electroencephalography source imaging", *Annals of Biomedical Engineering*, 28:1059–1065, 2000.

[150] C. H. Wolters, A. Anwander, M. Koch, S. Reitzinger, M. Kuhn, and M. Svensen, *Forschung und wissenschaftliches Rechnen, Contributions to the Heinz-Billing Award*, chapter Influence of head tissue conductivity anisotropy on human EEG and MEG using fast high resolution finite element modeling, based on a parallel algebraic multigrid solver, pages 111–157. Gesellschaft für wissenschaftliche Datenverarbeitung mbH Göttingen, 2001, pp. 111-157.

[151] C. H. Wolters, M. Kuhn, A. Anwander, and S. Reitzinger, "A parallel algebraic multigrid solver for finite element method based source localization in the human brain", *Computing and Visualization in Science*, 5: 165–177, 2002.

[152] C. H. Wolters, L. Grasedyck, and W. Hackbusch, "Efficient computation of lead field bases and influence matrix for the FEM-based EEG and MEG inverse problem", *Inverse Problems*, 20(4):1099–1116, 2004.

[153] C. H. Wolters, A. Anwander, X. Tricoche, D. Weinstein, M. A. Koch, and R. S. MacLeod, "Influence of tissue conductivity anisotropy on EEG/MEG field and return current computation in a realistic head model: a simulation and visualization study using high-resolution finite element modeling.", *Neuroimage*, 30(3):813–826, Apr 2006.

[154] C. H. Wolters, H. Köstler, C. Möller, J. Härdtlein, and A. Anwander, "Numerical approaches for dipole modeling in finite element method based source analysis", In *International Congres Series*, 2007, doi: 10.1016/j.ics.2007.02.014.

[155] C. H. Wolters, U. Hartmann, M. Koch, and F. Kruggel, "New methods for improved and accelerated fe-volume conductor modelling in eeg/meg-source localisation", *Proceedings of 4th Symposium on Computer methods in Biomechanics and Biomedical Engineering*, pages 489–494, 99.

[156] C.H. Wolters, *Influence of Tissue Conductivity Inhomogeneity and Anisotropy on EEG/MEG based Source Localisation in the Human Brain*, PhD thesis, Universität Leipzig, 2003.

[157] C.H. Wolters, A. Anwander, G. Berti, and U. Hartmann, "Geometry-adapted hexahedral meshes improve accuracy of finite-element-method-based eeg source analysis.", *IEEE Transactions in Biomedical Engineering*, 54(8):1446–1453, Aug 2007.

[158] C.H. Wolters, H. Köstler, C. Möller, J. Härdtlein, L. Grasedyck, and W. Hackbusch, "Numerical mathematics of the subtraction approach for the modeling of a current dipole in eeg source reconstruction using finite

element head models", *SIAM Journal on Scientific Computing, vol.30, issue 1, pp.24-45*, 30(1):24–45, 2007.

[159] Z. Zhang, "A fast method to compute surface potentials generated by dipoles within multilayer anisotropic spheres", *Physics in Medicine and Biology*, 40:335–349, 1995.

List of Publications

Publications in a Journal

[1] G. Crevecoeur, H. Hallez, P. Van Hese, Y. D'Asseler, L. Dupre and R. Van de Walle. "EEG source analysis using space mapping techniques". *Journal of Computational and Applied Mathematics*, 215:339–347, 2008.

[2] G. Crevecoeur, H. Hallez, P. Van Hese, Y. D'Asseler, L. Dupré and R. Van de Walle. "A hybrid algorithm for solving the EEG inverse problem from spatio-temporal EEG data". *Medical and Biological Engineering and Computing*, 2008.

[3] H. Hallez, M. De Vos, B. Vanrumste, P. Van Hese, K. Van Laere, P. Dupont, W. Van Paesschen, S. Van Huffel and I. Lemahieu. "Removing muscle and eye artifacts using blind source separation techniques in ictal EEG source imaging", 2008. Submitted to Clinical Neurophysiology.

[4] H. Hallez, B. Vanrumste, S. Assecondi, S. Staelens and I. Lemahieu. "Dipole estimation errors due to not incorporating anisotropic conductivities in realistic head models for EEG source analysis", 2008. Submitted to Neuroimage.

[5] H. Hallez, B. Vanrumste, P. Van Hese, S. Delputte and I. Lemahieu. "Dipole estimation errors due to differences in modeling anisotropic conductivities in realistic head models for EEG source analysis". *Physics in Medicine and Biology*, 53(7):1877–1894, 2008.

[6] P. Van Hese, B. Vanrumste, H. Hallez, G. Carroll, K. Vonck, R. Jones, P. Bones, Y. D'Asseler and I. Lemahieu. "Detection of focal epileptiform events in the EEG by spatio-temporal dipole clustering." *Clinical Neurophysiology*, 119(8):1756–1770, 2008.

[7] G. Crevecoeur, H. Hallez, P. Van Hese, Y. D'Asseler, L. Dupre and R. Van de Walle. "Influence of noise on EEG source analysis using space mapping techniques". *International Journal of Applications in Electromagnetics and Mechanics*, 25:383–387, 2007.

[8] H. Hallez, B. Vanrumste, S. Delputte, P. Van Hese, Y. D'Asseler and I. Lemahieu. "Importance of including anisotropic conductivities of grey matter in EEG source localization". *International Journal of Bioelectromagnetism*, 9:105–106, 2007.

[9] H. Hallez, B. Vanrumste, R. Grech, J. Muscat, W. D. Clercq, A. Vergult, Y. D'Asseler, K. P. Camilleri, S. G. Fabri, S. V. Huffel and I. Lemahieu. "Review on solving the forward problem in EEG source analysis". *Journal of Neuroengineering and Rehabilitation*, 4(46), 2007.

[10] J. D. Reuck, I. Claeys, S. Martens, P. Vanwalleghem, G. V. Maele, R. Phlypo and H. Hallez. "Computed tomographic changes of the brain and clinical outcome of patients with seizures and epilepsy after an ischaemic hemispheric stroke." *European Journal of Neurology*, 13(4):402–407, 2006.

[11] H. Hallez, P. Van Hese, B. Vanrumste, P. Boon, Y. D'Asseler, I. Lemahieu and R. Van de Walle. "Dipole Localization Errors due to not Incorporating Compartments with Anisotropic Conductivities: Simulation Study in a Spherical Head Model". *International Journal of Bioelectromagnetism*, 7:134–137, 2005.

[12] H. Hallez, B. Vanrumste, P. Van Hese, Y. D'Asseler, I. Lemahieu and R. Van de Walle. "A finite difference method with reciprocity used to incorporate anisotropy in electroencephalogram dipole source localization". *Physics in Medicine and Biology*, 50:3787–3806, 2005.

[13] H. Hallez, P. Van Hese, P. Claeys, I. Lemahieu and R. Van de Walle. "The influence of anisotropic electrical properties of brain tissues on EEG source localisation". *Epilepsia*, 45:177, 2004.

Publications in a Conference Proceeding

[1] S. Assecondi, H. Hallez, P. Van Hese, A. Bianchi, S. Staelens, P. Boon and I. Lemahieu. "Blind source separation to remove BCG artifact from EEG/fMRI data". In "Conferece Proceedings Liege Image Days 2008: Medical Imaging", page 1 pp. Liege, 2008.

[2] S. Assecondi, P. Van Hese, H. Hallez, Y. D'Asseler, I. Lemahieu, A. Bianchi and P. Boon. "Ballistocardiographic artifact removal from simultaneous EEG/FMRI recording by means of canonical correlation analysis". In "Proceedings of the International Conference on Bio-inspired systems and signal processing, BIOSIGNALS 2008", volume 2, pages 6 pp. on cd–rom. Funchal, 2008.

[3] S. Assecondi, H. Hallez, Y. D'Asseler and I. Lemahieu. "Comparison of different auto-solid angle approximations in BEM for EEG dipole source localization". In "Proceedings of the Joint Meeting of the 6th International Symposium on Noninvasive Functional Source Imaging of the Brain and Heart and the International Conference on Functional Biomedical Imaging (NFSI-ICFBI 2007)", pages 70–73. 2007.

[4] F. Chen, H. Hallez, P. Van Hese, Y. D'Asseler and I. Lemahieu. "Dipole Estimation Errors Due to Skull Conductivity Perturbations: Simulation Study in Spherical Head Models". In "Proceedings of the Joint Meeting of the 6th International Symposium on Noninvasive Functional Source Imaging of the Brain and Heart and the International Conference on Functional Biomedical Imaging (NFSI-ICFBI 2007)", pages 86–89. 2007.

[5] H. Hallez, M. De Vos, R. Phlypo, B. Vanrumste, P. Van Hese, Y. D'Asseler, W. Van Paesschen, S. Van Huffel and I. Lemahieu. "Can dipole modelling be improved by removing muscular and ocular artifacts from ictal scalp EEG?" In "Proceedings of the 3rd international IEEE EMBS conference on Neural Engineering", pages 252–255. Kohala Coast, Hawaii, 2007.

[6] H. Hallez, B. Vanrumste, S. Delputte, P. Van Hese, S. Assecondi, Y. D'Asseler and I. Lemahieu. "Dipole estimation errors in EEG source localization due to not incorporating anisotropic conductivities of white matter in realistic head models". In "Proceedings of the joint meeting of the 6th International Symposium on Noninvasive Functional Source Imaging of the Brain and Heart and the International Conference on Functional Biomedical Imaging", pages 90–93. 2007.

[7] G. Crevecoeur, H. Hallez, P. Van Hese, Y. D'Asseler, L. Dupré and R. Van de Walle. "Space mapping techniques for solving the inverse problem of EEG source analysis from spatio-temporal EEG data". In "OIPE 2006 - Proceedings of the 9th Workshop on Optimization and Inverse Problems in Electromagnetics", pages 169–170. Sorrento, 2006.

[8] H. Hallez, B. Vanrumste, S. Delputte, P. Van Hese, Y. D'Asseler, R. Van de Walle and I. Lemahieu. "Dipole localization errors due to not incorporating anisotropic conductivities in realistic headmodels". In "Proceedings of the IEEE/EMBS Benelux symposium, Belgian Day on Biomedical Engineering", page 91. Brussel, 2006.

[9] H. Hallez, A. Vergult, R. Phlypo, P. Van Hese, W. De Clercq, Y. D'Asseler, R. Van de Walle, B. Vanrumste, W. Van Paesschen, S. Van Huffel and I. Lemahieu. "Muscle and eye movement artifact removal prior to EEG source localization". *Proceedings of the 28th Annual International Conference of the IEEE Engineering in Medicine and Biology Society (EMBS)*, 1:1001–1005, 2006.

[10] R. Phlypo, P. V. Hese, H. Hallez, P. Boon, R. V. de Walle, Y. D'Asseler and I. Lamhieu. "Extracting the spike process from the EEG by spatially

constrained ICA." *Conference Proceedings of the IEEE Engineering in Medicine and Biology Society*, 1:5286–5289, 2006.

[11] R. Phlypo, P. Van Hese, H. Hallez, P. Boon, R. Van de Walle, Y. D'Asseler and I. Lemahieu. "PSVD:a method for robust, real time eye movement artifact rejection from the EEG". In "Proceedings of the 3rd International Conference on Advances in Medical, Signal and Information Processing", pages 4 pp on CD–rom. Glasgow, 2006.

[12] G. Crevecoeur, H. Hallez, P. Van Hese, Y. D'Asseler, L. Dupre and R. Van de Walle. "EEG source analysis using space mapping techniques". In "Book of abstracts 3rd International Conference on Advanced Computational Methods in Engineering", page 1 pp. Gent, 2005.

[13] G. Crevecoeur, H. Hallez, P. Van Hese, Y. D'Asseler, L. Dupre and R. Van de Walle. "EEG source analysis using space mapping techniques". In "Proceedings of the 3rd International Conference on Advanced Computational Methods in Engineering", page 8 pp. Gent, 2005.

[14] H. Hallez, P. Van Hese, B. Vanrumste, P. Boon, Y. D'Asseler, I. Lemahieu and R. Van de Walle. "The anisotropic versus the isotropic head model in the presence of noise". In "Proceedings of the 3rd European Medical and Biological Engineering Conference", page 6 pp on CDrom. Prague, 2005.

[15] H. Hallez, P. Van Hese, B. Vanrumste, P. Boon, Y. D'Asseler, I. Lemahieu and R. Van de Walle. "Dipole Localization Errors due to not Incorporating Compartments with Anisotropic Conductivities: Simulation Study in a Spherical Head Model". In "Abstract book of the 5th International Symposium on Noninvasive Functional Source Imaging within the Human Brain and Heart", page 21. Minneapolis, 2005.

[16] H. Hallez, B. Vanrumste, P. Van Hese, P. Boon, Y. D'Asseler and I. Lemahieu. "Dipole Localization Errors due to not Incorporating Compartments with Anisotropic Conductivities: Simulation Study in a Spherical Head Model". In "Sixth FirW PhD Symposium", page on CD. 2005.

[17] P. Van Hese, H. Hallez, B. Vanrumste, K. Vonck, G. Carroll, Y. D'Asseler, P. Boon, R. Van de Walle and I. Lemahieu. "Evaluation of spatial and temporal detection algorithms for interictal epileptiform EEG activity". In "Proceedings of the 1st annual IEEE BENELUX/DSP Valley Signal Processing Symposium, SPS-DARTS", pages 139–142. Antwerpen, 2005.

[18] P. Van Hese, J.-P. Martens, H. Hallez, P. Claeys, Y. D'Asseler, P. Boon, R. Van de Walle and I. Lemahieu. "Long-term analysis and description of interictal epileptiform activity in intracranial EEG records". In "Proceedings of the 3rd European Medical and Biological Engineering Conference", page 5 pp on CDrom. Prague, 2005.

[19] H. Hallez, B. Vanrumste, P. Van Hese, P. Boon and Y. D'Asseler. "Can FDM be used to incorporate Anisotropy in EEG Dipole Source Localisation?" In "Abstracts of the 5th FTW PhD symposium", Gent, 2004.

[20] H. Hallez, B. Vanrumste, P. Van Hese, P. Boon, Y. D'Asseler and R. Van de Walle. "Can finite difference methode be used to incorporate anistropy in EEG dipole source localisation?" In "Abstract book of the 4th Belgian day on Biomedical Engineering", page 31. Brussel, 2004.

[21] P. Van Hese, H. Hallez, B. Vanrumste, Y. D'Asseler and P. Boon. "Evaluation of Temporal and Spatial EEG Spike Detection Algorithms". In "Abstracts of the 5th FTW PhD symposium", Gent, 2004.

[22] P. Van Hese, H. Hallez, B. Vanrumste, Y. D'Asseler, P. Boon, R. Van de Walle and I. Lemahieu. "Evaluation of temporal and spatial EEG spike detection algorithms". In M. Nyssen, C. Veraart and P. Verdonck, editors, "Abstract book of the 4th Belgian day on Biomedical Engineering", page 28. Brussel, 2004.

[23] H. Hallez, P. Van Hese, P. Boon, I. Lemahieu and R. Van de Walle. "Incorporation of anisotropy in realistic head models for EEG source localisation". In "Abstracts of the 4th FTW PhD symposium", Gent, 2003.